Stabilité des paires de tourbillons contra-rotatifs: application au tourbillon de jeu dans les turbomachines

Vincent Brion

THÈSE DE DOCTORAT
DE L'ÉCOLE POLYTECHNIQUE

présentée par

Vincent Brion

pour obtenir le titre de

Docteur de l'Ecole Polytechnique

Spécialité : Mécanique

Stabilité des paires de tourbillons contra-rotatifs: application au tourbillon de jeu dans les turbomachines

soutenue le 7 octobre 2009

devant le jury composé de :

M.	P. Brancher	
M.	G. Casalis	
M.	L. Jacquin	*Directeur de thèse*
M.	F. Leboeuf	
M.	T. Leweke	*Rapporteur*
M.	M. Rossi	*Rapporteur*
M.	P. J. Schmid	
M.	D. Sipp	*Encadrant*

Résumé

La stabilité du tourbillon de jeu d'aubage dans les compresseurs est étudiée au travers d'un modèle équivalent de paires de tourbillons. L'objectif consiste à contrôler ce tourbillon en excitant ses instabilités hydrodynamiques, ce qui permettrait de le dissiper plus rapidement et d'augmenter les performances des turbomachines.

La première partie est dédiée à l'étude théorique des instabilités dans les paires de tourbillons. Un mode instable 2D du dipôle de Lamb-Chaplygin est d'abord présenté. On s'intéresse ensuite aux instabilités 3D, et à leur contrôle. Les instabilités de Crow et de Widnall, notamment avec champ de vitesse axial, sont calculées. L'utilisation d'un code de perturbation optimale permet ensuite d'optimiser la croissance de ces instabilités, ce qui fait apparaître l'importance des points de stagnation hyperbolique dans les croissances transitoires, et des possibilités de contrôle prometteuses pour les sillages d'avion de transport.

Le tourbillon de jeu est ensuite étudié en soufflerie, grâce à un montage permettant, dans une première configuration, de générer une paire de tourbillons tandis qu'une deuxième configuration, grâce à l'introduction d'une plaque séparatrice, génère un tourbillon en interaction avec la paroi. L'étude de l'écoulement moyen montre que la plaque plane modifie fortement le comportement du tourbillon. En ce qui concerne les instationnarités, l'instabilité de Crow est détectée dans le cas sans plaque mais pas dans le tourbillon avec plaque, ce qui semble indiquer que la paroi inhibe cette instabilité.

Mots clés : turbomachine, tourbillon, jeu, stabilité hydrodynamique, Crow, Widnall, perturbation optimale, point hyperbolique, Particle Image Velocimetry, fil chaud, sonde de pression 7 trous, contrôle, soufflerie.

Abstract

The stability of the tip leakage vortex in compressors is investigated through the model of vortex pairs. The goal is to control this vortex by boosting its hydrodynamic instabilities, in order to mitigate it more rapidly with the surrounding flow and increase performances of turbomachines.

The first part is dedicated to the theoretical study of instabilities in vortex pairs. A 2D unstable mode of the Lamb-Chaplygin dipole is presented. We then focus on the 3D instabilities, namely Crow and Widnall, with and without axial flow. An optimal perturbation algorithm is used in order to optimize the growth rate of these instabilities. We find that the hyperbolic stagnation points play a major role in the transient growth of energy, and that interesting possibilities exist to control aircraft trailing vortices.

The tip leakage vortex is then investigated in a wind tunnel, with an apparatus enabling two configurations. The first configuration produces two opposed and equal vortices while the second one, with a splitter plate, produce one vortex that interacts with the wall. The study of the mean flow shows that the wall modifies significantly the behaviour of the vortex. The Crow instability is detected without the splitter plate only. This suggests that the wall prevents the development of the Crow instability.

Keywords : turbomachinery, vortex, clearance, hydrodynamics stability, Crow, Widnall, optimal perturbation, hyperbolic point, Particle Image Velocimetry, hot-wire, 7-hole pressure probe, control, wind tunnel.

Remerciements

De longues années de thèse, beaucoup de personnes formidables rencontrées en chemin, et des souvenirs inoubliables ...

Merci à Denis Sipp de m'avoir accueillit dans son unité, de m'avoir lancé sur les tourbillons, et d'avoir partagé avec moi ses bonnes idées. Le projet côté soufflerie a pu être mené à bien grâce au concours d'un grand nombre d'acteurs, que je tiens à remercier vivement : François Lambert, qui a dessiné le montage d'après un cahier des charges difficile, Jean-Pierre Tobeli, qui a redémarré la soufflerie de zéro, Jean-François Pulizzi et Michel Agrapart, qui ont par un tour de main incroyable, réussi à monter la maquette et ses appendices en veine, Michel Vegran, Philippe Huet, Pascal Audo, les spécialistes des rafales, Jean-Marc Luyssen et Didier Coponet, Michel Gouhier de S3 pour les bouillies, la laser team, et les rois de l'expérimentation, Gilles Losfled et François Becavin, Didier Soulevant, Nicolas Severac pour la bonne ambiance de S5, Patrik Servel et Michel Erard pour leur soutien informatique. Je n'oublie pas Philippe Mourer qui a supervisé la fabrication du montage à l'atelier central.

Je ne compte pas les heures passées en soufflerie en compagnie de Michel Alaphilippe. Il m'est impossible de lui rendre ici tout ce qu'il m'a apporté. Je crois tout simplement que sans lui je n'aurais pas fait le dixième de ce que j'ai fait. Témoin de mes galères et de mon enthousiasme, compagnon de solitude, il a marqué mon séjour ici.

Ma thèse aurait été beaucoup plus triste aussi si je n'avais pas partagé beaucoup d'excellents moments avec les autres personnes du département. Je lance un immense merci à Serge Petit et à Florence Bouvier pour leur humour décapant. Je dois beaucoup également au temps passé avec Guy Rancarani, Claire Planchard, Yves Lesant, Marie-Claire Merienne, Corinne de Pablo, Angélique Baudelot, Dominique Grandson et Kurita Mitsuru, qui a décoré d'une joyeuse teinte japonaise ma dernière année ici.

La course à pied dans le bois de Meudon a été un vrai bonheur hebdomadaire. J'adresse donc ici ma profonde gratitude à Sébastien Girard, Yves Carpels, Thierry Pot, Jean-Paul Antony, Benjamin Leclaire, Yves Carpels, Pascal Molton et Gérald Courant. Ils ont été des compagnons d'effort extraordinaires.

J'adresse un merci très ému à tous mes proches compagnons de thèse. Ils m'ont beaucoup apporté et je n'oublierai pas de si tôt la franche camaraderie qui a régné ici. Un grand merci donc à Bruno Mangin, Paul Quantin Elias, Philippe Meliga, Benoît Gardarin, Olivier Marquet, Benjamin Leclaire, Samuel Davoust et Hugues Dekerret. Un grand merci également à Sarah Benbaba qui a su me supporter dans le bureau ces deux dernières années. Et puis je remercie aussi les autres stagiaires que j'ai eu le plaisir de rencontrer ici: Jean-Yves Andro, Olivier Thomas, Alexandre Barbagallo, Grégory Dergham, Cyril de Champvallins, Rasika Fernando.

Je ne peux pas oublier non plus le soutien de ma famille, et particulièrement celui de Anne qui a été à mes côtés tout le temps et a su s'adapter à mes humeurs vagabondes. Je ne pourrais jamais assez les en remercier.

Merci enfin à Laurent Jacquin d'avoir accepté d'être mon directeur de thèse, et de m'avoir fait confiance. Sans sa magie, je n'en serais sûrement pas là où j'en suis aujourd'hui.

Contents

Nomenclature **vii**

1 General introduction **1**
1.1 Tip clearance vortex . . . 3
1.1.1 Description . . . 3
1.1.2 Losses . . . 6
1.1.3 Flow unsteadiness . . . 6
1.1.4 Control . . . 7
1.2 Objectives of the thesis . . . 7
1.3 Approach . . . 8
1.4 Organization of the thesis . . . 8

2 Review on the stability of vortices **11**
2.1 Single vortices . . . 11
2.1.1 Existing models . . . 11
2.1.2 Stability . . . 13
2.1.3 Transient growth . . . 17
2.2 Vortex pairs . . . 19
2.2.1 Existing models . . . 19
2.2.2 Stability . . . 20
2.3 Important problems of vortex dynamics . . . 21
2.3.1 Vortex meandering . . . 21
2.3.2 Turbulence . . . 22
2.3.3 Vortex decay . . . 22

I Methods **25**

3 Numerical method **27**
3.1 Perturbation theory . . . 27
3.1.1 Description of the flow . . . 27
3.1.2 Perturbation theory . . . 29
3.2 Numerical simulations . . . 33
3.2.1 Time scheme . . . 33
3.2.2 Space discretization . . . 34
3.2.3 Finite elements . . . 35
3.2.4 Uzawa algorithm . . . 36
3.2.5 Case of the linearized equations . . . 36
3.2.6 Implementation of the boundary conditions . . . 36
3.3 Normal modes . . . 36
3.3.1 Equations . . . 36
3.3.2 Arnoldi method . . . 37

3.4 Optimal perturbations . . . 39
3.4.1 Energy of the perturbation . . . 39
3.4.2 Transient growth . . . 39
3.4.3 Optimization method . . . 39

4 Experimental set-up **43**
4.1 Wind tunnel . . . 43
4.1.1 Presentation . . . 43
4.1.2 Experimental model . . . 44
4.1.3 Flow separation over the wing . . . 45
4.1.4 Data acquisition . . . 46
4.1.5 Boundary layer on the splitter plate . . . 47
4.1.6 Control of the angle of attack . . . 48
4.2 Measurement techniques . . . 49
4.2.1 Seven hole pressure probe . . . 49
4.2.2 Hot-wire . . . 50
4.2.3 Temperature sensor . . . 52
4.2.4 PIV . . . 53
4.2.5 Tomoscopy . . . 53
4.2.6 Effect of the adjustment of the apparatus on the data . . . 54

II Theoretical results **57**

5 Two-dimensional instability of vortex pairs **59**
5.1 Methodology . . . 61
5.1.1 Base flow . . . 61
5.1.2 Numerical simulation . . . 62
5.2 Stability analysis . . . 63
5.2.1 Linearized simulation with white noise . . . 63
5.2.2 Normal mode approach . . . 64
5.2.3 Comparison of the growth rate with previous work . . . 66
5.2.4 Effect of k and Re . . . 66
5.2.5 Discussion . . . 67
5.2.6 Symmetric instability . . . 69
5.3 Non-linear evolution . . . 69
5.3.1 Fully non-linear . . . 69
5.3.2 Frozen base flow . . . 71

6 Optimal perturbations in vortex pairs **77**
6.1 Method . . . 78
6.1.1 Steady state . . . 78
6.1.2 Perturbations . . . 78
6.1.3 Optimal perturbation . . . 80
6.2 Results . . . 80
6.2.1 2D vortex pair . . . 80
6.2.2 Optimal perturbation at the Crow wavelength . . . 82
6.2.3 Optimal perturbation at the Widnall wavelength . . . 88
6.2.4 Effect of the axial flow . . . 91

III Experimental results **97**

7 Time-averaged properties of the vortices **99**
7.1 Flow in C1 . . . 99
7.1.1 Formation of the vortex at large gap . . . 99
7.1.2 Driving mechanism of the leakage flow . . . 100
7.1.3 Characteristics of the tip vortex . . . 100
7.1.4 Large/small gap regimes . . . 105
7.2 Influence of the splitter plate . . . 107
7.2.1 Evolution of the vorticity . . . 107
7.2.2 Drifting motion . . . 107
7.2.3 Vortex rebound . . . 108
7.2.4 Vortex characteristics . . . 108
7.3 Comparison between C1 and C2 . . . 109
7.3.1 Vortex properties . . . 109
7.3.2 Flow stability . . . 110
7.4 Losses due to the tip leakage flow . . . 111
7.4.1 Governing equation . . . 111
7.4.2 Observation of the pressure losses . . . 112
7.4.3 Influence of τ on the mass-averaged loss . . . 113

8 Experimental analysis of the Crow instability **117**
8.1 A first glimpse of the flow unsteadiness . . . 118
8.2 Detection of the Crow instability . . . 119
8.2.1 Comparison between experiments and theory . . . 119
8.2.2 Location for the observation of the Crow instability . . . 120
8.2.3 Discussion . . . 123
8.3 Statistical analysis of unsteady flow field . . . 124
8.3.1 Comparison between experiments and theory . . . 124
8.3.2 Results . . . 125
8.3.3 Vortex displacement . . . 125
8.3.4 Effect of the gap and the wall . . . 128

9 Conclusion **131**
9.1 Summary of the results . . . 131
9.2 Issues for practical applications . . . 132
9.3 Recommendation for future works . . . 133

IV Appendix **135**

A Control of the Crow instability **137**
A.1 Details of the apparatus . . . 138
A.2 Results . . . 140
A.2.1 Effect of the string diameter . . . 140
A.2.2 Effect of the forcing frequency . . . 142

B Calibration of multi-hole pressure probes **145**
B.1 Data processing . . . 147
B.1.1 Definition . . . 147
B.1.2 Calibration . . . 148
B.1.3 Calibration points and determination of the interpolation coefficients . . . 149
B.2 Illustration . . . 150

B.2.1 Calibration facility . . . 150
B.2.2 Probes . . . 150

C Optimal perturbation of vortex pairs based on a reduced order model 151
C.1 Model reduction . . . 151
C.1.1 Method . . . 151
C.1.2 Numerical implementation . . . 152
C.2 Results . . . 153
C.2.1 Spectrum . . . 153
C.2.2 Optimal gain . . . 153
C.3 Conclusion . . . 154

D Impulse of a vortex in the vicinity of a wall 155
D.1 Definition . . . 155
D.1.1 Circulation . . . 155
D.1.2 Impulse . . . 155
D.2 Time variation . . . 156
D.2.1 Circulation . . . 156
D.2.2 Variation of the impulse . . . 157
D.2.3 Inviscid limit . . . 157
D.2.4 Effect of the viscosity . . . 158

E Optimal perturbation of a vortex sheet for fast destabilization of the trailing vortices 161
E.1 Introduction . . . 162
E.2 The vortex sheet . . . 163
E.3 Perturbation analysis . . . 165
E.4 Results . . . 168
E.5 Conclusion . . . 171

F Optimal amplification of the Crow instability 173

References 180

Nomenclature

x, y, z	cartesian coordinates
$\boldsymbol{e}_x, \boldsymbol{e}_y, \boldsymbol{e}_z$	Unitary vectors corresponding to the directions x, y and z
$\boldsymbol{U}$	velocity vector
U_x, U_y, U_z	component of velocity along x, y, z
$\Omega_x, \Omega_y, \Omega_z$	component of vorticity along x, y, z
$\boldsymbol{u}$	perturbation velocity vector
u_x, u_y, u_z	component of perturbation velocity along x, y, z
$\omega_x, \omega_y, \omega_z$	component of perturbation vorticity along x, y, z
r, θ, z	cylindrical coordinates
U_r, U_θ, U_z	components of the velocity vector in cylindrical coordinates
u_r, u_θ, u_z	component of perturbation velocity in cylindrical coordinates
$\overline{u_x u_y}$	Reynolds stress
Ψ	Streamfunction
τ	gap size
U_∞	free stream velocity
R	Rotation rate in the axial direction z
c	wing chord
Γ	circulation
$Re_\Gamma = \dfrac{\Gamma}{\nu}$	Reynolds based on circulation

$Re_c = \frac{U_\infty c}{\nu}$	Reynolds based on chord
$\boldsymbol{I} = (I_y, I_x)$	flow impulse
$\boldsymbol{n}$	unitary vector normal to a boundary
a	vortex radius
b	distance between the vortex centers in the vortex pair
a/b	aspect ratio of the vortex pair
x_c, y_c	vortex center
$U_{drift} = \frac{\Gamma}{2\pi b}$	Inviscid drift velocity of the vortex pair
$q = \frac{\Gamma}{2\pi a \Delta U_z}$	swirl number
$t_b = \frac{2\pi b^2}{\Gamma}$	time scale for the cooperative instability
$t_a = \frac{2\pi a^2}{\Gamma}$	time scale of the period of rotation of the vortex
$t_\nu = \frac{2\pi a^2}{\nu}$	time scale of the evolution of the vortex pair
f_{Crow}	frequency characteristic of the Crow instability
f_f	forcing frequency
f_s	String oscillations frequency
$\mathcal{D}$	Computational domain
$\partial\mathcal{D}$	Boundary of the computational domain

1 General introduction

In the year 2000, the Advisory Council for Aeronautics Research in Europe (ACARE) published "European aeronautics : a vision for 2020", in which a board of experts taken among the top industrial European companies in aeronautics set challenging objectives for future aircrafts in terms of safety, transport management systems and environmental impact. Concerning environment one of the most ambitious goal was to reduce by 50% the fuel consumption compared with a year-2000 baseline aircraft. As an illustration of the impact of such a reduction on a real aircraft, let us consider the Airbus A380. Its total weight is 540 tons, which decomposes as follows: empty weight (280 tons), payload (80 tons) and fuel (180 tons). A reduction by half of the fuel consumption would lead to an impressive saving of 90 tons.

Ways of improvements are sought in a wide variety of domains, from aerodynamics to air traffic management. Concerning aerodynamics, much research is done for drag reduction (e.g. control of laminarity of the flow over lifting surfaces) and for more efficient jet engines. This latter domain is the main concern of this thesis and the corresponding ACARE objective is a reduction of 20% of the specific fuel consumption (see definition in the caption of figure 1.1.

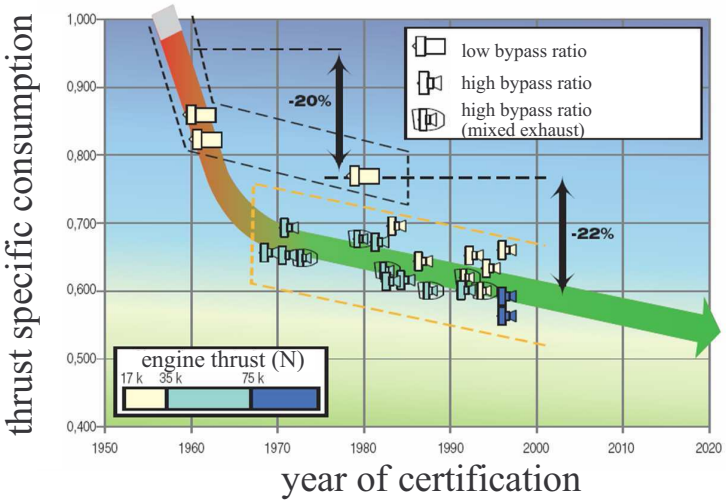

Figure 1.1: Thrust specific fuel consumption during cruising (elevation 10000m, speed 0.8Mach). This quantity is defined as the mass of fuel burned by an engine in one hour divided by the thrust that the engine produces. Bypass ratio is the ratio between bypass and core flows. The color of the arrow changes from red to green to indicate improvement. The background color changes from blue to green to indicate the change in specific consumption. Source: Snecma.

As shown in figure 1.1 the technology of turbofan for civilian airliners has greatly evolved over the past 50 years. This figure retraces the history of these evolutions in terms of efficiency. First jet engines were far less powerful than nowadays' and consumed more. About 45% reduction of fuel consumption have been achieved since 1960. If today's mean specific consumption is 0.6, the objective set by ACARE is to lower it to 0.5 by 2020. Nevertheless, if the current evolution

is maintained, only 0.55 will be achieved at that time. This means that great technological advances must be achieved in order to attain this objective.

A typical turbofan is shown in figure 1.2. The air entering the intake goes through the fan from where part of it, the bypass flow, goes directly to the nozzle (or to the afterburner in the case of a mixed exhaust engine) and the rest, the core flow, goes through the compressor stages (Low Pressure, LP, and High Pressure, HP), being then heated in the combustion chamber, passing through the turbine stages, and finally exiting at the nozzle. Turbines entrain compressors and fans thanks to multiple shafts.

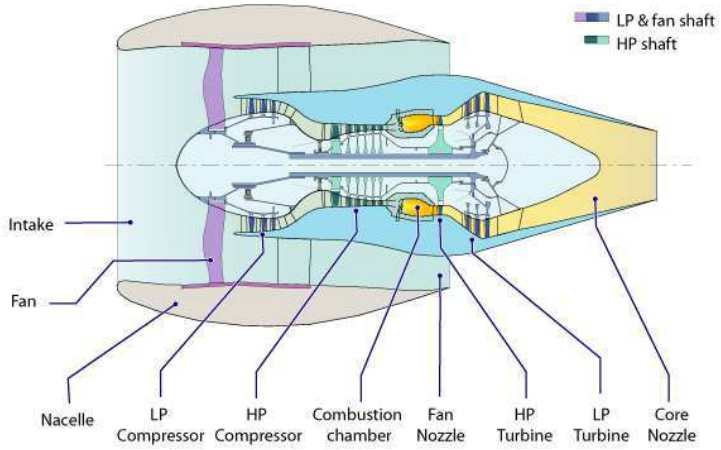

Figure 1.2: Schematic of a turbofan.

Figure 1.1 shows that the increase of bypass ratio (see the definition in the caption of the figure) of turbofan has led to important increase in efficiency. High bypass turbofans rely on the generation of thrust by large amount of air moving at speeds rather low compared to low bypass engines that moves less air but at larger speeds. This allows for quieter and more efficient engines at subsonic speeds. The increase of the bypass flow has led to a continuous increase in the size of engines. For instance the Caravelle (Sud-Aviation) in the sixties was powered by a Rolls-Royce Avon that was 1 meter of diameter and the GE90 engines that equips the new Boeing 777 Airliner are three times larger. Bypass ratios of $8:1$ are common nowadays.

The new generation of engines is illustrated in figure 1.3 featuring current and future engines by the engines manufacturers CFM and Snecma. Figure 1.3(a) represents the CFM56 that equips, among others, the A340. One of the future engine is the Leap-X shown in figure 1.3(b) that is expected to save 15% of fuel by 2016 (source: *Air and Cosmos, issue december 2008*). New architectures are also under way. One of these is the contra rotative fan, see figure 1.3(c), that should improve the performances by as much as 20%. The most far reaching architecture is the open rotor concept (CROR for contra rotative open rotor, see figure 1.3(d)) which could decrease by 30% fuel consumption. However certification is expected in 2018 at best, and the absence of casing is likely to make the issue of noise very important.

Along with these new architectures, there is a continuous effort in order to improve the internal aerodynamics of jet engines. This thesis is concerned with the flow through axial compressors. The goal of the compressor is to rise the pressure of the flow. This is accomplished by basically converting the inertia of the incoming flow into static pressure. Compressors work over a limited range of inlet mass flow rate. This is illustrated in figure 1.4 where the operating line of the compressor is depicted as a function of the efficiency - the pressure ratio between the inlet and the outlet - versus the inlet mass flow rate. The upper limit corresponds to the surge, at which important aerodynamic instabilities take place. A compressor surge, typically, causes an abrupt reversal of the airflow through the unit, as the pumping action of the aerofoils stalls (akin to an aircraft wing stalling). Issues on the other side of the performance map - at large

(a) (b) (c) (d)

Figure 1.3: Snecma and CFM jet engines. (a) CFM 56. (b) Leapx. (c) Contrarotative fan. (d) Open rotor.

mass flow rate and usually lower efficiency - are less understood. This region is referred to as the choke. It can be described by a marked, rapid loss of efficiency.

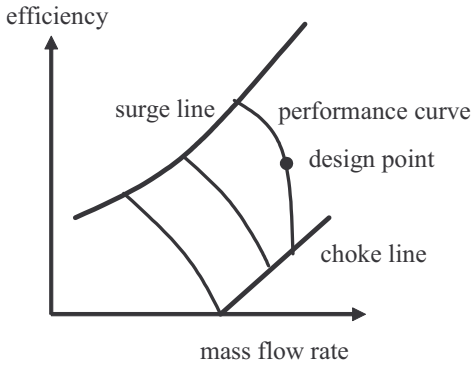

Figure 1.4: Performance map of a compressor. The mass flow rate is the mass of air going through the compressor per unit of time.

1.1 Tip clearance vortex

1.1.1 Description

This thesis deals with the tip leakage vortex that forms at the tip of rotor blades in compressors, as schematized in figure 1.5. As noted by several authors (see Storer[145], Chen[29] and Lakshminarayana[88]), the mechanism of tip leakage vortex is primarily inviscid. It is the static pressure field near the end of the blade which controls the chordwise distribution of the flow across the tip. The overall magnitude of the tip leakage flow hence remains strongly related to the aerodynamics loading of the blades. The tip leakage flow emerges at the suction side of the blade, where the pressure difference between the pressure and suction sides is maximum, in the form of a vortex sheet that rolls-up into a single vortex (Lakshminarayana[88]). In compressors, the relative motion between casing and blade is such as to increase the tip leakage vortex strength (Denton[38], Inoue[72]).

Being an important phenomenon in rotor dynamics, the tip leakage vortex has been the subject of numerous studies. We point out first the great variety of experimental and numerical tools that were found to be used in these investigations. On the experimental side, a frequently encountered apparatus is the linear cascade. It is composed of several blades put side to side and attached to a flat wall. Such an apparatus was used, among others, by Bae[10] and Devenport[40]. In order to take into account the relative motion of the casing wall, a moving belt is sometimes used (Ma[102]). Cascades have the advantage to allow easy measurement in the flow. More realistic apparatus include single or multi-stage compressors and complete

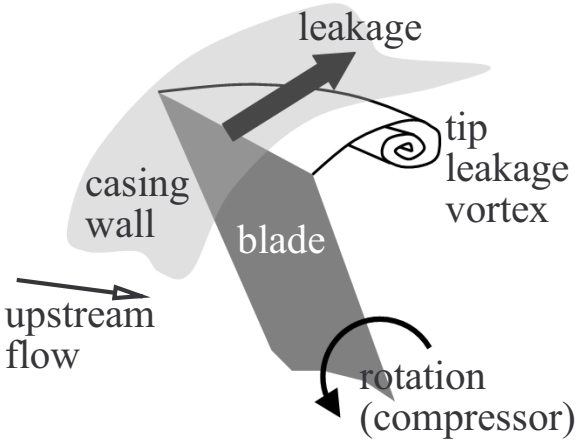

Figure 1.5: Schematic of the formation of the tip leakage vortex in a compressor stage. Taken from Bae[10].

turbomachines, see for instance the work of Inoue[73]. However in these cases measurement become difficult due to the increased complexity of the flow and of the geometries. On the numerical part, most investigations encountered in the literature use Reynolds Averaged Navier-Stokes (RANS) simulations (Yamada[157]). LES methods are also used (You[158]). Geometries mimic the experimental settings, from linear cascades to complete compressor stages. Results concerning the simulation of a full compressor stage obtained by Gourdain[54] are shown in figure 1.6.

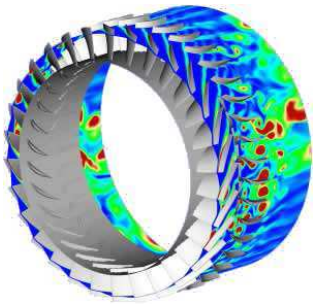

Figure 1.6: Example of numerical simulation. Taken from Gourdain[54].

The main influence parameter on the blade tip vortex is the clearance gap (You[158]. In a given engine, tip clearance gap size varies due to wear and thermal effects. Values of 1% to 3% are common in engineering practice. As noted by Storer[145], optimum performance is obtained at clearance smaller than that dictated by mechanical constraints. The tip clearance vortex is found to increase in size and strength as the tip clearance gap is increased (Storer[145], You[158]) and its origin is also delayed further downstream.

Importantly, the existence of the tip leakage vortex is not always observed. Inoue[72] reported that it is common that the vortex bursts before the trailing edge in compressors with high loading. Lakshminarayana[89] found no evidence of its existence when investigating the tip leakage flow in an axial compressor. This author observed that the tip leakage produced intense shearing and flow separation by mixing with the main stream but did not roll-up into a tip vortex. Storer[144] also evoked the ambiguity of the existence of the tip leakage in the case of a tip smaller than 1% in a linear cascade. This author performed flow visualizations that did not clearly show the vortex. However, if not all authors agree on the formation of a tip leakage

vortex, it should be stressed that the shedding of axial vorticity in the wake of the blade is a mandatory condition for the generation of lift. The ambiguity hence concerns the merging of this vorticity into a coherent vortex.

The dynamics of the tip leakage vortex is also of great interest in problems of cavitation in flow pumps. Cavitation occurs when the static pressure falls sufficiently far below the saturated vapor pressure. This can cause important damages to structures. The low pressure levels in the vortex core make it a preferred region for cavitation. An important issue is thus the prediction of the pressure in the tip vortex core. For that purpose, much effort has been dedicated to a better understanding of tip vortices. Boulon[22] investigated the effect of the tip clearance size on the tip vortex dynamics, by using an experimental set-up which consisted of an hydrofoil set perpendicularly to a flat wall. Using a complete turbomachine, Farrel[47] identified an optimal gap that minimized the inception of cavitation. Gopalan[53] investigated the effect of the tip gap size on the tip leakage flow and correlated the visual appearance of cavitation with high amplitude noise in data obtained by accelerometers. Meandering of the tip vortex was also observed (Boulon[22], Gopalan[53]) and its amplitude was shown to increase with gap size. Rains[125] studied experimentally and theoretically the tip clearance flow in axial flow pumps and noted the appearance of cavitation in the vortex core rather than on the blade surface. You[158] showed that larger tip gap sizes were more likely to induce cavitation in the vortex core due to lower pressure levels.

An interesting point of view on the tip leakage vortex is obtained by replacing the casing wall by an image vortex, which renders the problem similar to that of aircraft trailing vortices, see figure 1.7(a). This model is supported by the inviscid character of the roll-up of the vortex at the tip. It was first introduced by Lakshminarayana[88] to investigate the effect of the gap size. The apparatus used by this author consisted in a split wing in which a flat splitter plate could be introduced to study the real tip leakage flow. Comparisons of the flow characteristics between the two configurations showed good agreement. Bae[10], Boulon[22] and Chen[29] adopted this same model in their studies. Bae[10], in particular, justified the existence of the Crow instability in the tip leakage vortex based on this approach. As a result, the author showed that control by periodic blowing at the Crow frequency exhibited an optimal response. Note that Sirakov[137] found similar results. As we shall see later on, this suggested workability of the control of the vortex by using Crow instability represents a major motivation for the present thesis.

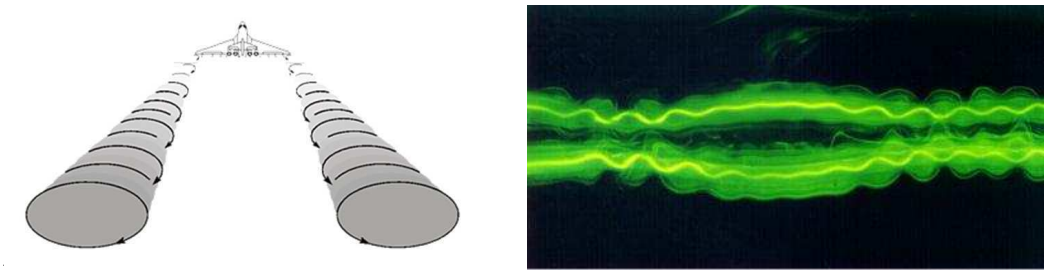

(a) (b)

Figure 1.7: (a) Schematic of trailing vortices. (b) Dye visualization of the long (Crow) and short wavelength (Widnall) instabilities in vortex pairs, from Leweke[98].

This image vortex model and the findings of Bae[10] support the idea that the tip leakage vortex has many similarities with trailing vortices illustrated in figure 1.7(a). It is interesting to note that there is a continuum between these two flows when the gap is varied from zero to very large values. In this latter case the influence of the wall becomes strictly identical to that of the image vortex. Interestingly, Lakshminarayana[88] distinguished different behaviors of the tip leakage depending on the gap size. Following the work of Bae[10], the important contribution that the research on the tip leakage flow can gain from the large literature on trailing vortices

concerns the dynamics of vortex instabilities. In this respect, the works of Crow[34] on the long wavelength instability of vortex pairs and that of Tsai[154] on the short-wavelength instability are particularly relevant, see figure 1.7(b) in which the Crow and Widnall are visualized.

1.1.2 Losses

The tip clearance flow is one of the most detrimental features in turbomachine rotors. As explained by Denton[38], losses result from entropy creation du to viscous effects, either in boundary layer, mixing processes or shocks, and to heat transfers across temperature differences. As we shall see in the course of this thesis, in incompressible flows, loss amounts to a decrease in total stagnation pressure. The tip region is a major source of loss where several phenomena add up: endwall boundary layer, tip leakage flow and subsequent vortex, and sometimes detached flow. As a result, it is often difficult to separate the tip clearance loss from these other sources.

Storer[146], Bindon[20] found that the tip clearance loss is proportional to the clearance size. For typical tip clearance sizes, Denton[38] evaluated the loss from the tip leakage to be responsible for one third of the total loss, while Storer[146] claimed that this loss is often overestimated, and closer to 10%. The main mechanism for loss production associated to the tip leakage flow corresponds to the action of viscosity in the shear layer separating the leakage flow and the mean stream (Storer[145], Crook[32]).

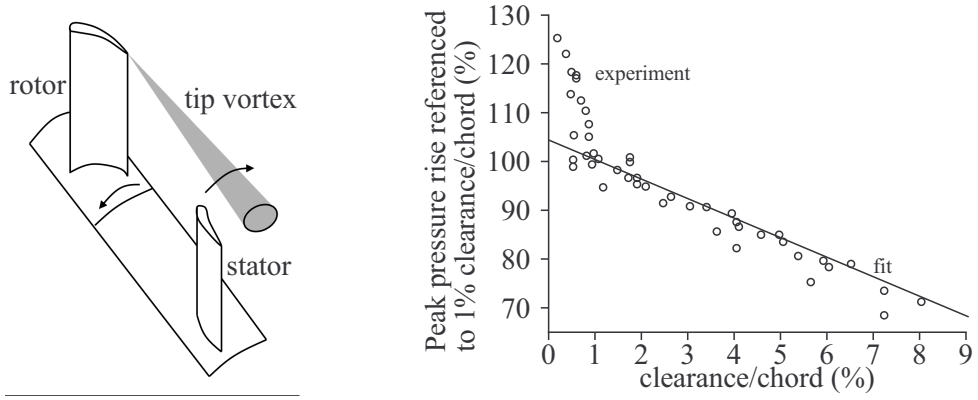

(a) (b)

Figure 1.8: (a) Impact of the tip clearance vortex on stator. (b) Peak pressure ratio versus clearance size (Source: Bae[10]).

Because the tip leakage flow concentrates low momentum fluid, it is also responsible for flow blockage in blade rows. In relation to this phenomenon, tip gap has a major effect on the pressure rise capabilities of compressors (You[158]). Figure 1.8(b), taken from Bae[10], shows that the peak pressure rise increases inversely to the tip gap size. This curve proves that one solution for the alleviation of the effect of the tip clearance is to reduce the clearance to a minimum. In practice, different techniques exist. Use of abrasive surfaces or control by thermal dilatation of the casing are common practice in engine design.

1.1.3 Flow unsteadiness

Large tip clearance is known to be detrimental to the stability of compressors (Storer[145]). The positive gradient pressure that exists in compressors makes the flow prone to separation (Denton[38]). This phenomenon is amplified by the simultaneous reduction of the axial velocity and increase of the tangential velocity in the endwall region, which together increase the angle of attack of the flow at the tip of the blade and render the flow at the suction side sensible to adverse pressure gradients.

Highly loaded compressors are also very critical in the tip region. Hah[61] reported that the tip clearance vortex oscillates substantially near stall. Gourdain[55][54] showed that the leakage region exhibits the first signs of the rotating stall which is characterized by detached flow occurring in a variable number of blade passages. As explained by Mailach[103], such phenomena are responsible for blade vibrations and noise generation.

Flow unsteadiness also exists due perturbations coming from upstream and downstream, and due to rotor/stator interactions. Graff [57] observed that the downstream stators imposed a pulsating back pressure on the rotor flow. Ma[102] investigated the effect of upstream unsteadiness generated by attaching vortex generators on the moving belt in a cascade facility. Also, as shown in figure 1.8(a), the impact of the tip leakage vortex on downstream mechanical structures generates mechanical wear and noise.

1.1.4 Control

The flow in the tip region induces penalties on the compressor in terms of efficiency, range of operability, noise and mechanical wear. Flow control is thus a primary objective to be achieved. Casing treatments have gained large interest for compressors as well for fans and turbines. An exhaustive review in the field of passive endwall treatment is given by Hathaway[63]. As illustrated in figure 1.9, these treatments consist in slots in the casing wall. According to Crook[32], there are two principal effects. The first one is the suction of low total pressure and high blockage fluid at the rear of the blade passage and the second one is the energizing of the tip leakage flow in order to suppress the blockage at its source. Use of grooves or slots in the endwall of a compressor can substantially increase the stability range of the machine (surge is postponed) although generally with a reduction in the efficiency. The periodicity of the slots seems to play an important role for the efficiency of the device. Jiang[79] (see figure 1.9) investigated the effect of curved skewed slot casing treatments in an axial compressor and showed that performances could be greatly increased if the frequency of the slots matched the characteristic frequency of flow in the baseline configuration.

Figure 1.9: Example of casing treatment. From Jiang[79].

Other solutions rely on synthetic jets, which blow air in the clearance or along the trajectory of the vortex like in the work of Bae[10]. The idea here is to reduce the blockage associated to the tip vortex by injecting momentum in the direction of the vortex trajectory. Another idea is to reduce the leakage by creating a fluidic barrier by blowing air perpendicularly to the gap (Kang[82], Bae[10]). This is illustrated in figure 1.10. It is in this configuration that Bae[10] reported the receptivity of Crow instability to the blowing frequency. However, as noted by these authors, the efficiency of these solutions remains poor.

1.2 Objectives of the thesis

The objective of this thesis is to evaluate the possibility to control the tip leakage vortex by using Crow instability. The investigation is based on the vortex pair model of the flow introduced by Lakshminarayana[88] and later used by Bae[10]. Recall that in this model the

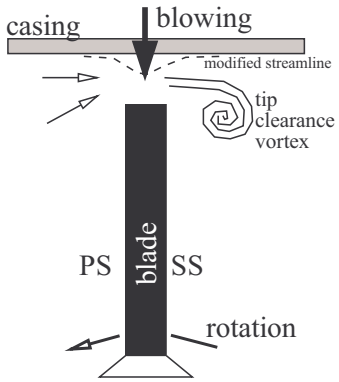

Figure 1.10: Normal blowing in order to reduce leakage flow, see Bae[10]. PS: Pressure Side, SS: Suction Side.

casing wall is replaced by an image vortex. The first goal is to find a way to control the instabilities of vortex pairs. The second objective is to apply the obtained results to the case of the real tip leakage vortex in interaction with the casing wall.

1.3 Approach

This thesis is based on theoretical investigations and wind tunnel experiments. The idea is to use theory in order to investigate the stability and control of vortex pairs and to analyze the experimental observations in the light of these findings. As a consequence the results obtained in the course of this thesis are split in two parts:

i- **Theoretical/Numerical part** this part is dedicated to the theoretical study of instabilities in vortex pairs based on a global stability analysis. We use direct numerical simulations and solve matrix eigenvalue problems to compute global modes. We first retrieve the Crow and the Widnall instabilities (growth rate, frequency) and then use an optimal perturbation algorithm to find physical mechanisms able to increase the growth rate of these instabilities. The global mode analysis is also applied to investigate the specificity of thick vortex pairs, that are characterisitic of the tip leakage vortex.

ii- **Experimental part** this part is dedicated to the study of the tip leakage vortex with varying tip clearance size in a low speed wind tunnel at ONERA in Meudon. The apparatus was specifically designed for the occasion, and can be set in two different configurations. Like the apparatus used by Lakshminarayana[88], the first configuration (C1) consists in a split wing set transversely to the free stream, in which the size of the gap can be varied by reducing the wing span. This configuration produces a vortex pair. The second configuration (C2) is obtained by materializing the symmetry plane of the vortex pair by a flat plate, and produces a single vortex in interaction with the wall. In order to study these flows, we first detail the mean properties of the vortices in each configuration and then compare them. In a second step, we investigate the flow unsteadiness, in order to verify the existence of the Crow instability suggested by the work of Bae[10]. This, in particular, makes use of the findings obtained in the first part. In a last step, we make an attempt to control Crow instability.

1.4 Organization of the thesis

The first chapter following this introduction is a review on the current knowledge on the stability of single and pairs of vortices. The thesis then divides in three parts.

The first part we present the methods of investigation. Chapter 3 deals with the details of the numerical methods used for the theoretical work. Chapter 4 presents the experimental set-up and some preliminary investigations of the flow characteristics.

The second part is dedicated to the theoretical results and comprises two chapters. The first one, chapter 5, deals with the stability of thick dipoles, and presents a special case of 2D instability that does not seem to have been studied before. The second one, chapter 6, deals with mechanisms of transient growth of energy in vortex pairs, in relation to known instabilities (Crow, Widnall).

The third part is dedicated to the experimental results and divides in two chapters. Chapter 7 presents the mean properties of the flow obtained in the two configurations of the experimental apparatus. Chapter 8 consists in an experimental study of the Crow instability, which relies on the results obtained in chapter 6 to conduct theoretical comparisons.

Eventually chapter 9 gives a summary of the work along with concluding remarks concerning the objectives of the thesis and recommendations for future investigations.

2 Review on the stability of vortices

In this chapter we present a review of the litterature on vortex dynamics, focusing in particular on vortex instabilities and on transient growth effects. We consider the case of the isolated vortex and that of the pair of symmetric counter-rotating vortices. Some important aspects of vortex dynamics, namely meandering, turbulence and vortex decay, that will be considered in the experimental part of this work, are presented in the end.

2.1 Single vortices

2.1.1 Existing models

Here we detail some simple models of vortex corresponding to the velocity distributions drawn in figure 2.1.

Rankine vortex

The Rankine model represents an inviscid vortex column surrounded by potential flow

$$U_\theta(r) = \begin{cases} \dfrac{\Gamma}{2\pi a^2} r & \text{if } r \leq a \\ \dfrac{\Gamma}{2\pi r} & \text{if } r > a \end{cases} \tag{2.1}$$

where Γ denotes the circulation of the vortex and a is its radius. The core region corresponds to $r < a$. There, the flow is in solid body rotation, which is representative of most central regions of swirling flows.

Lamb-Oseen vortex

The Lamb-Oseen (LO model) vortex models a two-dimensional vortex decaying by viscosity. Its velocity distribution follows a Gaussian law of the form

$$U_\theta(r) = \frac{\Gamma}{2\pi r}\left(1 - e^{-r^2/a^2}\right) \tag{2.2}$$

The radius a depends upon time through $a^2(t) = a_0^2 + 4\nu t$.

Batchelor vortex

Whereas the two previous models describe purely 2D motions, the Batchelor vortex also models the axial flow that usually exists in vortex cores. Batchelor [14] explains, by taking the example of the roll-up of a vortex sheet, that a pressure drop occurs in the core of the trailing vortex due to the curvature of the flow paths, which leads to an increase of the axial velocity. Far from the vortex generator, the trailing vortex becomes symmetric and grows by viscous

diffusion. The Batchelor vortex is a similarity solution which describes this far field solution. Its velocity profile at first order is

$$\begin{aligned} U_\theta(r) &= \frac{\Gamma}{2\pi r}\left(1 - e^{-r^2/a^2}\right) \\ U_z(r) &= U_\infty + \Delta U_z e^{-r^2/a^2} \end{aligned} \tag{2.3}$$

where U_∞ is the flow velocity in the far field and $\Delta U_z = U_z(r = 0) - U_\infty$. Note that no axial stretching is taken into account here since we retained only the leading order term of the formulation originally given by Batchelor[14]. This vortex is also called q-vortex, which refers to the swirl number

$$q = \frac{\Gamma}{2\pi a \Delta U_z} \tag{2.4}$$

defined as the ratio of the azimuthal and axial velocities. This template flow has been thoroughly used to study vortex breakdown.

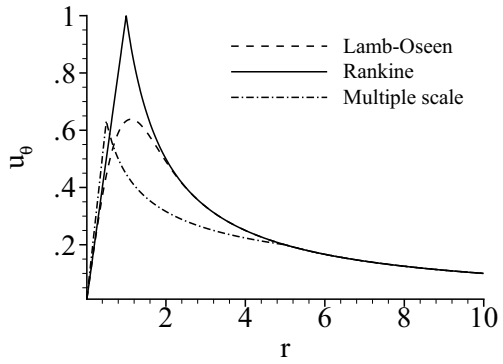

Figure 2.1: Distribution of tangential velocity u_θ for the LO, Rankine and multiple scales vortices. $\Gamma = 2\pi$, $a = 1$, $a_1 = 0.5$, $a_2 = 5$ and $\alpha = 0.5$.

Multiple scales model

Other models of vortices exist that reproduce more closely the distribution of real-life vortices (e.g. airplane trailing vortices, experimental vortices). The model with two radii was proposed by Fabre[43]:

$$u_\theta(r) = \begin{cases} \dfrac{\Gamma r}{2\pi a_1^{1+\alpha} a_2^{1-\alpha}} & \text{if } r \le a \\ \dfrac{\Gamma}{2\pi a_2^{1-\alpha} r^\alpha} & \text{if } a_1 < r < a_2 \\ \dfrac{\Gamma}{2\pi r} & \text{if } r \ge a_2 \end{cases} \tag{2.5}$$

where α defines the intermediate region between the two radial scales a_1 and a_2. A second version of this model was derived in order to regularize the transitions between the different regions, see Fabre[43]. Velocity distributions of trailing vortices in wind tunnel may be correctly fitted with such models.

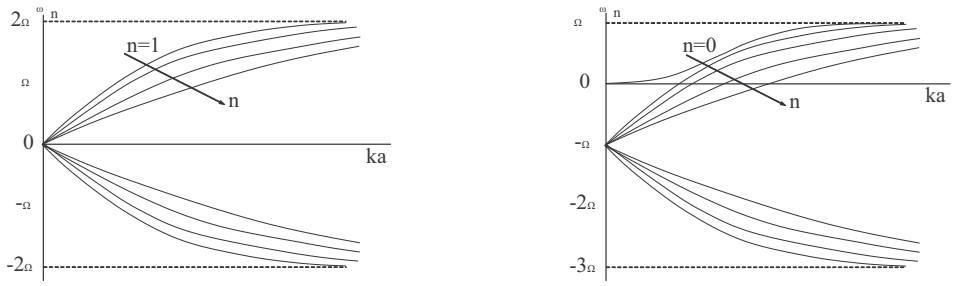

Figure 2.2: Oscillation frequency of Kelvin waves. (a) $m = 0$. (b) $m = 1$. Taken from Fabre [130].

2.1.2 Stability

Kelvin waves (KW)

We know from Lord Kelvin[150] that a vortex column is prone to small oscillations in the form of propagating waves, called Kelvin waves, when it is slightly perturbed. The wave phenomenon is attributed to the restauring force in the rotational motion, as explained by Tritton[152]. Suppose the vortex is perturbed initially in a given section. This will break the radial equilibrium

$$\frac{U_\theta^2}{r} = \frac{dp}{dr} \tag{2.6}$$

between pressure and tangential velocity, that characterizes vortices. According to (2.6), the modification of the velocity modifies the pressure, thereby causing a pressure difference in the axial direction that will be responsible for the axial propagation of the initial deformation. The solution of the initial value problem is a collection of Kelvin waves travelling along the axial direction (see Arendt[7] and Melander[111]). These waves being damped by viscosity, the vortex column returns to its steady state when the perturbation stops.

The existence of these waves has been proven both experimentally and numerically. Hopfinger [69] and Maxworthy[107] gave nice visualizations of the oscillations of a vortex column. Arendt[7] numerically showed how a straight vortex column evolves after an initial perturbation. Fabre[46] gave a thorough description of the Kelvin waves of the LO vortex and of the physics at play based on a normal mode analysis.

These waves are classically classified according to the azimuthal wave number m, see figure 2.3. For the Rankine vortex, see Saffman[130], the self-rotation rate of the oscillations is given by

$$\omega_n = mR \pm \frac{2Rk}{\sqrt{k^2+\beta^2}} \tag{2.7}$$

where R is the angular velocity of the vortex, k the axial wavenumber defined as $k = 2\pi/\lambda$ with λ the wavelength and β is the solution of

$$\frac{1}{\beta a}\frac{J'_m(\beta a)}{J_m(\beta a)} + \frac{K'_m(ka)}{kaK_m(ka)} \mp \frac{m\sqrt{k^2+\beta^2}}{ka^2\beta^2} = 0 \tag{2.8}$$

where J and K are Bessel functions. Waves at $m = 0$ are called "sausaging modes" because they produce periodic thickening and thinning of the vortex core, see figure 2.3. Waves with $|m| = 1$ are bending modes because they displace the vortex center. Waves with $|m| > 1$ exhibit complex shapes, including multiple helices. Waves that turn faster than the basic rotation are called "cograde waves". Those turning slower are called "retrograde waves" and those turning in the opposite direction are called "countergrade waves". At certain wavelengths these waves are

stationary ("stationary waves"), meaning that they exactly cancel the basic rotation and remain steady in the laboratory frame. Concerning Kelvin waves, it is important to keep in mind that

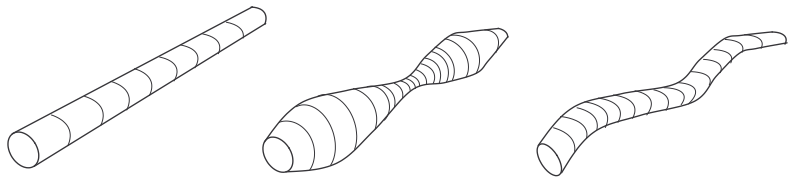

(a)

Figure 2.3: Schematic of the vortex deformation. From left to right : undeformed vortex, mode $m = 0$ and mode $m = 1$.

the rotation in the vortex core has a stabilizing effect, transforming any initial perturbation into a packet of travelling waves, the amplitude of which is finite and decreases due to visosity.

Centrifugal instability

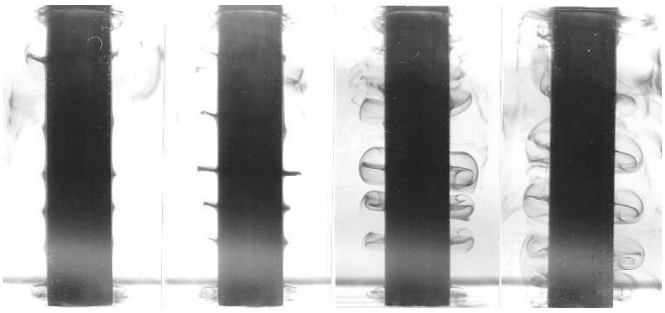

Figure 2.4: Development of the Taylor-Couette instability between two coaxial cylinders.

The centrifugal force that acts on particles in the swirling motion is a source of instability as was first shown by Lord Rayleigh [127] and later on by Chandrasekhar [27]. Rayleigh's criterion states that an inviscid rotating flow is stable to axisymmetric perturbations if the angular momentum Rr^2 constantly increases outwards and is unstable otherwise (R being the angular velocity in the flow). The corresponding inviscid growth rate is

$$\sigma = -\frac{1}{r^3}\frac{\partial \Gamma^2}{\partial r} \tag{2.9}$$

The pressure imposes an azimuthal stratification like gravity does in a mass of fluid. Instability occurs when this stratification reverses (lighter fluid under heavier fluid; angular momentum decreasing outwards). An example is the confined flow between two coaxial cylinders: if the external cylinder is at rest while the internal cylinder rotates at a speed R_1, then the flow is unstable, see figure 2.4. However viscosity has a stabilizing effect on the phenomenon and, in practice, the instability develops above a certain threshold in Reynolds number only. Centrifugal instability may also occur in turbulent trailing vortices that were shown (see Jacquin [76]) to exhibit circulation overshoot due to the transport of tangential momentum by axial velocity gradients.

Shear instabilities

A basic instability in shear flows is the Kelvin-Helmholtz (KH) instability. To present this instability we use an inviscid model of 2D vortex sheet, as sketched in figure 2.5. The sheet is

a sum of single vortices of equal strength that cause a velocity discontinuity in the flow. The vortex strength corresponds to the velocity difference across the discontinuity. When the red vortex in the figure 2.5(a) is moved up (dashed line) from its initial position (solid line), the induction effect from the neighboring vortices displace the vortex to the right, and not to its initial position. This traduces the instability of the system. The vortex moved to the right then moves the next vortex (to the right) downward, thereby spreading the initial unstable dynamics to the whole vortex sheet. The time sequence of the evolution of the KH instability is shown in figure 2.5(b). Details on the KH can be found, for instance, in Huerre[70] and Gallaire[49].

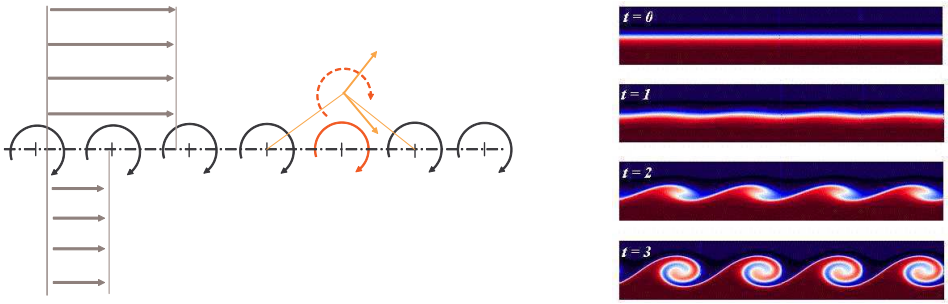

(a) (b)

Figure 2.5: (a) Schematic of the vortex sheet. (b) Time sequence of the evolution of a free shear layer and formation of the waves.

The growth rate of the instability reads

$$\sigma = \frac{\Delta U}{\lambda} \tag{2.10}$$

The velocity difference is ΔU and λ is the wavelength of the perturbation.

The more general case corresponding to a continuous variation of the velocity between the top and bottom regions is modelled by the spatial mixing layer. A necessary condition for instability in this case is the existence of an inflection point in the velocity profile (see Rayleigh[126]). The application of these results to the axisymmetric jet and azimuthal shear layer is now detailled:

i- **Axial shear** Figure 2.6 shows a round jet at small and large Reynolds numbers. While the first jet exhibits coherent structures in the form of KH waves, the second jet is fully turbulent. This proves the importance of the Reynolds number in the study of shear flows. The threshold in Reynolds number above which a jet becomes unstable is not known precisely because the flow is highly sensible to external disturbances, see Danaila[36] for a review on this topic. The flow is unstable if the quantity $\frac{rU_z'(r)}{m^2+k^2r^2}$ has an inflection point in the shear layer. Note that k is the axial wavenumber and m is the azimuthal wavenumber. The related growth rate reads

$$\sigma = k\frac{\Delta U_z}{2} \tag{2.11}$$

When the Reynolds is increased, the instability takes the form of an helical deformation. Above Reynolds numbers of several thousands, the flow becomes essentially turbulent, even though some large scale structures can still be observed.

ii- **Azimuthal shear** Azimuthal shear is $S = r\frac{\partial\left(U_\theta/r\right)}{\partial r}$. The flow is unstable, see Gallaire[49], if the vorticity $\Omega_\theta = \frac{\partial\left(rU_\theta\right)}{r\partial r}$ has a maximum in the shear layer. Instabilities

(a)

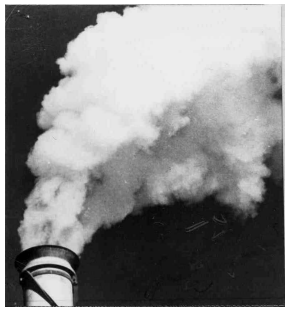

(b)

Figure 2.6: Example of jet flows. (a) KH instability in an axisymmetric jet. (b) Turbulent jet out of an industrial chimney.

take the form of KH waves in the azimuthal direction. An approximation of the inviscid growth rate is given by

$$\sigma \sim \frac{m}{a}\Delta U_\theta \tag{2.12}$$

where ΔU_θ is the tangential velocity jump, a the width of the shear layer and m the azimuthal wavenumber.

Instabilities in the Batchelor vortex

The Batchelor vortex is useful to investigate the compound effect of the two above described mechanisms. This flow encompasses a rich linear dynamics covering the case of a pure axisymmetric jet/wake, that of a 2D vortex and that of the sum of axial and tangential flow, the ratio of the two being adjusted by the swirl number (2.4). The dual nature of the flow led to interesting investigations on the absolute/convective nature of the instabilities, see Olendraru[117], which won't be adressed here, since we limit our review to temporal instabilities.

i- **Inviscid modes** These modes were first discovered by Lessen[97]. This author showed that inviscid instabilities occur for swirl numbers $q < 1.5$ in a large range of Reynolds number. This study was later refined by Leibovitch[96], Mayer[108], Ash[8], Stewartson[141][142] and more recently by Fabre[44] and Heaton[64]. A stability criterion was derived by Leibovitch[96] for inviscid flows in the limit of large m that tends to prove that the origin of this instability is a generalization of the centrifugal instability in presence of axial flow (standard Rayleigh's phenomenology is retrieved when $U_z = 0$). Heaton[64] showed that there was an infinite number of inviscid unstable modes for $q < 2.3$. However, when $1.5 < q < 2.3$, the growth rate of these instabilities is small. The growth rate at infinite Reynolds number and large azimuthal wavenumber is

$$\sigma_{|m|\gg 1} = -u_\theta \frac{dU_\theta/r}{dr}\left(\frac{dU_\theta/r}{dr}\frac{d\Gamma}{dr} + \left(\frac{dU_z}{dr}\right)^2\right) \tag{2.13}$$

ii- **Viscous modes** Khorrami[83] showed that viscosity was responsible for very weak instabilities in the Batchelor vortex when $q < 1.26$. His results were later confirmed by Mayer[108]. The particularity of these modes is that their growth rate increases with viscosity as Re_Γ^{-1}.

iii- **Viscous center modes** Fabre[44] found viscous instabilities in the form of perturbations highly localized in the vortex core, as shown in figure 2.7. The growth rate scales as $Re_\Gamma^{-1/3}$. This finding was preceded by those of Stewartson[143] and Olendraru[117] and

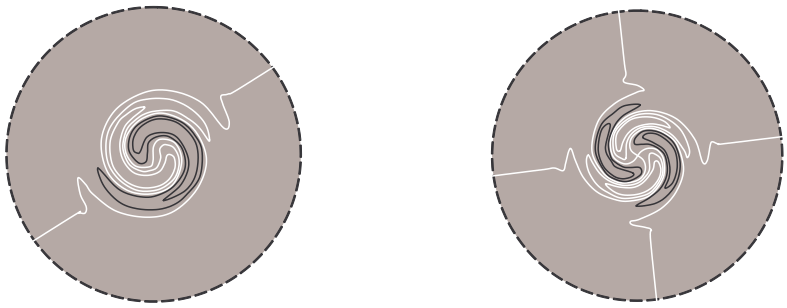

(a) (b)

Figure 2.7: Structure of the viscous center modes at $q = 2$ and $Re_\Gamma = 10^4$. The dotted circle shows the basic vortex. Modes $m = -1$ and $m = -2$ at large wavelength. Taken from Fabre [44].

followed by the works of Le Dizès[93] and Heaton[64]. The latter investigated the transient growth related to these instabilities. Viscous modes exist for all swirl numbers above a certain threshold in Reynolds. They are also found in other types of swirling flows, see Le Dizès[93]. However they have never been observed experimentally and their physics is not understood.

Cooperation between instability mechanisms

i- **KH/Centrifugal** Martin[104] investigated the linear instabilities associated to the resonance between the KH and centrifugal instabilities. The author finds that a centrifugal stable base flow becomes unstable when short wavelength KH instabilities arise. The non-linear evolution of these instabilities was investigated by the same author[105][106]. Snapshots of the axisymmetric and helical modes in their early evolution are shown in figure 2.8.

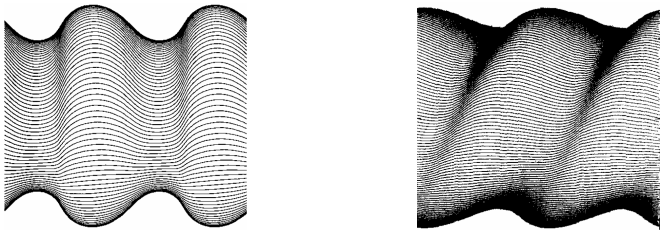

(a) (b)

Figure 2.8: Nonlinear deformation of the swirling flow du to Centrifugal and KH instabilities. (a) $m = 0$. (b) $m = 1$. Taken from Martin [105][106].

ii- **KH/KW** Loiseleux[100] investigated the linear stability of a Rankine vortex with a plug axial flow. The author found that the KH instability developping in the axial shear led to the formation of KW propagating along the vortex.

2.1.3 Transient growth

Up to now we have considered energy growth through the action of large time instabilities. However most flows have a potential for transient growth of energy. This is important regarding the problem of flow transition since transient growth can by-pass instabilities. A great deal of theoretical work attached to what is called flow non-normality has been developed over the past

decades. A thorough detail of the techniques and applications can be found in Schmid [133]. Here we illustrate the effect of non-normality by considering a simple example.

We first consider a dynamical system that is normal. It is described by

$$\frac{\partial \boldsymbol{x}}{\partial t} = A\boldsymbol{x} \tag{2.14}$$

with A a diagonal matrix with $A_{11} = a_1$ and $A_{22} = a_2$ and $\boldsymbol{x} = (x, y)^T$ the state vector. The solution of this system reads

$$\boldsymbol{x} = \beta_1 \boldsymbol{V}_1 e^{a_1 t} + \beta_2 \boldsymbol{V}_2 e^{a_2 t} \tag{2.15}$$

where $\beta_{1/2}$ are derived from the initial condition and $\boldsymbol{V}_{1/2}$ are the eigenvectors of A. These eigenvectors being orthogonal, the stability of the system is dictated by the values of a_1 and a_2. In this system, energy growth can occur only if it is unstable, i.e. if either a_1 or a_2 is positive.

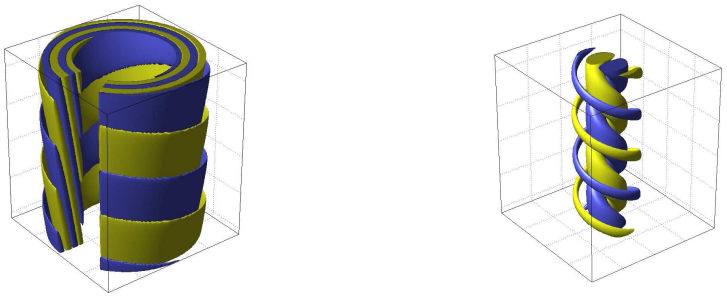

(a) (b)

Figure 2.9: Axial vorticity of the optimal perturbation of the LO vortex. (a) Initial perturbation. (b) Perturbation at optimal time. Perturbation $m = 1$ at $ka = 1.35$ and $Re = 5000$. Taken from Antkowiak [4].

Now we consider the same system, but we make it non-normal by adding the term $A_{21} = a_3$. The solution of the evolution of the system becomes

$$\boldsymbol{x} = \beta_1 \boldsymbol{V}_1 e^{a_1 t} + \left(\beta_2 e^{a_2 t} + \frac{a_3 \beta_1}{a_1 - a_2} \left(e^{a_1 t} - e^{a_2 t} \right) \right) \boldsymbol{V}_2 \tag{2.16}$$

If the system is stable, for instance $a_1 = -1$ and $a_2 = -2$, then we can choose an initial condition, for instance $\beta_1 = 1$ and $\beta_2 = 0$, for which the energy of the system $E(t) = x(t)^2 + y(t)^2$ grows as soon as a_3 is large enough. Figure 2.10 shows the transient growth obtained in the case $a_3 = 10$. Note that the maximum energy amplification increases with a_3. The system being non-normal, its eigenvectors are not orthogonal. Here $\boldsymbol{V}_1 = (a_1 - a_2, a_3)^T$ and $\boldsymbol{V}_2 = (0, 1)^T$. The scalar product equals a_3 which shows the importance of this term in the dynamics of the system. Non-normal systems hence exhibit transient growth, which results from the cooperation between eigen modes.

Transient growth in the LO vortex was first investigated by Antkowiak[4] and later by Pradeep[124]. Although stable, the LO vortex sustains strong transient growth at short time. It was shown that helical perturbations $|m| = 1$ lead to the highest growth of energy. Optimal perturbations exhibit spiral shapes surrounding the vortex core as shown in figure 2.9. More recently, Heaton[65] investigated the effect of axial flow on the transient growth in the Batchelor vortex. This work confirmed the dominance of bending modes $m = 1$ and showed that axial flow led to additional gains of energy amplification.

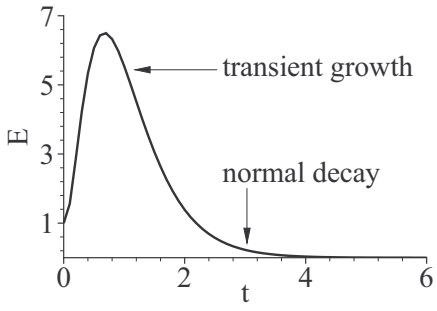

Figure 2.10: Non-normality in the system leading to transient growth of energy for $a_3 = 10$.

2.2 Vortex pairs

2.2.1 Existing models

The effect of a small external strain upon a single vortex results in an elliptical deformation of the vortex streamlines. This external strain models the influence of a second vortex placed in the vicinity of the first one. Based on this, the dynamic of a vortex pair can be investigated by the flow corresponding to a single vortex in a strain field, see Saffman [130]. The strain ϵ must remain small compared to the rotation rate of the vortex ($\epsilon << \Gamma/\pi a^2$), which amounts to vortex pairs in which vortices are far from each others (relatively to their width). The solution of this flow is given by

$$U_r(r) = \epsilon \frac{f(r)}{r} sin2\theta \tag{2.17}$$

$$U_\theta(r) = \bar{U}_\theta(r) + \epsilon \frac{f'(r)}{2} cos2\theta \tag{2.18}$$

$$\tag{2.19}$$

where the tangential velocity $\bar{U}_\theta$ can be chosen among the models of single vortices and f is defined by imposing that the strained flow is steady. This results in the following equation

$$\frac{d^2 f}{r^2} + \frac{1}{r}\frac{df}{dr} - \left(\frac{3dR/dr + rd^2R/dr^2}{rR} + \frac{4}{r^2} \right) f = 0 \tag{2.20}$$

where R is the angular velocity of the vortex.

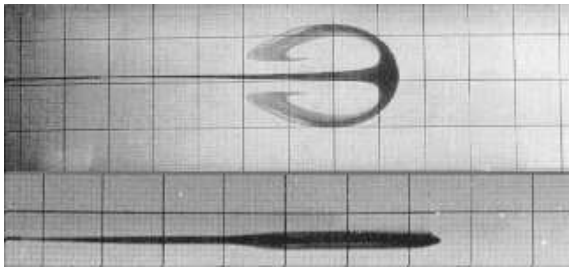

(a)

Figure 2.11: Example of experimental vortex pair drifting to the right.

Lamb-Chaplygin model

An exact solution of the Euler equations corresponding to a vortex pair is the Lamb-Chaplygin dipole (LC dipole) and was derived by Lamb [90] and Chaplygin [28]. Meleshko[112]

retraced the works of these two authors and gave the velocity field of this vortex pair

$$\Psi(r,\theta) = \frac{2U_{LC}R_{LC}}{\mu_1 J_0(\mu_1)} J_1\left(\mu_1 \frac{r}{R_{LC}}\right)\sin\theta \qquad \text{if } r \leq R_{LC} \tag{2.21}$$

(2.22)

$$\Psi(r,\theta) = U_{LC} r\left(1 - \frac{R_{LC}^2}{r^2}\right)\sin\theta \qquad \text{if } r \geq R_{LC} \tag{2.23}$$

with a the radius of the pair, U_{LC} the drift velocity of the dipole, μ_1 a constant, and R_{LC} the size of the dipole. Importantly, as shown by Sipp[136], every type of antisymmetric vorticity distribution seems to converge towards this dipole.

2.2.2 Stability

Cooperative instability

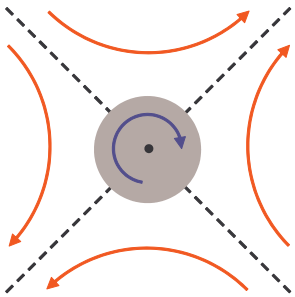

Figure 2.12: Schematic of the ingredients of the cooperative instability : strain ϵ (red), self rotation ω (blue) and vortex (grey area). Dashed lines denote the axis of strain.

Cooperative instabilities occur in pair of vortices. This is visualized in figure 1.7(b) which is taken from Leweke[98]. In this figure the basic vortices have equal strength and rotate in opposite directions. We observe that they are deformed in a sinusoidal shape at two different wavelengths. The short wavelength corresponds to the Widnall instability also refereed to as the elliptical instability and was first investigated by Tsai[154]. The long wavelength is the Crow instability, named in reference to the pioneering work of Crow[34]. The oscillations of the short wave instability scales on the vortex radius a while those of the long wave instability scale on the distance b between the vortices.

We know from previous sections that perturbation of vortices lead to the formation of KW. Let us consider a bending wave that remains stationary in the laboratory frame (this corresponds to the points in figure 2.2(b) where the curves and the abscissa cross). In a viscous medium this wave is bound to decay. However if a strain field is superimposed as in figure 2.12, then the oscillations of the vortex corresponding to the bending waves will be pulled outward by the strain field, with an increasing amplitude. This growing perturbation of the vortex due to the interaction of the KW with the external strain field is the physical mechanism responsible for cooperative instabilities.

Like previously, we denote ϵ the strain field imposed by each vortex of the pair upon the other and ω the self-rotation rate of the perturbation. As shown in Saffman [130], the dynamic of the perturbation is described by

$$\dot{x} = (\epsilon + \omega)\, y \tag{2.24}$$

$$\dot{y} = (\epsilon - \omega)\, x \tag{2.25}$$

where points denotes time derivative. The growth rate σ depends on ϵ and ω through $\sigma = \epsilon^2 - \omega^2$. The solution of this system of equations writes

$$\begin{pmatrix} x \\ y \end{pmatrix} = \begin{pmatrix} \cosh \sigma t & \frac{\epsilon+\omega}{\sigma} \sinh \sigma t \\ \frac{\epsilon-\omega}{\sigma} \sinh \sigma t & \cosh \sigma t \end{pmatrix} \begin{pmatrix} x_0 \\ y_0 \end{pmatrix} \tag{2.26}$$

A perturbation grows if the strain rate is large enough and the rotation of the perturbation small enough. In this case, flow particles follow an outward trajectory, which denotes instability. If the rotation rate is too large compared to the strain rate, vortex oscillations do not remain in the direction of strain, and decay. In this case, the trajectories of the flow particles are elliptical.

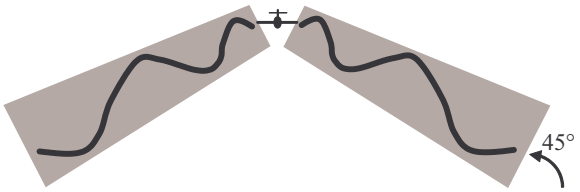

Figure 2.13: Schematic of the Crow instability.

Figure 2.13 shows the particular case of the Crow instability in the wake of an aircraft. The growth rate of the instability is normalized on the inverse of

$$t_b = \frac{2\pi b^2}{\Gamma} \tag{2.27}$$

which is the time scale of cooperative instabilities, and equals $\sigma \simeq 0.8$. The instability develops after several wingspans (typically around 10) and deforms the vortices in planes inclined at nearly 45^o about the symmetry plane of the vortex pair. The wavelength of the oscillations correspond to approximatively 10 wingspans. According to Spalart[138], time for vortex linking is about $6t_b$.

2.3 Important problems of vortex dynamics

2.3.1 Vortex meandering

Meandering corresponds to a chaotic and sinuous displacement of vortices. An illustration of this phenomenon is given in figure 2.14 which shows the seemingly aleatory displacement of the vortex column made visible by condensation particles. Movements induced by meandering have a long wavelength. As noted by Devenport[39] about 95% of the energy of the signal taken in the vortex center lies in the low frequencies ($fc/U_\infty < 1$ with c the wing chord). It is noteworthy that the instabilities that develop in the same frequency range may be hidden by meandering.

According to Bailey[11], there is a dominant wavelength of the meandering although many other wavelengths are present. The amplitude of meandering is observed to increase with downstream distance and with free stream turbulence whereas it decreases with larger vortex circulation (strength) as also noted by Heyes[66]. Jacquin[75] successively evaluates wind tunnel effects, turbulence and cooperative instabilities as an explanation for meandering and concludes that none can reasonably be privileged. Antkowiak[5] also suggested that meandering could result from transient growth of perturbations in vortices.

Note that a method to remove the effect of meandering in experimental measurement was developed by Devenport [39]. The smoothing effect of meandering results in an overestimation of the vortex width and in an underestimation of the tangential velocity. The method is based

on a gaussian dispersion model of the vortex, characterized by σ_x, σ_y and e respectively the dispersion in the x and y directions and the asymmetry between these directions.

Figure 2.14: Observation of the meandering of trailing vortices.

2.3.2 Turbulence

The are several possible origins of turbulence in vortices. First, concerning aircrafts, vortices generally develop in a turbulent atmosphere, see Gerz[52], Tombach[151] and Han[62]. Vortices can also accumulate turbulence from aircraft boundary layers[18][14][160]. Eventually turbulence can also occur in vortices because of instabilities. For instance, along with the development of cooperative instabilities, Devenport[41] noted increased level of turbulence.

Despite these numerous sources of turbulence, several studies showed that an isolated vortex remains laminar in the far field (Zilliac[160], Devenport[39], Phillips[120], Jacquin[76], Bandyopadhyay[13]). The main reason for this is the stabilizing effect of the rotation in the vortex that tends to stabilize all the perturbations evoked in the previous paragraph.

Another issue concerning vortices at high Reynolds number is modelling (Govindaraju[56]). Simple models like the LO and Rankine vortex do not fit experimental data, as noted by Jacquin[75] and Spalart[138]. Models with multiple scales are shown to work better. Inversely, experiments at low Reynolds number (see Leweke[98], Flor[48] and van Geffen[155]) show good comparison to simple models.

The effect of free-stream turbulence on the development of cooperative instabilities has been investigated by Spalart[139], Sarkpaya[132], Liu[99] and Risso[128]. They showed that the Crow instability appeared if the turbulence was weak and was precluded when turbulence was strong. In the latter case the evolution of the vortex was unclear. Some authors believed that a chaotic motion takes place whereas others suggested that vortex bursting takes place. On a general basis, strong turbulence leads to a profound destabilization of the vortex but this does not stem from a single known phenomenon. At last, the occurrence of the Crow instability is shown to favor the development of the Widnall instability in the region where the vortices of the pair get closer[91][98].

2.3.3 Vortex decay

Vortex decay is of prime interest concerning the risk of vortex encounter at landing, take-off and cruising. According to Spalart[138], most aircrafts are unable to counter the roll induced by the angular momentum of a trailing vortex issued by a preceding aircraft. This is why minimal separation distances between airplanes are imposed. Table 2.1 details the current regulation rules. Aircrafts are divided into three categories, depending on their weight: small, large and heavy. There are two additional categories for very large aircrafts, namely the A380 and the B747. For example an aircraft at departure after an A380 must wait three minutes if it belongs to the heavy category and two minutes if it belongs to either the medium or the small category. Systems aimed at detecting vortices above the runway (based on Lidar measurement) are currently engineered and could allow an adjustement of the time delay depending on the

observed dynamics of the trailing vortices. However, on the long term, a thorough understanding of vortex decay seems necessary in order to find means to hasten it.

Generating aircraft	**Separation distance for trailing aircraft, nmi**		
	Small	Large	Heavy
Small	2.5	2.5	2.5
Large	4	2.5	2.5
Heavy	6	5	4
B747	5	4	4
A380	10	8	6

Table 2.1: Current FAA standards for aircraft separation under IFR conditions. Aircrafts are sorted in three categories : small, medium and heavy. Specific rules apply for the B747 and A380.

In addition, the definition of safe flying conditions in the presence of trailing vortices is not obvious. Correlated to this problem is the definition of the vortex lifespan, see Spalart[139]. Vorticity can be rearranged but it never truly disappears. The expression "destruction of vortices" as is sometimes used in the literature is thereby ambiguous. For instance, can we consider vortex linking as a state that assures safe flight conditions? Details on this problem are discussed by Gerz[52].

Part I

Methods

3 Numerical method

In this chapter we present the theory and the numerical methods used to investigate the linear dynamics of vortex pairs in chapter 5 and 6. The first section deals with the perturbation theory. It includes a description of vortex pairs and a presentation of the equations of the base flow and of the perturbations. The numerical implementation of these equations is detailed in the second section. Finally we present the methods used to investigate some specific points of the linear dynamics, namely normal modes, with a generalized eigenvalue problem solver, and optimal perturbations, with an optimization algorithm. Note that the bulk of these tools existed prior to this thesis. For this reason, much of the work described here consists in the adaptation of the existing methods to the case of the vortex pair.

3.1 Perturbation theory

3.1.1 Description of the flow

Definition

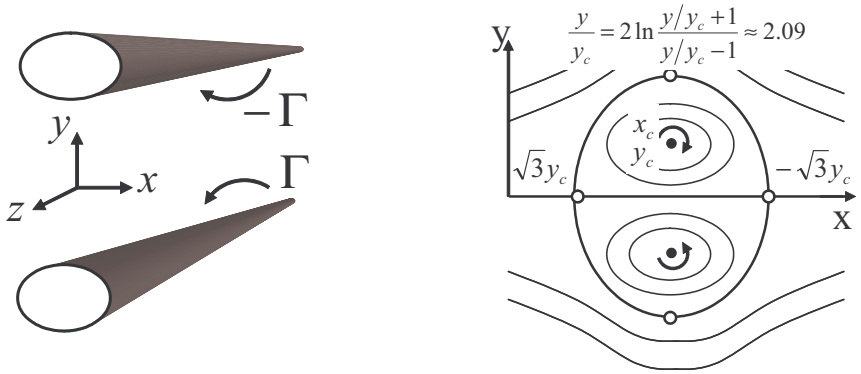

(a) (b)

Figure 3.1: (a) Schematic view of the vortex pair, (b) point vortex model. The limiting streamline of the vortex pair, also known as Kelvin oval, is shown in thick solid line.

We consider a vortex pair such as the one depicted in figure 3.1. Cartesian coordinates x, y and z are used, with z in the direction of the vortex axis and x and y the transverse directions. Unitary vectors corresponding to these directions are $\boldsymbol{e}_x$, $\boldsymbol{e}_y$ and $\boldsymbol{e}_z$. The vortex pair is symmetric about the plane $y = 0$. At $z = constant$, the center of the top vortex is (x_c, y_c), which is the barycenter of the axial vorticity Ω_z, calculated according to

$$\begin{aligned} x_c &= \frac{\int_{y>0} \Omega_z x dx dy}{\Gamma} \\ y_c &= \frac{\int_{y>0} \Omega_z y dx dy}{\Gamma} \end{aligned} \tag{3.1}$$

given the circulation Γ

$$\Gamma = \int_{y>0} |\Omega_z| dxdy \tag{3.2}$$

The circulation of the (top) bottom vortex is $(-)\Gamma$, Γ being positive. The distance between the vortex centers is

$$b = 2y_c \tag{3.3}$$

and the radius a is taken as the dispersion radius, given by

$$a^2 = \frac{\int_{y>0} \left((x-x_c)^2 + (y-y_c)^2 \right) \Omega_z dxdy}{\Gamma} \tag{3.4}$$

The aspect ratio of the vortex pair is taken as a/b, which is useful to compare the size of the vortices compared to that of the pair. The Reynolds number of the flow is defined by

$$Re_\Gamma = \frac{\Gamma}{\nu} \tag{3.5}$$

The velocity is $\boldsymbol{U} = (U_x, U_y, U_z)$, P is the pressure, ρ is the density and ν is the kinematic viscosity. The flow is supposed incompressible with uniform density. For this reason $div\,(\boldsymbol{U}) = 0$. Because of the velocity induced by each vortex upon the other, the pair moves to the left at a drift velocity equal to

$$\boldsymbol{U}_{drift} = \frac{\Gamma}{2\pi b} \tag{3.6}$$

at first order (see appendix D for details). The dynamics of the flow is described by the Navier-Stokes equations in the reference frame moving with the vortex pair

$$\begin{aligned} \frac{\partial \boldsymbol{u}}{\partial t} + (\boldsymbol{u}\cdot\nabla)\,\boldsymbol{u} &= -\nabla p + \frac{1}{Re_\Gamma}\Delta \boldsymbol{u} \\ div\,(\boldsymbol{u}) &= 0 \\ \boldsymbol{u}(\boldsymbol{x}\to\infty) &= U_{drift}\boldsymbol{e}_x \\ \boldsymbol{u}(t=0) &= \boldsymbol{u}_0 \end{aligned} \tag{3.7}$$

The momentum equation describes the equilibrium between inertia and internal forces in the flow (pressure and viscosity) in absence of external forces (none is taken into account here).

Kelvin oval

The Kelvin oval corresponds to the limiting streamline of the vortex pair. Figure 3.1 shows the Kelvin oval and the streamlines of the vortex pair. There are open streamlines outside the Kelvin oval and closed streamlines inside. In order to describe the oval, we use a superposition of two point vortices and a uniform incoming flow of velocity U_{drift} given in (3.6). The stream function of the resulting flow reads

$$\Psi = \frac{\Gamma}{4\pi y_c}\left(y + ln\left(\frac{x^2 + (y+y_c)^2}{x^2 + (y-y_c)^2} \right) \right) \tag{3.8}$$

The horizontal and vertical extent of the vortex pair correspond to $x = \pm\sqrt{3}y_c$ and $y = \pm 2.09 y_c$. The equation of the oval is $\Psi(x,y) = 0$, the solution of which can be calculated numerically.

3.1.2 Perturbation theory

The objective here being the investigation of the dynamics of small perturbations of the vortex pair, an adequate approach is provided by the framework of the theory of small perturbations. The full flow field is approximated by the sum in the small parameter ϵ

$$\boldsymbol{U} = \boldsymbol{U}_0 + \epsilon \boldsymbol{U}_1 + \epsilon^2 \boldsymbol{U}_2 + \dots \tag{3.9}$$

The first term in this sum is called the base flow and the second term is the perturbation flow. The base flow in the present situation is the vortex pair. The perturbation flow is three-dimensional and takes the form of small sinusoidal variations of the base flow along the direction z. An important assumption that gives us the right to use the tools of linear theory concerns the steadiness of the base flow. Although vortex pairs are unsteady (due to viscous diffusion), it is usual to consider that they are quasi-steady regarding the time scale of the evolution of the perturbations. The time scale of the base flow evolution is

$$t_\nu = \frac{2\pi a^2}{\nu} \tag{3.10}$$

while that of the perturbations is t_b (see definition (2.27)). The ratio between the two time scales is $t_\nu / t_b = Re_\Gamma \, (a/b)^2 >> 1$ for the values of $a/b = O(0.1)$ and $Re_\Gamma = O(10^3)$ investigated here. For this reason the base flow remains steady on the time scale of the perturbations.

In the following we truncate (3.9) at the second order. The higher order terms are thereby neglected, which precludes the investigation of the flow non-linear dynamics. Hereafter we note $\boldsymbol{U} = (U_x, U_y, U_z)$ and P the velocity and pressure fields of the base flow and $\boldsymbol{u} = (u_x, u_y, u_z)$ and p the velocity and pressure fields of the perturbations. The related vorticity fields are Ω_x, Ω_y and Ω_z for the base flow and ω_x, ω_y and ω_z for the perturbations. The decomposition of the

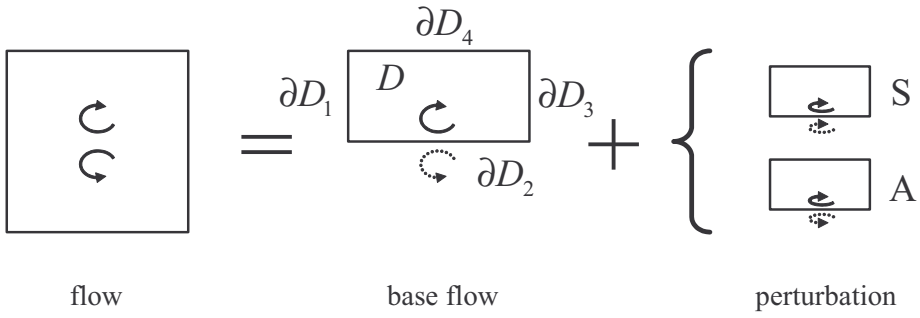

Figure 3.2: Schematic of the flow decomposition.

flow field into the base flow and the perturbations is schematized in figure 3.2. An important aspect shown by this figure is the computational domain used for the numerical investigations, which comprises only one vortex, and uses a symmetry boundary condition at the symmetry plane to account for the other vortex. Concerning perturbations, this leads to the definition of two independent problems, depending on the symmetry of the perturbation. This is detailed in the following.

Base flow

Equations The Navier-Stokes equations for the base flow read

$$\begin{aligned}
&\text{equations} \quad \begin{cases}
\dfrac{\partial U_x}{\partial t} + U_x\dfrac{\partial U_x}{\partial x} + U_y\dfrac{\partial U_x}{\partial y} &= -\dfrac{\partial P}{\partial x} + \dfrac{1}{Re_\Gamma}\left(\dfrac{\partial^2 U_x}{\partial x^2} + \dfrac{\partial^2 U_x}{\partial y^2}\right) \\
\dfrac{\partial U_y}{\partial t} + U_x\dfrac{\partial U_y}{\partial x} + U_y\dfrac{\partial U_y}{\partial y} &= -\dfrac{\partial P}{\partial y} + \dfrac{1}{Re_\Gamma}\left(\dfrac{\partial^2 U_y}{\partial x^2} + \dfrac{\partial^2 U_y}{\partial y^2}\right) \\
\dfrac{\partial U_z}{\partial t} + U_x\dfrac{\partial U_z}{\partial x} + U_y\dfrac{\partial U_z}{\partial y} &= \dfrac{1}{Re_\Gamma}\left(\dfrac{\partial^2 U_z}{\partial x^2} + \dfrac{\partial^2 U_z}{\partial y^2}\right) \\
\dfrac{\partial U_x}{\partial x} + \dfrac{\partial U_y}{\partial y} &= 0
\end{cases} \\
&\text{boundary conditions} \quad \begin{cases}
\boldsymbol{U}_{\partial\mathcal{D}_1} &= U_{drift}\boldsymbol{e}_x \\
\boldsymbol{U}_{\partial\mathcal{D}_2}\cdot\boldsymbol{n} &= 0 \\
\nabla\boldsymbol{U}_{\partial\mathcal{D}_3}\cdot\boldsymbol{n} &= 0 \\
\boldsymbol{U}_{\partial\mathcal{D}_4}\cdot\boldsymbol{n} &= 0
\end{cases} \\
&\text{initial condition} \quad \boldsymbol{U}_{t=0} = \boldsymbol{U}_0
\end{aligned} \tag{3.11}$$

The computational domain used to describe the base flow is restricted to the upper region Ω, as shown in figure 3.2. The symmetry of the base flow is accounted for by a symmetry boundary condition applied at the frontier $\partial\mathcal{D}_2$, corresponding to $U_y|_{\partial\mathcal{D}_2} = 0$. At the frontier $\partial\mathcal{D}_3$, an outflow boundary condition of the Neumann type is applied. Physically, this means that the right frontier must be placed far enough from the vortex pair for the flow to return to the far field uniform conditions.

Axial flow The equation for the axial velocity U_z is the same as that for the axial vorticity $\Omega_z = \dfrac{\partial U_y}{\partial x} - \dfrac{\partial U_x}{\partial y}$. This means that both the axial velocity and vorticity are simply convected by the plane flow and diffused by viscosity. Moreover the existence of a uniform axial velocity does not change the equations (it acts as a galilean transformation of the reference frame). We can thus consider the sole variations of the axial flow ΔU_z in the region of the vortex pair. Recall that the ratio of the tangential velocity to the axial velocity is parameterized by the swirl number already introduced in (2.4). The value of the swirl is very important for the stability of swirling flows as has been shown in the chapter 2.

Obtention of a vortex pair at a given aspect ratio a/b The base flow is initialized by a pair of single vortices like the Rankine vortex, the LO vortex or the Batchelor vortex (see chapter 2 for details on these models). It is shown by Sipp[136] that the initial distribution has no influence on the final form of the vortex pair in the range of Reynolds number $2000 < Re_\Gamma < 15000$. The initial superposition is not a solution of the Navier-Stokes equations. In order to get a realistic solution, we need to run a simulation that "regularizes" this initial flow. Here we monitor this regularization with the aspect ratio a_x/a_y of the vortices of the pair, where a_x is the semi-width of the vortices in the x direction and a_y that in the y direction, given by

$$\begin{aligned}
a_x^2 &= \frac{\int_{y>0}(x-x_c)^2\,\Omega_z dxdy}{\Gamma} \\
a_y^2 &= \frac{\int_{y>0}(y-y_c)^2\,\Omega_z dxdy}{\Gamma}
\end{aligned} \tag{3.12}$$

Figure 3.3 shows the evolution of this aspect ratio with time normalized on the rotation period

$$t_a = \frac{2\pi a^2}{\Gamma} \tag{3.13}$$

We observe oscillations for $t < 5$ and a smooth evolution later on. As explained by Sipp[136], these initial oscillations indicate the adaptation of the initial superposition of single vortices to the governing equations. The later stage indicates that the initial solution has been smoothed by viscosity and has become a realistic solution. The aspect ratio a/b increases with time due to viscous diffusion. The aspect ratio of the vortex pair can thereby be chosen by varying the time of simulation and the initial aspect ratio of the vortex pair, provided the simulation time is long enough for the adaptation to complete.

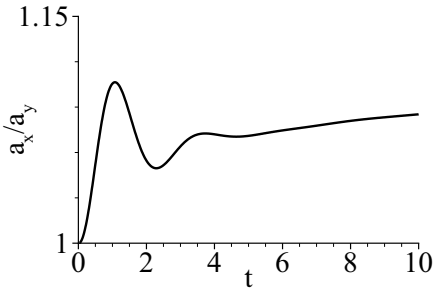

Figure 3.3: Aspect ratio of the vortices of the pair as a function of time normalized on t_a.

Perturbation

Direct equations We note $k = 2\pi/\lambda$ the axial wavenumber of the perturbation where λ is the wavelength. In general, the wavenumber is a vector denoted $\boldsymbol{k}$ but, because the base flow is planar, $\boldsymbol{k} = k\boldsymbol{e}_z$ and we shall mainly consider k. However, when needed, we will use k_x, k_y and k_z the components of $\boldsymbol{k}$ along x, y and z. The perturbation flow is written in the following form

$$(iu_x, iu_y, u_z, ip)\, e^{ikz} + c.c. \tag{3.14}$$

where *c.c.* is the complex conjugate. Therein we note $(\boldsymbol{u}, p) = (u_x, u_y, u_z, p)$ the complex perturbation field and keep in mind that the axial velocity u_z is out of phase compared to u_x, u_y and p. Introducing the first order approximation in the Navier-Stokes equations gives the linearized equations for the perturbations, which are also called direct equations

$$\begin{aligned}
\frac{\partial u_x}{\partial t} + U_x\frac{\partial u_x}{\partial x} + U_y\frac{\partial u_x}{\partial y} &= -u_x\frac{\partial U_x}{\partial x} - u_y\frac{\partial U_x}{\partial y} - ikU_z u_x - \frac{\partial p}{\partial x} + \frac{1}{Re_\Gamma}\left(\frac{\partial^2 u_x}{\partial x^2} + \frac{\partial^2 u_x}{\partial y^2} - k^2 u_x\right)\\
\frac{\partial u_y}{\partial t} + U_x\frac{\partial u_y}{\partial x} + U_y\frac{\partial u_y}{\partial y} &= -u_x\frac{\partial U_y}{\partial x} - u_y\frac{\partial U_y}{\partial y} - ikU_z u_y - \frac{\partial p}{\partial y} + \frac{1}{Re_\Gamma}\left(\frac{\partial^2 u_y}{\partial x^2} + \frac{\partial^2 u_y}{\partial y^2} - k^2 u_y\right)\\
\frac{\partial u_z}{\partial t} + U_x\frac{\partial w}{\partial x} + U_y\frac{\partial u_z}{\partial y} &= -iu_x\frac{\partial U_z}{\partial x} - iu_y\frac{\partial U_z}{\partial y} - ikU_z u_z + ikp + \frac{1}{Re_\Gamma}\left(\frac{\partial^2 u_z}{\partial x^2} + \frac{\partial^2 u_z}{\partial y^2} - k^2 u_z\right)\\
\frac{\partial u_x}{\partial x} + \frac{\partial u_y}{\partial y} + ku_z &= 0
\end{aligned} \tag{3.15}$$

The perturbation field being complex, every component has a real and an imaginary part. For instance, take the velocity u_x. We can write it as $u_x = u_{xR} + iu_{xI}$. Therefore the set of equations in (3.15) contains 4 equations in the complex plane but 7 equations in the real plane. Since it is numerically quicker to solve two problems with N degrees of freedom each rather than one single problem with $2N$ degrees of freedom, we solve separately the equations for the real and imaginary part of the perturbation field. This gives the following set of equations in the real

space

$$\begin{array}{rcl}
\frac{\partial u_{xR/I}}{\partial t}+U_x\frac{\partial u_{xR/I}}{\partial x}+U_y\frac{\partial u_{xR/I}}{\partial y} &=& -u_{xR/I}\frac{\partial U_x}{\partial x}-u_{yR/I}\frac{\partial U_x}{\partial y}\pm kU_z u_{xI/R}-\frac{\partial p_{R/I}}{\partial x}+\mathcal{V}u_{xR/I}\\
\frac{\partial u_{yR/I}}{\partial t}+U_x\frac{\partial u_{yR/I}}{\partial x}+U_y\frac{\partial u_{yR/I}}{\partial y} &=& -u_{xR/I}\frac{\partial U_y}{\partial x}-u_{yR/I}\frac{\partial U_y}{\partial y}\pm ikU_z u_{yI/R}-\frac{\partial p_{R/I}}{\partial y}+\mathcal{V}u_{yR/I}\\
\frac{\partial u_{zR/I}}{\partial t}+U_x\frac{\partial u_{zR/I}}{\partial x}+U_y\frac{\partial u_{zR/I}}{\partial y} &=& \pm u_{xI/R}\frac{\partial U_z}{\partial x}\pm u_{yI/R}\frac{\partial U_z}{\partial y}\pm kU_z u_{zI/R}\mp kp_{I/R}+\mathcal{V}u_{zR/I}\\
\frac{\partial u_{xR/I}}{\partial x}+\frac{\partial u_{yR/I}}{\partial y}+ku_{zR/I} &=& 0
\end{array} \tag{3.16}$$

where the viscous term is noted $\mathcal{V}=\frac{1}{Re_\Gamma}\left(\frac{\partial^2}{\partial x^2}+\frac{\partial^2}{\partial y^2}-k^2\right)$. All the real and imaginary terms are related through the imaginary terms of equations (3.15): the imaginary components influence the real components and vice versa. A particular case is when no axial flow U_z exists. In this case the equations for the real and imaginary components are identical and one needs only to solve the 4 equations (3.15). Numerical simulations in this case require nearly half less computational time than the case with axial flow.

Boundary conditions The set of perturbations can be split in two subsets, one containing symmetric perturbations and the other containing antisymmetric perturbations. The symmetry depends on the boundary condition at the frontier $\partial\mathcal{D}_2$, see figure 3.2.

i- ***Symmetric*** perturbations (S) entrains symmetric deformations of the vortices about the symmetry plane of the vortex pair. Everything happens as if the perturbed vortices were mirror images to each other. The perturbation axial vorticity ω_z is odd about the middle plane $\omega_z(x,-y)=-\omega_z(x,y)$. Therefore the boundary condition is $u_y|_{\partial\mathcal{D}_2}=0$ at $\partial\mathcal{D}_2$ (like in the case of the base flow),

ii- ***Antisymmetric*** perturbations (A) are characterized by odd axial vorticity about the symmetry plane, i.e. $\omega_z(x,-y)=\omega_z(x,y)$. The boundary condition at $\delta\Omega_2$ is $u_x|_{\partial\mathcal{D}_2}=u_z|_{\partial\mathcal{D}_2}=0$.

This decomposition corresponds to the following symmetries for the velocity and vorticity fields

$$\text{A}\quad\left\{\begin{array}{rcl}
\omega_x(x,-y) &=& \omega_x(x,y)\\
\omega_y(x,-y) &=& -\omega_y(x,y)\\
\omega_z(x,-y) &=& \omega_z(x,y)\\
u_x(x,-y) &=& -u_x(x,y)\\
u_y(x,-y) &=& u_y(x,y)\\
u_z(x,-y) &=& -u_z(x,y)\\
p(x,-y) &=& -p(x,y)
\end{array}\right.\qquad
\text{S}\quad\left\{\begin{array}{rcl}
\omega_x(x,-y) &=& -\omega_x(x,y)\\
\omega_y(x,-y) &=& \omega_y(x,y)\\
\omega_z(x,-y) &=& -\omega_z(x,y)\\
u_x(x,-y) &=& u_x(x,y)\\
u_y(x,-y) &=& -u_y(x,y)\\
u_z(x,-y) &=& u_z(x,y)\\
p(x,-y) &=& p(x,y)
\end{array}\right. \tag{3.17}$$

At the other frontiers, boundary conditions are the same for both subsets. A Dirichlet condition is imposed at the boundary $\partial\mathcal{D}_1$, i.e. $\boldsymbol{u}|_{\partial\mathcal{D}_1}=0$. At the top frontier $\partial\mathcal{D}_4$, a symmetry boundary condition is applied, i.e. $u_y|_{\partial\mathcal{D}_4}=0$. The frontier $\partial\mathcal{D}_3$ is where the flow exits the domain, therefore an outflow boundary condition is imposed, i.e. $p-\frac{1}{Re_\Gamma}\nabla\boldsymbol{u}|_{\partial\mathcal{D}_3}\cdot\boldsymbol{n}=0$.

This distinction between the S and A perturbation allows us to keep on using the computational domain $\mathcal{D}$ (used for the base flow) for the perturbations. Even though that doubles the case that need to be considered, it overall reduces the computational time needed thanks to a smaller grid.

Adjoint equations Adjoint equations are derived later on in this chapter, in the presentation of the optimal perturbation algorithm. They are the counter-part of the direct linearized

equations (3.15) and read

$$\begin{aligned}
\frac{\partial u_x^+}{\partial t} - U_x\frac{\partial u_x^+}{\partial x} - U_y\frac{\partial u_x^+}{\partial y} &= -u_x^+\frac{\partial U_x}{\partial x} - u_y^+\frac{\partial U_y}{\partial x} + iu_z^+\frac{\partial U_z}{\partial x} + ikU_z u_x^+ - \frac{\partial p^+}{\partial x} \\
&+ \frac{1}{Re_\Gamma}\left(\frac{\partial^2 u_x^+}{\partial x^2} + \frac{\partial^2 u_x^+}{\partial y^2} - k^2 u_x^+\right) \\
\frac{\partial u_y^+}{\partial t} - U_x\frac{\partial u_y^+}{\partial x} - U_y\frac{\partial u_y^+}{\partial y} &= -u_x^+\frac{\partial U_y}{\partial x} - u_y^+\frac{\partial U_x}{\partial y} + iu_y^+\frac{\partial U_z}{\partial y} + ikU_z u_y^+ - \frac{\partial p^+}{\partial y} \\
&+ \frac{1}{Re_\Gamma}\left(\frac{\partial^2 u_y^+}{\partial x^2} + \frac{\partial^2 u_y^+}{\partial y^2} - k^2 u_y^+\right) \\
\frac{\partial u_z^+}{\partial t} - U_x\frac{\partial u_z^+}{\partial x} - U_y\frac{\partial u_z^+}{\partial y} &= ikU_z u_z^+ + ikp^+ \\
&+ \frac{1}{Re_\Gamma}\left(\frac{\partial^2 u_z^+}{\partial x^2} + \frac{\partial^2 u_z^+}{\partial y^2} - k^2 u_z^+\right) \\
\frac{\partial u_x^+}{\partial x} + \frac{\partial u_y^+}{\partial y} + ku_z^+ &= 0
\end{aligned} \tag{3.18}$$

Note that the convection by the base flow is reversed compared to (3.15). For this reason, the boundary conditions applied at $\partial\mathcal{D}_1$ and $\partial\mathcal{D}_3$ are switched compared to the boundary conditions of the direct problem.

3.2 Numerical simulations

In this section we present the numerical resolution of the equations of the base flow and of the perturbations. We use a finite element method provided by *FreeFem++* which is a freely available software. We start by describing the time scheme. This is done according to the work of Kress[85]. Guided by the works of Pironneau[122] and Allaire[2], we then describe the implementation of the time scheme in the finite element method.

3.2.1 Time scheme

We consider the full Navier-Stokes equations (3.11) written in the following form

$$\begin{aligned}
\frac{\partial \boldsymbol{U}}{\partial t} + \mathcal{N}(\boldsymbol{U}) + \mathcal{L}(\boldsymbol{U}, P) &= 0 \\
\nabla\cdot\boldsymbol{U} &= 0
\end{aligned} \tag{3.19}$$

with $\mathcal{N}$ the non-linear terms representing the convection $\mathcal{N}(\boldsymbol{U}) = (\boldsymbol{U}\cdot\nabla)\boldsymbol{U}$ and $\mathcal{L}(\boldsymbol{U}, P) = \nabla P - Re_\Gamma^{-1}\Delta\boldsymbol{U}$ the linear terms. The solution $\boldsymbol{U}^{n+1}$ and P^{n+1} at time t^n is calculated as a function of previous solutions $\boldsymbol{U}^n$, $\boldsymbol{U}^{n-1}$, etc and P^n, P^{n-1}, etc, which qualitatively transforms (3.19) into

$$\frac{1}{\Delta t}\boldsymbol{U}^{n+1} + \mathcal{L}\left(\boldsymbol{U}^{n+1}, P^{n+1}\right) = \boldsymbol{f}^n_{explicit} \tag{3.20}$$

where $\Delta t = t^{n+1} - t^n$ is the time step. In this relation, the non-linear term $\mathcal{N}$ is treated explicitly and all the explicit terms are gathered in $\boldsymbol{f}^n_{explicit}$. The linear terms are treated semi-implicitly

	α_0	α_1	α_2	β_1	β_2
BDF1	1	-1		1	
BDF2	3/2	-2	1/2	2	-1

Table 3.1: Coefficients for the BDFr methods, see Kress[85]. r is the order of the BDF scheme.

with the Backward Differentiation Formula scheme of order 2 (BDF2), which transforms (3.20)

into

$$\begin{aligned} \sum_{j=0}^{r} \frac{\alpha_j}{\Delta t} \boldsymbol{U}^{n+1-j} + \mathcal{L}\left(\boldsymbol{U}^{n+1}, P^{n+1}\right) &= -\sum_{j=1}^{r} \beta_j \mathcal{N}\left(\boldsymbol{U}^{n+1-j}\right) \\ \nabla \cdot \boldsymbol{U}^{n+1} &= 0 \end{aligned} \tag{3.21}$$

Coefficients used in this relation are detailed in table 3.1. The explicit term is obtained by extrapolating $\mathcal{N}$ from time t^{n-r+1} up to t^n with an $(r-1)^{th}$ order polynomial. At order 1 the non-linear extrapolation corresponds to $(\boldsymbol{U}^n \cdot \nabla)\boldsymbol{U}^n$. The second order uses the next older value of the velocity field $\boldsymbol{U}^{n-1}$. Concerning the discretization of the time derivative, at order 1 it reads

$$\frac{\partial \boldsymbol{U}}{\partial t} \simeq \frac{\boldsymbol{U}^{n+1} - \boldsymbol{U}^n}{\Delta t} \tag{3.22}$$

while at order 2, it is given by

$$\frac{\partial \boldsymbol{U}}{\partial t} \simeq \frac{3\boldsymbol{U}^{n+1} - 4\boldsymbol{U}^n + \boldsymbol{U}^{n-1}}{2\Delta t} \tag{3.23}$$

The integration is started at t^0 with $r = 1$ and changes to $r = 2$ after t^1. Finally, if, in (3.21), we regroup the terms at $n+1$ at the LHS and the other (explicit) at the RHS, we have

$$\begin{aligned} \alpha_0 \boldsymbol{U}^{n+1} + \Delta t \mathcal{L}\left(\boldsymbol{U}^{n+1}, P^{n+1}\right) &= -\sum_{j=1}^{r} \left[-\alpha_j \boldsymbol{U}^{n+1-j} + \Delta t \beta_j \mathcal{N}\left(\boldsymbol{U}^{n+1-j}\right)\right] \\ \nabla \cdot \boldsymbol{U}^{n+1} &= 0 \end{aligned} \tag{3.24}$$

3.2.2 Space discretization

We use a finite element solver FreeFem++ (see Pironneau[122]) to solve (3.24). The finite element method is based on a variational formulation of the equations. We note $\mathcal{X} = [0,T]; H^1(\Omega)$ and $\mathcal{M} = [0,T]; \mathcal{L}_2(\Omega)$ the spaces of continuous function (and derivable for $\mathcal{X}$) in the physical domain Ω. We suppose that the velocity field $\boldsymbol{U}$ and the pressure field P belongs respectively to $\mathcal{X}^3$ and $\mathcal{M}$. We multiply these equations by test functions $\boldsymbol{V} \in (H_1(\Omega))^3$ and $Q \in \mathcal{L}_2(\Omega)$, which gives after integration and application of the Green's formula

$$\begin{aligned} \int_\Omega \alpha_0 \boldsymbol{U}^{n+1} \cdot \boldsymbol{V} &- \frac{1}{Re} \int_\Omega \nabla \boldsymbol{U}^{n+1} \cdot \nabla \boldsymbol{V} + \int_\Omega P^{n+1} (\nabla \cdot \boldsymbol{V}) \\ &= \int_\Omega \sum_{j=1}^{r} \left[-\alpha_j \boldsymbol{U}^{n+1-j} \cdot \boldsymbol{V} + \beta_j \left(\boldsymbol{U}^{n+1-j} \cdot \nabla\right) \boldsymbol{U}^{n+1-j} \cdot \boldsymbol{V}\right] \qquad \forall\, \boldsymbol{V} \in \mathcal{X}^3 \\ \int_\Omega Q \left(\nabla \cdot \boldsymbol{U}^{n+1}\right) &= 0 \qquad \forall\, Q \in \mathcal{M} \end{aligned} \tag{3.25}$$

where

$$\nabla \boldsymbol{U} \cdot \nabla \boldsymbol{V} = \sum_i \sum_j \frac{\partial U_i}{\partial x_j} \frac{\partial V_i}{\partial x_j} \tag{3.26}$$

Then we write (3.25) into a more concise form

$$\begin{aligned} \alpha_0 a(\boldsymbol{U}^{n+1}, \boldsymbol{V}) + \tfrac{1}{Re} b(\boldsymbol{U}^{n+1}, \boldsymbol{V}) + c(\boldsymbol{V}, P^{n+1}) &= (\boldsymbol{f}, \boldsymbol{V}) \qquad \forall\, \boldsymbol{V} \in \mathcal{X}^3 \\ c(\boldsymbol{U}^{n+1}, Q) &= 0 \qquad \forall\, Q \in \mathcal{M} \end{aligned} \tag{3.27}$$

with the explicit non-linear term noted $\boldsymbol{f}$ and

$$\begin{aligned} a(\boldsymbol{U},\boldsymbol{V}) &= \int_\Omega \boldsymbol{U}\cdot\boldsymbol{V} \\ b(\boldsymbol{U},\boldsymbol{V}) &= \int_\Omega \nabla\boldsymbol{U}:\nabla\boldsymbol{V} \\ c(\boldsymbol{U},P) &= -\int_\Omega P(\nabla\cdot\boldsymbol{U}) \end{aligned} \tag{3.28}$$

The computational domain is divided into finite elements $\mathcal{X}_h$ for the velocity and $\mathcal{M}_h$ for the pressure with $I = dim(\mathcal{X}_h)$ and $J = dim(\mathcal{M}_h)$. We consider $\boldsymbol{U}_h$, $\boldsymbol{V}_h$ in $\mathcal{X}_h^3$, P_h, Q_h in $\mathcal{M}_h$ and $\boldsymbol{f}_h$ in $\mathcal{X}_h$ the discretized forms of the previous variables

$$\begin{aligned} \boldsymbol{U}_h &= \sum_{i=1}^{I} \boldsymbol{U}_i(t)\phi_i(\boldsymbol{x}) \\ P_h &= \sum_{i=1}^{J} P_i(t)\psi_i(\boldsymbol{x}) \end{aligned} \tag{3.29}$$

Introducing these forms in the previous relations gives

$$\begin{aligned} \alpha_0 a\left(\boldsymbol{U}_h^{n+1},\boldsymbol{V}_h\right) + \frac{\Delta t}{Re} b\left(\boldsymbol{U}_h^{n+1},\boldsymbol{V}_h\right) + \Delta t c\left(\boldsymbol{V}_h,P_h^{n+1}\right) &= \left(\boldsymbol{f}_h,\boldsymbol{V}_h\right) \\ c\left(\boldsymbol{U}_h^{n+1},Q_h\right) &= 0 \end{aligned} \tag{3.30}$$

Finally we can use the following matrices A, B and C

$$\begin{aligned} A_{i,j} &= \int_\Omega \phi_i\cdot\phi_j \\ B_{i,j} &= \int_\Omega \nabla\phi_i:\nabla\phi_j \\ C_{i,j} &= \int_\Omega \psi_i(\nabla\cdot\phi_j) \end{aligned} \tag{3.31}$$

$$f_{h,\,i} = \sum_{j=1}^{r}\int_\Omega \left[-\alpha_j \boldsymbol{U}_i^{n+1-j} + \beta_j\left(\boldsymbol{U}_i^{n+1-j}\cdot\nabla\right)\boldsymbol{U}_i^{n+1-j}\right]\phi_i^2$$

write $D = \alpha_0 A + \frac{1}{Re}B$ and solve the following problem with an eigenvalue problem solver

$$\begin{pmatrix} D & C^T \\ C & 0 \end{pmatrix}\begin{pmatrix} \boldsymbol{U}_h^{n+1} \\ P_h^{n+1} \end{pmatrix} = \begin{pmatrix} \boldsymbol{f}_h \\ 0 \end{pmatrix} \tag{3.32}$$

3.2.3 Finite elements

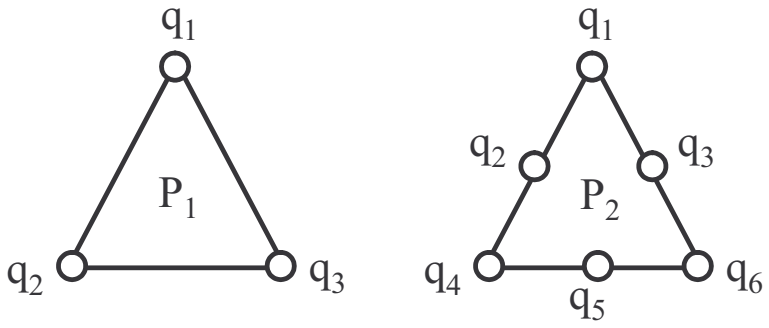

Figure 3.4: Schematic of finite element P_2 and P_1 discretization. Nodes are denoted q.

We use Taylor Hood finite elements of second order P_2 for the velocity components and of first order P_1 for the pressure. These elements are represented in figure 3.4. Every P_2 element has 6 degrees of freedom and every P_1 element has 3 degrees of freedom. In total there are $N_f = 3I + J$ degrees of freedom in the problem. Typical values of N_f is 10^6.

3.2.4 Uzawa algorithm

An Uzawa method is used to solve (3.32). This algorithm proceeds iteratively:

i- Choose an arbitrary initial pressure P_h^0 in $\mathcal{L}^2(\Omega)$

ii- Once P_h^n is known, calculate $\boldsymbol{U}_h^n$ according to equation (3.32)

$$\boldsymbol{U}_h^n = D^{-1}\left(\boldsymbol{f}_h - C^T P_h^n\right) \tag{3.33}$$

The inversion of the matrix D is achieved with *UMFPACK* (see Davis[37]).

iii- Define the new pressure P_h^{n+1} by

$$P_h n + 1 = P_h^n + \rho_n B^T \boldsymbol{U}_h^n \tag{3.34}$$

and restart from i. The parameter ρ_n is a given constant for the time step n.

This method converges quite slowly and requires preconditioning. Here, the Cahouet Chabart preconditioner is used.

3.2.5 Case of the linearized equations

The only difference between linear and non-linear simulations is the convection term. The implementation of the linear equations modifies the $\boldsymbol{f}_h$ in (3.32). In the linearized equations, the convection term $(\boldsymbol{u}\cdot\nabla)\,\boldsymbol{u}$ becomes $\boldsymbol{U}\nabla\boldsymbol{u}+\boldsymbol{u}\nabla\boldsymbol{U}$. The first term $\boldsymbol{U}\nabla$ represents the convection by the base flow and the second term $\nabla\boldsymbol{U}$ is the deformation of the perturbation by the basic strain. The base flow being frozen, these terms can be computed before the march in time of the simulation. For this reason, linearized simulations are faster than non-linear simulations.

3.2.6 Implementation of the boundary conditions

The Dirichlet boundary condition of the type $\boldsymbol{u} = \boldsymbol{u}_{boundary}$ is imposed by affecting a very large value δ (typically $\delta = 10^{30}$) in D_{ij} of (3.32) and by setting $f_{h,\,i} = \delta \boldsymbol{u}_{boundary}(i)$ at the nodes associated to this boundary.

3.3 Normal modes

3.3.1 Equations

Normal modes are elementary solution of the linearized equations in the form $\hat{\boldsymbol{u}}e^{\sigma t}$ where $\hat{\boldsymbol{u}}$ is the normal mode and $\sigma = \sigma_R + i\sigma_I$ is a complex value, with σ_R the growth rate and σ_I the temporal frequency. The mode is said unstable if σ_R is positive. After introduction into the linearized equations (3.15) one gets the following equation in a matrix format

$$A\hat{\boldsymbol{u}} = \sigma B\hat{\boldsymbol{u}} \tag{3.35}$$

with

$$A = \begin{pmatrix} -\frac{\partial U_x}{\partial x} - ikU_z - \mathcal{C} + \mathcal{V} & -\frac{\partial U_x}{\partial y} & 0 & -\frac{\partial}{\partial x} \\ -\frac{\partial U_y}{\partial x} & -\frac{\partial U_y}{\partial y} - ikU_z - \mathcal{C} + \mathcal{V} & 0 & -\frac{\partial}{\partial y} \\ -i\frac{\partial U_z}{\partial x} & -i\frac{\partial U_z}{\partial y} & -ikU_z - \mathcal{C} + \mathcal{V} & -k \\ \frac{\partial}{\partial x} & \frac{\partial}{\partial y} & -k & 0 \end{pmatrix} \tag{3.36}$$

and

$$B = \begin{pmatrix} 1 & 0 & 0 & 0 \\ 0 & 1 & 0 & 0 \\ 0 & 0 & 1 & 0 \\ 0 & 0 & 0 & 0 \end{pmatrix} \tag{3.37}$$

in which $\mathcal{C}$ denotes the convection by the base flow and $\mathcal{V}$ viscous diffusion. Adjoint modes are also defined in relation to the adjoint equations (3.18):

$$A^+\hat{\boldsymbol{u}}^+ = \sigma^+ B\hat{\boldsymbol{u}}^+ \tag{3.38}$$

with

$$A^+ = \begin{pmatrix} -\frac{\partial U_x}{\partial x} - ikU_z + \mathcal{C} + \mathcal{V} & -\frac{\partial U_y}{\partial x} & i\frac{\partial U_z}{\partial x} & \frac{\partial}{\partial x} \\ -\frac{\partial U_x}{\partial y} & -\frac{\partial U_y}{\partial y} + ikU_z + \mathcal{C} + \mathcal{V} & i\frac{\partial U_z}{\partial y} & \frac{\partial}{\partial y} \\ 0 & 0 & ikU_z + \mathcal{C} + \mathcal{V} & -k \\ \frac{\partial}{\partial x} & \frac{\partial}{\partial y} & -k & 0 \end{pmatrix} \tag{3.39}$$

Every adjoint mode $\hat{\boldsymbol{u}}_j^+$ corresponds to the direct mode $\hat{\boldsymbol{u}}_j$ such that $\sigma_j^+ = \sigma_j^*$, with $j = 1, .., N$ the number of normal modes. Every adjoint modes is normalized following $\left(\hat{\boldsymbol{u}}_j^+, \hat{\boldsymbol{u}}_j\right) = 1$ where the scalar product is defined by

$$(\boldsymbol{u}_1, \boldsymbol{u}_2) = \int_\Omega \boldsymbol{u}_1^* B \boldsymbol{u}_2 dS \tag{3.40}$$

Note that the norm based on this scalar product is the kinetic energy of the perturbation. The adjoint problem also verifies $(A\boldsymbol{u}_1, \boldsymbol{u}_2) = (\boldsymbol{u}_1, A^+\boldsymbol{u}_2)$ whatever $\boldsymbol{u}_1$ and $\boldsymbol{u}_2$.

3.3.2 Arnoldi method

Equations (3.35) and (3.38) constitute generalized non-Hermitian eigenvalue matrix problems. The matrix A built in the finite element method is a sparse $N \times N$ matrix of very large dimensions. A typical value for N is 10^6, and the sparsity is illustrated by the fact that only about 10^7 entries are non-zero. The best algorithm known to date to compute eigen solutions of such systems is the Implicitly Restarted Arnoldi Method (IRAM) for which a free software ARPACK (see Lehoucq[95] for details) exists. Its use allowed us to calculate normal modes of the linearized equations in different configurations of base flow, axial wavenumber, swirl number and Reynolds. In the following we illustrate the basic ideas of the Arnoldi method and then discuss the use of the IRAM method in our case.

Simple illustration of the method

The basic mechanisms of the Arnoldi method can be understood by considering the power iteration method. Let us take a classical eigenvalue problem

$$A\boldsymbol{x} = \lambda\boldsymbol{x} \tag{3.41}$$

and suppose the problem has N eigensolutions that can be sorted by decreasing order $\lambda_1 > \lambda_2 > ... > \lambda_N$ in terms of magnitude. The associated eigenvectors $\boldsymbol{x}_1$, $\boldsymbol{x}_2, \ldots$ form a basis for the variable $\boldsymbol{x}$

$$\boldsymbol{x} = \alpha_1\boldsymbol{x}_1 + \alpha_2\boldsymbol{x}_2 + \ldots + \alpha_N\boldsymbol{x}_N \tag{3.42}$$

Then multiplying m times the previous relation by the matrix A leads to

$$\begin{aligned} A^m\boldsymbol{x} &= \alpha_1 A^m\boldsymbol{x}_1 + \alpha_2 A^m\boldsymbol{x}_2 + \ldots + \alpha_N A^m\boldsymbol{x}_N \\ &= \alpha_1\lambda_1^m\boldsymbol{x}_1 + \alpha_2\lambda_2^m\boldsymbol{x}_2 + \ldots + \alpha_N\lambda_N^m\boldsymbol{x}_N \\ &= \lambda_1^m\left(\alpha_1\boldsymbol{x}_1 + \alpha_2\frac{\lambda_2^m}{\lambda_1^m}\boldsymbol{x}_2 + \ldots + \alpha_N\frac{\lambda_N^m}{\lambda_1^m}\boldsymbol{x}_N\right) \end{aligned} \tag{3.43}$$

Therefore we have, if m and the difference between the two largest eigenvalues λ_1 and λ_2 are large enough: $A^m \boldsymbol{x} = \lambda_1^m \alpha_1 \boldsymbol{x}_1$ from which the calculation of $\boldsymbol{x}_1$ can be achieved with the Rayleigh quotient (* being the transpose conjugate)

$$\lambda_1 = \frac{\boldsymbol{x}_1^* A \boldsymbol{x}_1}{\boldsymbol{x}_1^* \boldsymbol{x}_1} \tag{3.44}$$

The capacity of the sequence $\boldsymbol{x}, A\boldsymbol{x}, A^2\boldsymbol{x}, \ldots$ to converge to the largest eigenvalue of $A\boldsymbol{x} = \lambda \boldsymbol{x}$ is used in the Arnoldi algorithm through the Krylov subspace

$$\mathcal{K}_p = \{b, Ab, \ldots, A^{p-1}b\} = \{q_1, q_2, \ldots, q_p\} \tag{3.45}$$

where the initial vector $\boldsymbol{b}$ is chosen arbitrarily and p is the number of vectors. An orthogonalization of the Krylov subspace by a Gram-Schmidt process leads to the orthonormal vectors $\boldsymbol{q}_1, \boldsymbol{q}_2, \ldots$. The calculation of these vectors is done iteratively at each addition of a new member in the Krylov subspace. These vectors prove to be good approximations of the leading eigenvectors of A. The precision of this approximation increases with the number p. Therefore, to have a good precision, one should do this process over large subspace. However this would be computationally intensive and would cause storage problem.

To avoid such problems the idea of the IRAM is to restart the process before p is to large by improving the initial vector $\boldsymbol{b}$. A common habit is to take $\boldsymbol{b}$ as a linear combination of the vector $\boldsymbol{q}_{i=1..p}$. One drawback of the IRAM is that there is no a priori limit of the number of restarts needed to have a good convergence.

Shift and invert

This method can also be used to compute the smallest eigenvalue λ_N of A if A is inversible by considering the eigenvalues $\lambda_N^{-1} > \lambda_{N-1}^{-1} > \ldots$ of A^{-1}. More generally, the method allows to calculate any eigenvalue λ_j in the spectrum that is close to a guess value λ_g specified by the user. This is done by transforming the initial matrix system into

$$(A - \sigma_g B)\, \hat{\boldsymbol{u}}_j = (\sigma_j - \sigma_g)\, B \hat{\boldsymbol{u}}_j \tag{3.46}$$

and then

$$(A - \sigma_g B)^{-1}\, B \hat{\boldsymbol{u}}_j = \bar{\lambda}_j \hat{\boldsymbol{u}}_j \tag{3.47}$$

with

$$\lambda_j = \lambda_g + \frac{1}{\bar{\lambda}_j} \tag{3.48}$$

which is similar to (3.41).

Use of the ARPACK drivers

Problems (3.35) and (3.38) being non-Hermitian, we use the complex driver *zndrv4* of ARPACK. The user specifies the following information for the driver:

i- type of eigenvalue search. We chose the "LM" mode corresponding to eigenvalues with largest magnitude

ii- number of eigenvalues *nev*

iii- number of vectors in the basis p

iv- maximum number of iteration

v- guess value σ_g

In the particular case when the shift is real and there is no axial flow W, matrix A and A^+, defined in (E.20) and (E.22)) are real and one can use the real driver *dndrv4*, which is faster.

3.4 Optimal perturbations

3.4.1 Energy of the perturbation

In incompressible flows the energy of perturbations is the kinetic energy contained in a volume of length $\lambda = k/2\pi$ (λ being the wavelength) and infinite transverse extension

$$E(t) = \frac{k}{2\pi} \int_{\mathcal{R}} \int_{\mathcal{R}} \int_0^{k/2\pi} \left(\left(u_x e^{ikz} \right)^2 + \left(u_y e^{ikz} \right)^2 + \left(u_z e^{ikz} \right)^2 \right) dxdydz \tag{3.49}$$

After a few manipulation, one gets

$$E(t) = \frac{1}{2} \int_S \left(u_x^2 + u_y^2 + u_z^2 \right) dxdy \tag{3.50}$$

For simplicity, the term $1/2$ is discarded hereafter.

3.4.2 Transient growth

The optimal perturbation of the base flow is the perturbation that, based on an initial energy, and among all other possible initial perturbations, exhibits the largest gain of energy during a given time t_{opt}. This perturbation is interesting in order to investigate transient growth. Chapter 6 is dedicated to the study of optimal perturbations in the case of vortex pairs. Different techniques exist to calculate the optimal perturbation. The one we use is based on iterative direct/adjoint linearized simulations of (3.15) and (3.18). The operator A being non-Hermitian ($A \neq A^+$, A is also described as non-normal), direct and adjoint simulations bring the iterative process toward a non trivial solution that describes the linear mechanisms of energy growth in a given flow. Transient growth of energy is called **algebraic**. This term is used by opposition with the large time modal growth that is called **exponential**.

3.4.3 Optimization method

Objective and Lagrangian

The objective of the optimization is to calculate the initial perturbation $\boldsymbol{u}_0$ that gives the maximum energy gain G

$$G(t; \boldsymbol{u}_0) = \frac{E(t)}{E(0)} \tag{3.51}$$

at the optimization time $t = t_{opt}$. The maximization process includes this objective and the constraints that restrict the perturbation form and evolution, namely the linearized Navier-Stokes equations. Writing the latter $\mathcal{LNS}(\boldsymbol{u}) = 0$ (it includes the boundary conditions) and the initial condition $\boldsymbol{u}(t = 0) = \boldsymbol{u}_0$, the following Lagrangian functional holds

$$\mathcal{L}\left(\boldsymbol{u}, \boldsymbol{u}_0, \boldsymbol{u}^+, \boldsymbol{u}_0^+; t_{opt}\right) = G(t_{opt}) - < \mathcal{LNS}\left(\boldsymbol{u}\right), \boldsymbol{u}^+ > - \left(\left(\boldsymbol{u}(t=0) - \boldsymbol{u}_0\right), \boldsymbol{u}_0^+ \right) \tag{3.52}$$

where

$$< \boldsymbol{u}_1, \boldsymbol{u}_2 > = \int_0^{t_{opt}} \int_S \boldsymbol{u}_1^* B \boldsymbol{u}_2 dt dS \tag{3.53}$$

and $(\cdot, \cdot)$ is defined in (3.40). This problem is parameterized by t_{opt}, the properties of base flow and the wavenumber k of the perturbations. The solution gives the initial perturbation $\boldsymbol{u}_0$ for which $G(t_{opt}; \boldsymbol{u}_0)$ is maximum. However the computational effort to achieve the optimization over the parameter space spanned by t_{opt}, Re_Γ, q, a/b and k is too demanding. Instead we will calculate local optimal perturbations over specific values of k and q, and for a limited number of base flows, Re_Γ being fixed.

Condition for the optimum

At the optimum $\boldsymbol{u}_{opt}$ the derivative of the lagrangian (3.52) must cancel, which means that

$$\frac{\partial \mathcal{L}}{\partial \boldsymbol{u}} = 0 \quad , \quad \frac{\partial \mathcal{L}}{\partial \boldsymbol{u}_0} = 0 \quad , \quad \frac{\partial \mathcal{L}}{\partial \boldsymbol{u}^+} = 0 \quad , \quad \frac{\partial \mathcal{L}}{\partial \boldsymbol{u}_0^+} = 0 \tag{3.54}$$

Differentiation is achieved according to

$$\frac{\partial \mathcal{L}}{\partial \boldsymbol{u}} = \lim_{\epsilon \to 0} \frac{\mathcal{L}\left(\boldsymbol{u} + \epsilon\delta\boldsymbol{u}, \boldsymbol{u}_0, \boldsymbol{u}^+, \boldsymbol{u}_0^+\right) - \mathcal{L}\left(\boldsymbol{u}, \boldsymbol{u}_0, \boldsymbol{u}^+, \boldsymbol{u}_0^+\right)}{\epsilon\delta\boldsymbol{u}} \tag{3.55}$$

The last two derivatives in (3.54) correspond respectively to the linearized Navier-Stokes equations (3.15) and to the initial condition $\boldsymbol{u}(t=0) = \boldsymbol{u}_0$. The first condition in (3.54) leads to the adjoint equations already given in (3.18) (after an inversion of the time is introduced $t \to -t$) with the following initial condition

$$\boldsymbol{u}_0^+ = \frac{\boldsymbol{u}(t_{opt})}{E(0)} \tag{3.56}$$

The second term in (3.54) leads to

$$\frac{\partial \mathcal{L}}{\partial \boldsymbol{u}_0} = -2\frac{E(t)}{E(0)^2}\boldsymbol{u}_0 + \boldsymbol{u}^+(t_{opt}) \tag{3.57}$$

Optimal perturbation algorithm

The optimization is achieved with the following iterative strategy

i- Start from an arbitrary initial perturbation $\boldsymbol{u}_0^0$

ii- At iteration n, compute the perturbation flow at t_{opt} by a direct simulation of (3.15).

iii- The perturbation $\boldsymbol{u}^n(t_{opt})$ gives the initial condition for the adjoint $\boldsymbol{u}_0^{+n}$ thanks to relation (3.56).

iv- Compute the adjoint perturbation $\boldsymbol{u}^{+n}(t_{opt})$ at time t_{opt} by an adjoint simulation of (3.18) started with $\boldsymbol{u}_0^{+n}$

v- Calculate the derivative of the Lagrangian about the initial perturbation $\boldsymbol{u}_0^n$ with relation (3.57)

vi- Compute $\left(\frac{\partial \mathcal{L}}{\partial \boldsymbol{u}_0}\right)^n (t = t_{opt})$ by a direct simulation of (3.15) initialized by $\left(\frac{\partial \mathcal{L}}{\partial \boldsymbol{u}_0}\right)^n (t = 0)$

vii- Calculate the new perturbation $\boldsymbol{u}_0^{n+1} = \boldsymbol{u}_0^n + \alpha \left(\frac{\partial \mathcal{L}}{\partial \boldsymbol{u}_0}\right)^n (t = 0)$ where α is chosen in order to maximize

$$G^{n+1} = \frac{\|\boldsymbol{u}^{n+1}\|^2}{\|\boldsymbol{u}_0^{n+1}\|^2} = \frac{\|\boldsymbol{u}^n + \alpha \left(\frac{\partial \mathcal{L}}{\partial \boldsymbol{u}_0}\right)^n (t = t_{opt})\|^2}{\|\boldsymbol{u}_0^n + \alpha \left(\frac{\partial \mathcal{L}}{\partial \boldsymbol{u}_0}\right)^n (t = 0)\|^2} \tag{3.58}$$

over $\alpha \in \mathcal{C}$, since the velocity field is complex. The algorithm used to achieve this optimization is described in the next paragraph. When the new initial perturbation is calculated, the iteration is started gain (note that we don't need to do step (ii) since $\boldsymbol{u}^{n+1}(t_{opt})$ is already known). The convergence is achieved and the routine stopped when $|G^{n+1} - G^n|$ is less than a prescribed small value.

Optimal α

The variable coefficient α being complex, it can be written $\alpha = \alpha_R + i\alpha_I$. The following form of $G(\alpha)$ holds

$$G(\alpha) = \frac{\boldsymbol{u}_1 + \alpha\Delta\boldsymbol{u}_1}{\boldsymbol{u}_2 + \alpha\Delta\boldsymbol{u}_2} = \frac{A_1 + B_1\alpha_R + C_1\alpha_I + D_1\left(\alpha_R^2 + \alpha_I^2\right)}{A_2 + B_2\alpha_R + C_2\alpha_I + D_2\left(\alpha_R^2 + \alpha_I^2\right)} \tag{3.59}$$

with

$$\begin{array}{rcc} \boldsymbol{u}_1 & = & \boldsymbol{u}_{1R} + I\boldsymbol{u}_{1I} \\ \Delta\boldsymbol{u}_1 & = & \Delta\boldsymbol{u}_{1R} + I\Delta\boldsymbol{u}_{1I} \\ \boldsymbol{u}_2 & = & \boldsymbol{u}_{2R} + I\boldsymbol{u}_{2I} \\ \Delta\boldsymbol{u}_2 & = & \Delta\boldsymbol{u}_{2R} + I\Delta\boldsymbol{u}_{2I} \\ A_{1/2} & = & \|\boldsymbol{u}_{1/2}\|^2 \\ B_{1/2} & = & 2\int_S \left(\boldsymbol{u}_{1/2R}\cdot\Delta\boldsymbol{u}_{1/2R} + \boldsymbol{u}_{1/2I}\cdot\Delta\boldsymbol{u}_{1/2I}\right) dS \\ C_{1/2} & = & 2\int_S \left(\boldsymbol{u}_{1/2I}\cdot\Delta\boldsymbol{u}_{1/2R} - \boldsymbol{u}_{1/2R}\cdot\Delta\boldsymbol{u}_{1/2I}\right) dS \\ D_{1/2} & = & \|\Delta\boldsymbol{u}_{1/2}\|^2 \end{array} \tag{3.60}$$

The optimal α is found by solving

$$\frac{\partial G}{\partial \alpha_R} = 0 \quad , \quad \frac{\partial G}{\partial \alpha_I} = 0 \tag{3.61}$$

Writing these relation gives

$$\begin{array}{l} \left(B_1A_2 - B_2A_1 + \alpha_I B_1C_2 - \alpha_I B_2C_1 + \alpha_I^2 B_1D_2 - \alpha_I^2 B_2D_1\right) \\ +2\left(D_1A_2 - D_2A_1 + \alpha_I D_1C_2 - \alpha_I D_2C_1\right)\alpha_R + \left(D_1B_2 - D_2B_1\right)\alpha_R^2 = 0 \\ \\ \left(C_1A_2 - C_2A_1 + \alpha_R C_1B_2 - \alpha_R C_2B_1 + \alpha_R^2 C_1D_2 - \alpha_R^2 C_2D_1\right) \\ +2\left(D_1A_2 - D_2A_1 + \alpha_R D_1B_2 - \alpha_R D_2B_1\right)\alpha_I + \left(D_1C_2 - D_2C_1\right)\alpha_I^2 = 0 \end{array} \tag{3.62}$$

The solution α_R, α_I is calculated by a recursive algorithm

i- Start from an arbitrary α_I^0

ii- Calculate α_R^n

iii- Calculate the new α_I^{n+1} and restart the process until convergence

The required number of iteration for convergence is low.

4 Experimental set-up

This chapter deals with the presentation of the experimental apparatus. We first describe the wind tunnel and the model. We then present the preliminary investigations we made to fix the flow configuration and the experimental procedures. In the last part we present measurement techniques used for the study.

4.1 Wind tunnel

4.1.1 Presentation

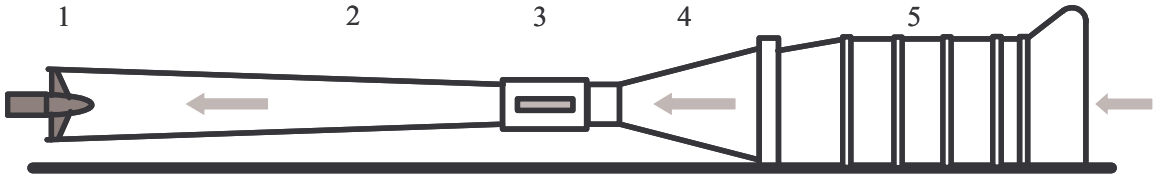

Figure 4.1: Schematic of the wind tunnel. 1-Axial fan 2-Diffuser 3-Test section 4-Contraction 5-Settling chamber. The flow is going from the right to the left.

Figure 4.1 shows a schematic view of the wind tunnel that is used in the present thesis. It is a low speed, open circuit wooden wind tunnel with a circular test section. The propeller generates a free stream velocity ranging from approximately 20 to 40m/s going from the right to the left in the figure. The turbulence level is 0.2%. From right to left, the wind tunnel comprises

i- The entrance of the wind tunnel: a filter to avoid particles can be placed there. However it was not used in the present experiment because it was shown to increase the level of turbulence in the test section by about a factor 2. Moreover it reduced significantly the free stream velocity (by about 20%).

ii- The settling chamber: a honeycomb made of square cells of $10cm^2$ is placed at the entrance of the settling chamber. Honeycomb are effective for making the flow uniform and reducing residual turbulence by removing swirl and lateral mean velocity variations.

iii- The contraction: there, the flow is accelerated to the desired velocity. A pitot tube is placed downstream of the contraction to measure the stagnation pressure P_{i0}. A thermocouple is placed at the entrance of the contraction to measure the stagnation temperature T_{i0}.

iv- Test section: it is about $1m$ in diameter and $2m$ long. It has vertical glass windows at its sides that cover almost its entire length. A pressure tap at the entrance of the test section is used to measure the static pressure and the velocity, based on the measurement of the stagnation pressure P_{i0}.

v- The diffuser: it is a gradually-expanding duct in which the flow velocity decreases and the pressure rises. The recovery of pressure from kinetic energy reduces the power needed to drive the wind tunnel. Note that the angle of expansion must remain small ($< 7^o$) in order to avoid flow separation in the diffuser boundary layer.

vi- The axial fan has a power of 15.5kW (this is comparable to a small car). The power of the fan must be adequate to cope with the resistive components such as the friction on the wind tunnel walls or the pressure losses associated with the model.

Details on the design of low speed wind tunnels can be found in Mehta[110].

4.1.2 Experimental model

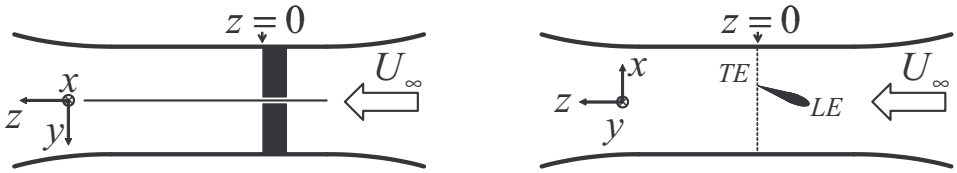

(a) Side view (b) Top view

Figure 4.2: (a) Side view and (b) top view of the model in the test section. The model is made of one wing split in its middle section. Each part is adjustable in incidence. A splitter plate modelling the casing wall of a compressor can be installed in order to split the test section in two equal parts.

The model consists of one aluminium wing split in two parts at its middle section, see figure 4.2 and 4.3. Cartesian coordinates are used, as indicated in figure 4.2. The longitudinal direction is z, x is the horizontal axis and y is the vertical axis (wing is vertical). The origin of the longitudinal direction z is set at the wing trailing edge (TE). The leading edge is denoted LE. The free stream velocity is U_∞. It is set at $38m/s$ if not otherwise stated. Distances are normalized on the wing chord c and time is normalized on c/U_∞. The Reynolds number based on the chord is $Re_c = cU_\infty/\nu = 4.8.10^5$. The size of the gap between the two wing tips is 2τ. The gap size τ is varied by variation of the wing span. A summary of the flow and wing characteristics is given in table 4.1. The wing section is that of a NACA0012. It can be set

Table 4.1: Main characteristics of the apparatus.

Airfoil	NACA0012
Chord, c	$0.2m$
Span	$0.4m$
Re_c	2.10^5 to 5.10^5
Incidence, α	-15^o to 15^o
Gap τ	0 to $25mm$

at angles of attack up to ± 15 degrees. The gap τ can be adjusted between 0 to $25mm$. Each part of the wing is equipped with 38 static pressure taps of $1mm$ diameter located along the mid-span section. The wing is attached to two metallic walls that fill the bottom and the top of the test section over a few centimeters as shown in figure 4.3(a) and 4.3(b). Importantly the model can be set into two different configurations depending on the presence or not of a splitter plate:

i- **Without splitter plate (C1)** the model consists in a split wing, like in Lakshminarayana[88]. The two wing tips serve as a vortex pair generator. In this study

we always set the two parts of the wing at the same angle of attack. The flow downstream is thereby symmetric. Pictures of the apparatus in this configuration are shown in figure 4.3.

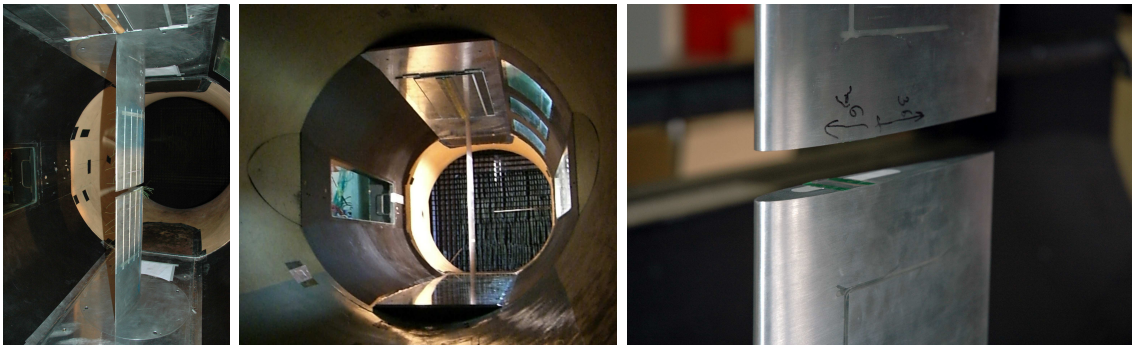

(a) (b) (c)

Figure 4.3: Picture of the model without splitter plate.

ii- **With splitter plate (C2)** the splitter plate plays the role of the casing wall in compressors. It materializes the symmetry plane of the vortex pair. The flow produced in the gap between the wing tip and the plate is similar to the flow produced at blade tips of compressors. In this configuration the distance between the wing tip and the plate is τ.

The model is located close to the entrance of the test section in order to dedicate the largest part of the test section to the measurement of the wake. Measurement in the wake and close to the wing, including the gap, were achieved. Carborandum grains (these are similar to sand grains) of size $80\mu m$ were placed at 17% of the wing leading edge to ensure boundary tripping and a fully turbulent boundary layer downstream. The transition was controlled by oil visualizations (see figure 4.5).

4.1.3 Flow separation over the wing

The incidence at which separation of the flow at the suction side of the wing occurs was looked for by sticking nylon tufts and using a UV light generator. It was shown that the flow separates when $\alpha > 10^o$. In this study the angle of attack is set at 8^o. This angle of attack is low enough to prevent flow separation but large enough to have a strong tip vortex.

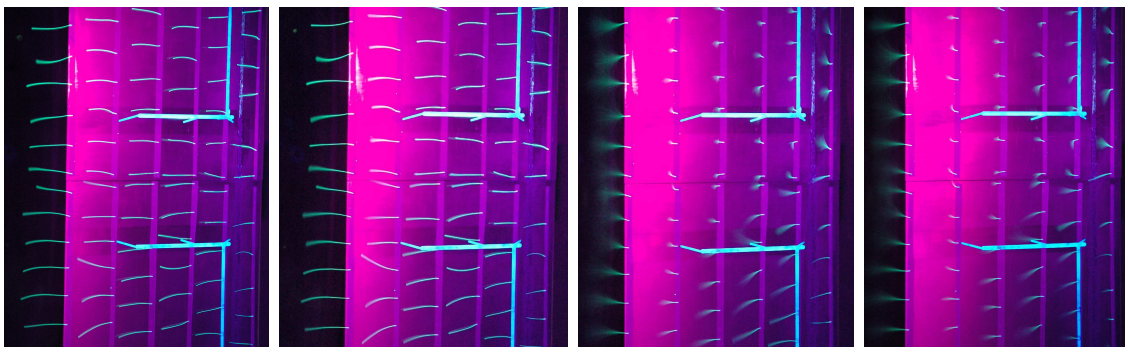

(a) $\alpha = 8^o$ (b) $\alpha = 10^o$ (c) $\alpha = 11^o$ (d) $\alpha = 12^o$

Figure 4.4: Nylon tufts attached at the suction side of the wing without splitter plate when $\tau = 0$ and for several angles of attack.

Figure 4.4 presents long time exposure pictures of the nylon tufts at the suction side of the wing at different angles of attack. In this figure the flow goes from right to left. Movements of the nylon tufts are evidenced thanks to the time of exposure of the camera. Up to 10^o the tufts do not move which means that no separation occurs. Above 11^o the tufts clearly move, which suggests that the flow separates.

In figure 4.5 we show oil flow visualizations on the suction surface at 8^o and 15^o angle of attack. The technique used for the oil flow visualization is the following: we first cover the entire suction surface downstream of the transition line with colored oil. We then turn on the wind tunnel. The oil is displaced under the action of the wall shear stress and is evacuated after reaching the trailing edge if the flow is attached, which is the case for $\alpha = 8^o$. Note that at $\alpha = 8^o$ the trailing edge region is characterized by an incipient flow separation, oil being not completely evacuated there. At the end most of the initial oil has disappeared (torn by the flow) and the rest indicates the wall flow. In practice, the duration of the process depends on the free stream velocity and the oil mixture viscosity. The pictures shown in figure 4.5 was obtained after several minutes.

(a) $\alpha = 8^o$ (b) $\alpha = 15^o$

Figure 4.5: Oil visualization at gap $\tau = 0$. Recall that wing is vertical.

Figure 4.5 proves that the flow at 8^o is 2D. Moreover by comparing oil flow visualization with and without boundary layer tripping, we observed more rapid oil removal at the wing surface with the boundary layer tripping. This corresponds to more intense shearing, and confirmed the turbulent state of the boundary layer. At 15^o, the oil flow pattern has become completely 3D under the combined effects of gravity (remember that the wing is vertical) and flow separation.

4.1.4 Data acquisition

The data acquisition system is composed of the following elements, see figure 4.6:

i- Probes. A Pitot tube located at the entrance of the test section controls the free stream velocity U_∞. Additional probes, seven hole probe, boundary layer probes or hot-wire probes, connected to the data acquisition system, are moved in the test section thanks to a 3D traversing system.

ii- Absolute sensor for the pressure: we use a DPI145 sensor that is directly connected to the stagnation pressure tap P_{i0} of the Pitot tube.

iii- Pressure sensors. We use differential pressure sensors with a range of 0.5PSI or 68.9mbar. The reference pressure is the stagnation pressure P_{i0} measured by a Pitot tube placed at the entrance of the test section.

iv- Thermocouple. The temperature in the flow is controled by means of a type K thermocouple located in the settling chamber.

v- Signal conditioning. Data issuing from the various sensors is conditionned by means of amplifiers and analog filters.

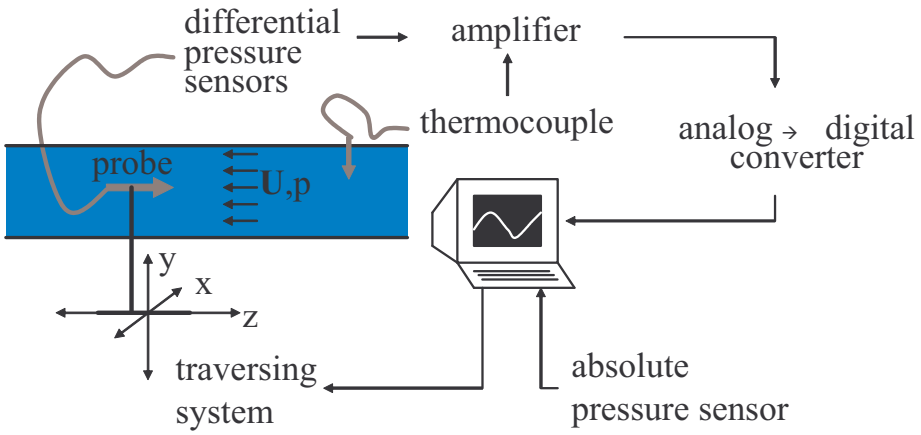

(a)

Figure 4.6: Schematic of the data acquisition system.

vi- Analog/digital converter. A 32 channels, 15 bits resolution is used for the analog/digital conversion. The system is sensible to voltage variation as low as $0.06mV$ ($\pm 10V$ divided by the bit resolution 2^{15}).

vii- Computer. The computer acquires the digital data from the converter through a dedicated software and PC card. In addition, it controls the traversing system and acquires the reference pressure P_{i0} through the DPI145 device.

Note that pressure are normalized on the dynamic pressure at the upstream uniform conditions, which leads to the definition of two pressure coefficients:

$$C_{pi} = \frac{P_{i,0} - P_i}{0.5\rho U_\infty^2}$$
$$C_{ps} = \frac{P_s - P_0}{0.5\rho U_\infty^2} \tag{4.1}$$

named respectively the stagnation and static pressure coefficient. The static pressure P_O is tapped at the entrance of the test section.

4.1.5 Boundary layer on the splitter plate

In figure 4.7(b) we show the configuration of the model with splitter plate. This plate is $10mm$ thick. It extends over 2 chords upstream of the leading edge of the wing and over 5 chords downstream of the trailing edge. Boundary layer tripping is achieved by carborundum grains located at $0.25c$ downstream of the leading edge of the plate.

The boundary layer at the wall is measured with a dedicated probe shown in figure 4.7(a) that includes a flattened pitot tube and a static tap. Measurement were achieved along the dashed line shown in figure 4.7(b). The evolution of the boundary layer thickness $\delta_{0.99}$ with the distance z is depicted in figure 4.8(a). A theoretical prediction corresponding to the growth of a turbulent boundary layer is also included for comparison

$$\delta_{0.99} = \frac{0.37z}{Re_z^{1/5}} \tag{4.2}$$

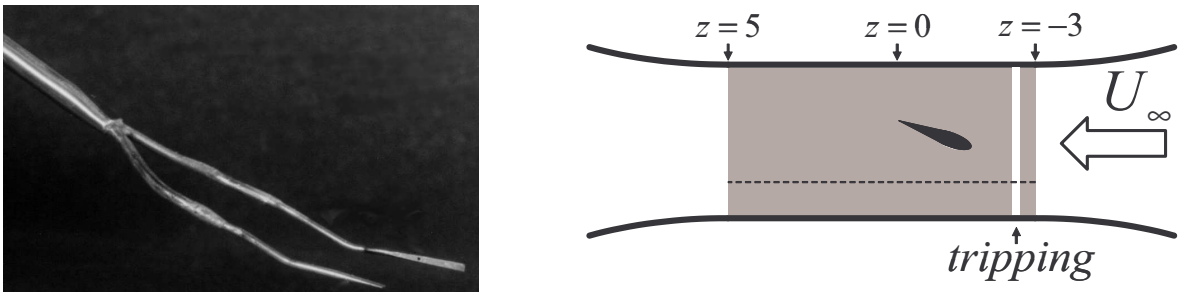

(a) (b)

Figure 4.7: (a) Boundary layer probe rake. It includes a flattened Pitot tube for the stagnation pressure at the left and a static tap at the right. (b) Splitter plate (in grey) seen from above. The boundary layer tripping is located 0.25 downstream of the leading edge of the wall. Distances in figure (b) are normalized on the chord c.

where $Re_z = zU_\infty/\nu$. There is a fair agreement between experiment and prediction. The value of the form factor $H = \delta^*/\theta$ (δ^* being the displacement thickness, and θ the momentum thickness) at each of the measured point is found to be almost constant, close to $H \simeq 1.4$, which means that the boundary layer is turbulent.

The mean velocity profile of the boundary layer at $z = 2.5$ is shown in figure 4.8(b) in wall units U^+ and y^+, with:

$$U^+ = \frac{U_z}{U_\tau} \quad , \quad y^+ = \frac{yU_\tau}{\nu} \quad \text{with} \quad U_\tau = \sqrt{\nu \left(\frac{\partial U_z}{\partial y}\right)_{y=0}} \tag{4.3}$$

Agreement with boundary layer theory is satisfactory. In particular we can distinguish the laminer sub-layer close to the wall, the buffer zone, and the turbulent layer where the velocity is proportional to the logarithm of the distance to the wall. Note that $Re_\theta = \theta U_\infty/\nu = 2000$ at $z = -1$.

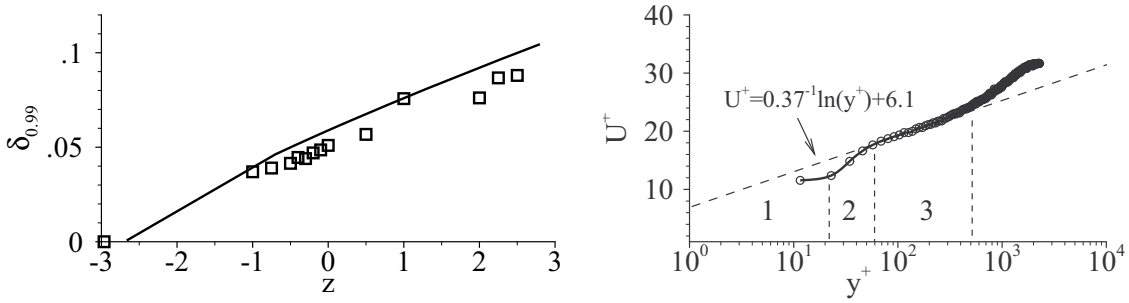

(a) (b)

Figure 4.8: (a) Longitudinal evolution of the boundary layer thickness. □ experiment, line: model. Distances in the figure are normalized on the chord c. (b) Boundary layer profile at $z = 2.5$. 1 - Laminar sub-layer. 2 - Buffer zone. 3 - Turbulent layer.

4.1.6 Control of the angle of attack

The angle of attack of the wing was adjusted with a help of a vernier attached to the test section. However because of the misadjustment between the test section and the rest of the wind tunnel, we had to control the real angle of attack of the incoming flow by comparing the distribution of C_p at mid span of the wing to numerical predictions obtained by a freely available

software called Xfoil. The pressure coefficient is defined in (4.1). In Xfoil the position of the boundary layer tripping can be specified ($0.17c$ downstream of the leading edge). In figure 4.9 we present this comparison for the angle of attack 8^o. The measurements compare favorably with the numerical prediction.

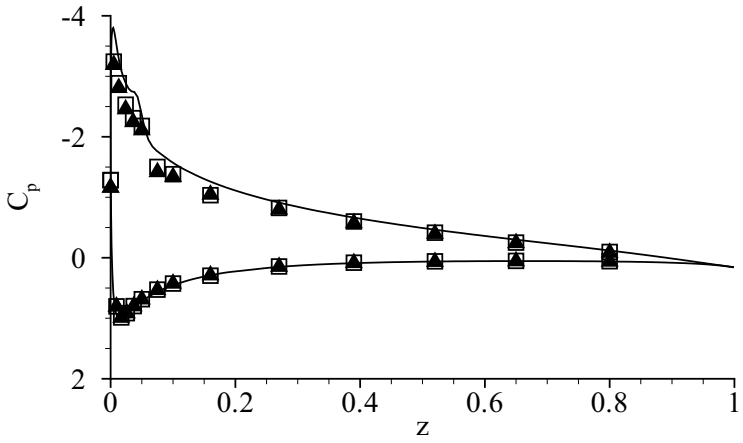

Figure 4.9: Distribution of C_p at mid chord of the two parts of the wing at $\alpha = 8^o$. Comparison with the numerical results obtained with Xfoil. ▲ wing $y < 0$. □ wing $y > 0$. Line: numerics (Xfoil).

4.2 Measurement techniques

4.2.1 Seven hole pressure probe

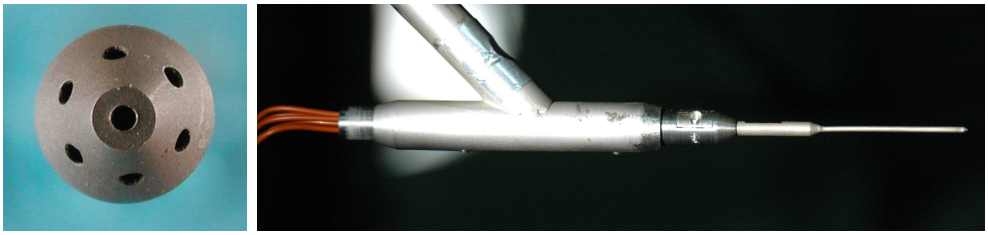

(a) (b)

Figure 4.10: Pictures of the seven hole pressure probe (a) without and (b) with holder.

We use a seven hole pressure probe to measure the time averaged properties of the flow in planes transverse to the free stream. The probe is shown in figure 4.10. It has a diameter of $1.5mm$. A presentation of the calibration method used for the probe is given in appendix B. The seven pressure sensors are located outside the test section and connected to the probe by vinyl tubes (in orange in figure 4.10). The seven hole pressure probe gives accurate results: Payne[119] reports errors of 1^o for the flow angle at low angles and 3.5^o at high angles, and a maximum error between 4% and 6.4% for the pressure coefficients depending on the flow angle of attack and sideslip.

A potential problem concerning probe measurements is the negative influence that the probe can have upon the flow. In the case of vortex flows, this influence was shown to be negligible providing the probe is small, see Devenport[39], as is the case here. In flows where the axial velocity in the vortex core is high, any probe induced perturbations can cause vortex bursting, see Payne[119]. But the critical conditions wherein this may occur are not met in the present experiment.

Characterization of the velocity field requires a small enough spatial resolution. In practice, we first interpolate the flow velocity and pressure provided by the seven hole pressure probe on a coarse mesh ($\Delta x, y = 0.05$) that allows rapid identification of the regions of interest (namely the tip vortex). In a second step, a finer mesh ($\Delta x, y = 0.01$) is used.

Adequate positioning of the probe to the measurement location (wing vicinity, wake) and to the model configuration (gap size, presence of the splitter plate) was achieved by using a set of three different probe holders. A three axis traversing system makes for the displacement of the holder along the x, y and z directions, as described in figure 4.6.

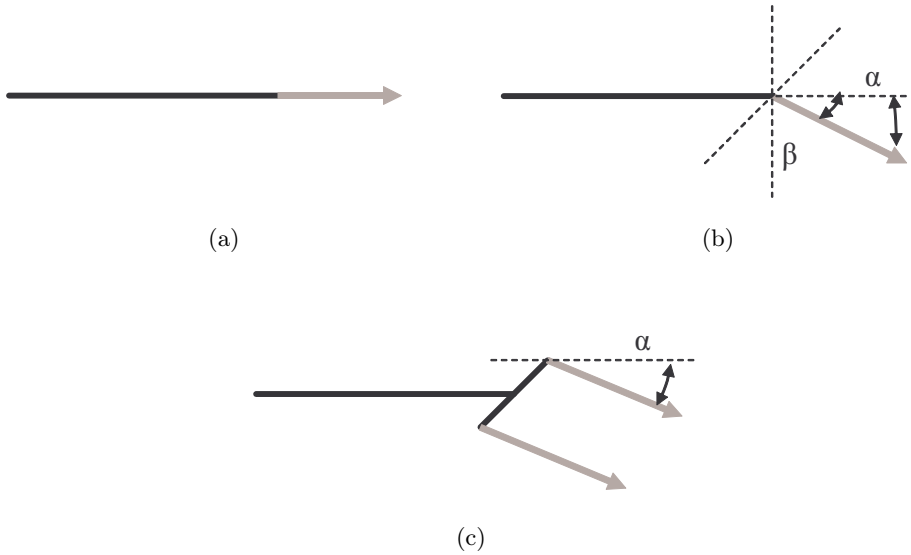

Figure 4.11: Schematic of the holder used for the probe. (a) straight. (b) pre-angled. (c) double holder with angle of attack.

i- The straight holder, shown in figure 4.11(a), allows the positioning of the probe in the direction of the free stream. It is used in regions where the angle of attack and side slip of the flow is in the range accepted by the probe (about 70^o), typically in the wake.

ii- The second type of holder, see figure 4.11(b), is used when the flow angle is too large for the probe. It allows a preliminary setting of an angle of attack α and a side slip angle β. It was mainly used to measure the flow in the regions close to the wing, and in the splitter plate configuration.

iii- The third type of holder, see figure 4.11(c), is designed to hold both a seven hole pressure probe and a single hot-wire. It allows the successive measurement of the mean velocity and pressure (with the seven hole probe) and of the unsteady component of velocity (with a hot-wire). This guaranties an excellent positioning of the hot-wire relatively to the seven hole pressure probe.

4.2.2 Hot-wire

The hot-wire anemometry technique is, together with the laser doppler anemometry, the best tool to measure turbulence in air flows. It is made (see figure 4.12) of a very thin wire (in general tungsten) of diameter $d \sim 0.5$ to $5\mu m$ and small length (length $l \sim 0.3$ to $1mm$, see Comte-Bellot[31]). Hot-wires work on a heat/convection correlation principle. Air flowing past the wire has a cooling effect on the wire. As the temperature of the wire changes, so does the electrical resistance. Most hot-wire are operated in a constant-temperature mode (constant temperature anemometer). That means that the electrical intensity is varied by means of a

feedback amplifier in order to keep the temperature of the hot-wire constant. Data acquisition with the hot-wire relies on a modelling of the relation between the flow velocity and the electrical voltage needed to make for constant temperature.

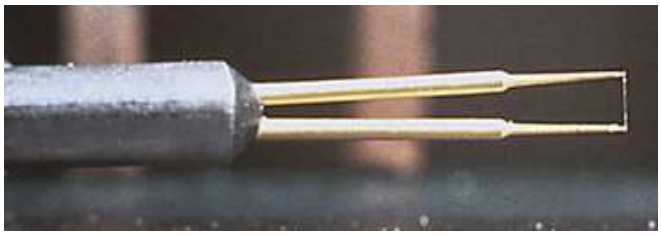

(a)

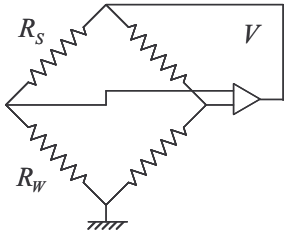

(b)

Figure 4.12: (a) Picture of a single hot-wire, (b) Wheatstone bridge used for the constant temperature technique.

Here we give some details on this model, based on the document of Haertig[60]. We first introduce the Reynolds number based on the diameter d of the wire

$$Re_d = \frac{U_w d}{\nu} \tag{4.4}$$

We denote Q the rate of heat transfer between the wire and the ambient flow. Physical considerations suggest that it depends upon the temperature T_0 of the wire without flow, the temperature T_w of the wire in operating conditions, and upon the thermal conductivity of the air, denoted by the coefficient k.

The electrical resistance of the hot-wire at temperature T_w is noted R_w. If the electrical intensity is I, then the electrical power dissipation is $R_w I^2$. The temperature of the hot-wire will hence change due to (i) electrical heating and (ii) flow cooling. This is readily expressed by

$$C_w \frac{dT_w}{dt} = R_w I^2 - Q \tag{4.5}$$

where C_w is the wire capacity at temperature T_w (in J/K).

Following Hinze[67], we introduce the Nusselt number

$$Nu = \frac{Q}{\pi l \left(T_w - T_0\right) k} \tag{4.6}$$

to characterize thermal exchange and suppose that the relation between flow velocity and heat transfer is in the form

$$Nu = a + b\sqrt{Re} \tag{4.7}$$

Using (4.4) to (4.7) , one gets

$$a + b\sqrt{\frac{U_w d}{\nu}} = \left(R_w I^2 - C_w \frac{dT_w}{dt}\right) \frac{1}{T_w - T_0} \frac{1}{\pi l k} \tag{4.8}$$

In the constant temperature mode, T_w (and thus R_w) is kept constant, which simplify the previous relation (4.8) into

$$a + b\sqrt{U_w} = \frac{R_w}{T_w - T_0} I^2 \tag{4.9}$$

If T_w and T_0 are close enough to a reference temperature T_{ref} (which is the case in most practical situations), one can consider that the resistance of the wire depends linearly upon temperature: $R = R_{ref}\left(1 + \alpha_r \left(T - T_{ref}\right)\right)$ with α_r a given coefficient for the wire. Therefore

$$\frac{R_w}{T_w - T_0} = \alpha_r \frac{R_{ref}}{1 - R_0/R_w} \tag{4.10}$$

The ratio $n = R_w/R_0$ being kept constant and set to an optimal value given by the manufacturer of the hot-wire, we thus end up with

$$a + b\sqrt{U_w} = I^2 \tag{4.11}$$

The constant temperature anemometer is composed of a Wheatstone bridge and of an electrical circuit that adjusts the output voltage to make for constant R_w, a resistance placed at one branch of the bridge, see figure 4.12(b). The current I being related to the resistances in the bridge through the output voltage $V = I\,(R_w + R_S)$, we eventually have the direct relation between the flow velocity U_w and the voltage V measured by the anemometer

$$U_w^{1/m} = k\left(V^2 - V_0^2\right) \tag{4.12}$$

According to (4.11), m is equal to 2.

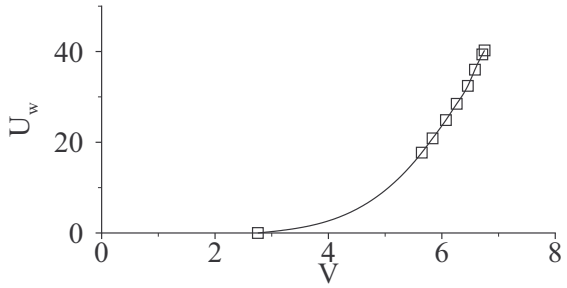

Figure 4.13: Calibration of the hot-wire at $T_0 = 294.1K$. The law is $U_w = K\left(V^2 - V_0^2\right)^m$ with $m = 1.83$, $K = 0.05$ and $V_0 = 2.755V$.

The rate of turbulence can be calculated, based on this relation. If we denote $\bar{V}$ the mean value of V and $V_{eff} = \sqrt{\left(\bar{V} - V\right)^2}$ the mean deviation, one gets

$$\frac{\sqrt{\left(U - \bar{U}\right)^2}}{\bar{U}} = \frac{2m\bar{V}V_{eff}}{\bar{V}^2 - V_0^2} \tag{4.13}$$

At last, we show in figure 4.13 a typical calibration curve for a hot-wire of type P11 which is the one we used in the present work. The curve is in good concordance with (4.12).

4.2.3 Temperature sensor

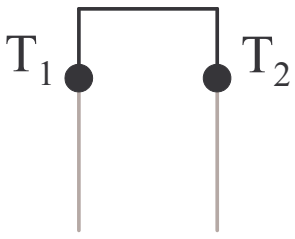

Figure 4.14: Schematic of the thermocouple. The two points represent the junction between the two metals.

The stagnation temperature T_i in the flow is measured with the thermocouple technique which is briefly recalled here. As shown in figure 4.14 a thermocouple is made of two metal parts connected by two junctions that are at temperature T_1 and T_2. Due to the Seebeck effect, the thermocouple produces a voltage that depends upon the temperature difference $\Delta T = T_1 - T_2$

$$\Delta T = \alpha V \tag{4.14}$$

with $\alpha = 24.39^o C/V$ for a type K thermocouple. The type K is made of chromel and alumel and can measure temperature in the range -200^o to $+1350^o$. By measuring the output voltage V, we hence have the value of T_2 once T_1 is maintained at a known temperature.

4.2.4 PIV

The velocity field has also been characterized by means of the stereoscopic Particle Image Velocimetry (PIV) technique. The PIV device is equipped with two pulsed Nd:Yag lasers and two cameras. The tracer particles are generated by a generator of special effect smoke. The whole setting is shown in figure 4.15. It allows the measurement of the three components of the velocity along x, y and z. Depending on the location of the measurement plane, cameras are either positioned at the left or at the right of the laser sheet. The PIV system acquires data at $4Hz$ therefore it is suitable for measuring ensemble averaged statistics of the velocity field. No time resolved signals can be obtained by this system.

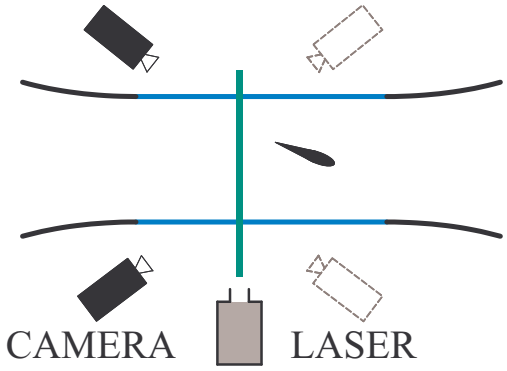

Figure 4.15: Setting of the laser and cameras for the stereo PIV. The green line corresponds to the laser sheet.

As explained by Jensen[77], the principle of PIV is to calculate the fluid velocity by measuring the displacement $\boldsymbol{d}$ of particles seeded in the flow from two closely recorded images of the interrogation volume illuminated by the laser sheet and dividing that displacement by the time interval Δt between the two pulses. The images are divided into small subsections called interrogation areas I_a. Each interrogation area corresponds to one velocity vector of the complete velocity field. Therefore the size of the interrogation area dictates the spatial resolution of the data. In order to measure the mean displacement $\boldsymbol{d}$ of the particles in each interrogation area I_a, the cross-correlation C between I, the image at time t, and I', that at time $t + \Delta t$, is performed, according to

$$C(\boldsymbol{s}) = \int_{I_a} I(\boldsymbol{x}) I'(\boldsymbol{x} + \boldsymbol{s}) d\boldsymbol{x} \tag{4.15}$$

where $\boldsymbol{s}$ is the separation vector and $I(\boldsymbol{x})$ is the pixel value at the point $\boldsymbol{x}$ in the image plane. The principle of the correlation is the following. The interrogation area I'_a is translated by the vector $\boldsymbol{s}$ and the cross-product of all the pixel of the overlapping surface of I_a and I'_a is computed. This is repeated for several $\boldsymbol{s}$ smaller than the interrogation area size. The value of C exhibits a peak at the translation $\boldsymbol{s}$ corresponding to the best match between I_a and I'_a. This value gives the mean displacement $\boldsymbol{d}$ of the particles in the interrogation area. In practice, the calculation of C is computationally intense and a Fourier Transform is used in order to accelerate the process.

4.2.5 Tomoscopy

Tomoscopy is an interesting visualization tool for qualitative flow analysis. With image post-processing it can also give valuable quantitative information. In tomoscopy experiments, the

flow is seeded with tracer particles, the plane where the analysis is performed being illuminated with a laser sheet, like in the PIV method. The light scatter by the smoke particles is then recorded with a high speed camera. Images of the vortices formed in the experiment without

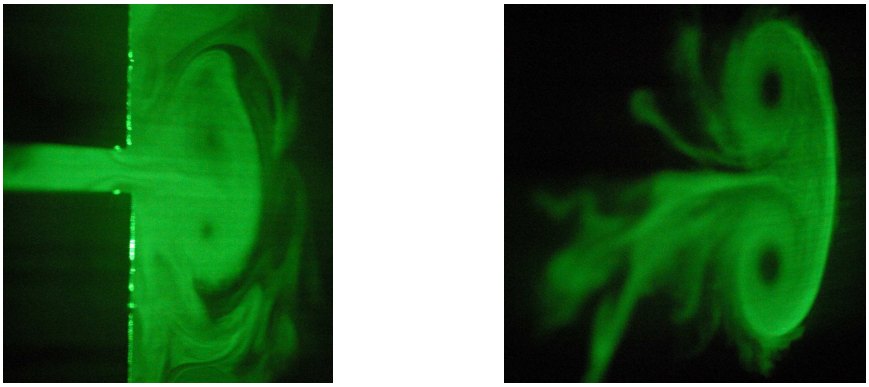

(a) (b)

Figure 4.16: Tomoscopy results in planes transverse to the free stream (a) at the trailing edge of the wing, (b) downstream of the model.

splitter plate are shown in figure 4.16. The flow is entrained in the vortices from the left and in between the vortices. The center of the vortices appears as a black hole where only few particles are present due to the centrifugal forces that expels them outward.

4.2.6 Effect of the adjustment of the apparatus on the data

Adjustment of the apparatus, which comprises the model and the traversing system, influences the quality of the seven hole pressure probe measurement. The following parameters lead to sligh uncertainties :

i- The size τ of the gap between the two parts of the wing. This distance is controlled with a wedge,

ii- The angle of attack: its value can slightly vary when the apparatus is manipulated,

iii- The origin position of the traversing system in the cartesian coordinate system attached to the test section. In this study the origin is taken as the intersection of the trailing edge of the wing $y < 0$ with the wing tip. The process is controlled visually.

iv- The probe holder. Its adjustment includes angular and longitudinal positioning.

In order to evaluate the influence of these parameters on the measurement obtained with the seven hole pressure probe, we repeated 10 times the same measure in the same configuration of the apparatus and derived statistical results. Every time the adjustment of the model and of the traversing system was restarted from scratch.

Confidence intervals were determined for the configuration without splitter plate at $\tau = 3\%c$. The dispersion of the measures is shown in table 4.2. Assuming a Gaussian dispersion of the result, 95% of the results are contained within $2\sigma(A)$ where A is a given variable. This investigation does not take into account the uncertainties due to the data-reduction of the seven-hole pressure probe (see appendix B for details). The results show that the adjustment of both the model and the probe does not influence greatly the raw data, i.e. the velocity and the stagnation pressure (see U and C_{pi} in the table) exhibit small errors. The vortex radius exhibits however larger uncertainties.

Note that this investigation of the accuracy of the system is valid for the seven hole probe measurement only. In particular, PIV does not have these errors, as no traversing system is

variables	U	C_{pi}	C_{ps}	Ω_z	Γ	a
$\sigma(A)/\bar{A}$ (%)	4	2	14	14	8	6

Table 4.2: Estimation of the uncertainties for various flow variables.

used, but it is affected by others (positioning and adjustment of the laser and cameras for example).

Part II

Theoretical results

5 Two-dimensional instability of vortex pairs

In this chapter, we show that the Lamb-Chaplygin dipole (noted LC dipole in chapter 2) is unstable for zero to very small wavenumbers $k = 2\pi/\lambda$ (λ is the wavelength). This 2D instability will be described through its linear and non-linear evolutions. Existence of such a 2D instability in vortex dipoles remains a matter of controversy so it is useful to make first a short review of the situation.

Available publications on the stability of counter-rotating vortex pairs may be split in two categories. A first group is based on a simplified approach of the dipolar flow in which the influence of one of the two vortices of the dipole on the other is reduced to an imposed strain field. In a second group the two vortices of the dipole are fully taken into account. In both groups, the vorticity field is taken either as uniform (patched) or continuous (the vorticity distribution is everywhere derivable). Some examples of uniform patches are the Rankine and Kirchhoff vortices. Some examples of continuous solutions are the Lamb-Oseen vortex, the translating vortex pairs of Pierrehumbert[121], or the LC dipole. The parameters used to define the geometry of the vortex pair are given in figure 5.1.

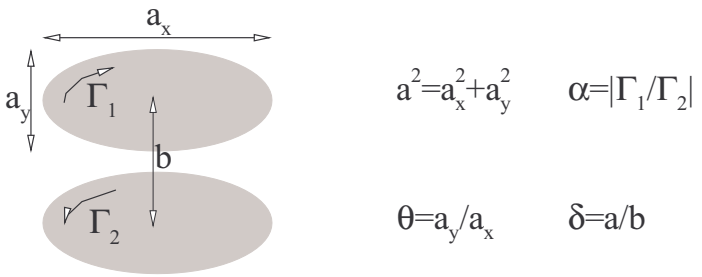

Figure 5.1: Definition of the different parameters used to define a pair of vortices which belong to the first group.

The works of Moore & Saffman[115] and Robinson & Saffman[129] show that a uniform vortex patch in a strain field is unstable to 2D perturbations. The instability takes the form of a $m = 1$ mode (m being the azimuthal wavenumber) that translates the patch along the axis of positive strain. The growth rate of the instability is equal to the strain rate ϵ. There is a limit for the existence of such strained vortices. Saffman[130] showed that a steady ellipse exists when the ratio $\theta = a_y/a_x < 2.9$ where a_x and a_y are the small and large axis of the ellipse, see figure 5.1. This condition is equivalent to the condition $\epsilon/\omega_0 < 0.15$ with ω_0 the vorticity in the patch. Moore & Saffman[115] noted that the vortices overlap before this limit is reached.

The question of the stability for the second group (vortex pair) was first investigated by Kamm[81] in the case of uniform patches but the author did not have enough confidence in his results to publish them. We believe that this failure reveals a real difficulty associated to this 2D instability. In Saffman[130] one reads that "the stability of counter-rotating vortex patches to infinitesimal 2D disturbances does not seem to have been studied in detail, but it is believed

that they are stable" (note that Saffman writes "counter-rotating" instead of "co-rotating" several times). This is however in contradiction with other studies.

First Dritschel[42] considered the stability of the equilibrated opposite signed vortex patches and eventually proved the existence of a 2D instability. His main results are reproduced in figure 5.2. The stability of the flow is described in figure 5.2(a) as function of α the area ratio of the two vortices (equivalent to the ratio of the circulation of the two vortices) and δ the ratio of the size of the smaller vortex to the external dimension of the dipole (equivalent to the aspect ratio a/b of the dipole where a is the radius and b the distance between the vortices), see figure 5.1. The shapes of the steady solutions have been added in the left side of the figure. We are concerned by the case $\alpha = 1$ (equilibrated pair). Figure 5.2(a) shows that the flow becomes unstable for large aspect ratios (thick vortices). The growth rate, as indicated in Dritschel's paper, is $\sigma_r \sim 0.1$. Its non-linear evolution has also been investigated by the author, see figure 5.2(b). This reveals the occurrence of an asymmetric instability which evacuates some vorticity from one vortex. This removed vorticity, actually a patch, in turn pulls out vorticity from the second vortex under the form of thin filaments. This filamentation is then regularized by a specific numerical filtering technique. In the end, a new steady flow emerges that is similar to the initial flow. The distinction between linear and non-linear mechanisms was not made by Dritschel[42]. We will describe quite similar results in the following.

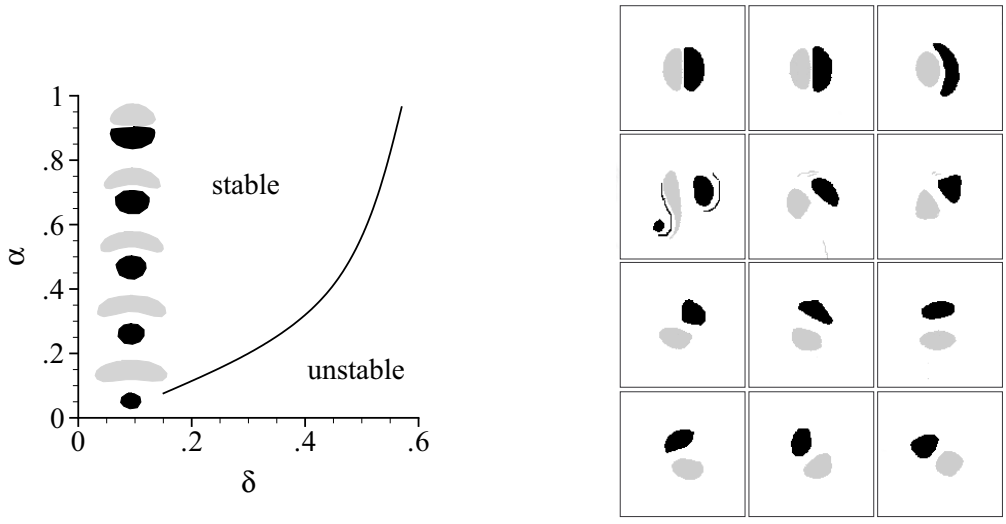

(a) (b)

Figure 5.2: (a) Stability of a counter-rotating vortex patch of uniform vorticity. (b) Non-linear evolution of the instability in the case $\alpha = 1$. Taken from Dritschel[42]. See figure 5.1 for the definition of α and δ.

Saffman & Szeto[131] also commented the stability of the equilibrated pair of opposed patch vortices with regards to the symmetry of the perturbation about the mid-plane of the vortex pair. As we will do below, the authors categorized the perturbation in symmetric and antisymmetric perturbations. Their analysis suggests that the vortex pair is in general only unstable to 2D antisymmetrical perturbations. Our results will infirm this finding by showing that an instability exists for both symmetries.

As for the case of non-uniform vorticity distribution this has not been treated in the literature. We found for instance no work on the stability to 2D perturbations of the Lamb-Oseen vortex in an external strain field. However Meleshko & van Heijst[112] evoked the concomitant findings of Lamb and Chaplygin on the LC model claiming that the "Chaplygin dipole is essentially unstable". But no detail nor reference were given in order to understand the meaning of this unstability.

To sum up, the 2D instability is proven for the cases of uniform patches of vorticity but not in the case of non uniform vorticity like the LC dipole or the Lamb-Oseen vortex in a strain field. As will be seen in the course of this thesis, the effect of the non-uniformity of the vorticity distribution is important regarding stability. However several examples taken in the literature exist for which the flow is unstable whatever the type of vorticity distribution. For instance, in the case of the elliptic instability, see Tsai & Widnall[154], results for both type of distribution agree. The results of Brion[23] on the Crow instability of a realistic dipole (at $a/b = 0.18$) also compares well with Crow's results[34] based on vortex filaments. As a consequence it is puzzling that in the numerical simulations of 2D dipoles (see Sipp[136], Lacaze[86]), the authors do not address the 2D stability of their flow.

The existence of a 2D instability such as that described by Dritschel[42], see figure 5.2, could play an important role in the 2D decay of a vortex pair. For instance, in the case of the trailing vortices shed by an airplane, the circulation of the vortices starts to decrease significantly when the two vortices touch. The regime of vortex overlapping seems important to understand the decay. The subject is also reminiscent of the difficulty to numerically obtain the LC dipole by performing two-dimensional numerical simulation initialized by two Lamb-Oseen vortices although the link between the two vortices was strongly suggested by Sipp[136]. The viscous evolution in time of the LC dipole was investigated by van Geffen and van Heijst [155] by numerical simulations. Their work shows the formation of a tail of vorticity and the fact that the LC dipole (also called the Lamb dipole) is a very stable structure. In particular the 2D steady flow condition $\omega = -k^2\Psi$ remains true despite viscous diffusion.

Another important application of the two-dimensional stability of the LC dipole concerns geophysical flows. Large-scale planetary motions are described by the barotropic vorticity equation (the Hasegawa-Mima equation in plasma physics) which corresponds to the 2D Euler equations in a rotating frame. Dipole vortices, also called modons, are evenly relevant to several other geophysical situations as explained by Holton [68]. In this domain the numerical simulations by Nycander [116] show that an atmospheric westward travelling dipole vortex is unstable. His article also shows that proofs of the stability of modons given by preceding authors were wrong.

The chapter is decomposed in the following way. The first section presents the two-dimensional linear instability and the numerical set-up used to march the linearized equations in time. The next section describes the instability by means of a normal mode decomposition of the linearized problem and an eigenvalue search algorithm. Influence of the Reynolds number and of the axial wavenumber is analyzed. In the third section we describe the non-linear evolution of the instability. In appendix, first we discuss a tricky aspect of 2D instability in system of two point vortices. Second, we give a validation of our normal mode calculation against the result of Billant et al. [19] and present a complete map of the 3D instabilities of the LC dipole with a description of the corresponding unstable modes.

5.1 Methodology

5.1.1 Base flow

The LC dipole is a solution of the incompressible Euler equations which is described by its stream function Ψ :

$$\begin{cases} \Psi(r,\theta) &= \dfrac{2U_{LC}R_{LC}}{\mu_1 J_0(\mu_1)} J_1\left(\mu_1 \dfrac{r}{R_{LC}}\right)\sin\theta & \text{if } r \le R_{LC} \\ \Psi(r,\theta) &= U_{LC} r\left(1-\dfrac{R_{LC}^2}{r^2}\right)\sin\theta & \text{if } r \ge R_{LC} \end{cases} \tag{5.1}$$

We use $Re_\Gamma = \Gamma/\nu$ where Γ is the circulation of each vortex. The value of R_{LC} is set to 1 and $U_{LC} = 0.91982$. The analytical expression is given in polar coordinate although in practice

we will use the cartesian coordinates with x spanning the horizontal direction parallel to the separating line between the two vortices, y the perpendicular direction in the plane and z the axial direction, see figure 5.3. Both the plane velocity $\boldsymbol{U} = (U_x, U_y)$, the stream lines Ψ constant ($\boldsymbol{U} = \nabla \times (\Psi \boldsymbol{e}_z)$) and vorticity are presented in this figure. Note that there is a

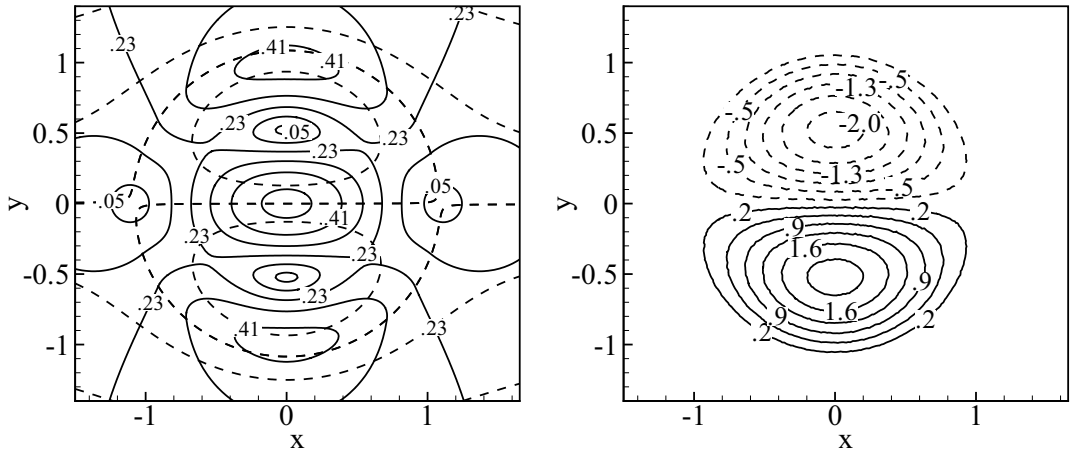

Figure 5.3: Lamb-Chaplygin dipole $a/b = 0.45$. (a) Streamlines in dashed lines and contours of iso-velocity $\|\boldsymbol{U}\|$ (solid line). (b) Iso-contour of axial vorticity Ω_z (solid lines: positive values, dashed lines: negative values).

substantial azimuthal asymmetry of the velocity field around the two vortex centers. We point out the existence of two types of stagnation points in the flow: two elliptical stagnation point corresponding to the vortex centers and two hyperbolic stagnation points at the right and left of the dipole.

Using the two length scales a and b, one gets two time scales: $t_a = 2\pi a^2/\Gamma \sim 0.17$, which is a measure of the rotational period in each vortex, and $t_b = 2\pi b^2/\Gamma \sim 0.85$ (therefore $t_b/t_a = 5$), which measures the strain rate induced by each vortex on the other.

5.1.2 Numerical simulation

The numerical part of the work is carried out by a finite element solver freely available *FreeFem++*[122]. We will solve the incompressible Navier-Stokes (NS) equations in three different forms: linearized, non-linear with frozen base flow, and fully non-linear. The starting point is the NS equations in two-dimensions with $(\boldsymbol{U}, P)$ the velocity and pressure fields:

$$\begin{aligned} \nabla \cdot \boldsymbol{U} &= 0 \\ \frac{\partial \boldsymbol{U}}{\partial t} + \boldsymbol{U}\nabla\boldsymbol{U} &= -\nabla P + \frac{1}{Re_\Gamma}\Delta\boldsymbol{U} \end{aligned} \tag{5.2}$$

The linearized velocity field is $\boldsymbol{U} + \boldsymbol{u}e^{ikz}$ where $(\boldsymbol{U}, P)$ is the base flow, $(\boldsymbol{u}, p)$ is the perturbation ($u \ll U$) and k is the axial wavenumber. The perturbation verifies the linearized version of the NS equations

$$\begin{aligned} \nabla \cdot \boldsymbol{u} &= 0 \\ \frac{\partial \boldsymbol{u}}{\partial t} + \boldsymbol{U}\nabla\boldsymbol{u} &= -\boldsymbol{u}\nabla\boldsymbol{U} - \nabla p + \frac{1}{Re_\Gamma}\Delta\boldsymbol{u} \end{aligned} \tag{5.3}$$

In these equations the base flow does not depend upon time and all the terms in $O(u^2)$ have been ruled out. A convenient approach to study the effect of non-linearities is to keep the $O(u^2)$

terms in these equations, while maintaining the base flow frozen. The system becomes:

$$\begin{aligned} \nabla \cdot \boldsymbol{u} &= 0 \\ \frac{\partial \boldsymbol{u}}{\partial t} + \boldsymbol{U}\nabla\boldsymbol{u} &= -\boldsymbol{u}\nabla\boldsymbol{u} - \boldsymbol{u}\nabla\boldsymbol{U} - \nabla p + \frac{1}{Re_\Gamma}\Delta\boldsymbol{u} \end{aligned} \tag{5.4}$$

The three sets of equations, (5.2), (5.3) and (5.4), will be computed in the following. The time scheme is based on a second order algorithm while the spatial numerical model makes use of P2 and P1 elements for the velocity and the pressure. The boundary conditions consist in a Dirichlet condition at the inlet (the left side of the computational domain), symmetry at the top and bottom boundaries and $p - 1/Re_\Gamma \nabla u \cdot n = 0$ at the outlet. The computational domain is 20Rx20R, which was shown to be enough to exclude the possible influence of the image vorticity by the upper and lower boundaries. A particular attention was dedicated to the mesh. We use a symmetric mesh about the mid plane of the dipole in order to respect the symmetry of the base flow. By doing so we are sure that the numerical model does not introduce any dissymmetry.

5.2 Stability analysis

5.2.1 Linearized simulation with white noise

The reaction of the base flow to an initial random noise is shown in figure 5.4 through the iso-contours of the vorticity ω_z of the perturbation at several time steps. The divergence of the initial random noise being non-zero, the first step of the simulation automatically enforces incompressibility. The early stage of the evolution which is noisy is not shown.

The first snapshot of the perturbation flow is taken at $t = 58.2$ (top left of figure 5.4). We identify a tripolar vorticity structure which is symmetric about the mid plane of the base flow. Further evolution of the perturbation indicates that the structure evolves in time. It rotates in each vortex in a direction opposite to the base flow. At $t = 90$ (see also $t = 140$) vorticity separates in two parts, one at the front and the other at the rear of the dipole. Afterwards an opposite signed tripolar structure reforms and the motion repeats periodically. In addition to the rotation of this tripolar structure, we observe an ejection of the perturbation vorticity which forms a tail behind the dipole. This occurs at the end of the transition from a tripolar structure to its opposite. This trailing vorticity changes sign periodically. Behind the base flow we see this succession of opposite signed vorticity regions that eventually leave the computational domain. These observations proves the existence of a 2D global mode in the LC dipole and they suggest that the linear dynamics comprises two main elements: a dominant unsteady tripolar mode whose structure changes sign periodically and an evacuation of vorticity at the rear stagnation point.

Figure 5.5 shows the evolution of the energy of the perturbation with time:

$$E(t) = \int_S \|\boldsymbol{u}\|^2 dxdy \tag{5.5}$$

where S is the computational domain. The time steps considered in the snapshots of figure 5.4 are depicted in figure 5.5. The frequency $\sigma = \sigma_r + i\sigma_i$ of the instability with σ_r the growth rate and σ_i the time frequency may be determined from this figure by considering, for instance, the time duration between two local minima of the curve. This gives

$$\begin{aligned} \sigma_i &= \frac{\pi}{\Delta t} \\ \sigma_r &= \frac{1}{2\Delta t} \ln \frac{\|\boldsymbol{u}(t+\Delta t)\|^2}{\|\boldsymbol{u}(t)\|^2} \end{aligned} \tag{5.6}$$

Applying this relations, we get $\sigma = 0.21 + i0.32$ (σ being normalized on t_b^{-1}).

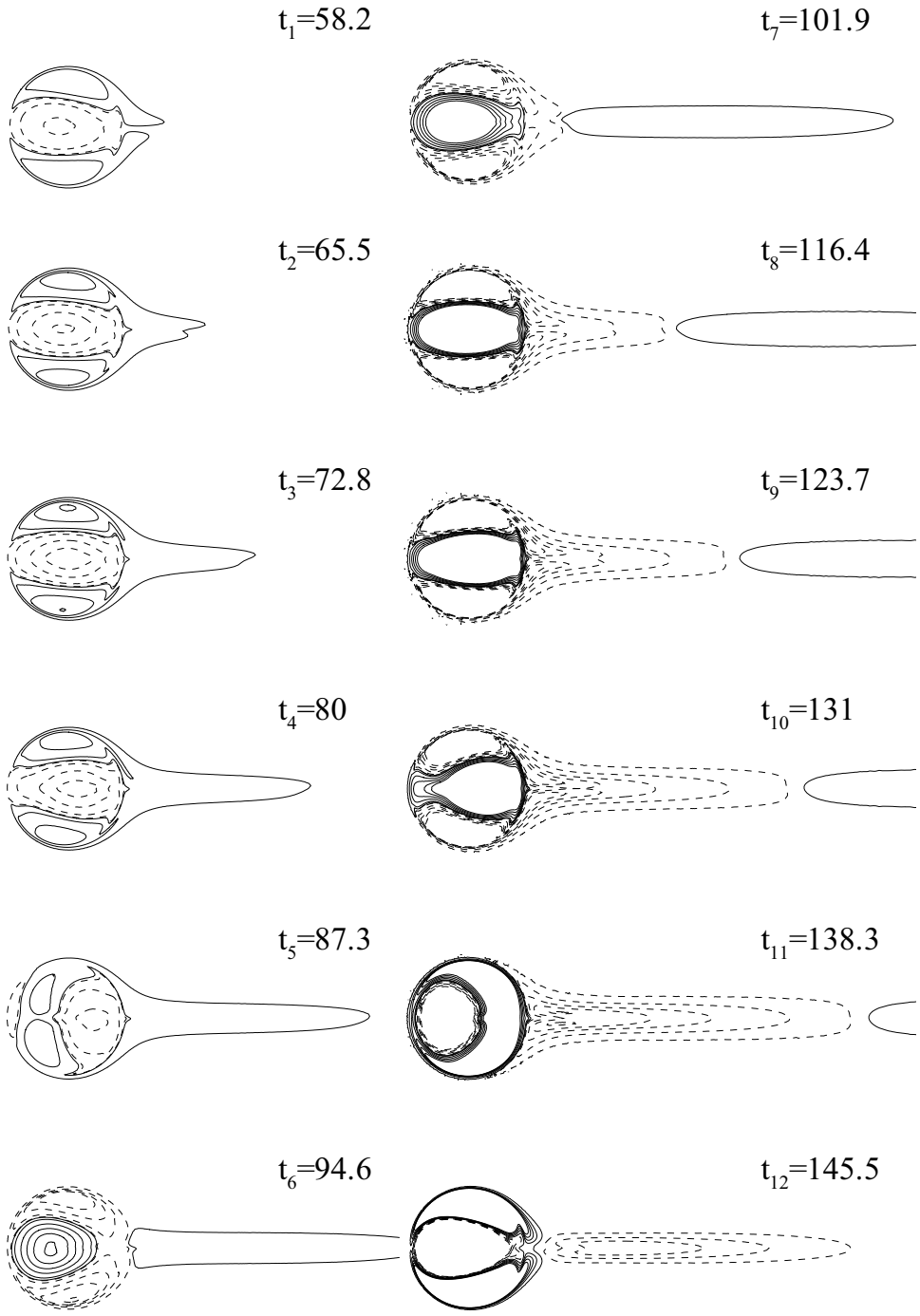

Figure 5.4: Time sequence showing the evolution of the LC dipole subjected to a white noise perturbation imposed to the base flow at $k = 0$. A global instability develops with a periodically evolving structure. Time is non-dimensionalized by t_a and subscript refers to figure 5.5. Contours show perturbation vorticity ω_z. The same values of the contour levels are used for all snapshots in order to capture the low level vorticity shed in the tail of the dipole. The growth of the perturbation explains the apparition of blanked regions within the dipole.

5.2.2 Normal mode approach

To further investigate the instability we perform a classical normal mode decomposition $\boldsymbol{u} = \hat{\boldsymbol{u}} e^{\sigma t}$ in which $\hat{\boldsymbol{u}}$ is the global mode . Introducing this form into the linearized equation (5.3)

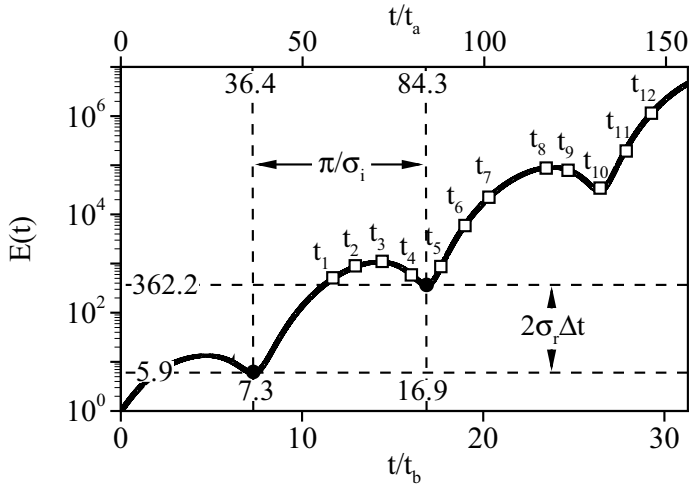

Figure 5.5: Energy $E(t) = \|\boldsymbol{u}\|^2$ of the perturbation as a function of time non-dimensionalized by t_a (top axis) and t_b (bottom axis). Elements used to calculate the frequency σ of the unsteadiness are also shown. Case $k = 0$.

and using a matrix format gives the following problem

$$\sigma B\hat{\boldsymbol{u}} = A\hat{\boldsymbol{u}} \tag{5.7}$$

The solution to this problem is given by a shift and invert technique based on an Arnoldi decomposition and a LU inversion. Determination of the unstable mode by this method is accomplished by setting the shift at the value of σ given by the previous linearized simulation. The axial vorticity of the real and imaginary parts of the mode are shown in figure 5.6. The evolution of the perturbation is a linear combination of these two components.

$$\boldsymbol{u} = \mathcal{R}[(\hat{\boldsymbol{u}}_R + i\hat{\boldsymbol{u}}_I)(cos(\sigma_i t + kz) + isin(\sigma_i t + kz))e^{\sigma_r t}] \tag{5.8}$$

where $\mathcal{R}$ denotes the real part. There is a good agreement between the frequency σ found by the normal mode decomposition compared to that determined above but the global mode approach is more accurate since no time scheme is involved. It is also faster as there is no need to wait for the appearance of the large time dynamics in the linearized simulation.

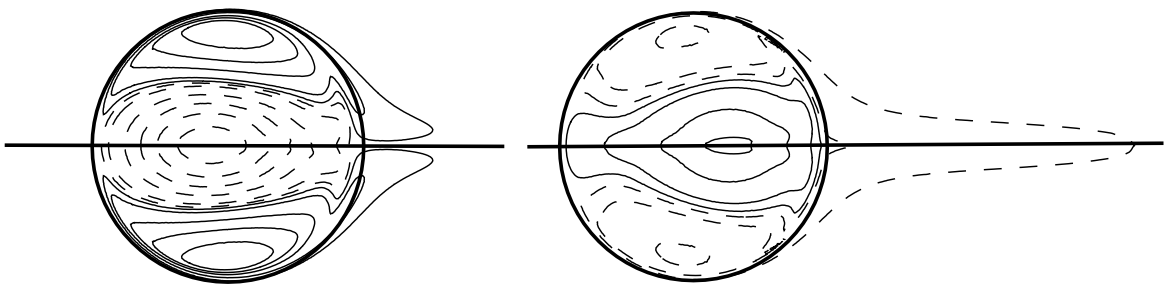

(a) (b)

Figure 5.6: Vorticity ω_z of the unstable mode calculated by the Arnoldi method. (a) real part ω_R. (b) imaginary part ω_I. Case $k = 0$. The eigenvalue of the mode is $\sigma = 0.23 + i0.31$ (normalized on t_b^{-1}. The streamline $\Psi = 0$ of the base flow is indicated by the thick line.

It should be noted here that the result of the calculation produces many spurious modes with positive growth rate.

5.2.3 Comparison of the growth rate with previous work

We can compare our results to those obtained by Robinson[129] and Dritschel[42]. Remember that these two authors used uniform patches of vorticity in a strain field to demonstrate their results. Robinson[129] used one elliptical patch in a strain field and Dritschel[42] used a pair of opposite patches. Robinson[129] gives the growth rate of the 2D instability for θ (see figure 5.1) varying between 1.1 and 2.9 while Dritschel[42] gives the marginal growth rate as a function of α and δ.

For comparison with Robinson[129], we need to assimilate the two vortices which compose the LC dipole with ellipses defined by radii a_x and a_y along respectively the x and y axis, defined by

$$\begin{aligned} a_x^2 &= \frac{\int_{\mathcal{D}} (x - x_c)^2 \, \Omega_z dxdy}{\Gamma} \\ a_y^2 &= \frac{\int_{\mathcal{D}} (y - y_c)^2 \, \Omega_z dxdy}{\Gamma} \end{aligned} \tag{5.9}$$

Doing so gives $\theta_{LC} = a_y/a_x \sim 1.6$. For this value of θ the instability found by Robinson[129] is characterized by $\sigma_R t_b \sim 0.5$. The comparison with Dritschel[42] is done at $\alpha = 1$ and $\delta = 0.45$. For these parameters the dipole of Dritschel[42] is stable. The marginal instability starts at $\delta = 0.55$ and equals $\sigma_R t_b = 0.5$ at maximum. We see that this value agrees well with that of Robinson[129].

In the present case, $\sigma_R t_b = 0.2$ which is notably lower than the value found by the previous authors. The difference may be attributed to the difference in base flow (patch versus distributed vorticity) and to the effect of viscosity.

5.2.4 Effect of k and Re

Figure 5.7(a) presents the variation of the growth rate of the instability with the axial wavenumber. It proves that the range $0 \leq k \leq 0.5$ is unstable, the greatest amplification occurring for $k = 0$. As a consequence the 2D instability belongs to a family of unstable modes in the region of very long wavelengths.

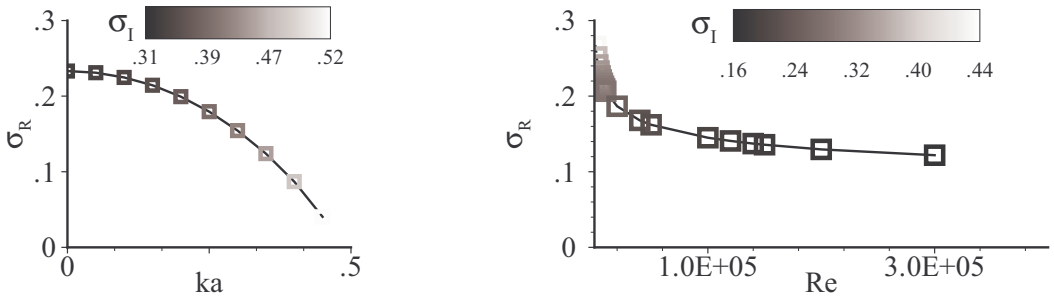

(a) (b)

Figure 5.7: Growth rate $\sigma = \sigma_R + i\sigma_I$ of the instability normalized on t_b^{-1}. (a) Effect of k. (b) Effect of Re.

The effect of the viscosity upon the growth rate and the frequency is depicted in figure 5.7(b). Interestingly, the growth rate decreases with decreasing viscosity. This suggests that the two-dimensional instability is viscous. The resolution at higher values of the Reynolds number would require a different numerical method therefore we could not know if an asymptote is reached in

the limit of inviscid flow. It is also observed that the frequency of the mode decreases with the Reynolds number.

5.2.5 Discussion

In this part we explore the physics of the instability described above. The 2D instability induces the growing displacement of the vortices of the pair about their initial positions. This dynamics is supported by displacement modes corresponding to $|m| = 1$ and $n = 0$ (m is the azimuthal wavenumber and n the number of radial nodes of the vorticity in the radial direction) Kelvin waves at $k = 0$ in each vortex.

The dynamics of Kelvin waves in single vortices has been largely documented in the past, see Saffman[130] for the theory. In a viscous medium Kelvin waves correspond to decaying oscillations of the vortex core. In the presence of an external strain such as the one induced by each vortex upon the other in a pair of vortices, such oscillations become unstable for several ranges of wavenumbers. This is the triadic resonance mechanism that explains the short-wavelength instabilities in vortex pairs, see Sipp[135], Lacaze[86], Billant[19] and Robinson[129]), and the Crow instability, see Crow[34] and Bristol[24]. The resonance between the displacement mode in the vortices and the strain is the basis of the present 2D instability as we will now see.

A preliminary remark about the 2D instability concerns the question of the conservation of the impulse of the vortices. On a general basis, this principle prevents the displacement of an isolated vortex, which may seem in contradiction with the physics of the 2D instability. However the displacement mode having a non-zero self-rotation, the mean position of the vortices is not changed by this instability. This situation is illustrated in figure 5.8. The initial disturbed position of the vortices corresponds to the smallest circle. The growth of the perturbation is represented by an enlargement of the circle. The vortices move in the same direction along y and in an opposite direction along x. This respects the conservation of the impulse

$$\int_{\mathcal{D}} y\Omega_z dxdy = 0 \tag{5.10}$$

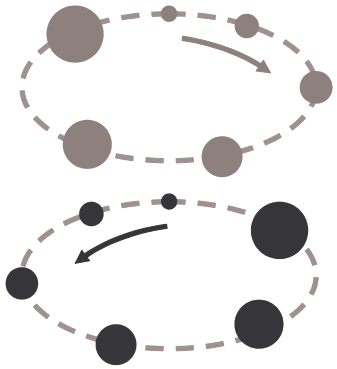

Figure 5.8: Schematic view of the movement of the vortices perturbed by the 2D instability.

Importantly one notes in figure 5.6 that the upper and lower regions of the perturbation vorticity are squeezed against the dividing streamline of the dipole. As a consequence these regions are characterized by large vorticity gradient normal to the streamline. Whereas the latter is impermeable in the inviscid limit, viscosity allows a diffusion of the vorticity outside the Kelvin oval. This is clearly observed in figure 5.4. Afterwards, vorticity is entrained by the external flow from the sides of the dipole to the rear and downstream towards the limit of the computational domain. This loss of vorticity by viscous detrainment occurs only when the displacement mode is oriented in the direction of strain (see instants t_{1-3} and t_{6-8} in figure 5.4)

because there, the strain displaces the vorticity outward and intensifies its gradients. On the contrary when the mode is in the direction where it is subjected to a compression (see instants t_{4-5} and t_{9-10} in figure 5.4), the vorticity is drawn inward and the gradients are decreased. There, expulsion of vorticity is stopped.

This viscous depletion of the mode may explain the rotation of the 2D instability. This rotation is in contradiction with the modal dynamics of the Rankine vortex in which the displacement mode $m = 1$, $n = 0$ does not rotate at $k = 0$, see Saffman[130]. This displacement mode is an equilibrium solution of the linear dynamics (in the inviscid limit) that results from the competition of the Coriolis, pressure, and centrifugal forces in the core of the Rankine vortex. We have seen that it is this same mode that participates in the 2D instability of the LC dipole. But unlike the Rankine vortex, in the vortices of the LC dipole, there is the additional action of the viscosity at the upper and lower downstream regions of the limiting streamline of the dipole that modifies the previous equilibrium. This additional effect of the viscosity can be modelled by a tangential force acting at the boundaries of the vortex core that induces the rotation of the displacement mode. The evolution of the frequency of the 2D instability with the Reynolds number in figure 5.7(b) sustains this explanation by showing that the rotation of the mode decreases with decreasing viscosity. In the inviscid limit it could happen that the mode does not rotate anymore, a situation that we cannot confirm due to computational limitations. Incidentally the instability also becomes weaker (its growth rate decreases). In fact with less viscosity, less depletion of vorticity occurs at the dividing streamline and the period during which the mode remains in the strain and in the compression regions tend to balance each others. Therefore a viscosity decrease induces a decay of the mode and the instability may happen to disappear in the limit of large Reynolds number. The energy curve of the pertur-

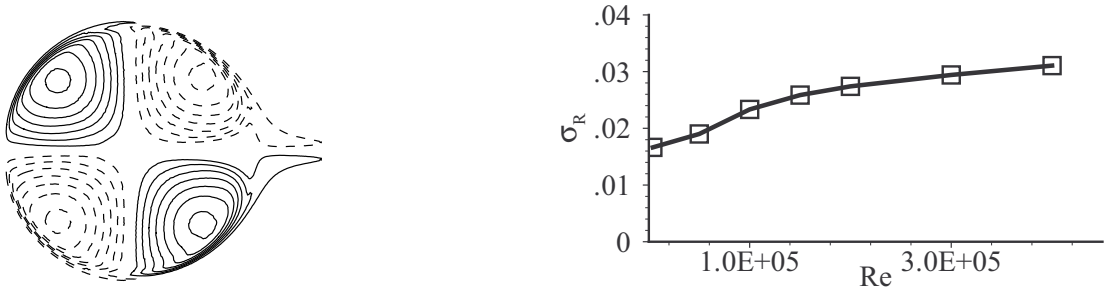

(a) (b)

Figure 5.9: (a) Vorticity ω_z of the symmetric mode at $k = 0$. The growth rate is $\sigma_R = 0.016 t_b^{-1}$. (b) Growth rate σ_R normalized on t_b^{-1} versus Re_Γ.

bation depicted in figure 5.5 reflects the mechanism just described. The growth lasts longer than the decrease and the expulsion of vorticity occurs when the perturbation is in the strain. The tail of vorticity that forms downstream of the dipole changes sign periodically. The above described instability would correspond to an interesting mechanism that dynamically reduces the circulation contained in the vortices by viscous depletion. The time scale of this instability being t_b, and that of the viscous diffusion $t_\nu = 2\pi a^2/\nu$, the ratio of the two equals $a^2/b^2 Re_\Gamma$ which shows that at moderate to high Reynolds number, the decrease of the circulation by the instability is much higher than by viscous diffusion. Our analysis suggests that the instability introduces a new length scale for the action of the viscosity, which is the width of the shear layer of the mode in the vicinity of the dividing streamline. This length being much smaller than a, viscosity is allowed to act on a much smaller time scale. This suggests that the mechanism of the 2D instability is potentially interesting for the decay of vortex pairs.

5.2.6 Symmetric instability

The existence of a symmetric displacement mode is a matter of interrogation. The arguments given above to explain the two-dimensional instability do not exclude this possibility. The linear simulation described above selects the most amplified mode which is the antisymmetric displacement mode. In fact, an exploration of the symmetric case proves that such a mode exists. Its vorticity is depicted in figure 5.9(a). This mode is stationary. Its growth rate is much smaller than the antisymmetric one (see figure 5.7(a)) but it increases with the Reynolds number, see figure 5.9(b). Unlike the antisymmetric instability, its nature is hence inviscid.

5.3 Non-linear evolution

5.3.1 Fully non-linear

The non-linear evolution of the 2D antisymmetric instability is now investigated. The initial condition consists in the superposition of the LC dipole with the 2D instability mode. The ratio of the energy of the perturbation E to the energy of the base flow E_b is controlled by the parameter $\epsilon' = E/E_b$. We performed three simulations, at $\epsilon' = 0$, $\epsilon' = 0.05$ and $\epsilon' = 0.15$. On the account that the energy of the perturbation in the second simulation is small, we compare it with the first simulation at $\epsilon' = 0$ by looking at the difference between the two vorticity fields at every time step. The results of this comparison are shown in figure 5.10. On the left frame we show two snapshots of the vorticity fields for $\epsilon' = 0$ (top) and $\epsilon' = 0.05$ (bottom). On the right frame we show the vorticity field (top) and the energy (bottom) of the perturbation. The third simulation allows us to investigate the non-linear saturation of the instability. The evolution of the vorticity field of the flow for this case is plotted in figure 5.11.

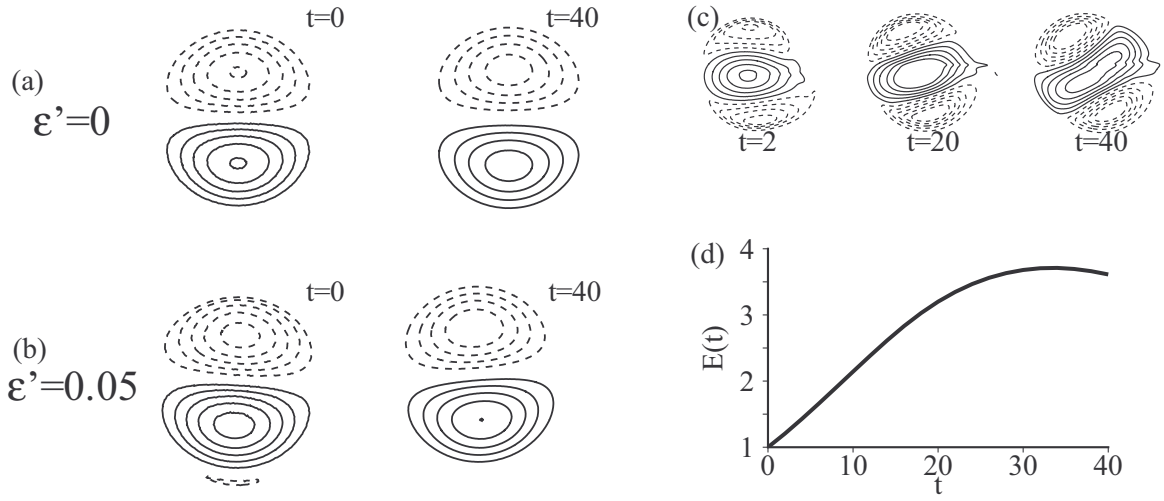

Figure 5.10: Non-linear evolution of the perturbed LC dipole. (a) Vorticity field of the flow at $\epsilon' = 0$ and (b) $\epsilon' = 0.05$. (c) Evolution of the perturbation in terms of vorticity and (d) energy. The perturbation is taken as the difference between the flows at $\epsilon' = 0$ and $\epsilon' = 0.05$.

Figure 5.10 on the left shows that the effect of the perturbation is to slow down the drifting motion of the dipole and to make it slightly rotate. Difference between these two flows, see on the right frame (d), shows that the energy of the perturbation increases at first and then saturates. The form and duration of the growth is in qualitative accordance with the linear dynamics described before but the growth rate is notably smaller than the linear one. The evolution of the vorticity field of the perturbation exhibits also a different behavior. These observations suggest that the decrease of the energy after $t = 40$ is not the consequence of the periodicity of the linear instability but rather that of a non-linear disruption of the linear

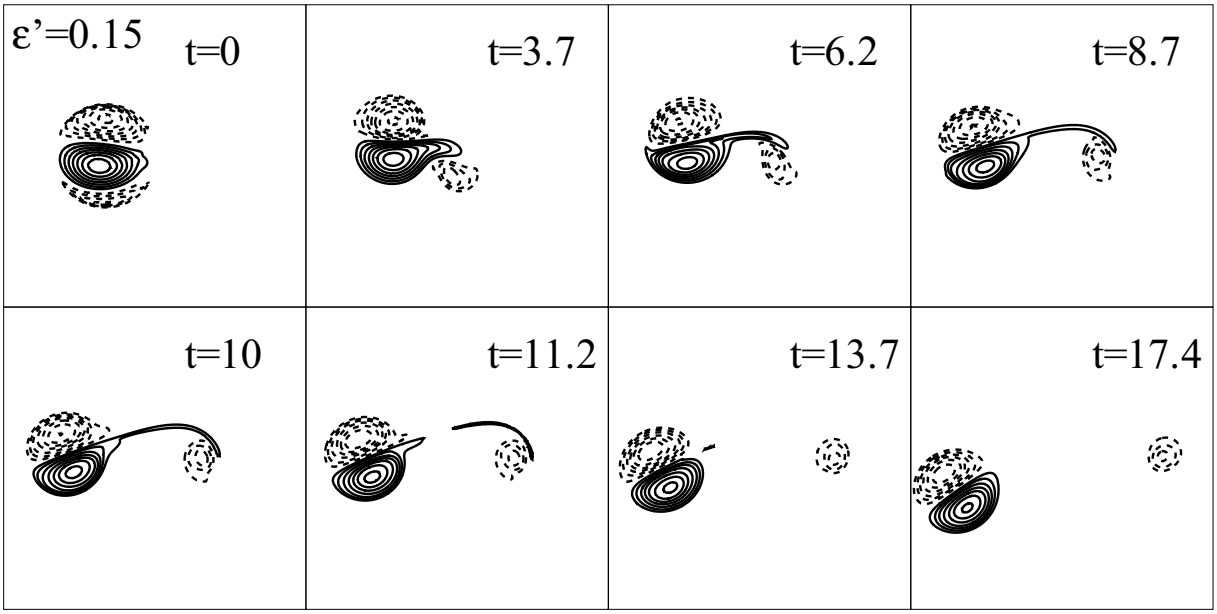

Figure 5.11: Time sequence of the evolution of the flow at $\epsilon' = 0.15$ and $k = 0$. Contours of the vorticity ω_z. Time is given in t_a units.

dynamics. To support this view the snapshots of the perturbation vorticity field in (c) show that, unlike the linear dynamics, the tripolar structure moves in a solid body rotation that we suggest is the result of the entrainment of the outer part of the vorticity (negative) by the inner part (positive). This entrainment is the consequence of the non-linear term $(\boldsymbol{u} \cdot \nabla)\, \boldsymbol{u}$ representing the self-convection of the perturbation. This effect does not exist in the linear dynamics as it is supposed small and discarded from the equations. The non-linear simulation shows that this term rapidly becomes non negligible.

The substraction method cannot be used anymore when the two flows are too different. Therefore we investigate the further evolution of this non-linear dynamics by looking at the simulation at $\epsilon' = 0.15$ in figure 5.11. The first snapshot of the flow shows that even though the energy of the perturbation is small, the total flow is significantly marked by the instability due to the offset of the vorticity maximum in the unstable mode compared to the base flow. This creates an isolated zone of vorticity at the bottom of the dipole that is subsequently displaced along the bottom boundary of the dipole and finally ejected. We observe that the entire dipole rotates simultaneously to this ejection, which is mandatory to conserve angular momentum of the flow. Note that the rotation of the dipole depends upon the phase of the initial unstable mode. The final snapshot of the flow shows the ejected vorticity downstream of the dipole. Interestingly, if we compare the relation $\Psi = f(\Omega_z)$ (not shown), we see that the dipole has regained its original LC dipole shape.

The sum of these non-linear simulations show that the 2D instability does not survive to the non-linearities but modifies significantly the flow. Concerning the perturbation, we have seen that the linear mechanism is rapidly stopped by the non-linear term corresponding to the convection of the perturbation by itself and that the perturbation is then ejected out of the dipole. Concerning the LC dipole, we have seen that disturbing it with the unstable mode induces its rotation in response to the ejection of angular momentum. The identification of this behavior is important because it means that in a turbulent environment the LC dipole will continuously be moved by the turbulent structures even if they are weak.

5.3.2 Frozen base flow

To verify this scenario we performed a non-linear simulation initialized by the LC dipole perturbed by a white noise that models turbulence. In order to reduce the computational cost of the simulation, we adopt the frozen base flow model described by the set of equations (5.4). This means that the perturbation evolves non-linearly on a non-diffusing base flow. The simulation is performed with $\epsilon' = 0.005$ hence simulating weak turbulence. The evolution of the total flow is plotted in figure 5.12 and the evolution of the energy of the perturbation is shown in figure 5.13.

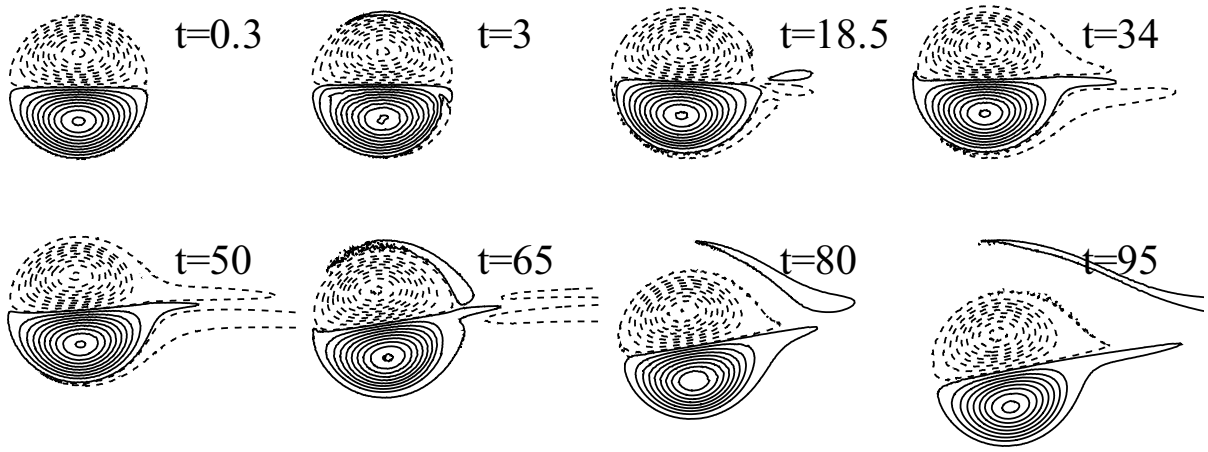

Figure 5.12: Time sequence of the contours of the total vorticity showing the non-linear evolution of the flow when the frozen base flow is disturbed with the 2D instability mode and $\epsilon' = 0.005$. Time is given in t_a units. Case $k = 0$.

The first stage of the evolution agrees well with the linear dynamics. The growth of the perturbation is linear and the dipole is seen to oscillate in rotation and to leave vorticity at its left boundary by viscous perspiration through the limiting streamline. However the frequency and the growth rate are slightly smaller than linearly predicted, which means, as expected from the previous non-linear study, that non-linearities modifies the linear dynamics. After $t = 70$ the energy reaches an asymptote and the dipole is seen to rotate permanently, thus indicating the non-linear rotation of the perturbation and its ejection which is visible downstream of the dipole.

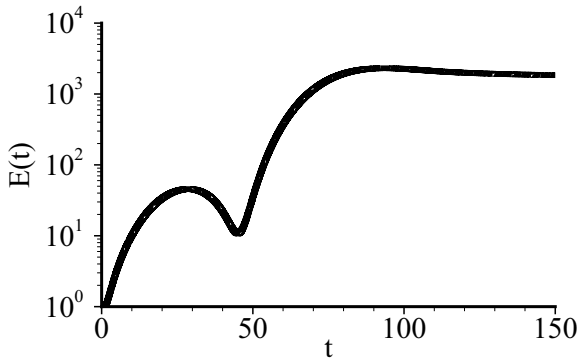

Figure 5.13: Energy of the perturbation as a function of time in t_a units for the non-linear with frozen base flow simulation at $k = 0$.

Conclusion

In this chapter we have investigated the 2D instability of the LC dipole. In the introduction we first reviewed the existing literature. It emerged that the existence of this instability had not received much attention since its demonstration by Robinson[129]. More importantly there seemed to be a misunderstanding pertaining to the different models used to investigate the stability of counter-rotating vortex pairs that resulted in the ignorance of this instability by several authors. This review hence helped clarify the knowledge in this field. We then investigated the linear evolution of the 2D instability in the LC dipole by means of a normal mode approach. This instability takes the form of a displacement mode in each vortex of the dipole. It was shown to belong to a thin band of unstable modes in the region of ultra long wavelengths. Our analysis suggests that the instability mechanism is monitored by viscosity which moves vorticity from the inside of the dipole to the outside by diffusion through the limiting streamline. Non-linearly, the instability is seen to grow in the LC dipole and to be quickly disrupted by it self-rotation before being ejected outside of the dipole in the form of trailing vorticity. By conservation of angular momentum, this disruption entrains the rotation of the entire dipole. This suggests that the 2D instability might play an important role in the dynamics of vortex pairs in turbulent flows. Therefore it would be interesting for future investigations to look for experimental or real life (in geophysical flows for instance) manifestation of this instability.

Appendix

Note on the dynamics of two point vortices

It is useful to make mention here to a specificity of the flow formed by two point vortices. Systems of several points vortices becomes chaotic when there are more than three vortices, see Moffatt[113]. In particular, systems of two point vortices are intrinsically stable. Surprisingly we show in the following that the system of two point vortices is linearly unstable. In order to do so, we first consider a point vortex placed at the origin. The velocity of a particle at a point x, y is

$$\begin{aligned} u_x &= -\frac{\Gamma y}{2\pi(x^2+y^2)} \\ u_y &= \frac{\Gamma x}{2\pi(x^2+y^2)} \end{aligned} \tag{5.11}$$

Now we assume that the particle is in $(x, 0)$ and it is slightly displaced by the translation $(\delta x, \delta y)$. The velocity at the new position is obtained by linearizing the relations (5.11).

$$\begin{aligned} u_x(x+\delta x, \delta y) &= -\epsilon \delta y \\ u_y(x+\delta x, \delta y) &= -\epsilon \delta x \end{aligned} \tag{5.12}$$

where $\epsilon = \Gamma/2\pi x^2$ is the rate of strain imposed by the vortex at the position of the particle. Considering a rotation of 45^o of the axis and the following variables $\eta_\pm = \delta x \pm \delta y$, it is straightforward to see that $\eta_\pm = \eta_0 e^{\pm \epsilon t}$. Therefore the position of the particle is unstable and its motion will grow with a rate ϵ dictated by the strain imposed by the vortex.

There is, in fact, no contradiction between this linear instability and the stable character of the system of two point vortices. This stability means that the the linear instability does not survive non-linearly. The displacement of one vortex of the pair only rearranges the direction of travel of the pair, but does not disorganize the system, unlike systems of three or more point vortex. For this reason the flow is trivially stable. This tricky pattern is interesting because it highlights the phenomenological difficulties pertaining to 2D flows.

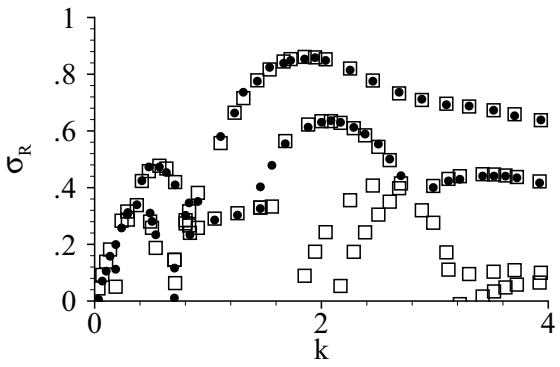

(a)

Figure 5.14: Validation of our result with the data of Billant[19] concerning the value of the growth rate σ_R normalized on t_b^{-1} as a function of k normalized on a^{-1}. • Billant's results. □ present results.

Validation

The calculation were first verified against the results of Billant[19] for $Re = 2732$ which corresponds to $Re_b = 400$ the Reynolds number used by Billant[19]. We see that the agreement between the two spectra is very good. The figure contains both antisymmetric ($\omega_z(x,-y) = \omega_z(x,y)$) and symmetric ($\omega_z(x,-y) = -\omega_z(x,y)$) modes.

3D instabilities

Map in the wavenumber domain

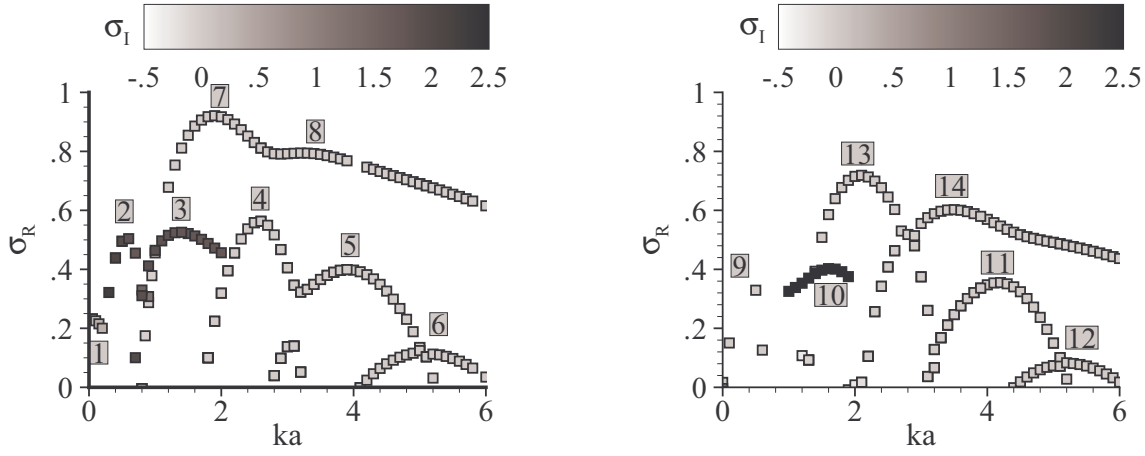

(a) (b)

Figure 5.15: Three-dimensional spectrum of the LC dipole: growth rate normalized on t_b^{-1} as a function of the axial wavenumber. (a) Antisymmetric modes $\omega_z(x,-y) = \omega_z(x,y)$. (b) Symmetric modes $\omega_z(x,-y) = -\omega_z(x,y)$.

Figures 5.15(a) and 5.15(b) show the full map of 3D antisymmetric and symmetric instabilities of the LC dipole at $Re = 4000$. The matrix method presented in 5.1.2 is used over a range of guess values that covers a large part of the parameter space σ of interest. These calculations were achieved on a half mesh compared to the mesh used in the core of the study in order to

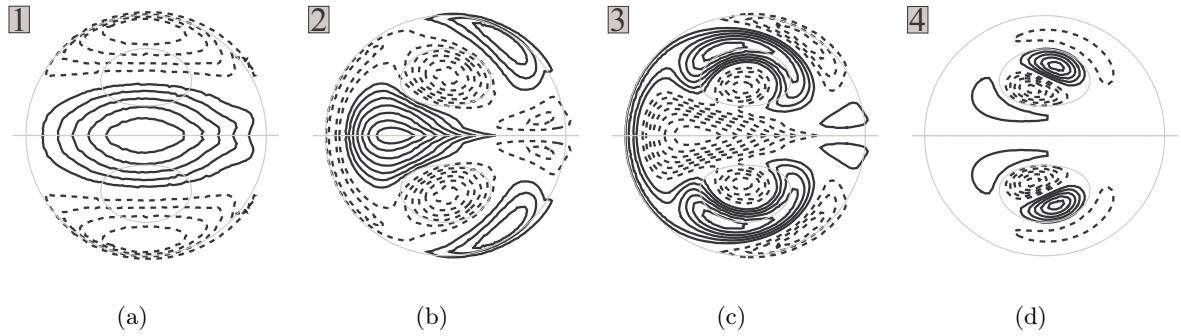

Figure 5.16: Antisymmetric modes. Contours of axial perturbation vorticity ω_z. The light grey lines show the streamlines of the base flow.

reduce the computational cost of the investigation. The mesh thus comprises only the top vortex and models the influence of the bottom one by a symmetry or an antisymmetry boundary condition depending on the type of mode that is looked for. The results were compared to the results obtained with the fine mesh used in the core of the study for several modes which showed good agreement.

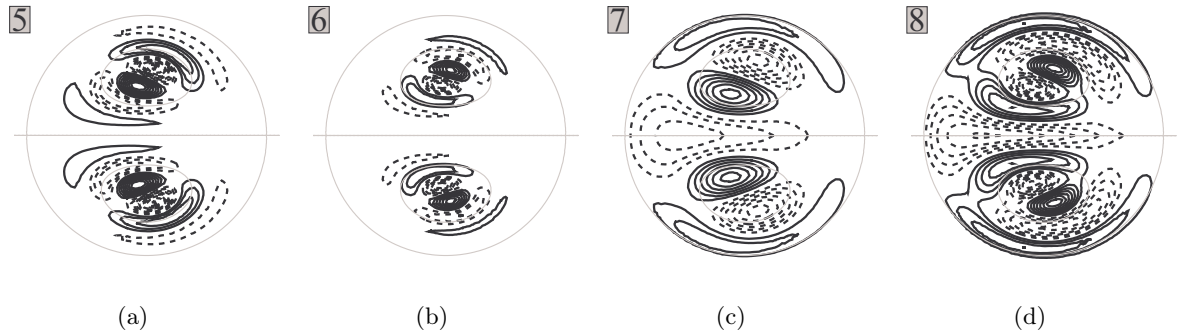

Figure 5.17: Antisymmetric modes. Contours of axial perturbation vorticity ω_z.

The matrix method allows the calculation of a large part of the spectrum, including the modes that are not the most unstable. This is not the case of the method based on linearized simulations that was used by Billant[19] and in 5.2.1 since it gives only the most unstable mode. The matrix approach is also interesting when two equally amplified modes exist. It happens at $k = 2$ in the antisymmetric subset (see figure 5.15(a)). It is possible that such a situation makes linearized simulations unstable and prevent the calculation of the modes by such a method.

Description of the modes

The leading modes of the branches shown in the spectra 5.15(a) and 5.15(b) are depicted in figures 5.16, 5.17, 5.18 and 5.19 in terms of the axial perturbation vorticity ω_z. Figures 5.16 and 5.17 represents antisymmetric modes and figures 5.18 and 5.19 represents symmetric modes. Each mode is numbered according to the numbering adopted in the plots of the spectra 5.15.

The spectra 5.15 contain modes that are oscillatory and modes that are not. Non-oscillatory modes are contained in branches 4, 5, 6, 7 and 8 for the antisymmetric subset and 9, 11, 12, 13 and 14 for the symmetric subset. The branch 9 corresponds to the Crow instability (see Crow[34]). The other branches exhibit modes that resemble to the modes of the Widnall instability (see Tsai[154] and Sipp[135]). Two types of distribution can be distinguished among these modes. Modes that are localized in the core of the vorticity of the dipole and modes that span the entire region of the dipole, with vorticity that extends up to the limiting streamline of

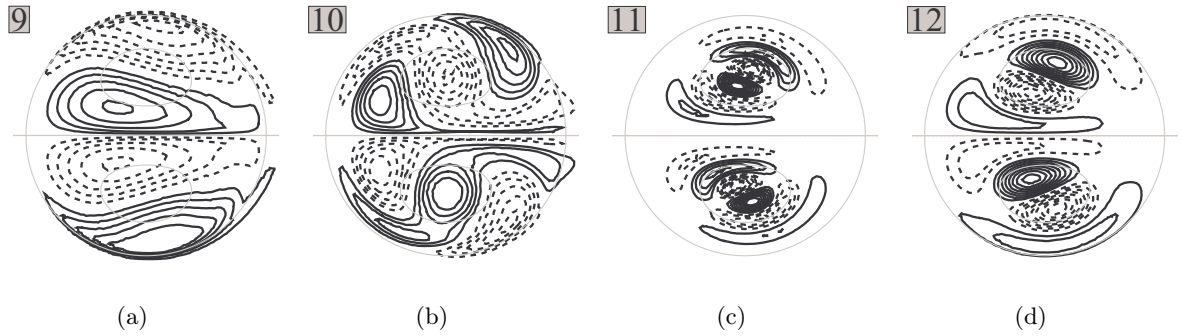

(a) (b) (c) (d)

Figure 5.18: Symmetric modes. Contours of axial perturbation vorticity ω_z.

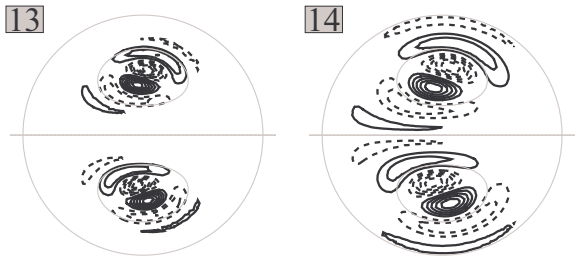

(a) (b)

Figure 5.19: Symmetric modes. Contours of axial perturbation vorticity ω_z.

the recirculating base flow. The radial structure of these modes, characterized by n the number of the zeros of the axial vorticity in the radial direction, exhibits increasing value with increasing k.

The oscillatory modes are contained in branches 1,2 and 3 for the antisymmetric subset and 10 for the symmetric subset. Billant[19] was the first to find these modes. The branch of the 2D instability has a small temporal frequency but branches 2,3 and 10 have large frequencies. The instability in these cases rotates more rapidly than the base flow (in absolute value of the rotational velocity). This is very surprising from the viewpoint of the oscillating modes of an isolated vortex for this azimuthal periodicity ($m = 0$ in the core of the vortex and $m = 2$ in the outer region) because these high oscillation rates are generally observed for large axial wavenumber $ka \gg 1$, see the case of the Rankine vortex already discussed and presented by Saffman[130], whereas here they are seen at $ka \sim 1$.

6 Optimal perturbations in vortex pairs

This chapter deals with linear mechanisms of energy growth in counter-rotating vortex pairs with axial flow. It is based on the calculation of the optimal linear perturbations of the flow depending on the perturbation wavenumber k and the swirl number q (see (2.4)). The method relies on an optimization code described in chapter 3, which itself proceeds through iterative simulations of the direct and adjoint linearized equations, (3.15) and (3.18). Results of the optimal perturbation analysis are discussed in the light of those obtained by solving two different eigenvalue problems corresponding to the dynamics at short and large times.

Previous works in the field of transient growth analysis of vortex flows concern the isolated Lamb-Oseen (LO) and the Batchelor vortex. Antkowiak[5][6] and Pradeep[124] investigated the mechanisms of transient growth in the LO vortex. It was already said in chapter 2 that the LO vortex is exponentially stable. However these authors showed that this vortex exhibits a potential for transient energy growth due to the non-normality of the linearized Navier-Stokes equations. The effect of non-normality is detailed in Schmid[133]. Perturbations characterized by $|m| = 1$ (m being the azimuthal wavenumber of the perturbation) exhibit the strongest transient growth over all other m. Two mechanisms of transient growth were identified. The first one is a shearing mechanism which is an analog of the Orr mechanism in plane shear flows. In the case of the isolated vortex, it takes the form of thin spirals coiled at the edge of the vortex core. The uncoiling of these spirals leads to transient growth of energy. The second mechanism applies for 3D perturbations and corresponds to the tilting and stretching of radial vorticity into the tangential direction by the basic differential rotation. This mechanism leads subsequently to induction of a core dynamics (in the form of Kelvin waves) by the tangential vorticity located in the potential region of the vortex. An interesting characteristic of this mechanism is a selection of the radius of the initial perturbation by a resonant effect between (i) the rotation of the base flow and (ii) the angular rotation speed of the Kelvin wave induced in the last stage of the transient dynamics. Transient 3D perturbation result from the combination of the shearing and induction mechanisms. In the first mechanism, growth arrest is the consequence of the uncoiling of the initial spirals of vorticity while in the second mechanism, it is the consequence of the stability of the core dynamics. Viscosity in both cases reduces the strength of transient growth.

Heaton[65] investigated transient growth in the Batchelor vortex and its possible connection with vortex breakdown. The author showed that the mechanisms at work are similar to those governing transient growth in the LO vortex. He observed resonance for $|m| = 1$ perturbations and showed that stronger growth is possible in the presence of axial flow. Heaton[64] also investigated the competition between transient growth and the effect of viscous center modes (identified by Fabre[44]) at large Reynolds number and large swirl. Transient growth is dominated by center modes instabilities at large time. The transition towards this regime leads to higher levels of energy contained in the center modes. In the present case of vortex pairs, we will also have to balance the effects of transient growth and those of instabilities.

Velocity gradients in vortex pairs exhibit several regions of interest where energy growth is possible. These comprise the vortex centers where each vortex imposes a finite strain upon the

other, causing cooperative instabilities by resonance with Kelvin waves, the region surrounding the hyperbolic stagnation points upstream and downstream of the Kelvin oval (the words "upstream" and "downstream" refer to the drifting motion of the vortex), and the vortex core where differential rotation and axial velocity can contribute to perturbation growth. Understanding cooperation between these ingredients for energy growth is the main objective of this study.

The organization of the chapter is the following. The first section is dedicated to the methods used for the optimal perturbation analysis and details the characteristics of the vortex pair. Note that more details on these topics can be found in chapter 3 and that this short section is included here for the overall coherence of the chapter. The next section details the results obtained in the case of the vortex pair without axial flow. Analysis of the results are carried out by solving eigenvalue problems and looking at the basic velocity gradients. The effect of axial flow is then discussed. In particular we suggest the existence of a general resonant effect for optimal perturbation at large time. Concluding remarks are given in the last section. Note that the part of this work corresponding to the optimization of the Crow instability is the object of a dedicated publication[23] that is given in appendix F.

6.1 Method

6.1.1 Steady state

The steady state used in the perturbation analysis is a pair of two counter-rotating vortices of equal strength with axial flow in their cores. A description of this flow is given in figure 6.1. Figure 6.1(a) shows the vorticity field, along with the streamlines and a vertical profile of the axial velocity. Figure 6.1(b) shows a schematic view and details important designations, like the elliptic and hyperbolic stagnation points, the Kelvin oval that separates the internal recirculating flow and the external flow and the symmetry plane of the pair. The velocity field is noted (U_x, U_y, U_z) in cartesian coordinates x, y, z. Note that due to the velocity induction of each vortex upon the other, the vortex pair moves in the direction $-x$. In the following, we work in the reference frame attached to the vortex pair. The vortex pair is obtained by numerical simulations started from a flow composed of two Batchelor vortices (see chapter 3 for details).

The vortex pair is characterized by the radius a (see (3.4)) of the vortices, their circulation $\pm\Gamma$, the distance b (see (3.3)) between the vortex centers and the swirl number q of the flow in the cores. The aspect ratio of the vortex pair is a/b. The center of the top vortex is denoted (x_c, y_c) (see (3.1)). In the following $a/b = 0.25$, if not otherwise stated. Recall that the swirl number defined in (2.4) reads

$$q = \frac{\Gamma}{2\pi a \Delta U_z} \tag{6.1}$$

The axial flow U_z is concentrated in the vortex cores, as depicted in figure 6.1(a). The effect of viscosity is controlled by the Reynolds number $Re_\Gamma = \Gamma/\nu$ (already given in (3.5)). Unless otherwise stated $Re_\Gamma = 4000$ throughout this chapter. The two length scales of the problem are a and b. Time is normalized on t_b (see (2.27)), and distances are normalized on a. We will use t_a (given in (3.13)) to normalize the strain rate and frequencies.

6.1.2 Perturbations

Equations

We suppose that the flow departs little from the base flow. We hence consider a perturbation field in the form $\boldsymbol{u} = (iu_x, iu_y, u_z, ip)e^{ikz} + c.c.$ where $c.c.$ denotes the complex conjugate and k is the axial wavenumber. The corresponding vorticity field is $(\omega_x, \omega_y, i\omega_z)$ with

$$\omega_x = \frac{\partial u_z}{\partial y} + ku_y \quad , \quad \omega_y = -ku_x - \frac{\partial u_z}{\partial y} \quad , \quad \omega_z = \frac{\partial u_y}{\partial x} - \frac{\partial u_x}{\partial y} \tag{6.2}$$

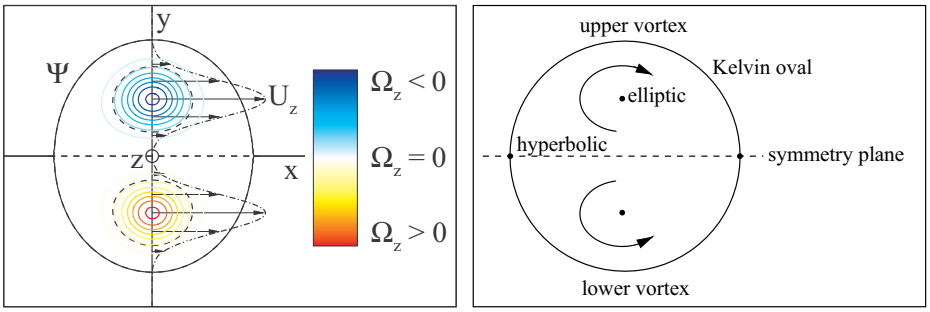

(a) (b)

Figure 6.1: Base flow $a/b = 0.25$ in a plane $z = constant$ as a function of x and y. (a) Color contours represent the axial vorticity Ω_z. The (bottom) top vortex turns (anti) clockwise. Plain and dashed lines represent streamlines (dashed lines correspond to negative Ψ). Dotted dashed lines correspond to the axial velocity profile U_z. Note that, for illustration purpose, it is depicted in the x, y plane, although it is directed along the z axis. (b) Schematic view of the flow.

Perturbations are split into symmetric ($\omega_z(x,-y) = -\omega_z(x,y)$) and antisymmetric ($\omega_z(x,-y) = \omega_z(x,y)$) perturbations. The perturbations must verify the linearized Navier-Stokes equations

$$\frac{\partial \boldsymbol{u}}{\partial t} + \boldsymbol{U}\cdot\nabla\boldsymbol{u} = -\boldsymbol{u}\cdot\nabla\boldsymbol{U} - \nabla p + \frac{1}{Re_\Gamma}\Delta\boldsymbol{u} \tag{6.3}$$

$$\nabla\cdot\boldsymbol{u} = 0 \tag{6.4}$$

In these equations the base flow does not depend on time. This approach is supported by the fact that perturbations evolve on a time scale of the order of t_b whereas the base flow evolves by viscous diffusion on a time scale t_ν (see (3.10)). The ratio of the two time scales equals $a^2/b^2 Re$ which is a large value since $Re_\Gamma = 4000$ and $a/b = O(0.1)$. The linearized equations can now be written in a matrix format

$$A\boldsymbol{u} = B\frac{\partial \boldsymbol{u}}{\partial t} \tag{6.5}$$

with A and B given in (3.36) and (3.37).

Normal modes

Perturbations are decomposed into a set of normal modes in the following way

$$\boldsymbol{u} = \sum_j \alpha_j\, \hat{\boldsymbol{u}}_j\, e^{\sigma_j\, t} + c.c. \tag{6.6}$$

In this expression, $\hat{\boldsymbol{u}}_j$ is the normal mode and σ_j a complex value associated to the eigenvalue problem

$$A\hat{u}_j = \sigma_j B\hat{u}_j \tag{6.7}$$

The real part σ_R of the eigenvalue σ is the growth rate of the mode and its imaginary part σ_I is its temporal frequency. Coefficients α_j in (6.6) are defined by

$$\alpha_j = \left(\hat{\boldsymbol{u}}_j^+, B\boldsymbol{u}_0\right) \tag{6.8}$$

Here we make use of the scalar product $(\boldsymbol{u}_1, \boldsymbol{u}_2) = \int_S \boldsymbol{u}_1^* B\boldsymbol{u}_2 dS$ (* denoting the complex conjugate and S the computational domain) and $\hat{\boldsymbol{u}}_j^+$ denotes adjoint modes, solution of the adjoint eigenvalue problem

$$A^+\hat{\boldsymbol{u}}^+ = \sigma^+ B\hat{\boldsymbol{u}}^+ \tag{6.9}$$

The decomposition is hence achieved by a projection of the initial perturbation on the set of direct modes. The adjoint modes are normalized following $\left(\hat{\boldsymbol{u}}_j^+, B\hat{\boldsymbol{u}}_j\right) = 1$. Adjoint eigenvalues are the complex conjugate of the direct eigenvalues, meaning that $\sigma^+ = \sigma^*$.

6.1.3 Optimal perturbation

In an incompressible open flow with no heat transfer, the energy of the flow varies through the kinetic energy of the perturbations, given by

$$E(t) = \int_S \boldsymbol{u}^* B\boldsymbol{u}\, dS \tag{6.10}$$

In this chapter we analyze the possibility of transient growth in the vortex pair as a function of the wavenumber k and the swirl number q. To this end, we look for initial perturbations $\boldsymbol{u}_0$ that exhibit maximum energy amplification between $t = 0$ and t_{opt}. In mathematical terms, this can be expressed as follows

$$\max_{\boldsymbol{u}_0} G(\boldsymbol{u}_0; t_{opt}, k, q) \tag{6.11}$$

where

$$G(t) = \frac{E(t)}{E(0)} \tag{6.12}$$

is the energy gain. This is a classical optimization problem that we solve by a gradient method. The recursive routine starts from an arbitrary $\boldsymbol{u}_0$ and iterates until convergence. We observed that the number of iterations for convergence increases when t_{opt} decreases. Instead of spanning the entire parameter space (t_{opt}, k, q), which would be computationally intense, we focus on a limited range of k at $q = \infty$ and on a few values of k at $q = 2$, in order to investigate the effect of axial flow. The value of t_{opt} is varied up to $6t_b$.

6.2 Results

6.2.1 2D vortex pair

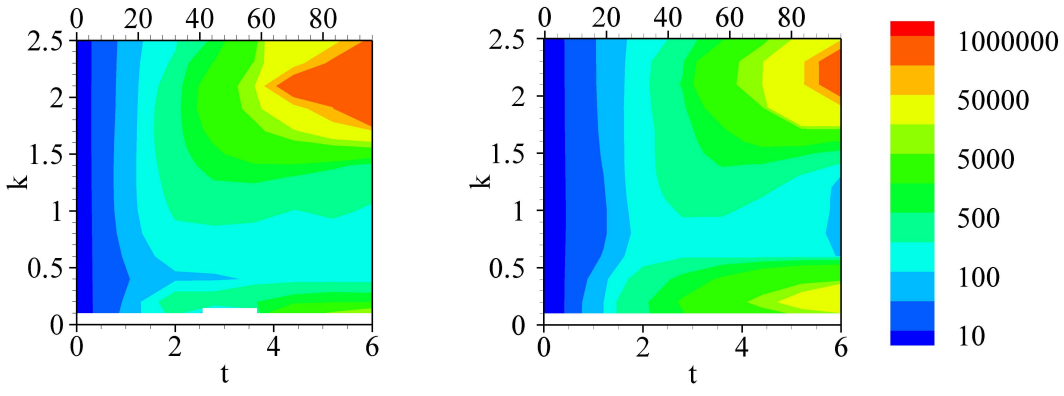

(a) Antisymmetrical perturbations

(b) Symmetrical perturbations

Figure 6.2: Contour levels of optimal amplification G as a function of k and t in the (a) antisymmetric and (b) symmetric cases. The lower axis shows time normalized on t_b while the upper axis shows time normalized on t_a, and k is normalized on a^{-1}. Note that iso-contour levels follow an exponential distribution.

In figure 6.2 we show the map of optimal gains as a function of k and t_{opt} in the case $q = \infty$ for symmetric and antisymmetric perturbations. These results were obtained by meshing

uniformly the parameter space (t_{opt}, k) with $\Delta k = 0.2$ for $0.1 < k < 2.5$ and $\Delta t_{opt} = 0.8$ for $0.4 < t_{opt} < 6$. Overall the map shows increasing energy amplification with time, except in the region $0.5 < k < 1.5$ where energy increases at first and is then constant or decreasing depending on the symmetry. Maximum amplification is obtained at large time in the region of $1.5 < k < 2.5$ for both symmetries and $0 < k < 0.5$ for symmetric perturbations. This result is not surprising since the vortex pair is exponentially unstable. As we shall see in the following part, the top region of large growth corresponds to the Widnall instability and the bottom one to the Crow instability. The figure shows that the antisymmetric Widnall instability is more amplified than its symmetric counter part.

The influence of these instabilities on the energy growth dominates for $t_{opt} > 2$. At earlier optimization times, the evolution of the energy amplification is seen to evolve little with k. We observe that the amplification is slower in the region $0.5 < k < 1$ for both symmetries. In the following we detail first the exponential instabilities and then the optimal perturbations in the case of the Crow and Widnall instabilities, as well as in the stable case $k = 1$.

Exponential instabilities

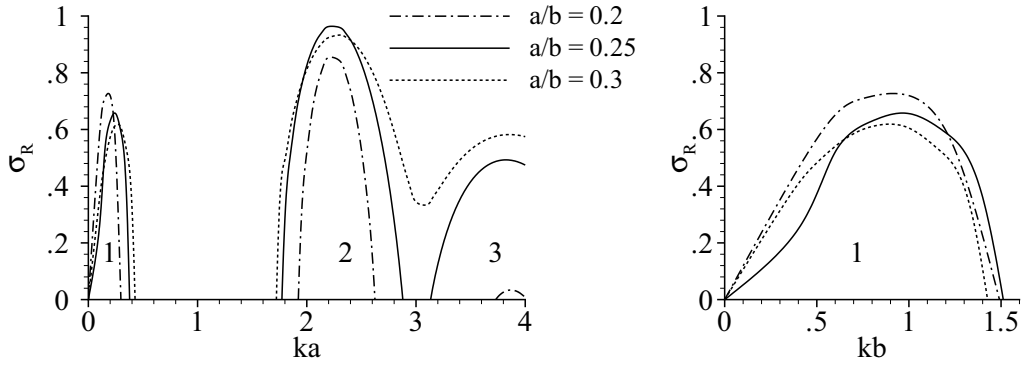

Figure 6.3: Growth rate σ_R normalized on t_b^{-1} of the unstable mode of the vortex without axial flow versus k for three different values of a/b. Band 1 corresponds to the Crow instability and bands 2 and 3 to the first and second Widnall instabilities. (a) Crow and Widnall instabilities with k normalized on a^{-1}. (b) Crow instability with k normalized on b^{-1}.

The unstable modes of Widnall and Crow are calculated by the normal mode approach presented in chapter 3. Figure 6.3(a) shows the growth rate of these instabilities as a function of the axial wavenumber k for three values of a/b. The first band of instability, denoted 1, corresponds to the Crow instability. The second one corresponds to the first Widnall instabilities, whose maximum is attained at $k = 2.26$ and the third band corresponds to the second Widnall instability, whose maximum is at $k = 3.8$. These maxima agree well with known results (Sipp[135]) and with figure 6.2. Note that $\sigma_I = 0$ for these instabilities, which means that they are stationary.

The Crow instability is only slightly modified when the aspect ratio is increased. Figure 6.3(b) shows that the range of wavelengths of the Crow instability does not change with k when k is normalized on b^{-1} (recall that b characterizes the length scale of these instabilities, see Fabre[45]). We see that the maximum growth rate is always obtained at $kb = 1$, which corresponds to $ka = a/b$. As expected, we observe that this maximum increases steadily with a/b over the range investigated. Concerning the Widnall instabilities, we see that the main effect of the increasing aspect ratio is to widen the range of unstable wavelengths. In particular it is interesting to note that at $a/b = 0.3$ no cut-off occurs between the first and the second Widnall

instabilities. This shows that instabilities occur over a wider range of wavelengths when the aspect ratio is increased. This was already apparent in the stability of the LC dipole, which is unstable over a wide range of wavelengths (see chapter 5).

Some unexplained variations are observed between the curves corresponding to different values of a/b, in particular in the case of the Crow instability where the shape of the curve changes significantly. In addition the evolution of the maximum of amplification of the Widnall instability is non monotonous with a/b. As will be proven later on, with the satisfactory agreement between our results and those of Lacaze[86], the mesh convergence of the results is good and thus does not explain these variations. Instead we suggest that it is the method used to obtain the vortex pair at a given a/b that is at stake. Indeed the process (described in chapter 3) that involves the non-linear simulations of the base flow, and the completion of an adaptation period, is complex. However no further investigation was achieved to validate this hypothesis.

An additional remark concerns the antisymmetric 2D instability discussed in chapter 5. It is this instability that is responsible for the strong amplification observed in the vicinity of $k = 0$ in the antisymmetric case in figure 6.2. The form of the related final perturbation supports this finding. However we do not discuss this instability in the following.

The axial vorticity ω_z of the perturbation of the Crow and Widnall instabilities are depicted in figure 6.4 in the symmetric case. These instabilities correspond to $|m| = 1$ Kelvin modes.

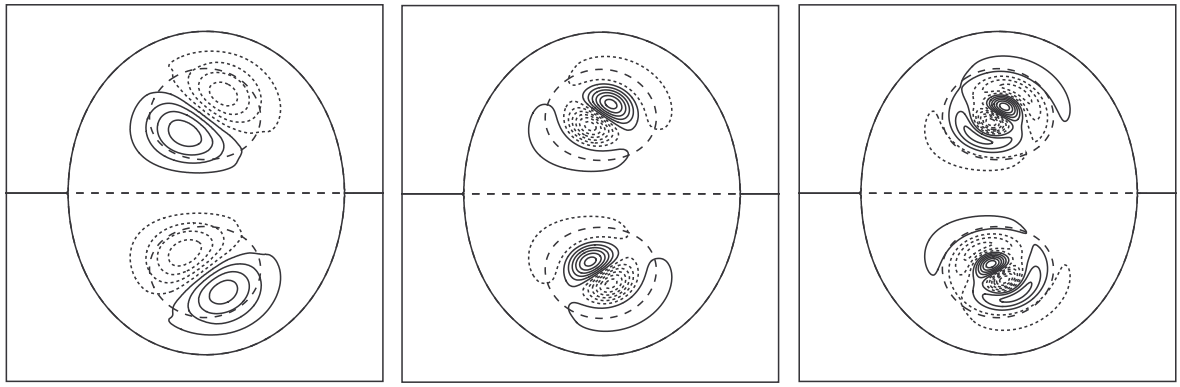

(a) $k = 0.2$ (b) $k = 2.26$ S (c) $k = 3.8$ S

Figure 6.4: Axial vorticity ω_z of the Crow and Widnall instabilities at $a/b = 0.25$ and $q = \infty$. Dashed lines indicate negative vorticity. A few streamlines of the base flow are indicated for clarity. k is normalized on a^{-1}.

The Kelvin mode that participates in the Crow instability is characterized by $n = 0$ where n is the number of radial nodes in the vorticity distribution. The value of n is 1 for the first Widnall mode and 2 for the second one.

6.2.2 Optimal perturbation at the Crow wavelength

Figure 6.5 shows the energy growth of several initial symmetrical and antisymmetrical perturbations at the Crow wavelength. The long dashed line corresponds to the direct mode of the Crow instability. The growth of this instability being exponential, the increase is linear in log scale. Symbols correspond to the energy of the optimal perturbations as a function of the optimization time t_{opt}. The solid line corresponds to the adjoint modes of perturbation associated to the Crow instability and the small dashed line corresponds to the optimal perturbation at large time of the stable antisymmetric mode. Finally the dot-dashed and the dot-dot-dashed lines correspond respectively to the optimal perturbation at short time and at $t_{opt} = 0.4$ in the symmetric case.

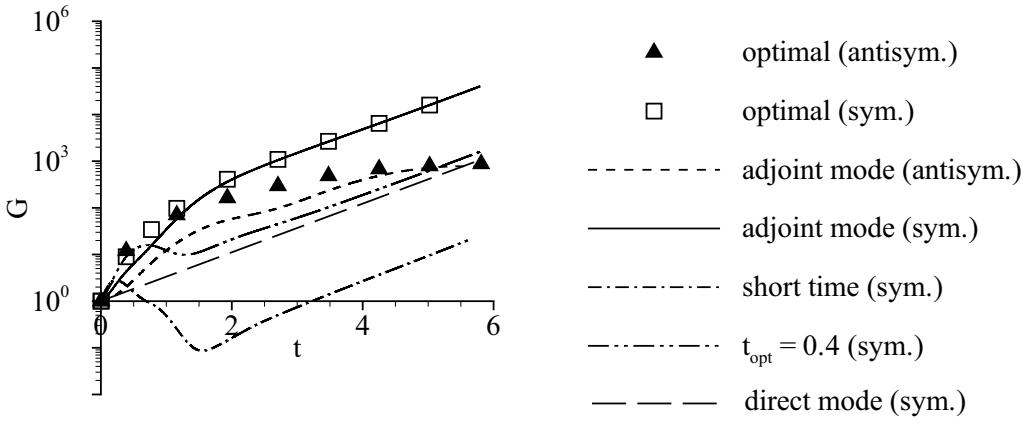

Figure 6.5: Energy growth with different initial perturbation at $k = 0.25$ as a function of time in log-lin scale. Plain curves show the adjoint growth rate. Symbols show the optimal solution computed by the optimization algorithm. ▲ (dashed lines) correspond to antisymmetrical perturbations. □ (solid lines) correspond to symmetrical perturbations. t is normalized on t_b.

At large time, all symmetric perturbations evolve towards the Crow instability. This is shown by the fact that all perturbation amplification end up following the growth rate of the direct mode of the Crow instability. The antisymmetric normal mode at the wavelength of Crow being stable, the corresponding curve (small dashed line) shows a damping of the associated energy growth at large time. However at short time, energy growth is similar to that of the symmetric perturbations. This suggests that the transient growth at the Crow wavelength does not depend upon the symmetry of the perturbation. In the following we analyze separately the short time and large time dynamics.

Short time dynamics

Effect of the strain In order to analyze the short time dynamics, we resort to the following equation that relates the instantaneous energy growth rate to the linearized operator A

$$\frac{1}{E}\frac{dE(t)}{dt} = \frac{((A + A^+)\,\boldsymbol{u}, \boldsymbol{u})}{(\boldsymbol{u}, B\boldsymbol{u})} \tag{6.13}$$

A similar expression is given in Schmid[133]. The solution of this problem is obtained by solving the eigenproblem given by $A + A^+$ and B. This solution is derived by adapting the numerical method used to solve the eigenproblem defined by A and B. The additional step consists in the calculation of the transpose conjugate of A and in the subsequent sum of A and A^+. The leading eigenvalue λ_I of $(A + A^+)\,\boldsymbol{u}_I = \lambda_I B\boldsymbol{u}_I$ corresponds to the largest possible instantaneous energy growth rate over all perturbations. The perturbation that allows this maximum growth rate is the associated eigenmode $\boldsymbol{u}_I$. As a consequence the energy of this perturbation grows linearly $G(t) = \lambda_I t$.

It is important to note that neglecting viscosity and pressure terms, $A + A^+$ reduces to the deformation tensor $D = \nabla \boldsymbol{U} + \nabla \boldsymbol{U}^T$. This means that, at short time, energy growth occurs in the regions where the basic velocity gradients are the strongest. In order to localize these regions, we calculate the strain rate S and the direction $\boldsymbol{V}$ of the strain in the vortex pair. In the vortex pair without axial flow, these quantities are given by

$$S^2 = \left(\frac{\partial U_x}{\partial x}\right)^2 + \frac{1}{4}\left(\frac{\partial U_y}{\partial x} + \frac{\partial U_x}{\partial y}\right)^2 \qquad \boldsymbol{U_y} = \begin{pmatrix} S + \dfrac{\partial U_x}{\partial x} \\ \\ \dfrac{1}{2}\left(\dfrac{\partial U_x}{\partial x} + \dfrac{\partial U_y}{\partial y}\right) \end{pmatrix} \tag{6.14}$$

Figure 6.6(a) shows S and $\boldsymbol{V}$ for the vortex pair at $a/b = 0.25$. This figure illustrates the

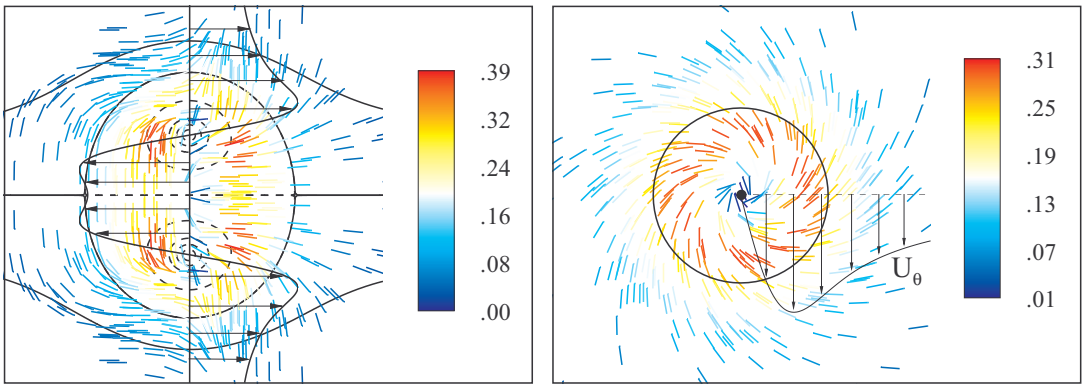

(a) Vortex pair $a/b = 0.25$ (b) LO vortex

Figure 6.6: Basic strain field. Colored vectors indicate the direction of strain $\boldsymbol{V}$ and colors indicate the strain rate S associated to the color map. Strain S is normalized on t_a^{-1}. Several streamlines of the base flow are depicted. Velocity profiles correspond to the tangential velocity. (a) Vortex pair at $a/b = 0.25$, (b) LO vortex.

complexity of the flow generated by the vortex pair, as was evoked in the introduction. Lines in the figure indicate the direction of strain while color indicates the strain rate. Regions corresponding to the upstream and downstream hyperbolic stagnation points are characterized by pure straining flows (aligned with the streamlines). Regions around the vortex centers are characterized by strong shearing like in the case of the LO vortex, shown in a similar fashion in figure 6.6(b). An important difference in the case of the vortex pair is that these regions are not axisymmetric. Finally there is a finite strain rate at the vortex centers which is exactly oriented at 45^o about the x axis (this is not clearly visible in the figure due to the small size of the associated regions). Regions of maximum strain correspond to the shearing regions in the vicinity of the vortex centers. As a result, we expect that the perturbation $\boldsymbol{u}_I$ for maximum instantaneous growth rate should be localized in this region. Note that larger values of the strain rate are found in the vortex pair.

Figure 6.7(a) shows $\boldsymbol{u}_I$ along with the strain field. As expected the perturbation axial vorticity is located in the region of maximum strain. This vorticity is organized in a succession of spirals of opposite sign in the left region of maximum strain.

Previous works In order to analyze the mechanism at play in the short time dynamics, we first detail the case of the isolated vortex following the findings of Antkowiak[5] and Pradeep[124]. In this case, the relation of the energy growth (6.13) takes the following form

$$\frac{dE}{dt} = -\int_V u_r u_\theta \left(r \frac{\partial}{\partial r} \left(\frac{U_\theta}{r} \right) \right) dV \tag{6.15}$$

where U_θ is the tangential basic velocity and u_θ and u_r are the tangential and radial velocities of the perturbation. This equation relates the growth of energy with the strain rate $S = r \dfrac{\partial}{\partial r} \left(\dfrac{U_\theta}{r} \right)$ induced by the base flow. Since $S \geq 0$, energy growth occurs whenever $u_r u_\theta < 0$. This configuration of planar velocity is illustrated in figure 6.7(c) and corresponds to negative tilt streamlines. Perturbation with (positive) negative tilt streamlines are characterized by (anti-)clockwise spiralling iso-contours of axial vorticity (starting from the vortex center). Considering figure 6.6(b), we see that this corresponds to iso-contours of axial vorticity that are oriented perpendicular to the direction of strain, see figure 6.6. The growth mechanism, similar to the Orr mechanism in plane shear flows, consists in a concentration of the axial vorticity ω_z by the

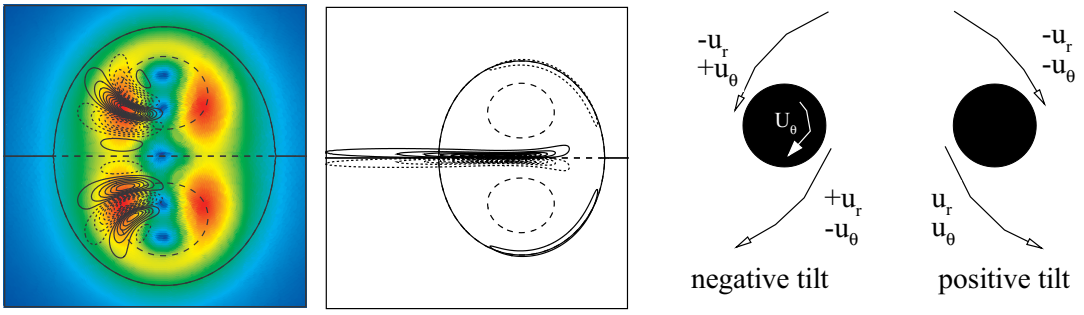

(a) Short time (b) Large time (c)

Figure 6.7: (a) Axial vorticity ω_z of the initial perturbation that maximizes the growth of energy at short time ($\boldsymbol{u}_I$) and, (b) at large time. $k = 0.25$. Dashed lines indicate negative vorticity. In (a) color indicate iso-contours of the strain rate S normalized on t_a^{-1}, which was already depicted in figure 6.6(a). In both frames the base flow is shown with a few streamlines. (c) Schematic of streamline tilt for a single vortex (black disc) rotating clockwise. Reproduced from Pradeep[124].

base flow, which results in a transient increase of the kinetic energy of the perturbation. As shown by Pradeep[124], the stretching induced by the basic differential rotation progressively modifies the perturbation into positive tilt $u_r u_\theta > 0$, which arrests the energy growth.

Application to the vortex pair In order to apply these results to the case of the vortex pair, we look at the evolution of the product $u_r u_\theta$ of the perturbation $\boldsymbol{u}_I$ which gives the maximum instantaneous amplification. Note that the streamlines of the base flow in the vortex core are not circles therefore the use of u_r and u_θ is rigorously not correct. However the ellipticity of the streamlines in the vortex core remains small. Indeed it is of the order of the strain at the vortex centers $S(x_c, y_c)$ (imposed by each vortex of the pair upon the other), which is equal to $(a/b)^2 = 0\left(10^{-2}\right)$ since $a/b = 0.25$.

The curve of the energy growth corresponding to $\boldsymbol{u}_I$ as initial condition is shown in figure 6.5 (dash dotted line). As expected, the initial energy growth generated by this perturbation is in agreement with λ_I and with the optimal energy growth ($\square$). The growth stops at $t = 0.25$. For $0.25 < t < 1.5$ the energy decreases. After $t = 1.5$ it increases again due to the occurrence of the Crow instability.

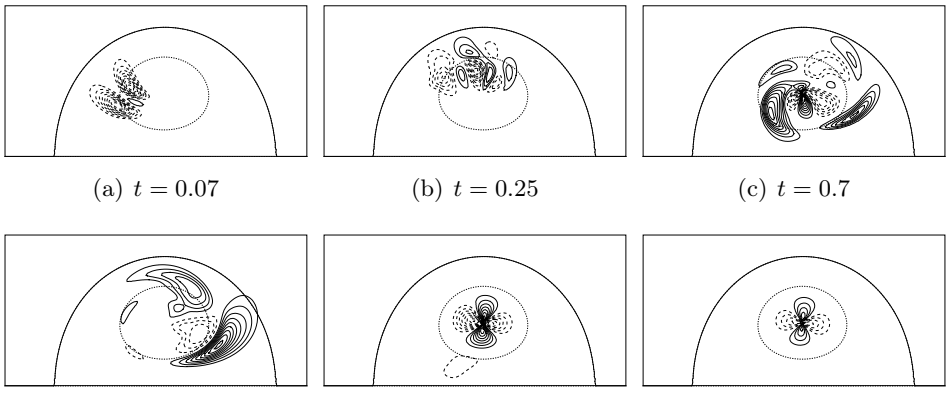

(a) $t = 0.07$ (b) $t = 0.25$ (c) $t = 0.7$

(d) $t = 1.5$ (e) $t = 2.8$ (f) $t = 3.5$

Figure 6.8: Iso-contours of $u_r u_\theta$ at different times of the optimal perturbation $\boldsymbol{u}_I$ at $k = 0.25$. Negative values are dashed. t is normalized on t_b.

In figure 6.8 we show snapshots of $u_r u_\theta$ at different times. At $t = 0.07$, $u_r u_\theta < 0$, which allows the initial energy growth. At $t = 0.25$ we see that positive and negative $u_r u_\theta$ balance each other, which corresponds to the arrest of the energy growth. Between $t = 0.25$ and $t = 1.5$ when the minimum of energy amplification is reached, the part of the positive $u_r u_\theta$ dominates and increases, resulting in the decrease of the energy. At later times, snapshots show the development of the Crow instability in the vortex core in the form of a quadripolar and steady structure. Comparing dE/dt at $t = 3.5$ and $t = 4.2$ (not shown) with (6.15), and using $E \sim e^{\sigma t}$, we retrieve $\sigma \sim 0.8$, in fair agreement with the growth rate of the Crow instability $\sigma_{Crow} \sim 0.7$ (see figure 6.3(b)). Qualitatively, although the Crow pattern shown in figure 6.8(f) is an equilibrated quadripole, energy growth occurs because the regions where $u_r u_\theta < 0$ are characterized by a strain rate S which is larger than the strain characterizing the regions where $u_r u_\theta > 0$, as evidenced in figure 6.6(a).

Large time dynamics

In the following we analyze the dynamics at large time with the help of the adjoint mode. We first show that the adjoint mode is the optimal perturbation at large time. To do this, we consider the leading eigenmode $\hat{\boldsymbol{u}}_m$ associated to the eigenvalue $\sigma_m = max_j\,(\sigma_j)$. Following equation 6.6, the solution of the initial value problem becomes $\boldsymbol{u}(t) = (\hat{\boldsymbol{u}}_m^+, B\boldsymbol{u}_0)\,\hat{\boldsymbol{u}}_m e^{\sigma_m t} + c.c.$. The amplification of kinetic energy (6.12) produced by this perturbation equals $(\hat{\boldsymbol{u}}_m^+, B\boldsymbol{u}_0)^2\, e^{2\sigma_m t}$ and is maximum when the initial perturbation is chosen as $\boldsymbol{u}_0 = \hat{\boldsymbol{u}}_m^+$. In physical terms, that means that the adjoint perturbation is the initial perturbation $\boldsymbol{u}_0$ that generates the maximum amplification of the energy contained in the leading eigenmode at large time.

The energy growth corresponding to the adjoint mode of the Crow instability was depicted in figure 6.5 and we saw that the energy growth generated by this perturbation remains close to the optimal ($\square$) at all times. Strong transient growth occurs before $t = 2$ and the subsequent evolution results from the development of the Crow instability. The axial vorticity ω_z of the adjoint mode has been shown in figure 6.7(b). Because of the small value of the wavenumber k of the Crow instability, the axial vorticity dominates by more than one order of magnitude the transverse components of the perturbation vorticity (indeed $\omega_z \sim k^{-1}\omega_{x,\,y}$). The figure shows that the adjoint perturbation is localized on the streamline $\Psi = 0$ of the base flow. More precisely the perturbation axial vorticity is located in the region of the upstream stagnation point. This suggests that this point plays an important role in the energy growth generated by the adjoint perturbation.

In order to analyze this energy growth, we investigate the evolution of this perturbation at different times up to $t = 2$ (where the transient stage stops). Snapshots of the axial vorticity ω_z (black lines) and planar vorticity $\sqrt{\omega_x^2 + \omega_y^2}$ (colored contours) fields are displayed in figure 6.9. For $t < 0.4$ the initial perturbation is convected along the symmetry plane of the vortex pair to the linear flow region surrounding the upstream stagnation point. In this region the planar vorticity is oriented in the y direction. For $0.4 < t < 1.4$, the perturbation experiences strong straining in the y direction in agreement with the results of Lagnado[87]. Following this author, hyperbolic stagnation points are able to sustain energy growth for well suited initial perturbations. We illustrate his results for a hyperbolic stagnation point oriented like the upstream stagnation point. For a given initial perturbation $\boldsymbol{\omega}_0 = \left(\omega_x^0, \omega_y^0, \omega_z^0\right)$, the solution at later times t of the perturbation has the form

$$\boldsymbol{\omega} = e^{-i\left(e^{St}k_x x + e^{-St}k_y y + k_z z\right) - \frac{\pi(a/b)^2}{SRe}\left(k_x^2\left(e^{2St}-1\right) + k_y^2\left(1-e^{-2St}\right) - 2Sk_z^2 t\right)} \begin{pmatrix} \omega_x^0 e^{St} \\ \omega_y^0 e^{-St} \\ \omega_z^0 \end{pmatrix} \tag{6.16}$$

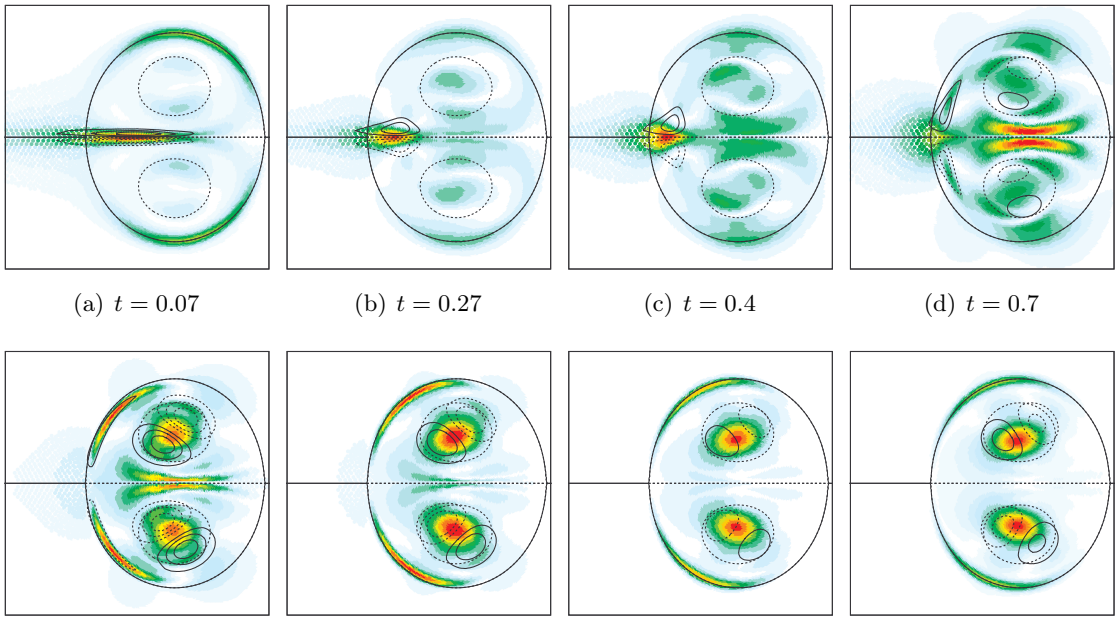

(a) $t = 0.07$ (b) $t = 0.27$ (c) $t = 0.4$ (d) $t = 0.7$

(e) $t = 1.07$ (f) $t = 1.4$ (g) $t = 1.6$ (h) $t = 2$

Figure 6.9: Snapshots of the axial vorticity ω_z (black lines) and planar vorticity $\sqrt{\omega_x^2 + \omega_y^2}$ (colored contours) of the perturbation initialized by the adjoint mode of the Crow instability at $k = 0.25$. Streamlines of the base flow are included. t is normalized on t_b.

where the wavenumber k is normalized on b and is decomposed in its three components along x, y and z. The strain rate at the stagnation point is $S > 0$. The strain is oriented in the y direction. According to this expression, exponential growth occurs if $k_x = 0$ and $k_z < \dfrac{SRe_\Gamma}{2\pi\,(a/b)^2}$. This last condition corresponds to $k_z a < 8$ in the vortex pair at $a/b = 0.25$ and is hence verified by all the perturbations considered here. In this case this means that the viscous decay of the initial perturbation is dominated by the stretching of the ω_y vorticity. Note however that the condition $k_x = 0$ implies that this exponential growth is possible only if the initial perturbation is uniformly distributed along the entire range of the x axis. This being not possible physically, the growth at the stagnation point is only transient. However (6.16) indicates that the initial growth of energy in the region of the hyperbolic stagnation point follows an exponential law of exponent S.

Stretching also occurs at the downstream stagnation point. There, part of the initial perturbation that was on the dividing streamline $\Psi = 0$ of the vortex pair, which consists in planar vorticity aligned in the x direction, experiences stretching. However this vorticity in the upstream hyperbolic region, cannot be amplified by stretching and it decays by viscosity. At time $t > 1.07$ the vorticity that has been amplified at the upstream stagnation point is convected by the base flow along the dividing streamline of the vortex pair. Meanwhile we observe that the perturbation grows in the vortex core, although it was not present initially. At $t = 2$ this core vorticity corresponds to the Crow instability already depicted in figure 6.4(a).

The evolution described above suggests that the amplification of energy produced by the adjoint mode first relies on (i) the amplification at the upstream and downstream stagnation points, with a dominant implication of the upstream one, (ii) a subsequent transfer of the energy produced there to the vortex core, and (iii) an exponential increase of energy occuring through the effect of the Crow instability. In order to elucidate this transfer of energy between the outer and inner parts of the vortices, we follow the approach proposed by Antkowiak[5] and write the equation for the axial vorticity in the cylindrical coordinate frame attached to one of the

vortices

$$\frac{\partial \omega_z}{\partial t} + \frac{U_\theta}{r}\frac{\partial \omega_z}{\partial \theta} = -u_r \frac{\partial R}{\partial r} + kRu_z + \nu \Delta \omega_z \tag{6.17}$$

where R is the basic angular velocity. The second term in the LHS corresponds to the convection of the axial vorticity by the base flow. The first two terms in the RHS lead to the increase of the axial vorticity by an induction mechanism. Indeed the planar vorticity that is amplified along the dividing streamline of the dipole consists of nearly tangential vorticity. This vorticity induces u_r and u_z in the vortex core which in turn interacts with the basic angular velocity R to increase ω_z. This mechanism of induction amounts to a transfer of energy from the outer to the inner regions of the vortices. Therefore the Crow instability develops with an initial energy obtained by a transient amplification at the stagnation points which is significantly higher than the initial energy contained in the direct mode of the instability. This explains the offset of the adjoint amplification compared to the direct amplification in figure 6.5.

Optimal perturbation

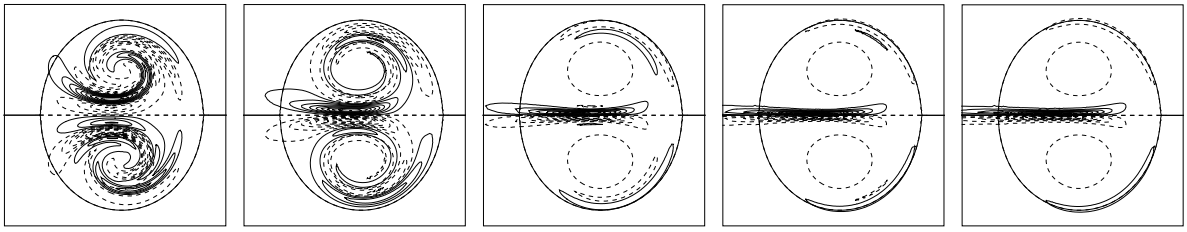

(a) $t_{opt} = 0.4$ (b) $t_{opt} = 1.15$ (c) $t_{opt} = 1.9$ (d) $t_{opt} = 2.7$ (e) $t_{opt} = 4.2$

Figure 6.10: Axial vorticity ω_z of the symmetrical optimal perturbation at several values of t_{opt} at the Crow wavenumber $k = 0.25$. t_{opt} is normalized on t_b.

The evolution of the form of the optimal perturbation with t_{opt} in the symmetric case is shown in figure 6.10. We observe that, with increasing t_{opt}, the optimal perturbation ω_z is progressively displaced outward. This is in continuity with the asymptotic cases discussed just before (short and large time). An analysis, not described here, similar to the one performed on the optimal instantaneous perturbation, shows that the initial perturbation at $t = 0.4$ exhibits energy growth by the same shearing mechanism. At large time, $t_{opt} > 2$, contours of ω_z are similar to the adjoint mode, indicating energy growth by tilting/stretching at the hyperbolic regions and induction of the core dynamics. At intermediate time, there is a trade-off between the short time mechanism and the large time mechanism. This means that, with increasing t_{opt} the short time mechanism is less important while the large time mechanism plays an increasing role. We will see later on that the induction mechanism is piloted by a resonant effect. In particular, this will explain why the initial perturbation tends towards the streamline $\Psi = 0$ surrounding the vortex pair with increasing t_{opt}.

6.2.3 Optimal perturbation at the Widnall wavelength

Figure 6.11 shows the optimal gain obtained at the wavenumber $k = 2.26$ corresponding to the first Widnall instability. Antisymmetric perturbations beneficiate from a larger energy increase. We observe that the transient regime stops at $t = 1.5$. At later times, all perturbations converge toward the growth rate of the Widnall instability. Optimal perturbations at several t_{opt} including the asymptotic solutions at short and large time are shown in figure 6.12 in the antisymmetric case.

At short time, the optimal perturbation grows thanks to the shearing mechanism, as can be inferred from the negative tilt streamlines localized in the region where S is large. At large

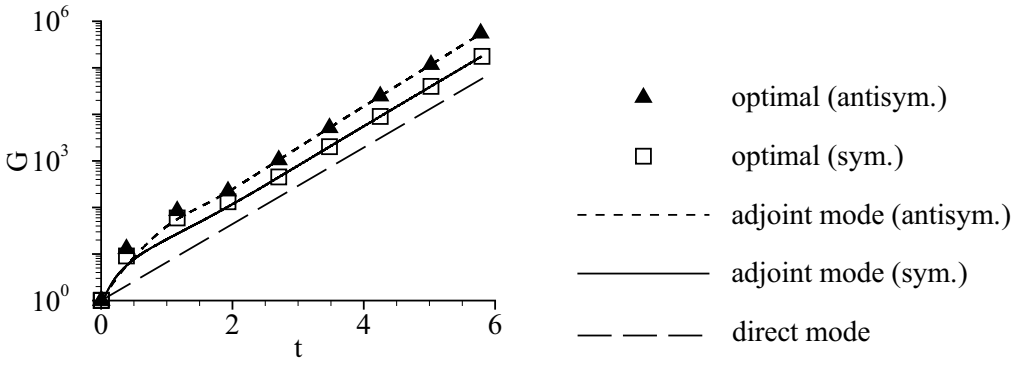

Figure 6.11: Energy growth with different initial perturbation at $k = 2.26$ as a function of time in log-lin scale. Same axis details as figure 6.5 are used to ease comparisons. Plain curves show the adjoint growth rate. Symbols show the optimal solution computed by the optimization algorithm. ▲ (dashed lines) correspond to antisymmetric perturbations. □ (solid lines) correspond to symmetric perturbations. t is normalized on t_b.

time, the optimal perturbation looks like the adjoint mode of Crow, which suggests that the mechanism of amplification relies on the stretching at the upstream and downstream stagnation regions and induction of the core dynamics by tangential vorticity located at the dividing streamline of the vortex pair. There is a significant difference however in the fact that the Widnall instability exists initially in the velocity field of the optimal perturbation, which was not the case concerning the Crow instability. We believe that this explains the smaller offset between the curve of the adjoint growth and the curve of the direct growth compared to the Crow case. At intermediate times, the optimal perturbation evolves continuously from the form at short time to that at large time, indicating the same trade-off as in the Crow case between the large time and short time mechanisms.

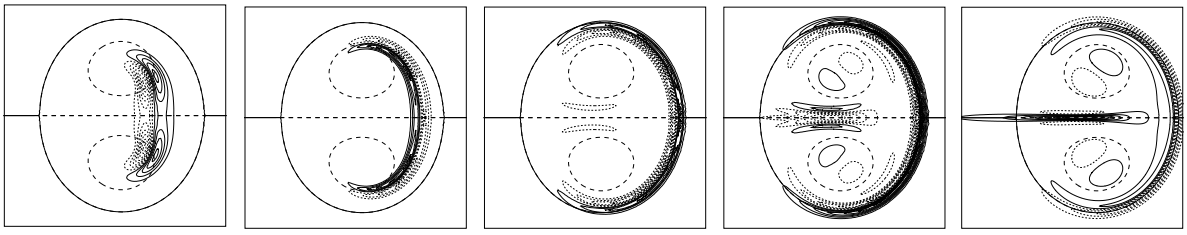

(a) short time (b) $t_{opt} = 0.4$ (c) $t_{opt} = 1.15$ (d) $t_{opt} = 1.9$ (e) large time

Figure 6.12: Axial vorticity of the optimal antisymmetric perturbation at several values of t_{opt} at the Widnall wavenumber $k = 2.26$. t is normalized on t_b.

Optimal perturbation at $k = 1$

Figure 6.13 shows the optimal amplification curves at $k = 1$. This configuration is stable but exhibits transient growth. The energy amplification corresponding to the optimal perturbation at large time $t = 5.8$ is close to the optimal at all times.

Figure 6.14 shows the axial vorticity ω_z of the optimal perturbation at different optimization times in the antisymmetric case. Like in the cases of Crow and Widnall, the optimal at short time is localized in the region of strong strain and corresponds to perturbation with negative tilt. At large time, the optimal perturbation is localized on the streamline $\Psi = 0$ which suggests the occurrence of the mechanism of stretching/induction by the upstream and downstream stagnation points.

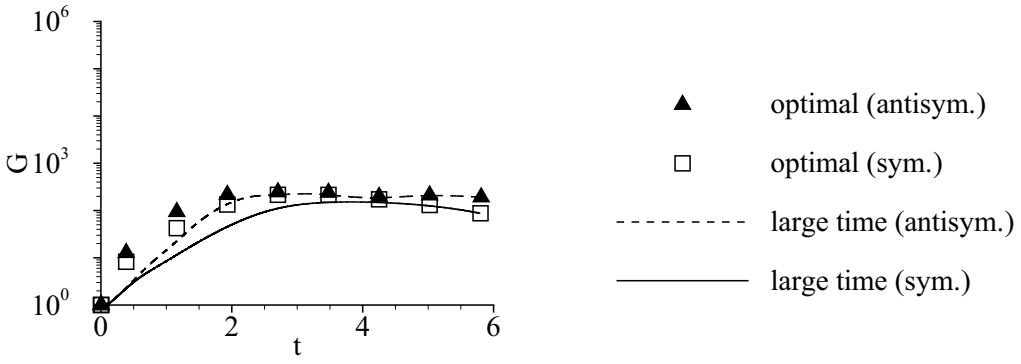

Figure 6.13: Energy growth with different initial perturbation at $k = 1$ as a function of time in log-lin scale. Same axis details as figure 6.5 are used to ease comparisons. The solid and dashed lines correspond to the optimal perturbation at $t_{opt} = 5.8$. Symbols show the optimal solution computed by the optimization algorithm. ▲ (dashed lines) correspond to antisymmetric perturbations. □ (solid lines) correspond to symmetric perturbations.

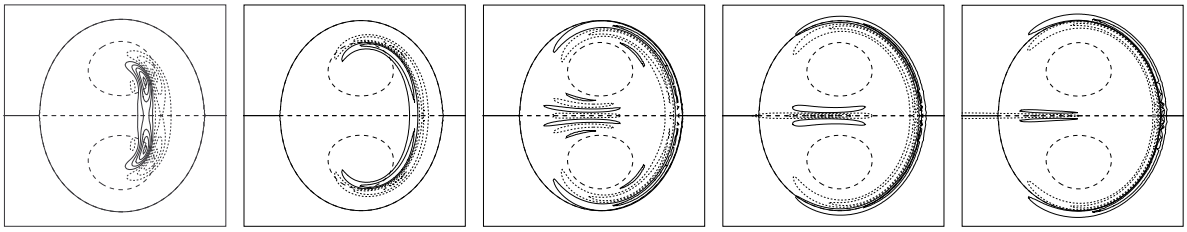

(a) short time (b) $t_{opt} = 0.4$ (c) $t_{opt} = 1.15$ (d) $t_{opt} = 1.9$ (e) $t_{opt} = 5.8$

Figure 6.14: Axial vorticity ω_z of the optimal perturbation at several values of t_{opt} at $k = 1$ in the antisymmetric case.

An interesting point concerns the effect of the symmetry of the perturbation on the role played by the upstream and downstream stagnation points on the energy amplification. Comparing the adjoint of the Crow instability (symmetric) in figure 6.7(b), that of the symmetric and antisymmetric Widnall instability in figures 6.15(a) and 6.12(e), and that of the symmetric and antisymmetric optimal perturbation at large time at $k = 1$ in figures 6.15(b) and 6.14(e), we observe that (anti)symmetric optimal perturbations at large time rather rely on the (downstream) upstream stagnation point.

This is explained by the amplification properties of the hyperbolic stagnation point. Recall that the optimal perturbation in the stagnation point region takes the form of vorticity aligned in the direction of strain and distributed as uniformly as possible along the direction of compression. Concerning the upstream stagnation point, this imposes vorticity in the y direction while at the downstream stagnation point, this imposes vorticity in the x direction. Considering the symmetry of the vorticity field, symmetric perturbations should experience small amplification at the downstream stagnation point since ω_x must be zero at $y = 0$. Therefore symmetric perturbation should rather take advantage of the upstream stagnation point, in agreement with the observations. The argument reverses for antisymmetric perturbations and agree again with our results.

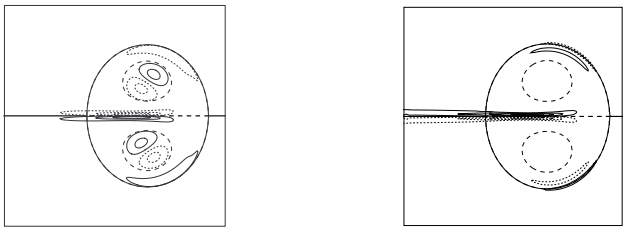

(a) (b)

Figure 6.15: Axial vorticity ω_z in the symmetric case. (a) Adjoint mode at the Widnall wavenumber $k = 2.26$, (b) optimal perturbation at $t_{opt} = 5.8$ at $k = 1$.

6.2.4 Effect of the axial flow

Normal modes

In order to investigate the effect of axial flow we consider the eigenmodes of the vortex pair found by Lacaze[86] at $q = 2$. In the presence of an axial flow, resonance between Kelvin modes and external strain occurs at non zero frequency. This effect is similar to a Doppler frequency shift. Lacaze[86] calculated the most unstable instabilities of the dipole at $a/b = 0.25$ and

		$Re_\Gamma = 20000$				$Re_\Gamma = 4000$
Mode		Lacaze[86]		Comparison		
$(m_1, m_2, [n_1, n_2])$	k	σ_R	σ_I	σ_R (symmetric)	σ_I (symmetric)	σ_R (symmetric)
(2,0,1)	1.88	1.23	0.26	1.26 (1.23)	0.29 (0.29)	1.130 (1.100)
(2,0,[2,1])	2.6	0.71	0.22	0.80 (0.77)	0.21 (0.21)	0.560 (0.510)
(3,1,1)	3.23	1.05	0.61	1.09 (1.09)	0.61 (0.58)	0.700 (0.700)
(3,1,[2,1])	3.85	0.69	0.60	0.80 (0.80)	0.52 (0.53)	0.310 (0.310)
(4,2,1)	4.57	0.80	1.04	0.94 (0.94)	0.99 (0.99)	0.098 (0.094)

Table 6.1: Eigenvalues for selected modes at $q = 2$, $a/b = 0.25$ and $Re_\Gamma = 20000$. Results are compared with Lacaze[86]. Note that antisymmetrical and symmetrical perturbations are distinguished (Lacaze[86] did not need to do this distinction as he used a computational domain including the two vortices of the pair). σ_R is normalized on t_b^{-1} and σ_I on t_a^{-1}. m is the azimuthal wavenumber of the perturbation and n the number of radial nodes of the axial vorticity distribution. Subscripts 1 and 2 refer to the two Kelvin modes playing in the cooperative instability.

$Re_\Gamma = 20000$. His results are given in table 6.1. We used these results in order to validate our code and to investigate the effect of the axial flow on the growth of energy in the vortex pair. The agreement between our results and those of Lacaze[86] at $Re_\Gamma = 20000$ are good overall. The growth rate and frequency of these unstable modes at $Re_\Gamma = 4000$ are also given in the table and will be used later on. Unlike the growth rate σ_R, σ_I is not modified by the Reynolds number and is therefore not included in the table for the case $Re_\Gamma = 4000$. Note that the positiveness of m and σ_I means that all these modes rotate in the same direction as the base flow.

Figure 6.16 shows the axial vorticity ω_z of these modes. Here again the agreement with the findings of Lacaze[86] is good. These modes exhibit the azimuthal periodicity m_1. The rotation of each mode in the laboratory frame is given by σ_I/m_1. This means that, depending on the value of m_1, a mode with large σ_I does not necessarily rotate fast. For example the case of the most unstable mode at $k = 4.57$ has a rotation rate 0.25 which is slightly higher than that of the mode at $k = 1.88$ that rotates at 0.12.

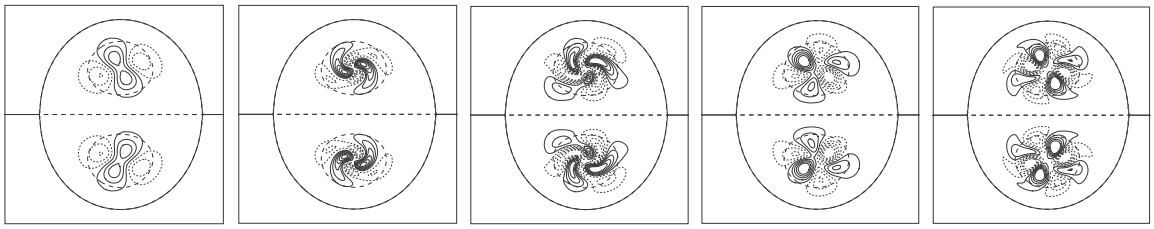

(a) $k = 1.88$ (b) $k = 2.6$ (c) $k = 3.23$ (d) $k = 3.85$ (e) $k = 4.57$

Figure 6.16: Axial vorticity ω_z of the real part of the antisymmetric direct modes at $q = 2$. k is normalized on a^{-1}

Optimal perturbation

The energy growth of the optimal perturbations at $q = 2$ are depicted in figure 6.17. We observe that the large time dynamics, which corresponds to the linear amplification of the energy with the growth rate of the instability, arises at different times depending on the instability considered. In the case $k = 1.88$ the transient regime corresponds to $t < 2$ whereas at $k = 3.85$ it stops at $t = 4$. The case at $k = 1.88$ resembles the cases of Crow and Widnall in the sense that the adjoint growth is almost optimal. However in the case at larger wavenumber $k = 3.23$, $k = 3.85$ and $k = 4.57$ the energy of the adjoint is much lower than the optimal at short time.

Short time dynamics In the following we show that the short time dynamics is not strongly modified by the axial flow at $q = 2$ since for this swirl number the flow is mainly tangential. In presence of axial flow, the deformation tensor becomes

$$\begin{aligned} D &= \begin{pmatrix} \frac{\partial U_x}{\partial x} & \frac{1}{2}\left(\frac{\partial U_y}{\partial x}+\frac{\partial U_x}{\partial y}\right) & -\frac{1}{2}\frac{\partial U_z}{\partial x} \\ \frac{1}{2}\left(\frac{\partial U_y}{\partial x}+\frac{\partial U_x}{\partial y}\right) & \frac{\partial U_y}{\partial y} & -\frac{1}{2}\frac{\partial U_z}{\partial y} \\ \frac{1}{2}\frac{\partial U_z}{\partial x} & \frac{1}{2}\frac{\partial U_z}{\partial y} & 0 \end{pmatrix} \\ &= \begin{pmatrix} \frac{\partial U_x}{\partial x} & \frac{1}{2}\left(\frac{\partial U_y}{\partial x}+\frac{\partial U_x}{\partial y}\right) & 0 \\ \frac{1}{2}\left(\frac{\partial U_y}{\partial x}+\frac{\partial U_x}{\partial y}\right) & \frac{\partial U_y}{\partial y} & 0 \\ 0 & 0 & 0 \end{pmatrix} + \begin{pmatrix} 0 & 0 & -\frac{1}{2}\frac{\partial U_z}{\partial x} \\ 0 & 0 & -\frac{1}{2}\frac{\partial U_z}{\partial y} \\ \frac{1}{2}\frac{\partial U_z}{\partial x} & \frac{1}{2}\frac{\partial U_z}{\partial y} & \end{pmatrix} \end{aligned} \tag{6.18}$$

In the second relation, we distinguish the effect of the plane flow (U_x, U_y) and the effect of the axial flow U_z. In order to understand the effect of the axial flow, we isolate the second term in (6.18) and calculate the associated strain rate and direction

$$S^2 = \left(\frac{\partial U_z}{\partial x}\right)^2 + \left(\frac{\partial U_z}{\partial y}\right)^2 \quad , \quad \boldsymbol{V} = \begin{pmatrix} \frac{\partial U_z}{\partial x} \\ \\ \frac{\partial U_z}{\partial y} \\ \\ S \end{pmatrix} \tag{6.19}$$

The direction of strain is 3D and the strain rate S depends only on the axial velocity gradients. Figure 6.18 shows the strain field in the vortex pair at $a/b = 0.25$. In the case of the Batchelor vortex, the strain induced by the axial flow is axisymmetric (not shown). Concerning the vortex pair the axial flow generates large strain above and below the vortex centers. The comparison between this figure and figure 6.6(a) shows that the magnitude of the strain rate induced by the axial flow is larger than that induced by the plane flow.

In order to see how the axial velocity gradients influence the optimal perturbation at short time, we focus on the case $k = 1.88$ and calculate $\boldsymbol{u}_I$ at several values of q. Results are shown

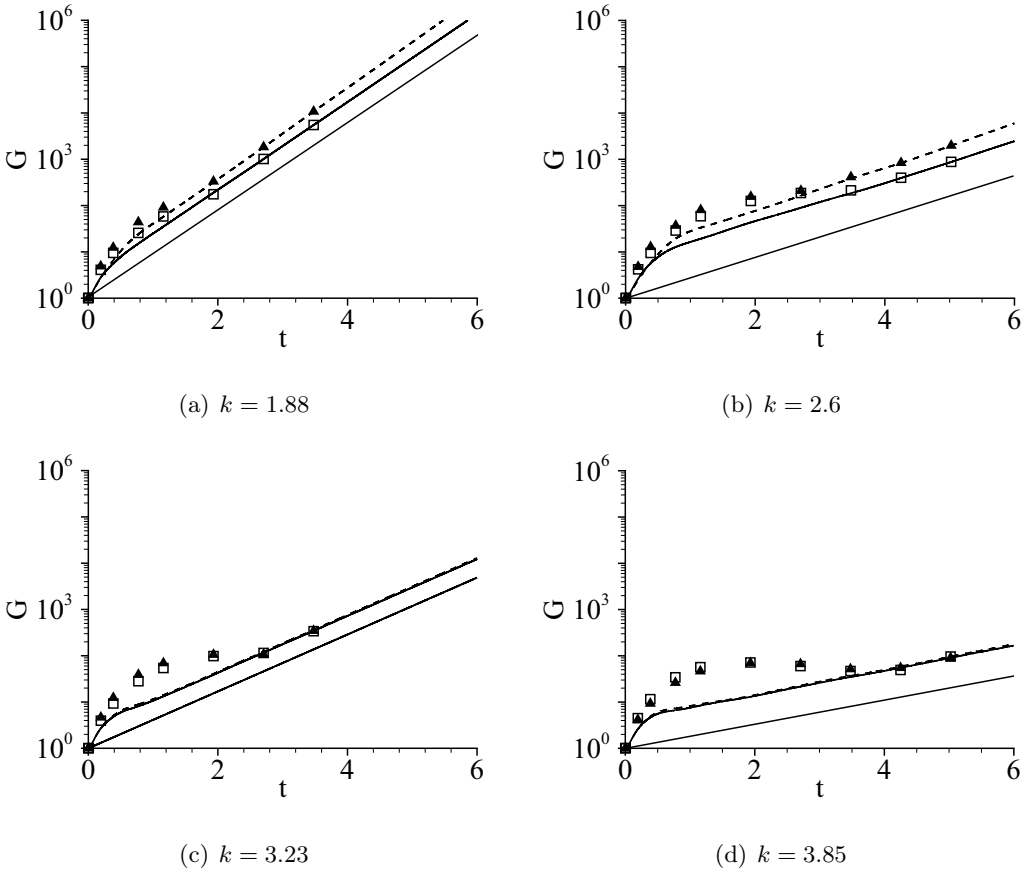

(a) $k = 1.88$ (b) $k = 2.6$

(c) $k = 3.23$ (d) $k = 3.85$

Figure 6.17: Energy growth with different initial perturbations for several wavenumbers at $q = 2$. Symbols: optimal. Lines: adjoint. ▲ (dashed lines) correspond to antisymmetrical perturbations . □ (solid lines) correspond to symmetrical perturbations. The case $k = 4.57$ is not shown because curves in this case are very similar to the case $k = 3.85$.

in figure 6.19 in terms of axial vorticity ω_z. As q decreases the initial perturbation is more and more localized in the region of strong strain induced by the axial flow. However at $q = 2$ the effect of the axial flow is small and the initial perturbation looks like the one which is obtained at $q = \infty$. This is not surprising since at $q = 2$ the flow is dominated by the swirl. The effect of axial flow becomes dominant when $q < 1$ but this range of swirl is not encompassed by this study.

Large time dynamics In figure 6.20 we show the antisymmetric adjoint modes corresponding to the instabilities at $q = 2$ listed in table 6.1. The overall structure of the vorticity distribution resembles that at $q = \infty$ but the complexity is significantly larger. We suggest that this is due to the higher azimuthal periodicity of the Kelvin waves that participate in the instabilities.

Like at $q = \infty$, the axial vorticity of the adjoint modes take the form of spirals. However these spirals are not necessarily located on the streamline $\Psi = 0$. In particular we observe that they get closer to the vortex centers when σ_I is larger. In the following we propose an interpretation of this observation in terms of a resonant effect which could explain why the Crow and Widnall optimal perturbations at large time are located on the dividing streamline $\Psi = 0$.

Resonance The works of Antkowiak[5], Pradeep[124] and Heaton[65] on the optimal perturbation of a columnar vortex showed the existence of a resonant mechanism at $|m| = 1$ between (i) the rotation rate R of the initial perturbation by the base flow and (ii) the rotation rate ω_I

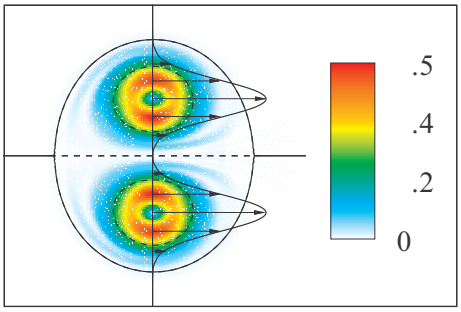

Figure 6.18: Contours of strain rate S normalized on t_a^{-1} induced by the axial flow for the vortex pair at $a/b = 0.25$. Vectors indicate the axial flow U_z.

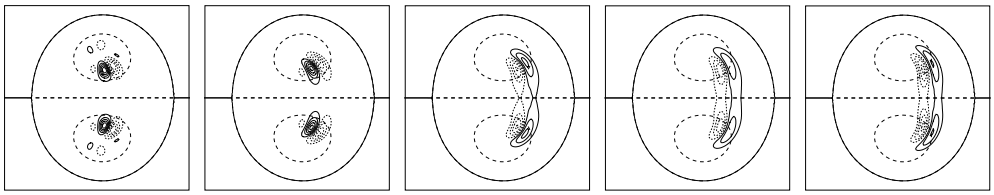

(a) $q = 0.5$ (b) $q = 1$ (c) $q = 1.5$ (d) $q = 2$ (e) $q = \infty$

Figure 6.19: Axial vorticity ω_z of the antisymmetrical optimal perturbation at short time for several values of q at $k = 1.88$.

of the Kelvin waves induced by the initial perturbation. According to these authors, the initial perturbation takes the form of negative tilt spirals located at a radius r_r where $R(r_r) = \omega_I$, R being the angular velocity of the base flow. This resonance was also shown to occur in the presence of axial flow (Heaton[65]).

The resonant effect is different from the critical-layer phenomenon. Modal perturbations of the vortex are critical at points r_c that satisfy $\omega_I = mR(r_c) + kU_z(r_c)$, meaning that the rotation of the mode equals the rotation rate R of the base flow, see Le Dizès[92]. The critical layer is a resonant effect between the perturbation and the base flow. Here the resonant effect is different. Although the previous authors did not identify the resonant effect at values of $|m|$ different from 1, we suggest, from the location of the initial perturbation in figure 6.20, that the resonant effect exists at all m. Following this hypothesis the resonant radius r_r must verify

$$R(r_r) = \frac{\omega_I}{m_1} \tag{6.20}$$

In order to verify relation (6.20) we compare the rotation of the base flow at the location of the initial vorticity with the rotation rate ω_I/m_1 of the instability. We first need to evaluate the rotation rate R of the base flow. In the case of the axisymmetric vortex, the rotation rate of a particle at a radius r is simple: $R = U_\theta(r)/2\pi r$. The case of the vortex pair is more complicated because the streamlines are not circles, especially outside the vortex core. The form of the streamlines change with the distance from the vortex centers. To evaluate the rotation rate we first evaluate the period of rotation for one particle on a given streamline. Note that the position is no longer referenced by the radius but by the stream function therefore relation 6.20 now reads

$$R(\Psi_r) = \frac{\omega_I}{m} \tag{6.21}$$

The generalization of the rotation period T stems from the axisymmetric case

$$T = \oint_{\mathcal{C}} \frac{\boldsymbol{U} \cdot \boldsymbol{dl}}{\|\boldsymbol{U}\|^2} \tag{6.22}$$

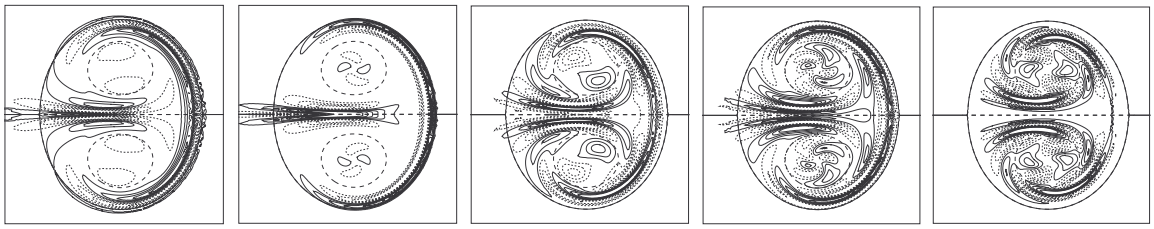

(a) $k = 1.88$ (b) $k = 2.6$ (c) $k = 3.23$ (d) $k = 3.85$ (e) $k = 4.57$

Figure 6.20: Real part of the axial vorticity ω_z of the antisymmetrical adjoint modes corresponding to the instabilities listed in table 6.1.

where $\mathcal{C}$ is a closed streamline. Thanks to the Green theorem, previous relation transforms into

$$T = \iint_{\mathcal{S}} \boldsymbol{rot}\left(\frac{\boldsymbol{U}}{\|\boldsymbol{U}\|^2}\right) \cdot \boldsymbol{n} dS \tag{6.23}$$

which is more convenient to compute since this relation relies on an integral that is easily calculated numerically. Note that $\boldsymbol{n}$ denotes the normal to the computational domain. The angular velocity of the base flow corresponding to T is $R = 2\pi/T$.

In the bottom of figure 6.21 we show R as a function of the stream function Ψ. Only the closed streamlines have been taken into account. As expected R decreases away from the vortex centers up to the dividing streamline enclosing the vortex pair. The rest of the figure shows the distribution of ω_z of the Crow mode and the modes at $q = 2$ as a function of Ψ. The streamline Ψ_r that verifies (6.21) is reported on the curve R versus Ψ in these different cases. Comparing the location of the initial perturbation and the streamline predicted by (6.21), we observe the good trend (Ψ_r increases with ω_I/m). Moreover in every case the arrows match with a part of the axial vorticity distribution of the perturbation. However this distribution being large, it is difficult to select one single streamline to characterize the position of the initial perturbation. These results support well the existence of a resonant effect. However the discrepancies between the initial distribution and the prediction suggest that additional effects apply. Therefore it would be worth investigating in greater depth this aspect of the optimal perturbation in future works.

Now coming back to the Crow and Widnall instability, we see that the resonant mechanism explains why the optimal perturbation at large times is located on the streamline $\Psi = 0$. Indeed at this location the rotation rate is minimum and close to zero, which agrees well with the stationarity of these instabilities. Axial flow allowed the existence of $\omega_I \neq 0$ for which we could see variations in the location of the initial optimal perturbation at large time.

Conclusion

In this chapter we have analyzed the transient growth of energy in vortex pairs. We first analyzed the case of the 2D vortex pair without axial flow and characterized the optimal energy amplification for $k < 2.5$ and $t_{opt} < 6$. This proved the existence of transient energy amplification at short time that either led to stronger growth rates of the Crow and Widnall instabilities or to energy decay in the stable range of wavelengths. Two mechanisms were identified, one that dominates the short time dynamics and that relies on energy amplification in the region of maximum strain and the second that dominates the large time dynamics and that relies on the stretching of vorticity in the hyperbolic regions and on the induction of a core dynamics in the vortices. In the second part of this chapter, we analyzed the effect of the axial flow on the optimal perturbation by focusing on several instabilities with non zero frequency that were first found by Lacaze[86] at $q = 2$. We found that at short time, the mechanism of energy growth

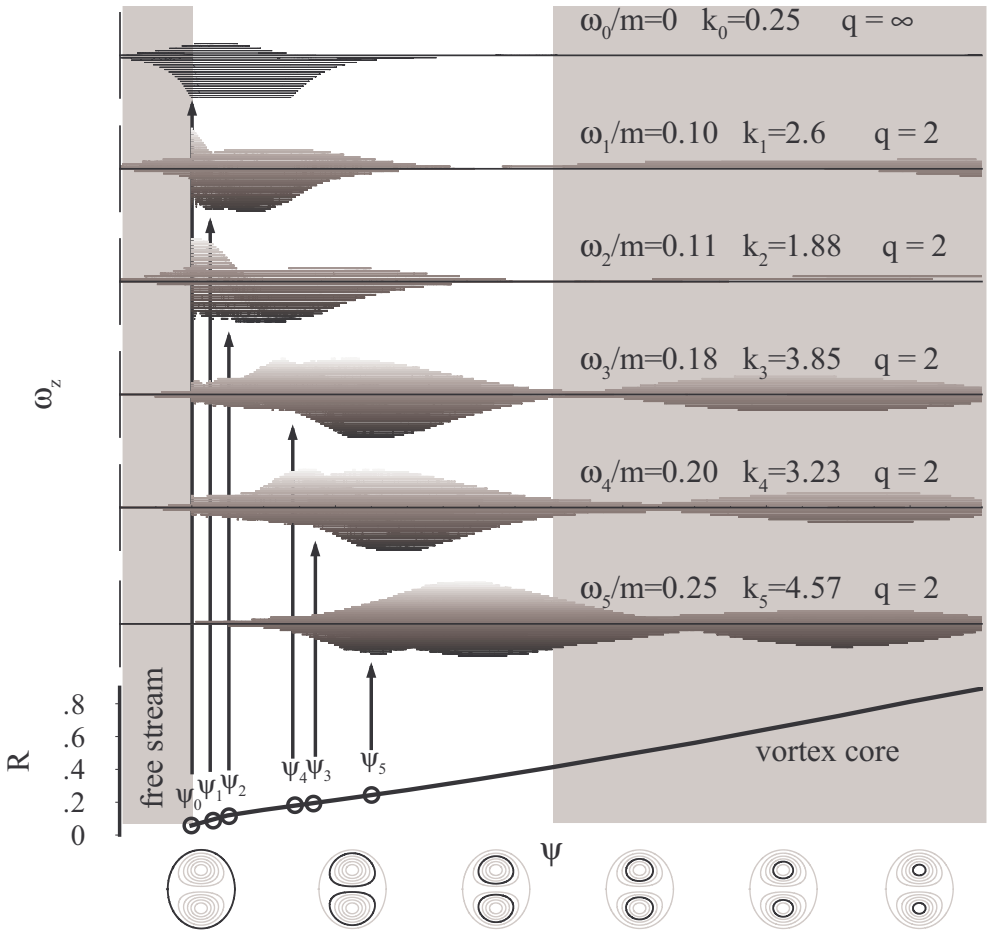

Figure 6.21: illustration of the resonant effect. The curve represents the rotation rate R as a function of the stream function of the basic state Ψ for the vortex pair at $a/b = 0.25$. The contour plots corresponds to the adjoint modes at different k and q. They show the axial vorticity of perturbation as a function of the stream function Ψ. The circles indicate the condition of resonance. The axis for the stream function encompasses the inside of the Kelvin oval of the dipole (closed streamlines).

is not strongly modified by the addition of axial flow since the plane velocity gradients dominate. At large time, we described a resonant effect between the location of the initial optimal perturbation and the frequency of the final instability.

Note that the optimal perturbation of Crow instability at large time, which corresponds to the adjoint mode of this instability, will be the basis of the design of a control device of the tip leakage vortex in appendix A. Moreover, in appendix E, we investigate transient growth in a plane vortex sheet that rolls-up into two distinct vortices and show that this additional dynamics provides further possibilities to increase the growth rate of the Crow instability.

Part III

Experimental results

7 Time-averaged properties of the vortices

This chapter deals with the time-averaged properties of the tip leakage vortex obtained in the wind tunnel. We recall that the experimental apparatus can be set in two different configurations:

i- C1 consists of a split wing producing two symmetric counter-rotating vortices

ii- C2 consists of a single wing with a splitter plate materializing the symmetry plane, isolating one vortex of the pair.

The velocity and pressure fields have been surveyed with a seven-hole pressure probe (details on the probe are given in chapter 4 and appendix B) in cross sections normal to the free stream at different longitudinal positions $-0.75 \leq z \leq 2.5$. Recall that $z = 0$ at the wing trailing edge. Variations of the gap size such as $1\% \leq \tau \leq 12.25\%$ have been considered. The wing is set at $\alpha = 8^o$ throughout the study. The free stream velocity is set at $U_\infty = 38m/s$ which corresponds to $Re_c = 4.8.10^5$.

The vortices produced by configurations C1 and C2 are described in the two first sections. We then analyze the loss mechanisms related to these flows.

7.1 Flow in C1

7.1.1 Formation of the vortex at large gap

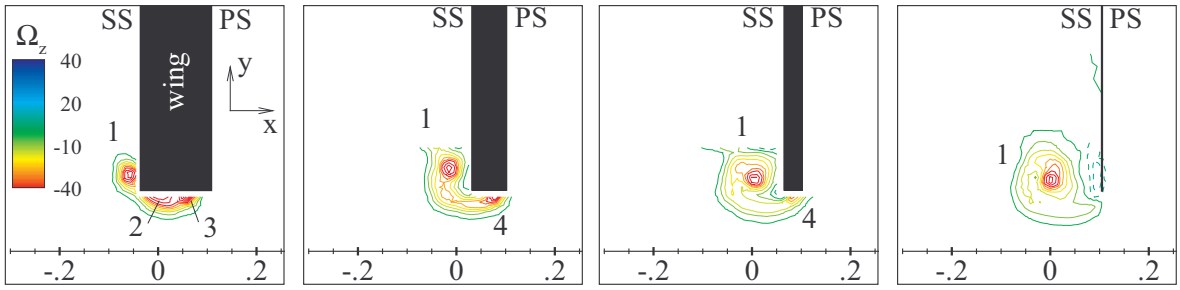

(a) $z = -0.5$ (b) $z = -0.3$ (c) $z = -0.1$ (d) $z = 0$

Figure 7.1: Mean axial vorticity Ω_z as a function of z (conf. C1). Gap size: $\tau = 12.25\%$. Positive vorticity is dashed. PS stands for Pressure Side and SS for Suction Side.

Figure 7.1 shows the mean axial vorticity Ω_z at $\tau = 12.25\%$ in transverse planes cutting the airfoil (corresponding to $-1 < z < 0$). The plots show the region $y > 0$ corresponding to negative axial vorticity. The vorticity field resulting from the second wing tip located at $y < 0$ does not appear here. Note that the cross section of the wing is included for clarity.

We observe an important evolution of the vorticity field with z. At mid-chord ($z = -0.5$) the vorticity field is composed of three regions (1, 2 and 3). Bailey[12] investigated the vortex roll-up at the tip of an isolated NACA12 wing and concluded on the existence of several vortices at the tip that eventually merge into a single vortex. This work suggests that each of the marked region corresponds to a distinct vortex. At $z = -0.3$ only one vortex remains at the wing tip surface (4). It is not clear whether there is a continuum between vortex 4 and the two previous vortices 2 and 3. Vortex 4 still exists at $z = -0.1$ but disappears downstream where only vortex 1 remains. These observations suggest that the final tip vortex results from the merging of several initial vortices. This is supported by figures 7.1(b) and 7.1(c) where the vorticity contours indicate vorticity going from region 2, 3 and 4 to region 1, probably due to the entrainment produced by this latter vortex.

7.1.2 Driving mechanism of the leakage flow

As mentioned in the introduction 1, the leakage flow through the gap has been the subject of numerous investigations. The inviscid nature of the leakage flow was advocated by Rains[125], who showed that the driving mechanism for the leakage flow is the pressure difference $\Delta C_p = P_{PS} - P_{SS}$ between the pressure side and the suction side of the wing. This leads to a flow velocity $U_t(z)$ normal to the chord

$$\frac{U_t(z)}{U_\infty} = \sqrt{\Delta C_p(z)} \tag{7.1}$$

This flow modifies in turn the pressure at the wing tip. The resulting leakage flow is an equilibrium between the longitudinal momentum generating ΔC_p and the transverse momentum through the gap that modifies ΔC_p in the vicinity of the wing tip.

As explained by Rains[125], an additional element in this equilibrium is the viscous friction at the wing surface. If e denotes the thickness of the wing, and supposing the flow is laminar, for small ratio τ/e, the flow through the gap can be modelled as a channel flow. On that basis, viscosity at the wall induces an adverse pressure gradient equal to

$$\frac{\Delta p}{1/2\rho U_\infty^2} = \frac{24\nu e}{\tau^2 U_\infty}\frac{U_t}{U_\infty} \tag{7.2}$$

Following Rains[125], this introduces a Reynolds number $Re_e = \dfrac{\tau^2 U_\infty}{24\nu e}$ which evaluates the influence of viscosity in the transverse flow through the gap. The gap at which the pressure difference imposed by the wing lift and the counter pressure gradient imposed by viscosity balance each other is $\tau = 0.1\%$. That means that the effect of the wall viscous friction can be neglected in all cases investigated here since $\tau > 1\%$.

7.1.3 Characteristics of the tip vortex

Vortex parameters

The vortex is defined by its strength Γ, its radius a, its swirl number q and the coordinates (x_c, y_c) of its center in the transverse plane. The vortex center is taken at the maximum of axial vorticity Ω_z. The vortex radius a is taken as the averaged distance between the vortex center and the maximum of tangential velocity. The circulation is calculated by integrating the axial vorticity over a disc centered on (x_c, y_c) and truncated at the symmetry line $y = 0$. The swirl q is defined in (2.4). Recall that it is given by

$$q = \frac{\Gamma}{2\pi a \Delta U_z} \tag{7.3}$$

where $\Delta U_z = U_z(x_c, y_c) - U_\infty$. In addition we use the distance $b = 2y_c$ corresponding to the distance between the two vortices either in the vortex pair (C1) or in the vortex image (C2) model.

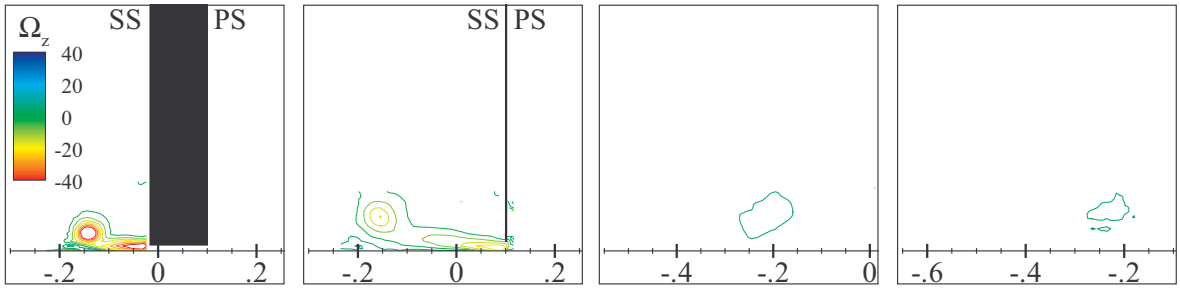

(a) $\tau = 1\%$

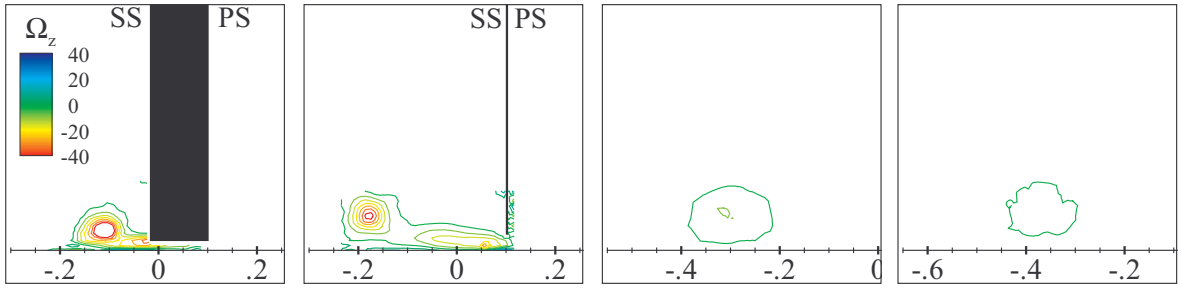

(b) $\tau = 2\%$

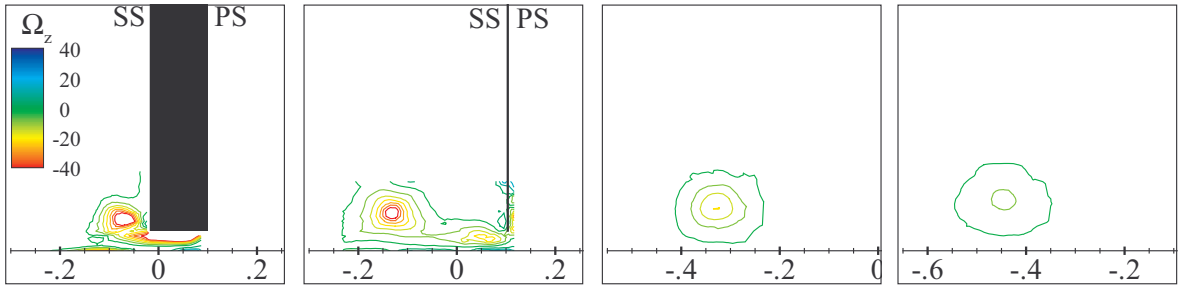

(c) $\tau = 4\%$

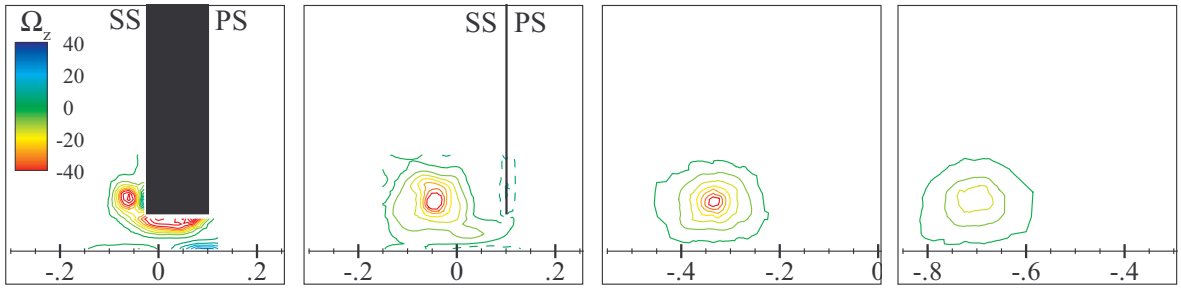

(d) $\tau = 7.5\%$

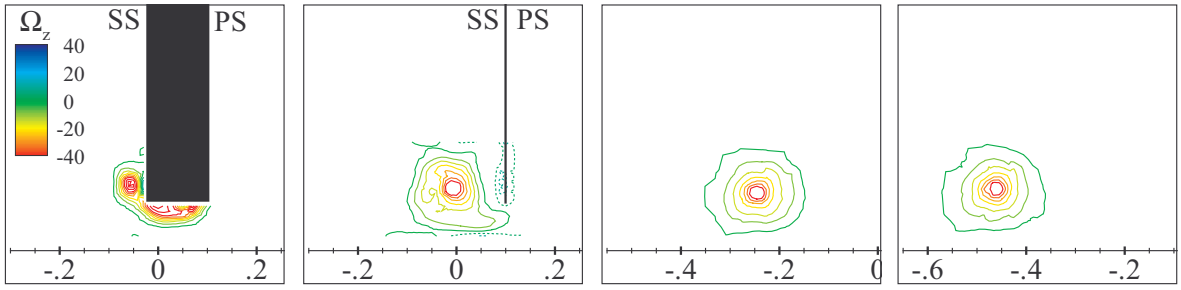

(e) $\tau = 10\%$

Figure 7.2: Mean axial vorticity Ω_z at several values of τ and several axial positions (configuration C1). From left to right: $z = -0.5$, $z = 0$, $z = 1$ and $z = 2$. Same iso-contours are used in all the frames. No sensing within the gap is done at $\tau = 1\%$ due to the lack of space (note that the probe diameter is 0.75% of the chord).

Initial position

Figure 7.2 shows the axial vorticity field for different τ in several transverse planes corresponding to $-0.5 \leq z \leq 2$. Note that the same contour levels are used in all the frames of the figure in order to ease comparisons.

We first look at the flow in the transverse plane at $z = -0.5$ where the position of the tip vortex 1 is seen to vary significantly with τ. At small gaps the leakage flow is nearly perpendicular to the chord. This suggests that the flow through the gap is channelled by the gap, in agreement with the channel flow model discussed earlier for small τ. The vortex forms far from the wing in the x direction and close to the tip in the y direction. At larger gaps, the opposite occurs: the vortex forms closer to the wing in the x direction and further from the tip in the y direction. These observations agree with those of Lakshminarayana[88].

Longitudinal evolution

The evolution of the vortex downstream of the trailing edge shown in figure 7.2 indicates a clear distinction between the vortex generated at small and large gaps. At small gap the vorticity is seen to decrease rapidly downstream, as indicated by the loss of contour levels whereas at large gap the vorticity is conserved. Another remarkable evolution is the displacement of the vortex in the x direction and almost zero displacement in the y direction. In order to visualize this displacement, the range in x is kept constant in every column of the figure, with only one exception at $\tau = 7.5\%$ and $z = 2$. In this case the transverse displacement is too large compared to the other cases and need an adjustment. In the following we investigate this "drifting" motion of the vortex.

Drifting motion

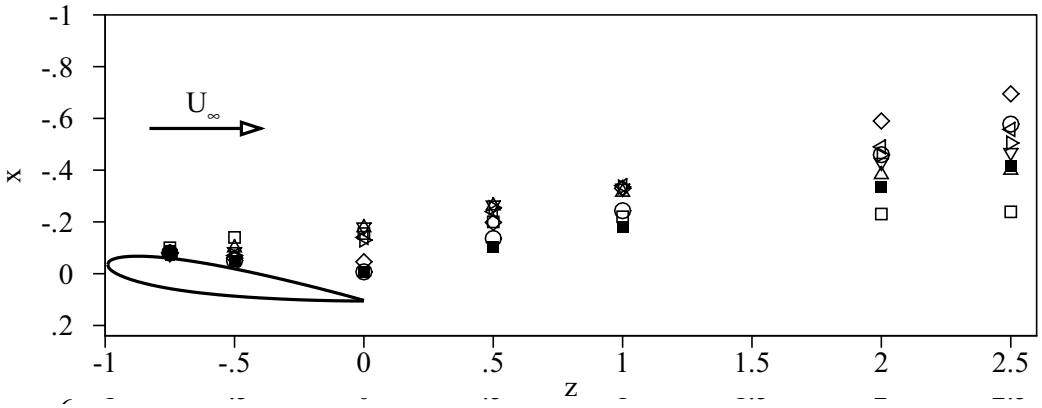

Figure 7.3: Trajectory of the tip vortex in the (x, z) plane for the different τ (conf. C1). □ $\tau = 1\%$. △ $\tau = 2\%$. ▽ $\tau = 3\%$. ▷ $\tau = 4\%$. ◁ $\tau = 5\%$. ◇ $\tau = 7.5\%$. ○ $\tau = 10\%$. ■ $\tau = 12.25\%$.

The motion of the vortex pair results from the induced velocity imposed by each vortex of the pair upon the other. For two point vortices, this drift velocity reads

$$U_{drift} = \frac{\Gamma}{2\pi b} \tag{7.4}$$

Figure 7.3 shows the trajectory of the vortex in the plane (x, z) for several τ. Note that in this chapter the vortex center (x_c, y_c) in transverse planes corresponds to the maximum of axial vorticity Ω_z. As observed in figure 7.2 maximum drift occurs at $\tau = 7.5\%$. Figure 7.4 shows the prediction of the drift velocity, based on (7.4) and on the measurement of Γ and b. This

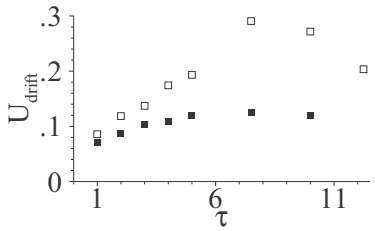

Figure 7.4: Drift velocity at $z = 2$, prediction based on the inviscid formula $U_{drift} = \Gamma/2\pi b$. □: C1, ■: C2.

figure confirms the maximum drift at $\tau = 7.5\%$. This maximum results from the decrease of the vortex circulation Γ at large gaps and of the simultaneous increase of b. Measurement of these quantities are shown in the next paragraph. At small gaps, the drift increases with the gap because b remains almost constant whereas Γ increases linearly.

Appendix D is dedicated to the calculation of the impulse of a vortex in the vicinity of a wall and gives important results concerning the time variations of the vortex parameters such as the circulation Γ and the vortex center (x_c, y_c). It gives a demonstration of relation (7.4), which is well known. However when viscosity is taken into account, the complete relation for the drift velocity of the vortex reads (see appendix D)

$$\Gamma U_{drift} = -\int_{-\infty}^{+\infty} \frac{u_x^2}{2}|_{y=0} dx - \nu \int_{-\infty}^{+\infty} x \frac{\partial \omega}{\partial y}|_{y=0} dx \tag{7.5}$$

The first term in the RHS corresponds to the inviscid value of the drift velocity when $\nu \to 0$. The second term in the RHS corresponds to the viscous diffusion of vorticity at the mid-plane of the vortex pair. Its sign is positive since the axial vorticity decreases when $y > 0$. This term leads to a decrease of the drift velocity of the vortex compared to the inviscid case. In table 7.1

Table 7.1: Drift velocities at $z = 2$: comparison between the measurement and the inviscid prediction in C1 and C2. Percentages relate the measured value to the inviscid value.

	C1		C2	
τ	measurement	$\Gamma/2\pi b$	measurement	$\Gamma/2\pi b$
1%	0.06 (70%)	0.086	0.045 (65%)	0.070
7.5%	0.21 (65%)	0.320	0.080 (65%)	0.125
10%	0.20 (75%)	0.27	0.080 (67%)	0.120

we evaluate this reduction for three values of τ. As predicted by (7.5), the measured drift is always smaller than the inviscid prediction (7.4). This reduction represents approximately 30% of the inviscid value.

Vortex characteristics

The evolution of the characteristics of the vortex are investigated in the (τ, z) parameter space. Results are shown in figure 7.5. The evolution of the circulation Γ shown in figure 7.5(a) reveals two main trends. First, as noted by previous investigations of the tip leakage vortex (see Ma[102] and You[158]), Γ increases with τ. This is however not true at the two largest gaps. The increase is directly related to the increase in leakage mass flow rate when τ increases. The decrease at large gap is due to the decrease in Γ which results from the reduction of the wingspan. Lakshminarayana[88] shows that the lift does not change significantly when the gap is below $\tau \sim 6\%$, which explains why this reduction of wingspan does not affect the small τ regime. However at larger gaps, the present results suggest that the reduction of the wingspan becomes significant and reduces the vortex strength.

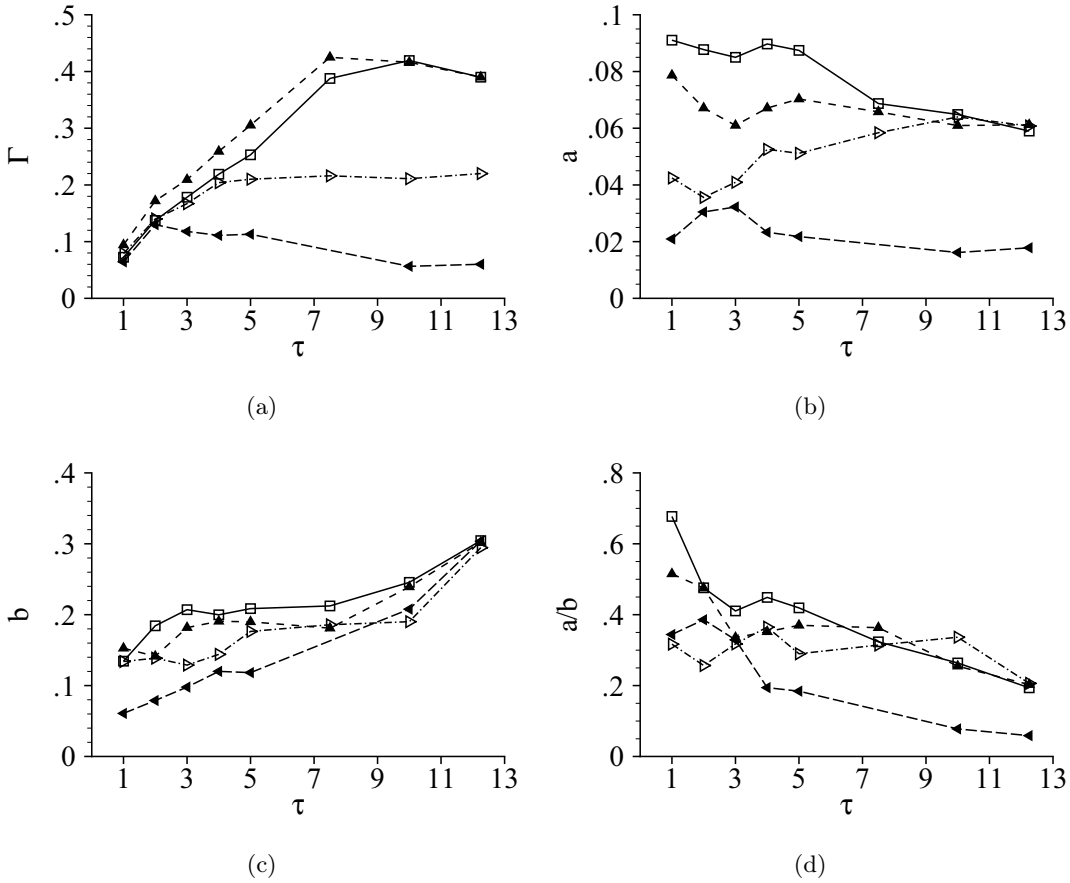

Figure 7.5: Vortex properties as a function of τ and z (conf. C1). ◀ $z = -0.5$. ▷ $z = 0$. ▲ $z = 1$. □ $z = 2$. (a) Vortex circulation, (b) radius a. (c) distance between vortex centers b, (d) vortex aspect ratio a/b.

Secondly, at constant τ, we observe that Γ increases at first and then slightly decreases in the axial direction, except at $\tau \geq 10\%$. The initial increase corresponds to the rolling-up regime of the vortex during which axial vorticity is continuously added to the tip vortex. There are two hypothesis to explain the subsequent decrease. The first one is based on viscous diffusion at the symmetry plane of the vortex pair, the equation for the time variation of Γ being, in 2D flows (see again appendix D)

$$\frac{d\Gamma}{dt} = -\nu \int_{-\infty}^{+\infty} \frac{\partial \omega}{\partial y} dx \tag{7.6}$$

This effect certainly explains part of the decrease, especially at small gaps, however the Reynolds number being large ($Re_c >> 1$), it is unlikely to explain the variations observed in the figure. The existence of the Crow instability in the flow put forward in chapter 8 suggests that the disruption of the vortices by this instability might explain these variations.

The evolution of the vortex radius a is shown in figure 7.5(b). The radius increases rapidly with z at large gaps, which is not the case at small gaps. Moreover, at the last axial position, there is a continuous decrease of a with τ. These variations correspond to two different regimes, that are analyzed further below.

The evolution of b is plotted in figure 7.5(c). As could be expected, b increases monotonously with τ. Slight deviations from linearity are observed though. In particular, b remains almost constant for $4\% < \tau < 8\%$. In the longitudinal direction, b increases significantly upstream of the trailing edge, especially at small τ, and becomes constant downstream.

The evolution of a/b is depicted in figure 7.5(d). Since b increases with τ, and because a is either constant or decreasing, the aspect ratio decreases as τ increases. Its value remains above 0.2 in all cases which is a large value in comparison to usual values found in single wing wakes ($a/b \sim 0.1$, see Fabre[43]).

7.1.4 Large/small gap regimes

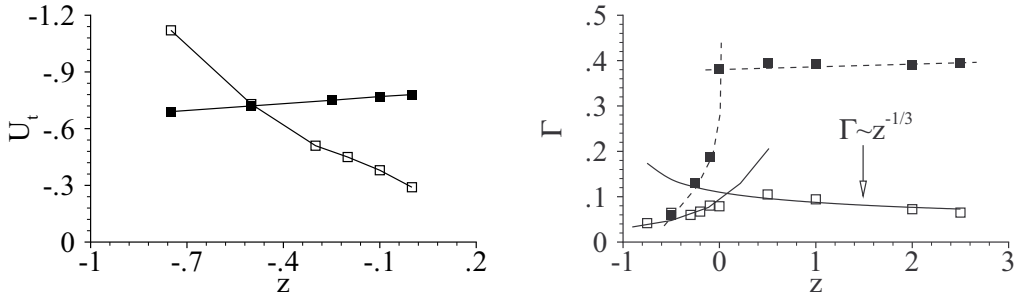

(a) (b)

Figure 7.6: Comparison between $\tau = 12.25\%$ (■) and $\tau = 1\%$ (□) as a function of the axial coordinate (conf. C1). (a) Maximum of transverse velocity of the flow emerging from the gap. (b) Circulation Γ of the tip vortex.

The previous observations suggest that two asymptotic regimes exist depending on τ. The formation of the tip vortex at large gap resembles the formation of a trailing vortex at the tip of an isolated wing (see Bailey[12]). At small gap our results suggest that the vortex is formed by a mechanism analog to the roll-up of a jet in cross flow. A detailed characterization of such a flow is given by Jacquin[74]. This analysis is supported by several arguments based on the evolution of the flow at $\tau = 1\%$ and $\tau = 12.25\%$. First, figure 7.6(a) shows that the transverse velocity U_t evolves quite differently at $\tau = 1\%$ and $\tau = 12.25\%$. At $\tau = 1\%$ there is a strong

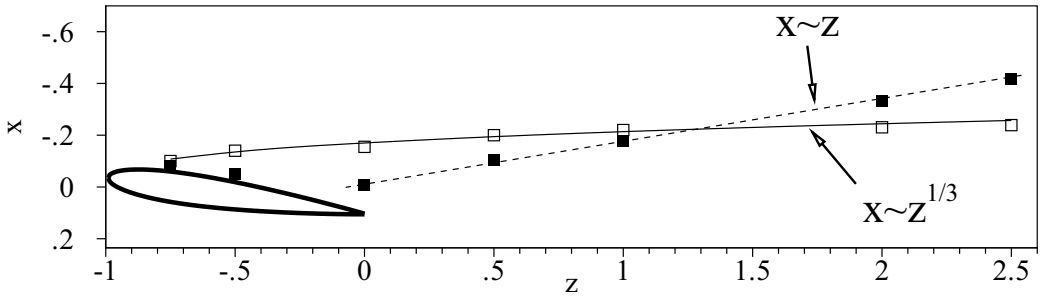

Figure 7.7: Vortex trajectory (conf. C1): comparison between $\tau = 12.25\%$ (■) and $\tau = 1\%$ (□).

transverse velocity close to the leading edge that then decreases monotonously downstream while at $\tau = 12.25\%$ the transverse velocity is lower and almost constant along the chord. This suggests that the vortex at $\tau = 1\%$ forms earlier than at $\tau = 12.25\%$. This was confirmed by looking at the vorticity field in a transverse plane at $z = -0.75$ (not shown) in which the vortex at $\tau = 1\%$ appears stronger than at $\tau = 12.25\%$, suggesting an earlier formation. This difference can be explained as follows: at small gap the pressure difference ΔC_p between the two sides of the wing is less modified than at large gap because less fluid is entrained into the gap. The peak ΔC_p over a NACA12 airfoil is very close to the leading edge (see part 4), therefore the leakage is very strong at this location when τ is small. We see that this results in a transverse

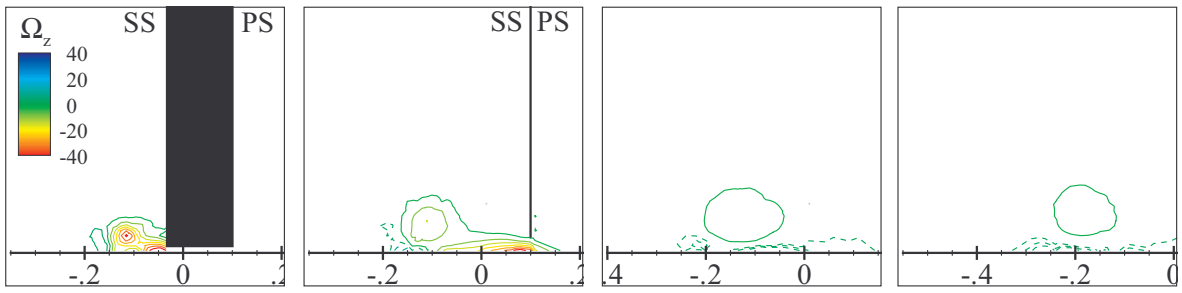

(a) $\tau = 1\%$

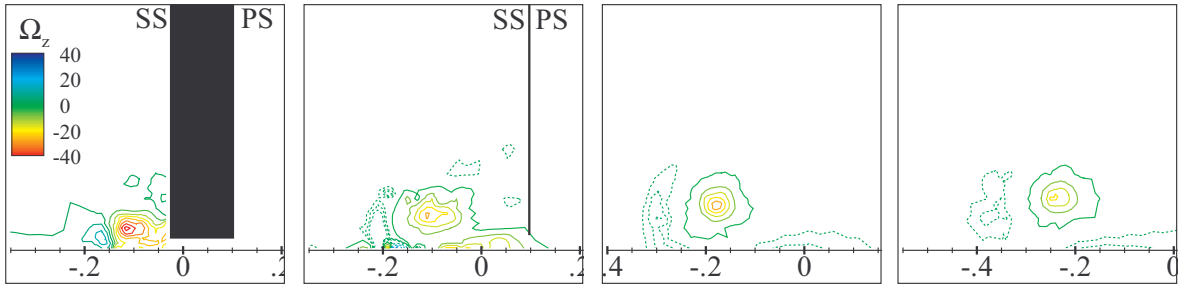

(b) $\tau = 2\%$

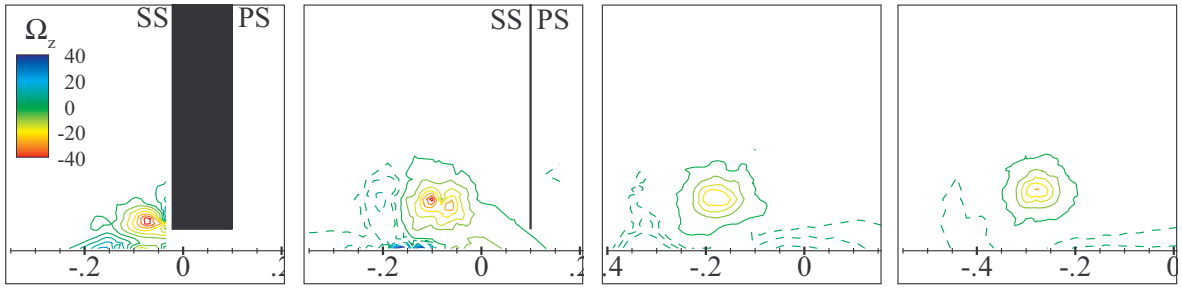

(c) $\tau = 4\%$

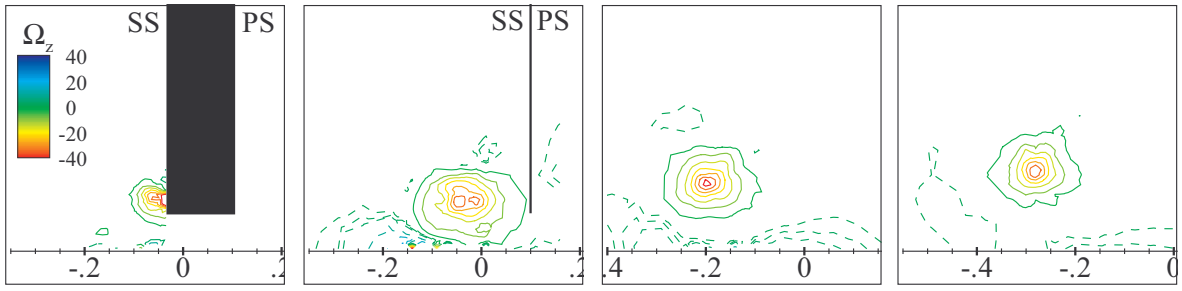

(d) $\tau = 7.5\%$

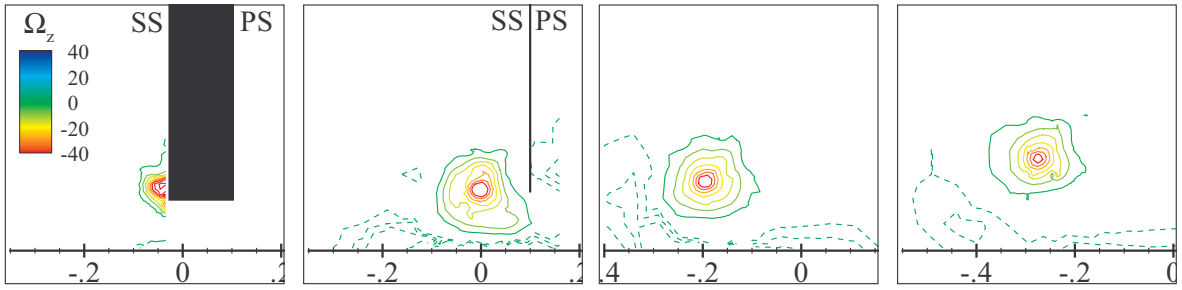

(e) $\tau = 10\%$

Figure 7.8: Mean axial vorticity at several values of τ and several axial locations (conf. C2). From left to right: $z = -0.5$, $z = 0$, $z = 1$ and $z = 2$. Same iso-contours as 7.2 are used in all the frames.

velocity about 20% larger than the free stream velocity. At large gap, the distribution of ΔC_p is significantly smoothed at the tip because of the large deviation of the streamlines in the wing tip regions. Therefore the leakage is more uniform which explains the low variation of the transverse velocity in this case.

The trajectories of the vortex in the two extreme cases $\tau = 1\%$ and $\tau = 12.25\%$ are depicted in figure 7.6. Jacquin[74] shows that the trajectory of the vortices issued from a jet in cross-flow follows a power law of exponent 1/3. This compares favorably with the experimental results at $\tau = 1\%$. Conversely, the trajectory of a trailing vortex (see relation (7.4)) follows a linear law with the axial distance and we see that the experimental results follow this trend. Looking at the evolution of the circulation Γ in figure 7.6(b), we see that at the larger gap the circulation increases up to the trailing edge and then becomes constant whereas at the smaller gap the vorticity also increases but starts decreasing as soon as it is free of the wing influence. This decrease is in satisfactory agreement with the power law of exponent $-1/3$ given by Jacquin[74].

7.2 Influence of the splitter plate

7.2.1 Evolution of the vorticity

Figure 7.8 shows the evolution of the vorticity in the flow in C2. The flow bears similar trends with the flow in C1. Indeed we observe a rapid decrease of the vorticity contained in the tip leakage vortex when τ decreases. At large gaps, the vorticity is conserved and there is a drifting motion of the vortex in the transverse direction. Concerning the initial position of the vortex, we see that at small gaps the vortex forms far from the wing and close in the y direction, again. Also, opposite trends are obtained at large gaps. However we can point out several important differences:

i- The drifting motion is attenuated by the splitter plate

ii- There is formation of secondary vorticity at the wall that is rolled-up by the tip vortex.

In the following we analyze these differences

7.2.2 Drifting motion

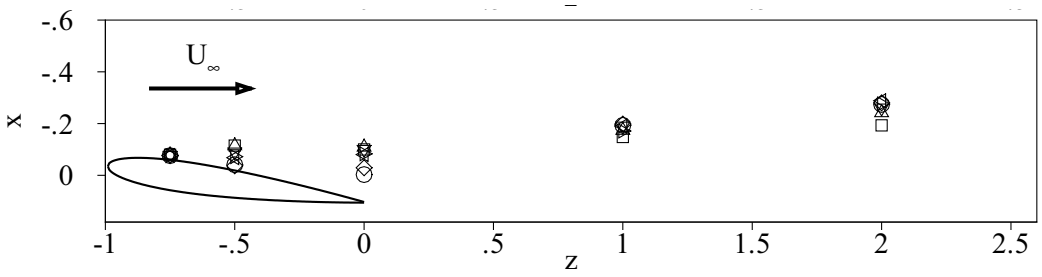

Figure 7.9: Trajectory of the tip vortex (conf. C2). Same legend as figure 7.3.

Figure 7.9 shows the trajectories of the tip vortex with the splitter plate. We observe that, compared to configuration C1, the drifting motion is strongly attenuated. This results in trajectories that are very similar when τ varies. Replacing the wall by an image vortex (see appendix D), we can use (7.4) to evaluate the drift velocity of the vortex. This is done in figure 7.4, in which the curve confirms the observation of the vortex trajectory, with, in particular, a maximum drift occurring at $\tau = 7.5\%$. We shall see in the next section that b is large in C2 due to a rebound effect, which, based on (7.4), explains why the drift is small in C2. Viscous friction at the wall reduces further the drift, which accounts for the difference

between the measured drift and that predicted by (7.4), which is illustrated in table 7.1 for three different τ. Like in C1, the reduction amounts to about 30% of the inviscid value.

7.2.3 Vortex rebound

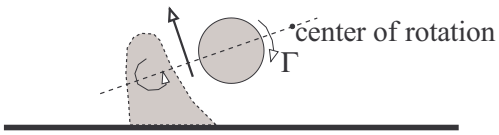

Figure 7.10: Schematic of the rebound effect induced by secondary vorticity at the wall.

The no-slip boundary condition at the wall provokes the creation of a transverse boundary layer with opposite signed axial vorticity (here again, details are given in appendix D). This secondary vorticity develops downstream of the wing for all values of τ. We observe in figure 7.8 that it is rolled-up by the tip vortex. The resulting flow is schematized in figure 7.10. The center of rotation of the vorticity being at the right of the tip vortex, the whole vorticity is entrained in the upper left direction, which corresponds to the rebound of the vortex.

7.2.4 Vortex characteristics

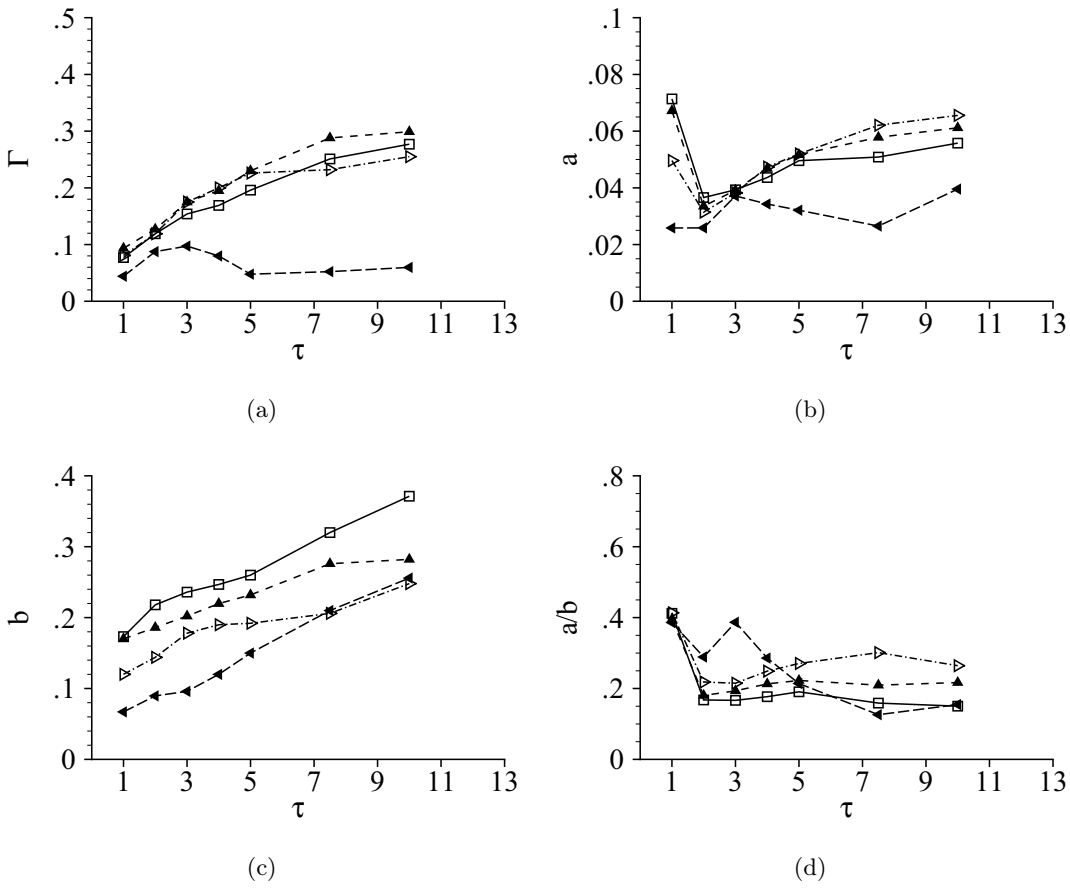

Figure 7.11: Vortex properties as a function of τ and z (conf. C2). ◀ $z = -0.5$. ▷ $z = 0$. ▲ $z = 1$. □ $z = 2$. (a) Vortex circulation, (b) radius a. (c) distance between vortex centers b, (d) vortex aspect ratio a/b.

The characteristics of the vortex in C2 are described in figure 7.11. The evolution of the circulation Γ is shown in figure 7.11(a). Downstream of the wing trailing edge, the circulation increases steadily with τ, as a result of the increased mass flow rate through the gap. As a function of z, the maximum circulation is obtained at $z = 1$. The formation of secondary vorticity at the wall may explain the subsequent reduction between $z = 1$ and $z = 2$. In chapter 8 we will see that the flow in C2 is less unsteady than C1 (in particular, the Crow instability does not occur) therefore the disruption of the flow can not be hypothesized to explain the decrease of the circulation.

In figure 7.11(b) showing a, two regimes can be distinguished. For $\tau < 4\%$, the vortex radius increases with z and decreases with τ. In this range of τ the wing tip is immersed in the boundary layer of the splitter plate ($\delta_{0.99} = 4\%$ of chord at the wing LE). The increase in a could come from the contribution of the horse shoe vortex which must form at the LE of the wing after tilting of the boundary layer vorticity, even when the gap is not completely closed (this horse shoe vortex is observed when the gap is completely closed). The strength of this horse shoe vortex would a priori increase as τ is decreased. If this is true then the vortex observed in the transverse planes may be the horse shoe vortex or the merging of the tip leakage vortex with the horse shoe vortex, which could thereby explain the radius variations. However, this hypothesis was not further investigated. A second regime corresponds to $\tau > 4\%$. In this case, the radius a increases for $0 < z < 1$ and then decreases. A monotonic increase is found as a function of τ. This probably results from the larger leakage mass flow when the gap is enlarged. The decrease of a with z remains however a matter of controversy. It is suggested that it may be related to the interaction with the secondary vorticity during the rebound.

The evolution of b depicted in figure 7.11(c) agrees well with the description of the rebound of the vortex since b increases at all τ. Moreover the parallelism of the curves corresponding to the different z suggests that the rebound is proportional to the initial distance from the wall. The simultaneous increase of a and b results in an aspect ratio of the dipole formed by the tip leakage vortex and its image about the splitter plate almost constant with τ and z, see figure 7.11(d). This mean value is $a/b \sim 0.2$.

7.3 Comparison between C1 and C2

7.3.1 Vortex properties

Figure 7.12 compares the vortex properties between C1 and C2 at $z = 2$. Figure 7.12(a) shows that the difference in vortex circulation increases with τ, the vortex in C1 being slightly stronger than in C2. At $\tau = 1\%$ the two vortex are equally strong, which may again be related to the possible formation of a horse-shoe vortex. The existence of this vortex is supported by the subsequent evolution when τ is increased since up to $\tau = 4\%$, which corresponds to the value of $\delta_{0.99}$ at the wing LE, the difference between C1 and C2 remains small. For $\tau > 4\%$ the vortex in C1 becomes however significantly stronger than in C2.

Figure 7.12(b) presents the comparison of a. The vortex width is smaller in C2 when τ is small but becomes similar when τ is large. At small τ the interaction between the vortex and the splitter plate, especially the induced boundary layer, may explain these differences. However, as was said earlier, this interaction is not well understood. At large gap, the similarity between the two flows results from the weaker influence of the splitter plate.

The comparison of b, shown in figure 7.12(c), which exhibits larger value in C2 than in C1, traduces the effect of the vortex rebound. Interestingly, the effect of the rebound is felt even at large gaps. This results in the absence of convergence of the results in this limit. Finally, as a consequence of the evolution of a and b, the aspect ratio of the vortex pair is also lower in C2 than in C1, see figure 7.12(d).

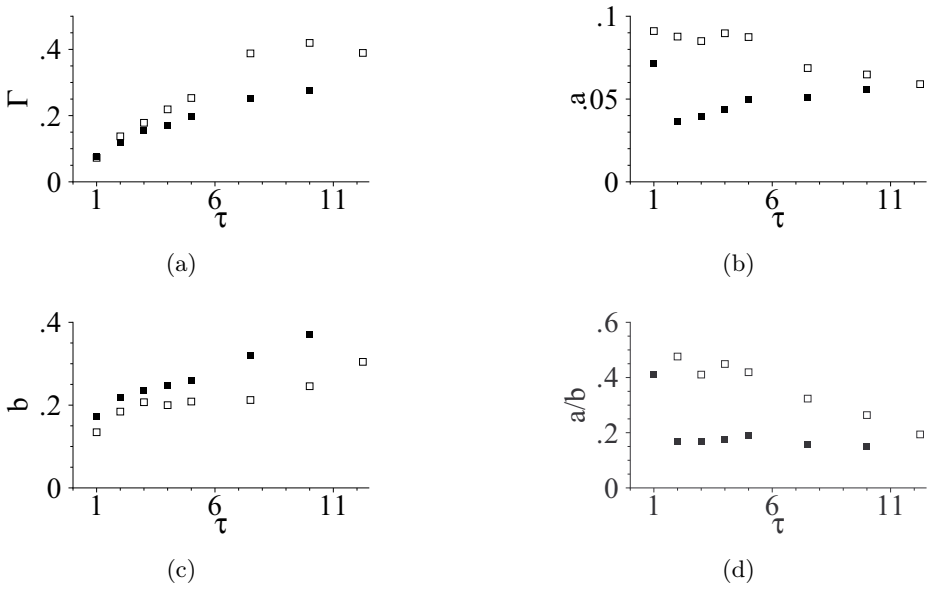

Figure 7.12: Comparison of the vortex properties between C1 and C2 as a function of τ at $z = 2$. □: C1, ■: C2. (a) Circulation, (b) vortex radius, (c) distance b, (d) vortex aspect ratio.

7.3.2 Flow stability

Axial flow

As seen in chapter 3, an important parameter for the stability of vortices is the swirl number q (see definition in (2.4). In figure 7.13(b) we present the evolution of the inverse of q as a function of τ in C1 and C2 at $z = 2$. In these two configurations the swirl number increases with τ up to $\tau = 7.5\%$ and then decreases. Figure 7.13(a) shows the corresponding difference of axial velocity between the vortex center and the free stream. When $\tau < 7.5\%$ the axial velocity in the core is wake-like and becomes jet-like for larger τ.

Vortices are known to be unstable to strong inviscid instabilities for $q^{-1} > 0.6$ (see chapter 2). This limit is depicted in the figure. The flow C1 at $\tau < 3\%$ and the flow C2 at $\tau < 6\%$ are prone to develop such instabilities. It is possible that the strong decrease of the vortex at small gap might be explained by this unstable mechanisms.

Cooperative instabilities

Figure 7.13(c) shows the time scale t_b (see definition (2.27)) of the cooperative instabilities (Crow, Widnall) as a function of τ at $z = 2$. Multiplying t_b by c/U_∞ transforms time into longitudinal distance (in chord c). Cooperative instabilities are likely to develop in the tip vortex due to the presence of a second vortex in configuration C1 and due to the influence of the splitter plate in configuration C2. The mean values of t_b in the two configurations are respectively $t_b \sim 1.2$ and $t_b \sim 2.5$ so that cooperative instabilities are more likely to develop in C1 than in C2. The larger value of b obtained in C2 due to the rebound effect and the fact that b is squared in (2.27) explain this difference. The development of the Crow instability is investigated in great details in chapter 8.

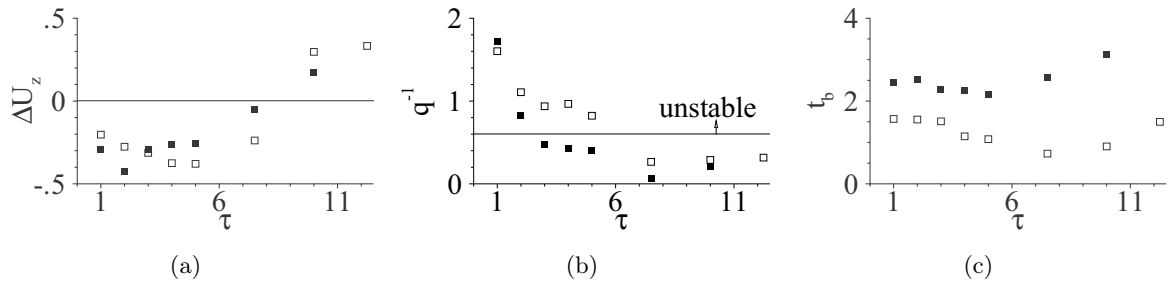

(a) (b) (c)

Figure 7.13: Comparison of the vortex properties regarding stability between C1 and C2 as a function of τ at $z = 2$. □: C1, ■: C2. (a) axial velocity difference $\Delta U_z = U_z(x_c, y_c) - U_\infty$, (b) inverse of the swirl number. The horizontal line corresponds to the neutral condition $q^{-1} = 0.6$. (c) Time scale t_b of cooperative instabilities.

7.4 Losses due to the tip leakage flow

7.4.1 Governing equation

Loss is commonly defined as an increase of entropy, see Denton[38]. Variations of entropy are described by the following relation

$$T_i ds = dH_i - \frac{1}{\rho} dP_i \tag{7.7}$$

with $h_i = e + \frac{1}{2}u^2 = C_p T_i$ the enthalpy, and subscript i indicating stagnation quantities. Sources of entropy in incompressible flows are viscous effects in regions where velocity gradients are non-zero (boundary layers, flow mixing) and heat transfers across temperature differences as shown by the following relation derived from the second law of thermodynamics and the conservation of mass and internal energy

$$\rho \frac{ds}{dt} = -div\left(\frac{\boldsymbol{q}}{T}\right) + \frac{2\mu \boldsymbol{d} : \boldsymbol{d}}{T} - \frac{\boldsymbol{q} \cdot \boldsymbol{grad}\, T}{T^2} \tag{7.8}$$

Here $\boldsymbol{q}$ is the heat flux across the flow domain (remember that for two tensors A and B, $A : B = \sum_i \sum_j A_{ij} B_{ji}$) and $\boldsymbol{d}$ is the deformation tensor. Note that this relation is classical and is usually found in manuals. The first term in the RHS of (7.8) describes the heat exchanged between the fluid particles and the surroundings. The second term is the creation of entropy by viscous friction and the third term corresponds to heat production by temperature gradients inside the flow.

To evaluate the losses corresponding to the tip leakage flow, we integrate (7.7) over a portion of a stream tube between an upstream section S_1 transverse to the free stream where far field conditions apply and a downstream transverse section S_2, at a given z. Assuming that there is no heat transfer at the boundaries (hence $dh_i = 0$), one has

$$T_i ds = -\frac{1}{\rho} dP_i \tag{7.9}$$

After integration, using mass conservation between S_1 and S_2, one gets

$$T_i \int_{S_2} U_z \Delta s dx dy = -\frac{1}{\rho} \int_{S_2} U_z \left(P_{i\,0} - P_i\right) dx dy \tag{7.10}$$

Writing this expression in terms of mass averaged quantities finally gives

$$\frac{T_i}{1/2 U_\infty^2} \Delta s^m = C_{pi}^m \tag{7.11}$$

where the superscript ^{m} denotes the mass averaged quantity

$$A^m = \frac{\int_S U_z A dx dy}{\int_S U_z dx dy} \tag{7.12}$$

and $C_{pi} = \dfrac{P_{i\,0} - P_i}{1/2\rho U_\infty^2}$ is the stagnation pressure coefficient. Relation (7.11), well known in internal flows (see Greitzer[59]), states that the loss of entropy is readily evaluated by the mass averaged stagnation pressure loss coefficient.

7.4.2 Observation of the pressure losses

Contours of C_{pi} at several transverse planes and different τ are depicted in figures 7.14 and 7.15 for configurations C1 and C2, respectively. These measurements allow us to identify the following regions where losses occur

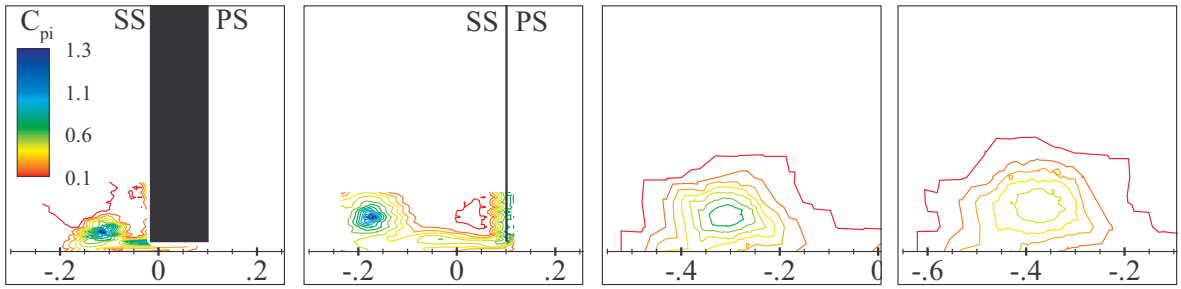

(a) $\tau = 2\%$

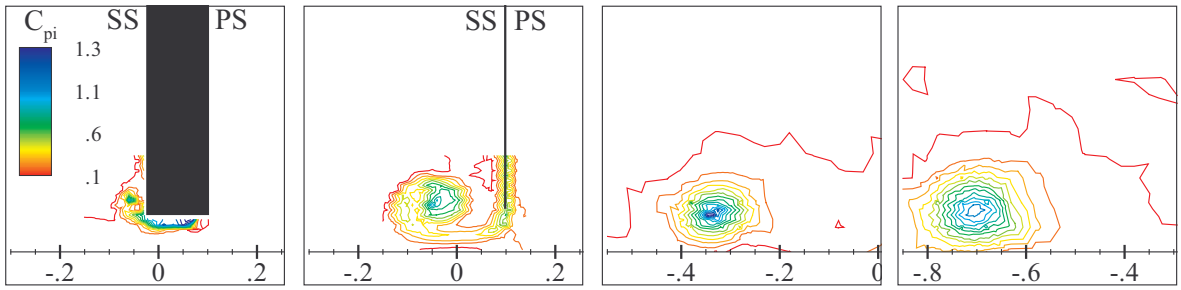

(b) $\tau = 7.5\%$

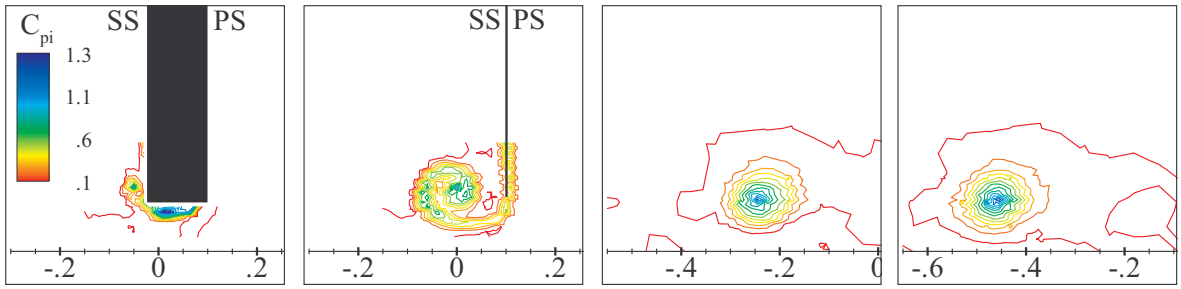

(c) $\tau = 10\%$

Figure 7.14: C_{pi} at several τ and different axial locations (conf. C1). From left to right: $z = -0.5$, $z = 0$, $z = 1$ and $z = 2$. The same iso-contours are used in all the frames.

i- At the **wing trailing edge**, the two boundary layers formed at the surfaces of the wing merge and form a zone of low stagnation pressure. In addition there is a base pressure at the TE due to the non zero thickness of the geometry there that likely increases loss (see Greitzer[59]).

ii- **Flow separation** occurs at the wing tip surface due to the sharp corners of the geometry. Large values of the stagnation pressure coefficient are found there.

iii- In configuration C2, entropy is also generated in the **splitter plate boundary layer**. The existence of this loss is the main difference between the two configurations C1 and C2. In figure 7.15, one can observe that the losses are large close to the surface and decrease upward. Right below the tip vortex, the stagnation pressure decreases due to flow acceleration. When the gap increases, the vortex strengthens and entrains the high stagnation pressure fluid contained in boundary layer. This shows that there is a strong coupling between the loss from the tip vortex and the loss from the boundary layer.

iv- The **shear layer** between the leakage flow and the mainstream causes strong pressure loss. This shear layer rolls-up into the **tip vortex**. At large gaps, loss contained in the tip vortex is transported downstream. At small gaps it is strongly diffused by viscosity.

It is interesting to look at the evolution of C_{pi} in the vortex core. We observe in figure 7.14 and 7.15 a decrease of C_{pi} with z at small gaps and an increase at large gaps. In the following we show that these variations are correlated to the jet-like or wake-like form of the axial velocity profile in the core. We start from the equation for the z-component of velocity in cylindrical coordinates at the vortex center

$$\rho U_z \frac{\partial U_z}{\partial z} = -\frac{\partial P}{\partial z} + \nu \left(\frac{1}{r} \frac{\partial}{\partial r} \left(r \frac{\partial U_z}{\partial r} \right) + \frac{\partial^2 U_z}{\partial z^2} \right) \tag{7.13}$$

Introducing $P_i = P + 1/2\rho U_z^2$ in this relation shows that the evolution of C_{pi} at the vortex center is ruled by viscous diffusion. This diffusion term can be simplified by neglecting the axial variations in front of the radial one, as in the Batchelor vortex model (Batchelor[14]). This gives

$$\frac{\partial P_i}{\partial z} = \nu \frac{1}{r} \frac{\partial}{\partial r} \left(r \frac{\partial U_z}{\partial r} \right) = -\nu \frac{1}{r} \frac{\partial}{\partial r} \left(r \Omega_\theta \right) \tag{7.14}$$

where Ω_θ denotes the azimuthal mean vorticity. This equation states that the axial variations of the total pressure depends only upon the sign of the variations of $r\Omega_\theta$. In a jet (wake) type vortex, Ω_θ is positive (negative) and nil at the axis. The derivative is hence positive (negative) and the stagnation pressure decreases (increases). These variations are confirmed by the experiments, see figure 7.16(a), where the values of C_{pi} are plotted as a function of ΔU_z. The scatter mainly occupies the upper right and lower left quadrants, thus relating increase (decrease) of C_{pi} with jet (wake) flow.

The physics of this evolution is the following. The C_{pi} of flow particles at the vortex axis varies due to viscous friction in the core of the flow. In the case of a jet, the flow in the core entrains the surrounding fluid, which results in a loss of energy corresponding to an increase of C_{pi}. In the case of the wake, it is the surrounding fluid that entrains the core axial flow which therefore receives energy and exhibits a decrease of C_{pi}.

7.4.3 Influence of τ on the mass-averaged loss

Large gaps are known to be detrimental in terms of loss. This was proven in particular by Bae[10] and Storer[147]. These authors show that C_{pi}^m increases linearly with τ.

The evaluation of the stagnation pressure loss coefficient C_{pi}^m at $z = 2$ is depicted in figure 7.16(b). The domain of integration is the same for all τ and includes the tip vortex and the boundary layer at the splitter plate. We see that C_{pi}^m increases linearly when $\tau \leq 5\%$, in agreement with the studies of Bae[10] and Storer[147]. The fact that the increase is linear suggests that the primary mechanism of loss is the mixing of the leakage flow with the mainstream. A simple model of mixing concerning injected flow with a mainstream flow proposed in Greitzer[59] shows that the increase in pressure loss is linear with the mass flow rate of the

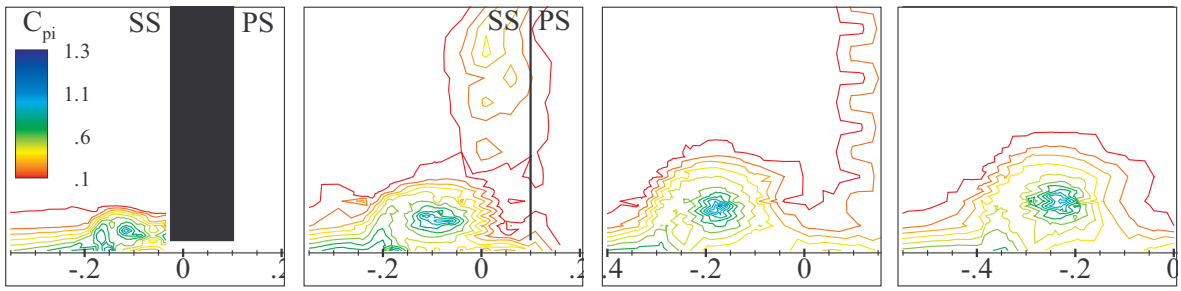

(a) $\tau = 2\%$

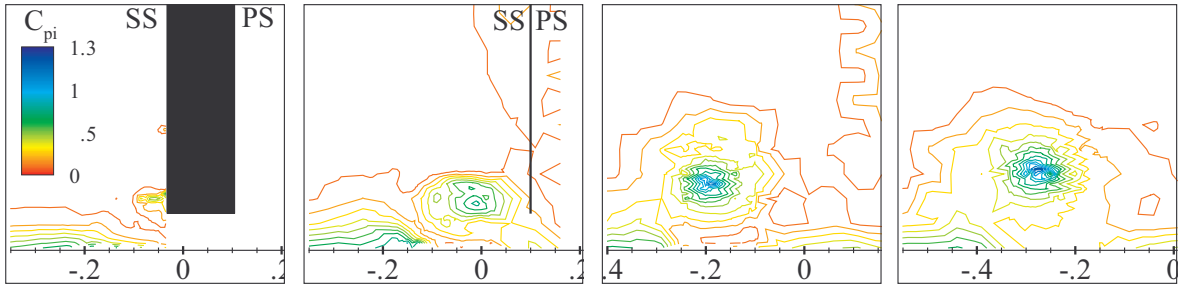

(b) $\tau = 7.5\%$

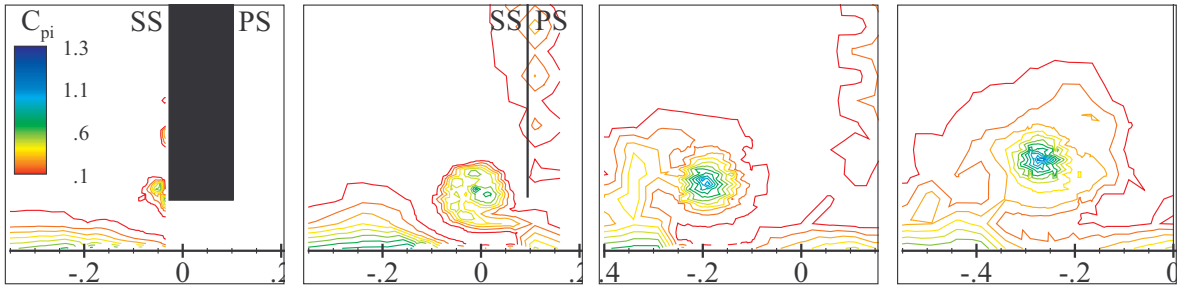

(c) $\tau = 10\%$

Figure 7.15: C_{pi} at several τ and different axial locations (conf. C2). From left to right: $z = -0.5$, $z = 0$, $z = 1$ and $z = 2$. The same iso-contours as in figure 7.14 are used in all the frames.

injected flow, providing this mass flow rate remains small. This condition is fullfilled here since at small gap the leakage mass flow rate remains small. Moreover the linear increase of the leakage mass flow rate with τ, although not proven here, seems reasonable and the other sources of loss identified earlier (boundary layer, corner separation, base pressure) are not expected to be strongly modified when the gap is varied. As a consequence the increase in leakage mass flow rate is the primary mechanism leading to increased loss.

When $5\% < \tau < 8\%$ losses decrease however. This evolution is not documented in the literature, because usual gap sizes considered are those found in turbo machineries ($\tau \sim 1\% - 4\%$). The most probable scenario for this decrease, based on the previous analysis at small gaps implying mixing as a dominant mechanism, is that the leakage mass flow rate does not increase anymore when $\tau > 5\%$ and even decreases. This is supported by the fact that, when τ increases, part of the gap region becomes occupied by the mainstream. Moreover the modification of the pressure distribution at the tip may also lead to a decrease in the leakage mass flow rate. The fact that the decrease is much smaller in C2 than in C1 is likely the consequence of the additional loss produced by the entrainment of the induced boundary by the vortex in C2.

Figure 7.16(b) also shows that a constant difference exists between the loss measured with splitter plate and that measured without, in the small gap regime. Losses with the splitter plate

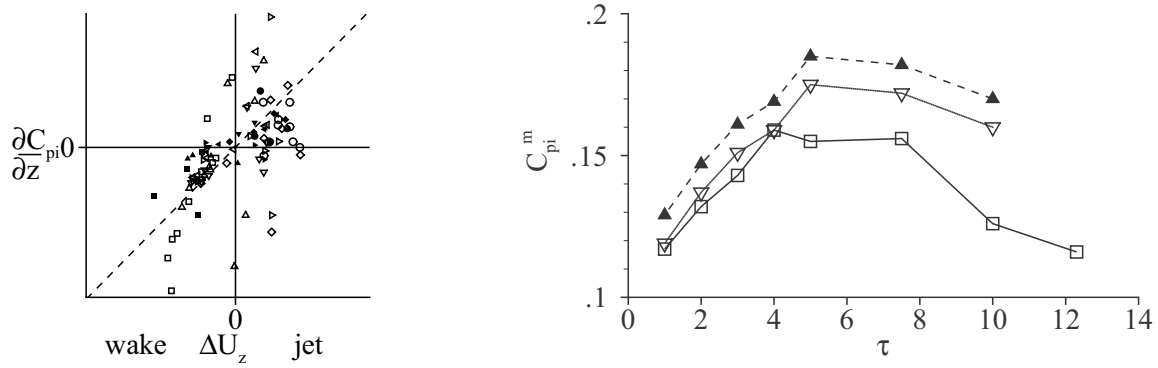

(a) (b)

Figure 7.16: (a) Stagnation pressure coefficient versus the jet/wake axial velocity profile. open symbols: C1. plain symbols: C2, (b) mass averaged stagnation pressure loss C_{pi}^{m} versus τ at $z = 2$. □: C1. ▲: C2. ▽ boundary layer correction in conf. C2.

includes those produced by the boundary layer so, in order to compare the two configurations C1 and C2 on a similar basis, we must evaluate the loss corresponding to the boundary layer in C2 and subtract it from the total loss. Entropy production in boundary layers is related to a dimensionless parameter called the dissipation coefficient C_d, see Denton[38]. This parameter varies with the Reynolds number Re_θ based on the momentum thickness as

$$C_d = 0.0056 Re_\theta^{-1/6} \tag{7.15}$$

This law is a good approximation for $Re_\theta > 1000$ for a constant pressure boundary layer. Here $Re_\theta = 2000$ at the wing leading edge so this law is adequate. According to the formula given in Denton[38], the mass averaged pressure loss coefficient associated to the boundary layer is

$$C_{pi,\,bl}^{m} = 2 C_d \Delta x \Delta z \tag{7.16}$$

where Δx is the transverse length of the boundary layer taken into account and Δz is the length over which the boundary layer develops. The curve corrected by this effect is shown in figure 7.16(b). There is a good agreement of the corrected curve with the curve of the flow in C1 at small τ. This is interesting because it shows that, at small gaps, the effect of the boundary layer on loss production is linear, and can hence be substracted from the total loss to isolate the contribution of the vortex, whereas at large gaps, the contribution of the boundary layer is non-linear and produces additional loss by cooperation with the vortex (mainly entrainment of the boundary layer around the vortex).

Conclusion

The tip leakage vortex was investigated by means of an experimental apparatus comprising two configurations. The effect of the gap size was investigated in order to describe the vortex mean properties. At small gap the vortex decays rapidly downstream while it is conserved at large gaps. Comparing the two configurations, we found that C1 produces a vortex pair of large aspect ratio, which exhibits an important drifting velocity. The vortex in configuration C2 is characterized by a smaller drift and rebounds at the surface of the splitter plate. It is also slightly weaker than the vortex in C1. In the end we evaluated the stagnation pressure loss downstream of the tip clearance gap and found a linear increase in the range of small gaps, and a stagnation/decrease at larger gaps. For the continuation of the present work, we also evaluated t_b in C1 and C2 and showed that cooperative instabilities are more likely to develop

in C1. Therefore in the following chapter 8 dedicated to the study of the Crow instability, we focus on the flow in C1.

8 Experimental analysis of the Crow instability

This chapter deals with the investigation of the Crow instability in the tip vortex. According to the mean value of t_b (see definition (2.27)) obtained at $z = 2$ in chapter 7 (see figure 7.13(c)), it was shown that the vortex in C1 (no splitter plate) is more likely to develop the Crow instability than the vortex in C2 (with splitter plate). This difference is explained by an increase of b obtained in C2 due to the vortex rebound phenomenon, which results in larger t_b. We also showed that in C1, the case $\tau = 7.5\%$ was the most favorable. We chose this case for the present investigation.

Table 8.1: Previous works on the Crow instability in which the instability was observed. Details of the experimental apparatus as well as characteristics of the instability, when they are available, are provided. The present apparatus is included for comparison. We distinguish the split wing apparatus and others. Frequency is normalized on U_∞/c and time on c/U_∞ if not otherwise stated.

Split wing apparatus		Re_c, Re_Γ	t_b	a/b	Detection time	frequency
Present study	$\tau < 12\%$ $\alpha = 8^o$	$Re_c \sim 10^5$	< 3	> 0.2	$1.5t_b$	0.75
Devenport[41]	$\tau = 15.5\%$ $\alpha = 5^o$	$Re_c \sim 10^5$	10.8	0.2	$2.8t_b$	0.36
Pailhas[118]	$\tau = 12.5\%$ $\alpha = 5.45^o$	$Re_c \sim 10^5$	4.5	0.15	$1.3t_b$	0.38 $kb = 0.75$
Bearman[16][17]	$\tau = 17.5\%$ $\alpha = 8^o$	$Re_c \sim 10^5$	24.6	0.2		
Other apparatus						
Bae[10]	linear compressor cascade $\tau < 4\%$ $\alpha = 5^o$	$Re_c \sim 10^5$	1	0.3	$0.04t_b$	0.75
Leweke[98]	vortex pair generator	$Re_\Gamma \sim 10^3$		0.2		
Thomas[149]	rotating plate	$Re_\Gamma \sim 10^4$	1s	0.2		

The experimental method used here includes tomoscopy, hot-wire and PIV measurements. The tomoscopy provides preliminary and qualitative information on the evolution of the flow unsteadiness with streamwise distance. Hot-wire allows the determination of energy spectra, from which noteworthy frequencies and energy levels can be derived. Finally PIV allows to characterize spatial properties of the unsteady flow field. Note that, like in chapter 7, velocities and distances are normalized on U_∞ and c, respectively. The Reynolds number $Re_c = U_\infty c/\nu$ is still fixed at $4.8.10^5$ ($U_\infty = 38m/s$) and the wing angle of attack, at $\alpha = 8^o$.

In table 8.1 we present previous experimental investigations of the Crow instability. Devenport[41], Pailhas[118] and Bearman[16] used an apparatus similar to ours but with larger gaps. Since the growth rate of the Crow instability varies as the inverse of b^2, large gaps means that instability becomes mature far downstream of the wing. The work of Leweke[98] and Thomas[149] relied on specific experimental set-up installed in water. These authors also observed the Crow instability. Eventually Bae[10] observed the Crow instability in the tip leakage vortex at a distance downstream very close to the trailing edge of the blade. The author noted a good agreement of the frequency and of the growth rate with the prediction of Crow[34]. This result is surprising because it is the first time that the Crow instability is observed so close to the point where the vortex is generated. The hot-wire measurements of Bae[10] were reproduced in our experiment at the corresponding axial position but did not show the existence of the Crow instability. These results shall be discussed in the conclusion 9.

The chapter is organized as follows: we first qualitatively describe the longitudinal evolution of the flow unsteadiness. In a second part we show the procedure and the results concerning the detection of the Crow instability in the flow C1 at $\tau = 7.5\%$. We then use PIV measurements to investigate the effect of the Crow instability on the velocity fields in planes transverse to the free stream and analyze the displacement of the vortex center. Effects of τ and that of insertion of the splitter plate are analyze in a last part. We end up with concluding remarks.

8.1 A first glimpse of the flow unsteadiness

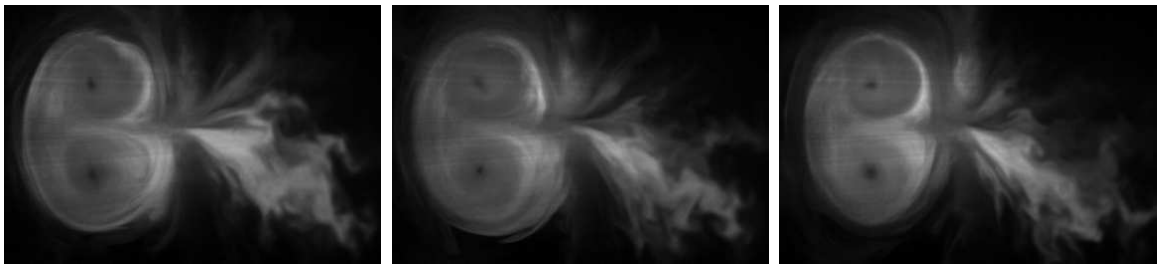

(a) (b) (c)

Figure 8.1: Snapshots of the vortex pair taken at three different times at $z = 0.5$. Acquisition frequency is set at 800Hz.

The longitudinal evolution of the vortex pair unsteadiness is first investigated with tomoscopy visualizations recorded with a high speed camera. Several snapshots extracted from the movies are shown in figure 8.1 and 8.2 at $z = 0.5$ and $z = 2.5$. The vortex pair is visible in the first figure (straight lines in the snapshots are caused by laser sheet inhomogeneities). Note that the (bottom) top vortex rotates (anti)clockwise. The snapshots show the typical flow pattern of a vortex pair, including vortex centers, which appear as black regions due to the centrifugal effect, surrounded by a uniform white region, the limiting streamline corresponding to the Kelvin oval and the incoming smoke from the right. The three snapshots at $z = 0.5$ suggest that the vortex pair unsteadiness is low at this position.

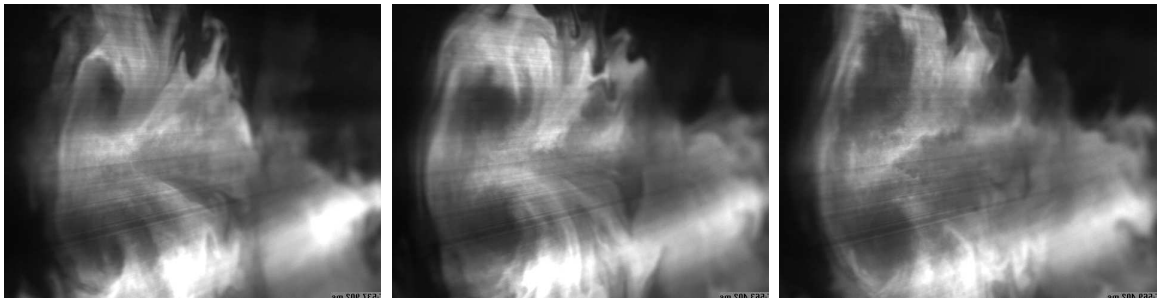

(a) (b) (c)

Figure 8.2: Snapshots of the vortex pair taken at three different times at $z = 2.5$. Acquisition frequency is set at 2000Hz.

On the contrary, at $z = 2.5$ the flow patterns look significantly unsteady. One sees in particular that the interface separating the pair from the ambient flow is very smoothed. This evolution is not attributable to viscous effects only, and suggests the existence of stronger unstable dynamics. Based on the available knowledge on vortices, we can mention that this is a possible consequence of either the axial flow in the core, meandering, or cooperative instabilities.

If cooperative instability is at work, it is possible that the latest stage of evolution of the vortex pair is linking of the two vortices. Note that Bearman[16][17] performs PIV measurement of the vortex pair produced by a wing and finds that vortices sometimes disappear from the measurement plane. The author attributes this phenomenon to vortex break-up, a term that corresponds to the apparition of vortex linking and the subsequent formation of vortex rings. No evidence of the disappearance of the vortices was found in the high frequency movies obtained by tomoscopy up to $z = 2.5$. However PIV measurements, some of which are shown in a later section, shall also suggest this possibility.

8.2 Detection of the Crow instability

8.2.1 Comparison between experiments and theory

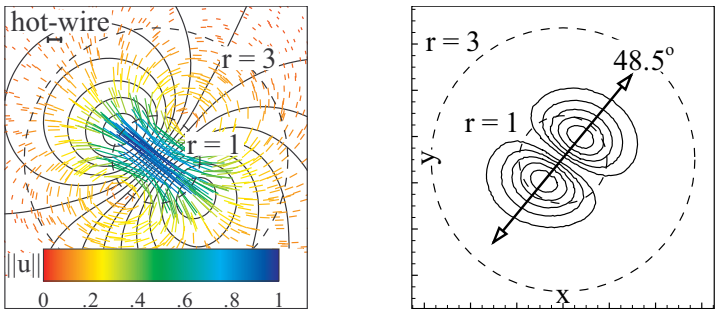

(a) (b)

Figure 8.3: Crow mode at $a/b = 0.2$ and $Re_\Gamma = 4000$: a hot-wire is materialized by a small segment, (a) perturbation velocity field of the mode (plane velocity vectors in color, iso-contours of axial velocity in solid lines), (b) axial vorticity. The arrow shows the direction of displacement of the vortex center due to Crow instability. The orientation is 48.5^o about the x axis. Positions $r = a$ and $r = 3a$ are shown by two dashed circles .

The Crow instability was computed by using the perturbation method detailed in chapter 3. It is described as a global mode $\hat{\boldsymbol{u}}$ which evolves spatially with a wavenumber $k \in \mathbb{R}$ oriented

in the axial direction and temporally with a growth rate $\sigma \in \mathbb{R}$. Figure 8.3(b) plots the corresponding axial vorticity field. The dipolar shape induces an oscillation of the vortex in the direction of the arrow outlined in the figure. This mode being a linear perturbation to the mean flow $\boldsymbol{U}$, the complete flow field corresponding to the vortex pair perturbed by the Crow instability reads

$$\boldsymbol{U} + \hat{\boldsymbol{u}} cos(kz) e^{\sigma t} \tag{8.1}$$

with $\hat{u} << U$. Another important point is that, in the theoretical model, this flow is described in the reference frame moving at U_∞ (hereafter called the instability frame), where the instability grows uniformly with time. The experimental flow is however investigated in the reference frame attached to the laboratory (hereafter called the laboratory frame). The axial coordinate z' in the instability frame is related to z in the laboratory frame by

$$z' = z + U_\infty t \tag{8.2}$$

This means that the probe used in the experiment moves at a speed $-U_\infty$ in the instability frame. The temporal growth rate of the instability in the instability frame becomes a spatial growth rate in the laboratory frame and the axial periodicity in the instability frame introduces a time periodicity in the laboratory frame. Therefore, in the laboratory frame the flow reads

$$\boldsymbol{U} + \boldsymbol{u} cos(kz + kt) e^{\sigma z} \tag{8.3}$$

This relation shows that k is evaluated by sensing the flow at a fixed position in z while σ is obtained by sensing the flow at different z.

8.2.2 Location for the observation of the Crow instability

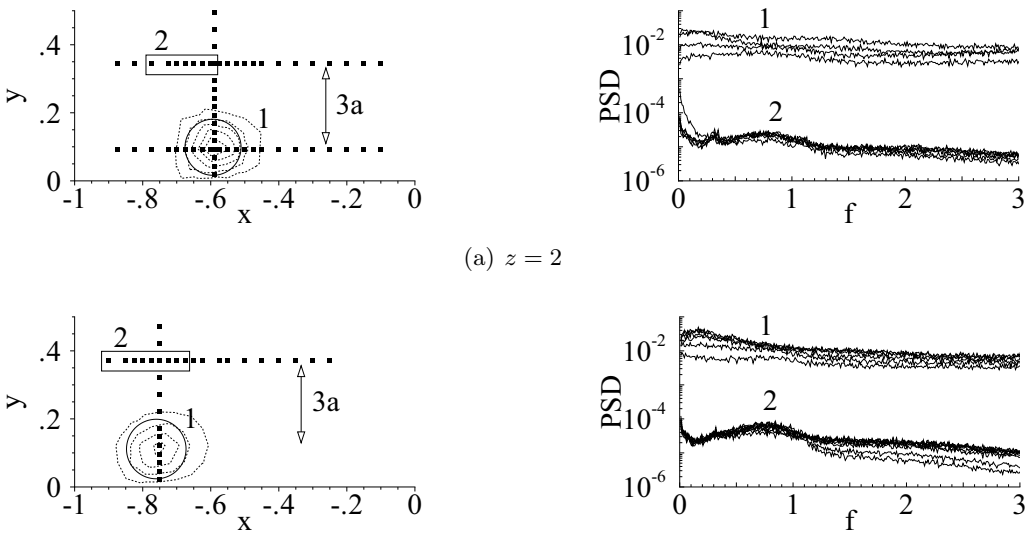

(a) $z = 2$

(b) $z = 2.75$

Figure 8.4: Location of the hot-wire measurement and iso-contours of axial vorticity Ω_z in dashed lines. The circles indicate the vortex radius. Location denoted 1 corresponds to the vortex core and location 2 corresponds to $r = 3a$ above the vortex (left). Spectra obtained in the regions 1/2 as specified in the left frame (right). f is normalized on c/U_∞.

Figure 8.4 shows the spectra determined by hot-wire in two different subsets, denoted 1 and 2, of the data. Subset 1 corresponds to the vortex core and subset 2 corresponds to the region located at $r = 3a$ above the vortex center. The first region exhibits large energy levels at low frequency that suggest the presence of important meandering.

In the second region, the energy levels are substantially lower. We note however the existence of a peak at the two longitudinal locations. This peak was hardly distinguishable at $z = 1$ and completely absent more upstream (not shown here). The appearance of this peak after some distance downstream suggests the development of a growing instability in the flow. Because the peak is found outside the vortex, it is not straightforward to attribute its origin to the vortex pair dynamics. In order to check this hypothesis, we repeated these measurements at $z = 2.75$ for different values of τ, in particular at $\tau = 0\%$ which is interesting for the discrimination since no vortex exist in the flow. The results are shown in figure 8.5. We see that the peak disappears at $\tau = 0\%$, which proves that it is the consequence of the vortex pair dynamics only.

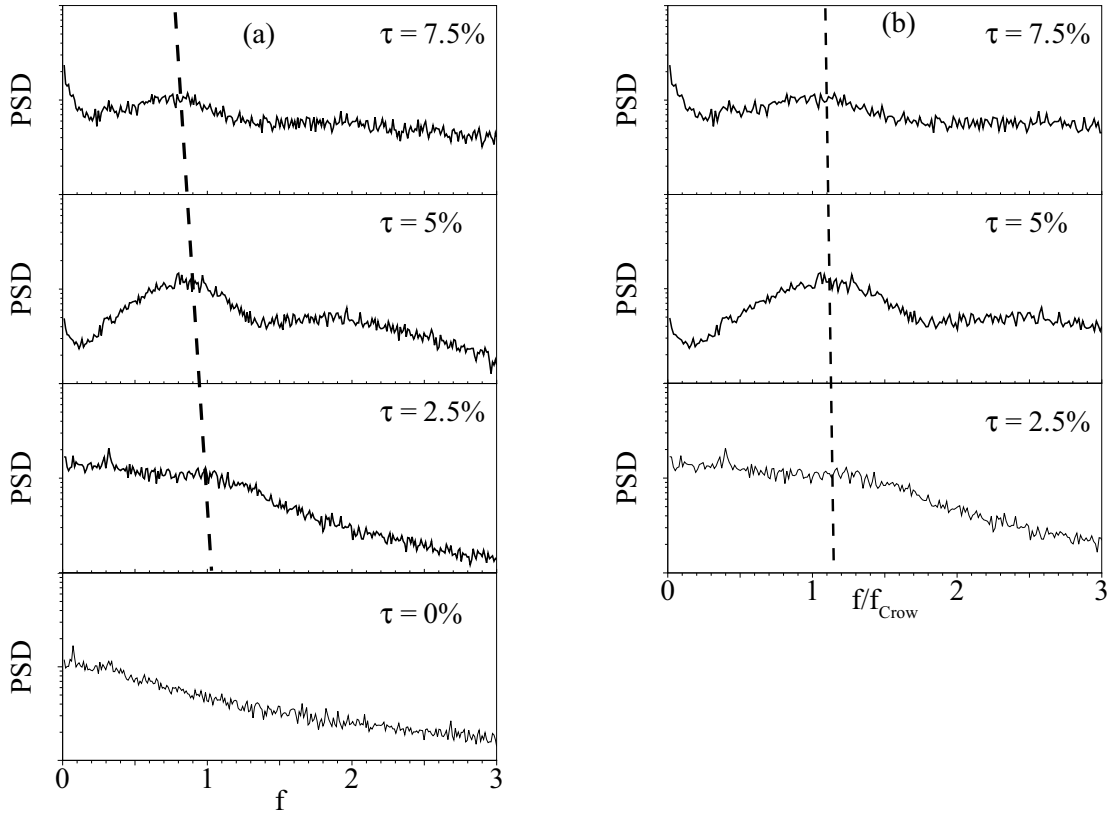

Figure 8.5: (a) Power spectral density of u normalized on the peak value at $r = 3a$ above the vortex for different τ at $z = 2.75$. (b) Effect of the normalization of the frequency by the Crow frequency f_{Crow} on the Power spectral density of u. In the two figures, the dashed line indicate the position of the peak. Note that the same y range is used in all frames. in (a) f is normalized on c/U_∞.

Secondly we observe that the frequency of the peak decreases with τ. The growth rate of the Crow instability versus the axial wavenumber k predicted by the theory is plotted in figure 8.7(a). Amplification is maximum at $kb = 1$. This corresponds to the frequency

$$f_{Crow} = \frac{1}{2\pi b} \tag{8.4}$$

In this relation f_{Crow} is normalized on c/U_∞. This relation means that the frequency of the peak must increase when the gap decreases, since b varies almost linearly with τ. In figure 8.7(b) we compare the measured value of f_{Crow} with the value predicted by (8.4), based on the value of b obtained in chapter 7. Measurements and theory agree within 20% (the frequency of the peak is slightly higher than that predicted). In addition, normalizing the frequency on f_{Crow}, see figure 8.5(b), confirms that the peak occurs at the same normalized frequency at the three values

τ investigated, and that this frequency agrees well with the Crow frequency since $f \simeq f_{Crow}$ as indicated by the dashed line in the figure.

Evaluation of the growth rate

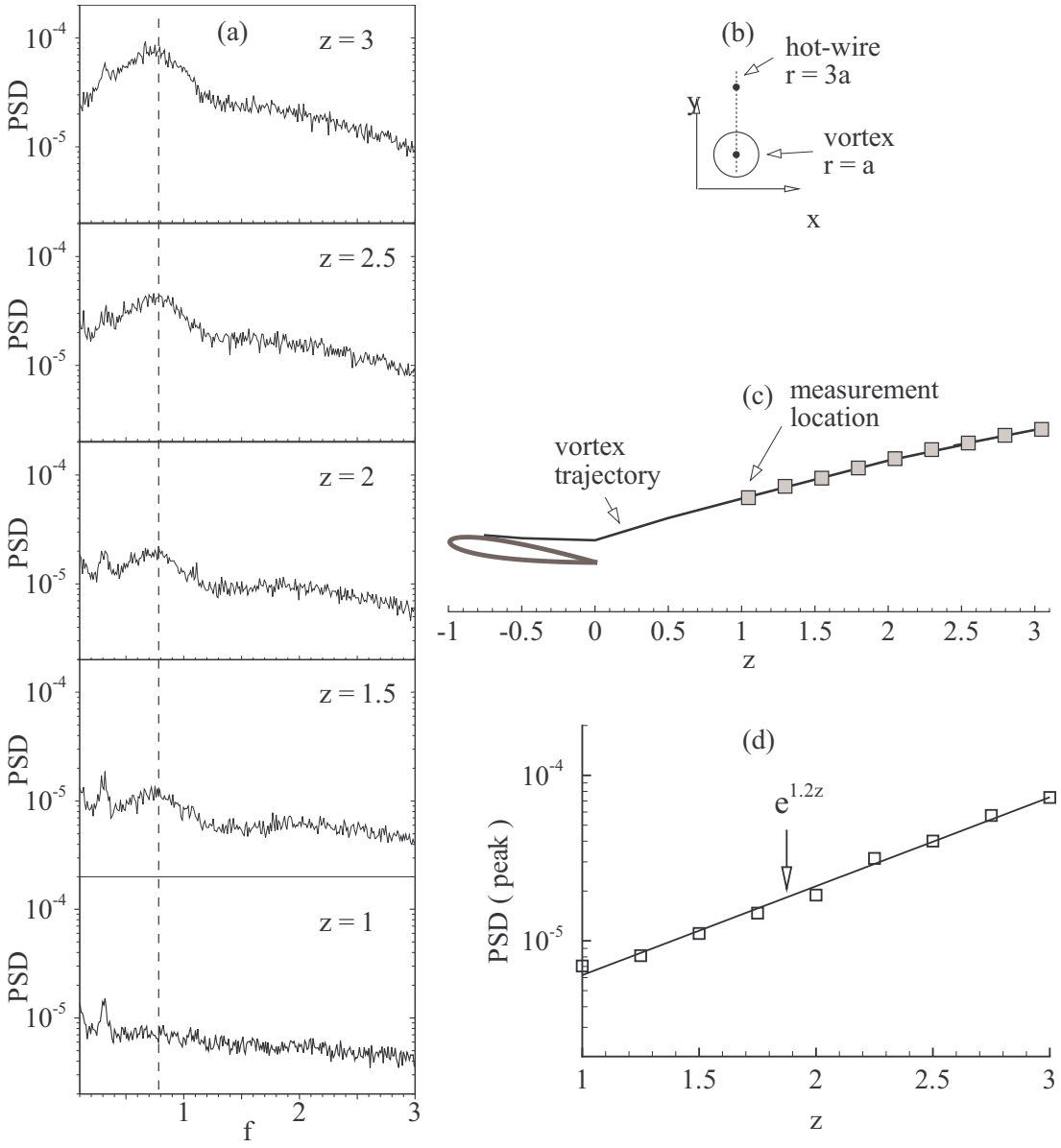

Figure 8.6: (a) Power spectral density of u at $r = 3a$ above the vortex for different axial positions, (b) schematic of the measurement location in transverse planes, (c) locations of the hot-wire measurements along the trajectory of the vortex, (d) Energy of the fluctuation u corresponding to the peak as a function of z. f is normalized on c/U_∞. Recall that z is normalized on c and that $z = 0$ at the wing trailing edge.

The growth rate of the instability is evaluated by measuring the energy of the peak at various locations along the trajectory of the vortex, maintaining the distance $r = 3a$ in the $y > 0$ direction from the vortex center, as schematized in figure 8.6(b). The resulting spectra are shown in figure 8.6(a). In figure 8.6(c), the trajectory of the vortex is depicted along with the location of the hot-wire measurement. The measurement locations are uniformly distributed between $z = 1$ and $z = 3$. At $z = 1$ the peak corresponding to the Crow instability is almost unnoticeable but it grows continuously downstream down to the last measurement location.

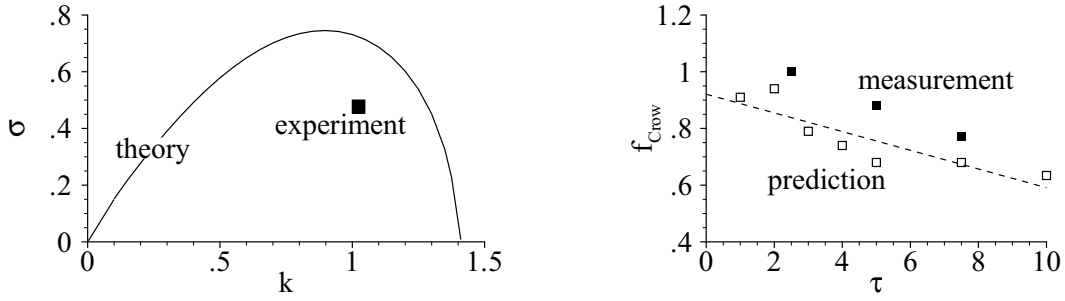

(a) (b)

Figure 8.7: Growth rate σ of the Crow instability (normalized on t_b^{-1}) versus the wavenumber k (normalized on b^{-1}) for $a/b = 0.2$ and $Re_\Gamma = 4000$, (b) frequency f_{Crow} normalized on U_∞/c of the Crow instability at $z = 2$. □ : prediction of f_{Crow} with the values of Γ and b measured in chapter 7. ▲ : measured frequency.

The Power Spectral Density corresponding to the peak is plotted in figure 8.6(d) as a function of the axial distance z. Note that the vertical axis is set in log scale. The data points are well fitted by an exponential law of exponent $\beta = 1.2$. The growth rate of perturbation which corresponds to this exponent is given by

$$\sigma = \beta \frac{1}{2} t_b \frac{U_\infty}{c} \sim 0.5 \tag{8.5}$$

where σ is normalized on t_b^{-1}. The $1/2$ term is included because the Power Spectral Density is $O\left(u^2\right)$ and we consider the growth of the perturbation u. In this relation, the value of t_b is $0.8c/U_\infty$ which is the average of the values of t_b calculated at $z = 0$, $z = 1$, $z = 2$ and $z = 2.5$ thanks to the values of Γ and b obtained in chapter 7. In figure 8.7(a) we plot the growth rate of the Crow instability as a function of the axial wavenumber k for a vortex pair $a/b = 0.2$, taken from appendix F. The experimental growth rate is about 30% lower than the theoretical maximum, and the wavenumber is 10% higher. The agreement between the experimetal point and the theoretical maximum is very satisfactory considering the differences between the theoretical and experimental flows. Indeed, the experimental flow exhibits strong turbulent effects, as well as longitudinal non uniformity (in particular, t_b varies along the axial direction), and probably differs in terms of vortex structure.

8.2.3 Discussion

We have presented many arguments which support the occurrence of the Crow instability in the flow. The fact that the Crow instability is found outside the vortex core is however intriguing. Signature of the Crow instability outside the vortex core was already noted by Bae[10]. The absence of the peak of Crow instability in the spectra measured in the core region is believed to be the consequence of the meandering (whose presence is suggested by figure 8.13 representing the dispersion of the vortex centers obtained by PIV measurements). Devenport[39] showed that meandering exists at all axial positions and results in spectra that have 95% of the energy lying at frequency below $f = 1$, with no distinguishable peak. The location of the Crow instability within the range of the meandering frequencies may explain why the phenomenon can not be discriminated in the vortex core. Moreover the axial locations investigated encompass the early development of the instability for which the energy associated is expected to be low. Another mechanism that could be responsible for strong fluctuations in the core region is the shear resulting from the axial velocity profile. However the frequency associated to this instability mechanism is $f \simeq \Delta U_z/a$, which corresponds to $f \simeq 6U_\infty/c$ at $z = 2$, and is of no interest for the present investigation.

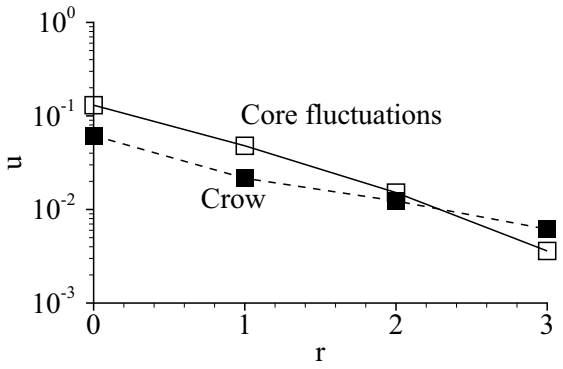

Figure 8.8: Decrease of the fluctuation associated to the Crow instability (▲) and to other sources (□). r is normalized on a, the vortex radius.

In the following, we call "core fluctuations" the fluctuations contained in the core, whose spectra are shown in figures 8.4(a) and 8.4(b). As noted previously, the origin of these fluctuations is not known for sure. However it is clear that these fluctuations decrease outward and that the fluctuations associated to the Crow instability dominate at $r = 3a$. Based on these radial evolutions of the fluctuations associated to the "core fluctuations" on one side and that associated to the Crow instability on the other side, it is interesting to confirm with the theory that the Crow instability can not be observed in the vortex core. Crow theory, see figure 8.3(a), provides the spatial evolution of the associated fluctuations. For instance, at $r = 3a$ fluctuations are only 10% of the maximum, which occurs at the vortex center. Figure 8.8 shows the comparison between the radial evolution of the "core fluctuations" and that of the fluctuations due to the Crow instability. Fluctuations from the "core fluctuations" are measured in the spectra of figure 8.4(a) while fluctuations associated to the Crow instability are calculated by the theory, and initialized with the energy of the peak measured at $r = 3a$ in figure 8.4(a). This comparison shows that the Crow fluctuations decrease at a slower rate than those of the "core fluctuations" which explains why it is not observed at the core, but dominates outside.

In addition, while the previous paragraph confirms the agreement between theory and experiment concerning the detection of the Crow instability at $r = 3a$ above the vortex center, it is not clear why this detection occurs when $x < x_c$ and not when $x > x_c$, see figures 8.4(a) and 8.4(b). Our hypothesis here is that this is the consequence of the orientation of the single hot-wire along the x axis. This orientation plays as a filter on the velocity vectors that can be measured. More specifically, the signal f measured by the hot-wire depends upon the vector product of the velocity vector $\boldsymbol{U}$ with the vector $\boldsymbol{V}_{hw}$ representing the hot-wire. This reads

$$f(U) = \boldsymbol{U} \times \boldsymbol{V}_{hw} \tag{8.6}$$

For instance, no measure can be obtained with the hot-wire if it is oriented parallel to the stream. The direction of the velocity vectors of the Crow instability, see figure 8.3(a), for optimal sensing with the hot-wire, is the upper left region, because there the velocity vector is almost perpendicular to the wire, which is not the case elsewhere. This confirms the observations.

8.3 Statistical analysis of unsteady flow field

8.3.1 Comparison between experiments and theory

Turbulent stress field $\overline{u_x u_y}$ and preferred direction of vortex oscillations

Crow instability is now investigated by means of PIV. In the following we analyze the correlation between the orientation of the oscillations of the vortex and the $\overline{u_x u_y}$ field in the

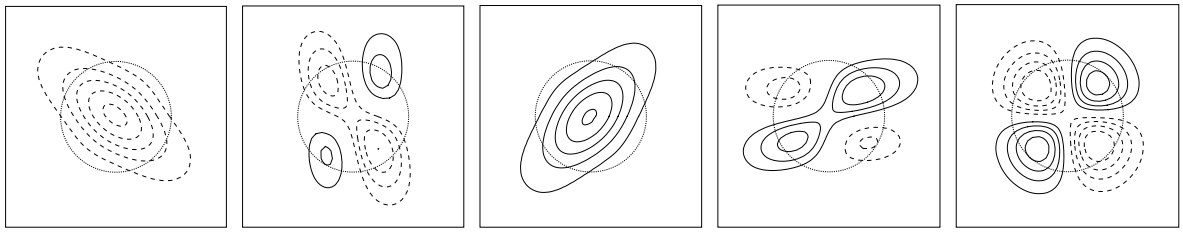

(a) (b) (c) (d) (e)

Figure 8.9: Effect of the oscillation of the vortex in a preferred direction α on the $\overline{u_x u_y}$ field: (a) Crow instability. (b) $\alpha = 0^o$, (c) $\alpha = -45^o$, (d) $\alpha = 90^o$, (e) no preferred direction. Dashed lines correspond to negative values.

light of Crow theory. Note that

$$\overline{u_x u_y} = \frac{1}{T}\int_O^T u_x(t)u_y(t)dt \simeq \frac{1}{N}\sum_N u_{xi}u_{yi} \tag{8.7}$$

corresponds to a time average, which, in PIV, amounts to the calculation of the mean value over N realizations of the variables. Figure 8.9(a) shows the $\overline{u_x u_y}$ field of to Crow instability presented in figure 8.3(a). The oval shape oriented at about -45^o stems from the oscillation of the vortex in the direction oriented at 48.5^o about the x axis, see figure 8.9(a). This must be compared to figures 8.9(b) to 8.9(e) which correspond to the case of vortex displacement with preferred direction at, respectively, 0^o, -45^o, 90^o and without preferred direction. Note that the shape of the $\overline{u_x u_y}$ field depends upon the reference frame.

8.3.2 Results

The iso-contours of the Reynolds stress $\overline{u_x u_y}$ are depicted in figure 8.10 for different axial positions. The shape of this field is quadripolar at $z = 0.5$. At $z = 1.5$ it becomes organized like in the case of the Crow instability. At $z = 2.5$ this structure is conserved but with larger levels. Between $z = 0.5$ and $z = 2.5$ the value of $\overline{u_x u_y}$ at the mean vortex center increased continuously. At $z = 4$ the levels have considerably decreased, the vortex cores being now completely disorganized.

Based on the correlation between the $\overline{u_x u_y}$ structure and the preferred orientation of the vortex displacement illustrated in figure 8.9, the previous observations suggest the following analysis. At $z = 0.5$ the vortices sustain slight meandering. At $z = 1.5$ and $z = 2.5$ meandering becomes oriented, presumably due to the occurrence of the Crow instability. At $z = 4$ the structure of the Crow instability has disappeared which, in addition to the significant decrease in turbulent levels, suggests that some non-linearities have modified the flow. As in Bearman[16], it is possible that vortex linking occurs, here between $z = 2.5$ and $z = 4$. This mechanism will be considered further in the next section.

8.3.3 Vortex displacement

Vortex identification Γ_2 criterion

Identification of the vortices (center, radius) from instantaneous flow field is delicate. In particular, tracking of the vortex center with time becomes difficult in the presence of small scale turbulence. This makes the use, as was done in previous chapters, of the instantaneous vorticity Ω_z to detect vortex centers inadequate. Self-similar decay of the turbulent motion is characterized by a vorticity $\left(\epsilon/l^2\right)^{1/3}$ where ϵ is the rate at which energy is transferred from large to small scales and l is the typical size of the turbulent eddies. This relations shows

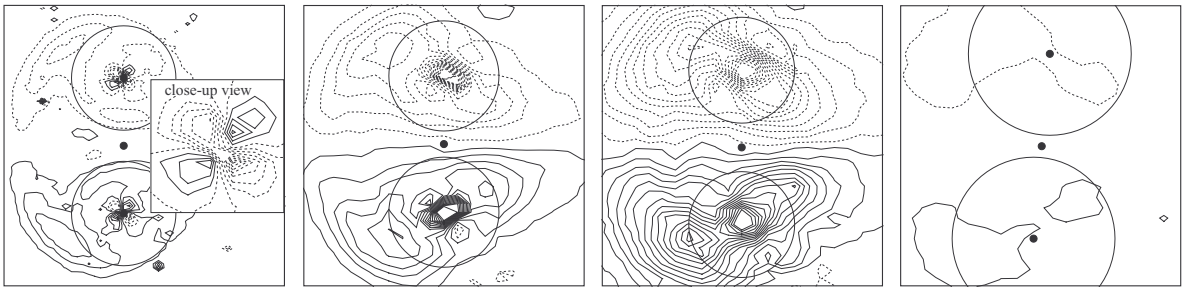

(a) $z = 0.5$ (b) $z = 1.5$ (c) $z = 2.5$ (d) $z = 4$

Figure 8.10: Iso-contours of $\overline{u_x u_y}$ at several axial position. The close-up view magnifies the region of the top vortex core in frame (a). Dashed lines corresponds to negative value. Circles corresponds to $r = a$ the vortex radius, and points show vortex centers (none is shown when it interferes with the $\overline{u_x u_y}$ field).

that the levels of vorticity detected in instantaneous PIV snapshots strongly vary with spatial resolution. High levels of vorticity may be reached within the whole turbulent regions of the instantaneous flow.

(a) (b)

Figure 8.11: (a) Schematic of the Γ_2 criterion. (b) Truncation of the window if P is less than r_0 away from boundaries.

In order to identify the vortex core in the instantaneous flow field, we thus need a different criterion. Several criteria (λ_2, Q, Δ or N_k) exist that are based on invariants of the velocity gradient tensor, see Jeong[78]. However unlike numerical simulations, the evaluation of the velocity gradients in experimental data may be hazardous due to the lack of spatial resolution. It is preferable instead to use criteria based on the sole velocity field, like the Γ_2 criterion which was proposed by Graftieux[58] to localize vortex centers in PIV data. The Γ_2 criterion mimics the intuitive idea one can have of a vortex: a homogeneous region close to symmetric rotation. At every point P of the measured plane, this criterion evaluates how well the point P is the center of rotation of the surrounding flow by a quantity $\Gamma_2(P)$ in the range 0 to 1. If $\Gamma_2(P) = 1$ this means that all the particles in the vicinity of P rotate around P. On the contrary, $\Gamma_2(P) = 0$ means that no rotational motion exists around P. Experimental values are always in between due to numerous factors (spatial resolution, turbulence). The mathematical expression for this criterion is given by

$$\Gamma_2(P) = \frac{1}{S} \int_{M \in S} \frac{\boldsymbol{PM} \times \left(\boldsymbol{U}_M - \bar{\boldsymbol{U}}_P\right)}{\|\boldsymbol{PM}\| \cdot \|\boldsymbol{U}_M - \bar{\boldsymbol{U}}_P\|} dS \tag{8.8}$$

where S is the interrogation windows around the point P as depicted in figure 8.11(a) and where

$$\bar{\boldsymbol{U}}_P = \frac{\int_S \boldsymbol{U} dS}{S} \tag{8.9}$$

is the mean velocity vector of the flow in the region S. This makes the criterion Γ_2 invariant by Galilean transformation. The selection of the size of the flow region interrogated is the radius r_0 of the interrogation window S. Hence r_0 plays the role of a low pass filter. According to Graftieux[58], the vortex radius corresponds to

$$|\Gamma_2(r = a)| = \frac{2}{\pi} \tag{8.10}$$

In figure 8.12 we have plotted Γ_2 corresponding to the mean flow at $z = 1.5$ (figure 8.12(a))

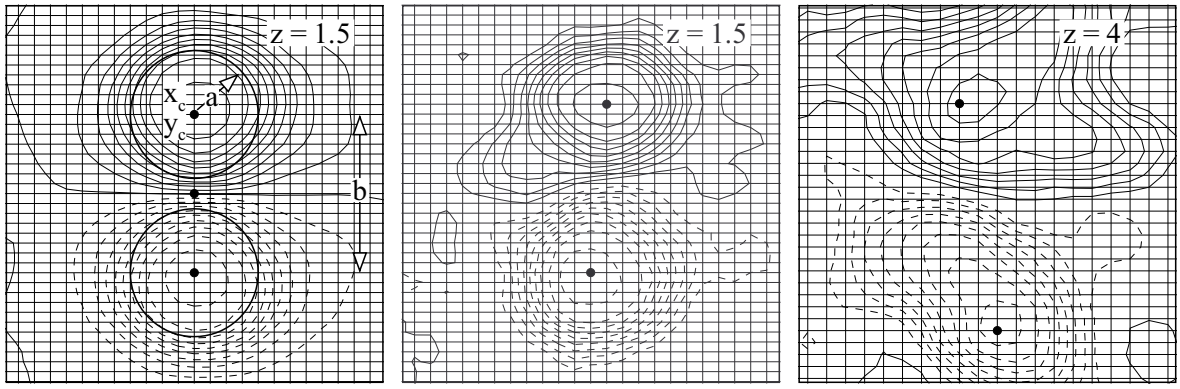

(a) (b) (c)

Figure 8.12: Γ_2 for (a) the mean flow, (b) an instantaneous snapshot at $z = 1.5$, (c) instantaneous snapshot at $z = 4$. Dashed lines denotes negative values. Circles indicate the vortex radius a corresponding to $|\Gamma_2(r = a)| = 2/\pi$ and points correspond to maximum of $|\Gamma_2|$. Vortex characteristics (a, b and x_c, y_c) are indicated in (a). Grids indicate spatial resolution.

and to instantaneous snapshots at $z = 1.5$ (figure 8.12(b)) and $z = 4$ (figure 8.12(c)). The top (bottom) vortex corresponds to positive (negative) Γ_2. The vortex radius corresponds to $\Gamma_2 = 2/\pi$ and the vortex center are determined by the maximum of $|\Gamma_2|$ over the grid vertices. The mean radius obtained by application of the method to the mean flow, as in figure 8.12(a), is used to get the size of the window for the calculation of the instantaneous fields. Note that the Γ_2 criterion is calculated even in the boundary regions, by truncating the window S as shown in figure 8.11(b).

Results

Results of the detection of the instantaneous positions of the vortices deduced from PIV data by applying the Γ_2 criterion are shown in figure 8.13. Every point denotes the passage of the vortex center and the color indicates the passage frequency. The orientation of the data is determined qualitatively. The dispersion of the data increases longitudinally. A preferred orientation appears at $z = 1.5$, persists at $z = 2.5$ and disappears downstream. At $z = 0.5$ the dispersion is small and the histogram is almost symmetric in each vortex core, denoting small displacement of the vortices and no preferred direction. The preferred orientation observed downstream is about 30^o, which is notably lower than the theoretical orientation of the Crow instability. However, like the theory, the orientations of the displacement of the two vortices are symmetric about the symmetry plane of the vortex pair. At $z = 4$ the dispersion has increased significantly, along with the mean radii of the vortices. There, in several snapshots, the distance b was found to be smaller than the mean radius a of the vortices, which suggests the possibility that vortex linking occurs before $z = 4$.

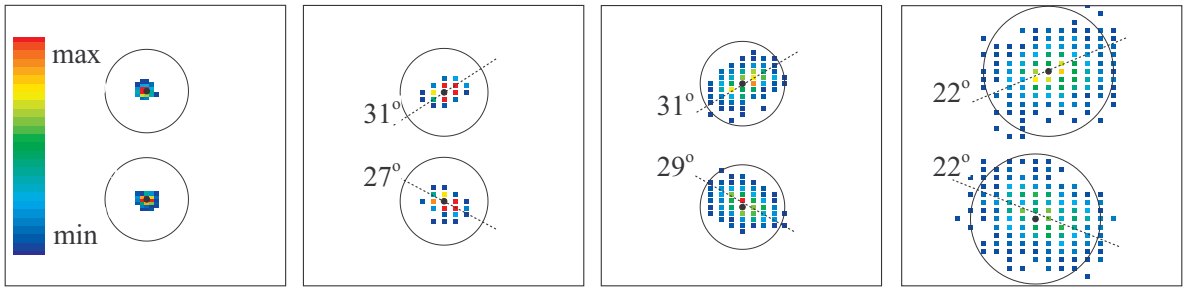

(a) $z = 0.5$ (b) $z = 1.5$ (c) $z = 2.5$ (d) $z = 4$

Figure 8.13: Histograms of the vortex center position at several axial position. Color indicates the passage frequency at a given grid vertex. Circles indicate the vortex radius.

8.3.4 Effect of the gap and the wall

Influence of the gap

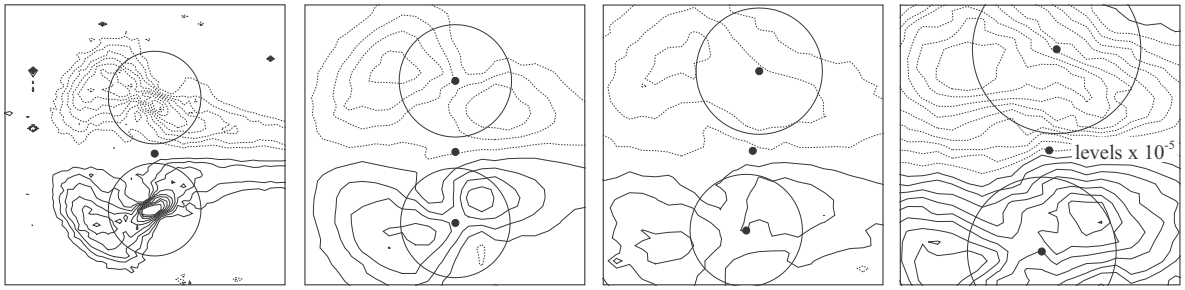

(a) $z = 0.5$ (b) $z = 1.5$ (c) $z = 2.5$ (d) $z = 4$

Figure 8.14: Iso-contours of $\overline{u_x u_y}$ at several axial position and $\tau = 3\%$. Circles indicate the vortex radius. Note that levels of $\overline{u_x u_y}$ in (d) have been multiplied by 10^5 in order to make iso-contours visible.

Iso-contours of $\overline{u_x u_y}$ at $\tau = 3\%$ are shown in figure 8.14. Comparing this figure with figure 8.10 which corresponds to $\tau = 7.5\%$ shows that the Reynolds stress at $\tau = 3\%$ exhibit the same characterization, but earlier. In particular the $\overline{u_x u_y}$ pattern of the Crow instability is already present at $z = 0.5$. Levels of $\overline{u_x u_y}$ have already decreased at $z = 1.5$ and this continues down to $z = 4$, for which a normalization of levels had to be performed in order to make the contours visible.

The histograms of the vortex positions shown in figure 8.15 confirm that at $z = 0.5$ the vortex is displaced in a direction close to that prescribed by the Crow instability. Downstream the dispersion becomes very important and the preferred direction is lost. These results suggest that at $\tau = 3\%$ the Crow instability occurs earlier than at $\tau = 7.5\%$. A more rapid disorganization of the vortices is also observed.

Figure 8.16 shows $\overline{u_x u_y}$ at $z = 1.5$ for several values of τ. The figure confirms the trends noted previously: Crow instability develops earlier with smaller τ. The patterns of $\overline{u_x u_y}$ show that the flow is already in the latest stage of evolution at $\tau = 1\%$ whereas high $\overline{u_x u_y}$ corresponding to the Crow instability pattern develops in the vortex core as τ increases.

Effect of the splitter plate

Figures 8.17 show $\overline{u_x u_y}$ in C2 (with the splitter plate) at $\tau = 7.5\%$. At all axial positions the pattern corresponds to vortex displacements without preferred direction. Meandering in

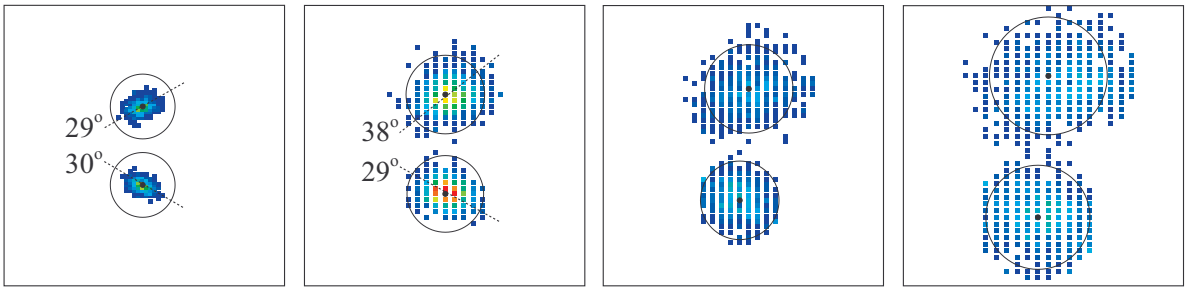

(a) $z = 0.5$ (b) $z = 1.5$ (c) $z = 2.5$ (d) $z = 4$

Figure 8.15: Histograms of the vortex center position at several axial positions and $\tau = 3\%$. Same color map as in figure 8.13. Circles indicate the vortex radius.

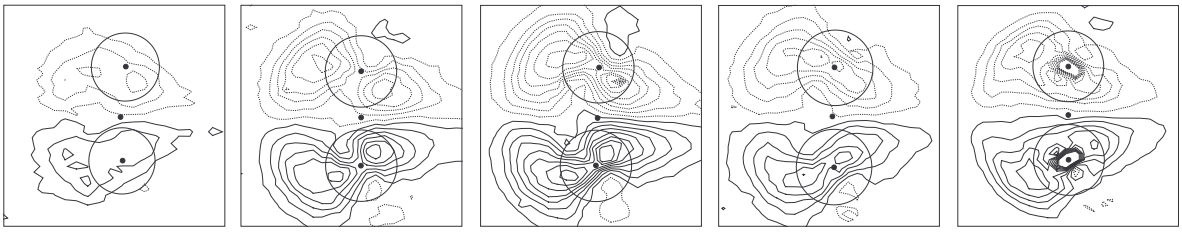

(a) $\tau = 1\%$ (b) $\tau = 3\%$ (c) $\tau = 4\%$ (d) $\tau = 5\%$ (e) $\tau = 7.5\%$

Figure 8.16: Contours of $\overline{u_x u_y}$ for several values of τ. Circles indicate the vortex radius.

the tip leakage vortex has already been observed by Devenport[39]. This suggests that the wall prevents the early occurrence of the Crow instability and confirms the prediction based on the values of t_b that was given in chapter 7. We may conclude that the splitter plate tends to stabilize the flow.

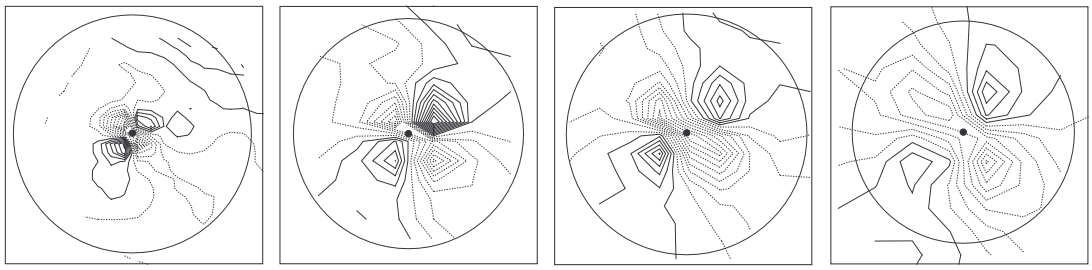

(a) $z = 0.5$ (b) $z = 1.5$ (c) $z = 2.5$ (d) $z = 4$

Figure 8.17: Iso-contours of $\overline{u_x u_y}$ at several axial position and $\tau = 7.5\%$, in C2 (with the splitter plate). Circles indicate the vortex radius.

Conclusion

In this chapter we showed that the Crow instability develops in the flow in C1. The detection of the instability is done outside the vortex core, because the vortex core is dominated by other fluctuations, which are possibly due to meandering. The Crow instability seems to appear earlier when τ decreases. The flow unsteadiness is strongly reduced when the splitter plate is inserted and the Crow instability is not detected.

The reduction of the unsteadiness by the splitter plate is surprising because it contradicts the results of Bae[10] who predicted the occurrence of the Crow instability in the tip leakage vortex. There are two hypothesis that may explain why it does not appear in the present situation.

Firstly, the time scale of the appearance of the Crow instability in C2 is larger than in C1. For this reason, it is possible that the instability appears further downstream after the test section. However no measurement could be achieved there to confirm this hypothesis.

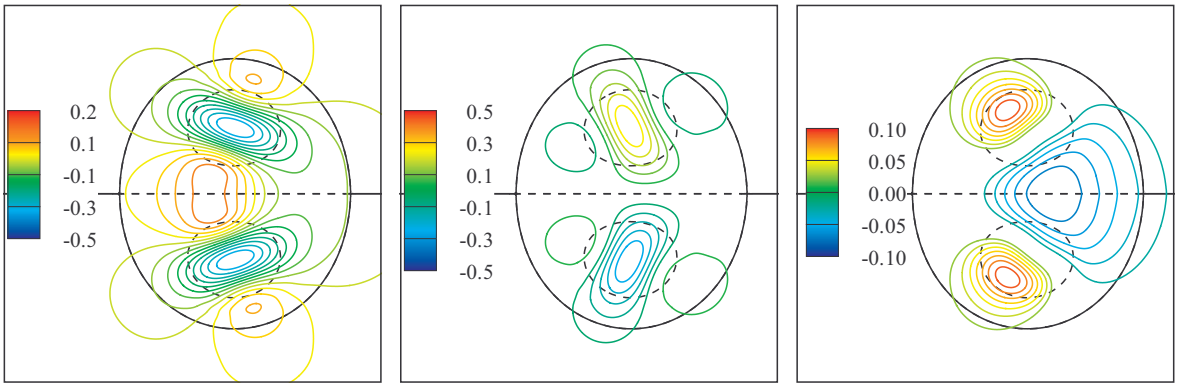

(a) u_x (b) u_y (c) u_z

Figure 8.18: Iso-contours of perturbation velocity corresponding to Crow instability.

Secondly, the symmetry, about the symmetry plane of the vortex pair, of the perturbation corresponding to the Crow instability is not compatible with the no-slip boundary condition at the splitter plate. Figure 8.18 shows the u_x, u_y and u_z fields corresponding to the Crow instability computed in chapter 6. We see that the Crow instability exhibits non-zero u_x and u_z at the symmetry plane. Therefore, on a theoretical basis, the wall must prevent the formation of Crow instability, by cancelling velocity fluctuations along the wall. It is interesting to note that a similar result of instability prevented by a splitter plate was observed by Bearman[15] in the case of vortex shedding in the wake of the blunt trailing edge.

9 Conclusion

9.1 Summary of the results

i- **Theory: stability of vortices.** We reviewed the current knowledge on the stability of single and pairs of vortices. Vortices are highly unstable at low swirl number ($q < 1.5$) due to the occurrence of strong inviscid instabilities. Above this threshold, a single vortex is in general considered stable even though weak instabilities exist (center modes). This stable character is however broken when an additional vortex is introduced, thereby forming a vortex pair. The strain mutually induced by each vortex upon the other entrains the destabilization of the pair by cooperative instabilities (Crow, Widnall).

ii- **Theory: thick dipoles.** The stability of vortex pairs is now well understood. However, the aspects covered by literature mainly concern dipoles of small aspect ratio. We thus presented a map of the 3D instabilities of the Lamb-Chaplygin dipole which was used as a paragon of thick dipoles. We showed the existence of a 2D instability which has never been described before and which might occur in dipoles with smaller aspect ratio as well.

iii- **Theory: optimal perturbation.** The search for perturbations able to destabilize the vortex pair more rapidly than what is naturally achieved by cooperative instabilities led us to investigate transient growth of energy in vortex pairs. This was done for the Crow and Widnall instabilities and for instabilities at finite swirl numbers. We proved that strong transient effects can be expected in vortex pairs. An important mechanism for this transient growth was found to be the destabilization of the vortex cores by perturbation vorticity stretched and amplified in the hyperbolic stagnation regions of the flow. A resonance mechanism relating the initial radial location of the perturbation and the final frequency of the instability has been proposed.

iv- **Experiment: mean flow.** The tip leakage flow has been explored experimentally by means of a setup producing a vortex pair and a single vortex when the symmetry plane is materialized with a splitter plate. The mean flow obtained with a 7-hole pressure probe showed differences in the kinematics of the tip vortex between the two configurations. The splitter plate provokes a reduction of the drift of the vortex and its rebound. It also modifies its mean properties (circulation, radius, aspect ratio). As for the vortex dynamics, the evaluation of the time scale of the cooperative instabilities showed that the splitter plate delays the occurrence of cooperative instabilities.

v- **Experiment: detection of the Crow instability.** We focused on the unsteady properties of the vortex pair without splitter plate. Tomoscopy and PIV measurement showed that unsteadiness in this flow is significantly stronger than that with splitter plate. The results confirmed the development of the Crow instability. Interestingly, we show that the detection of the Crow instability by means of hot-wire measurements is possible outside the vortex core, but not inside, due to the dominating influence of strong perturbations of different origins in the vortex core. Moreover the splitter plate is shown to prevent the Crow instability.

9.2 Issues for practical applications

Our motivations were based initially on the idea that knowledge on tip clearance vortices could benefit from recent research on the stability and control of trailing wake vortices. Research works at MIT (Bae[10]) illustrated the interest in the subject by the turbo machinery community. They demonstrated the need to take into account the Crow instability to control the tip leakage flow with normal synthetic jets. In the context of trailing wake vortices, investigations for the control of the Crow instability had started earlier, and strategies had already been developed (Fabre[45], Crouch[33]). However, open questions remained. In particular, although the physics of the Crow instability had been known for quite a long time (Crow[34]), its numerical computation in realistic vortex pairs posed problems. The subject of instabilities in thick vortex pairs, partially investigated by Billant[19], was also a matter of interrogation.

Concerning the tip leakage flow, we needed to carefully describe the mean properties of the tip vortex (circulation, radius, aspect ratio) produced by a blade, in particular through the variation of the gap size. Concerning flow unsteadiness, we had to confirm that the Crow instability was a dominant unsteady mechanism and we wanted to evaluate the possibility to control it.

Our theoretical investigations allowed a better understanding of cooperative instabilities in vortex pairs, and proved that there are possibilities to augment the associated energy growth. The vortex pair formed by the tip leakage vortex and its image about the casing wall being thick like the one formed in the far field of an aircraft wake, we also investigated the linear dynamics of thick vortex pairs and found new instabilities. On the experimental side, the decision was taken to proceed gradually, namely by introducing the casing wall in a second step, expecting this would allow a better discrimination of the specific effect of the wall boundary layer on the flow dynamics. This showed that the vortex with the casing wall differs from that in the wall free situation, mainly as a consequence of the induced boundary layer. This results in a lower vortex circulation, in a rebound of the vortex at the casing wall and in a strong damping of the drifting motion. We could also confirm the increase of energy loss with increasing gap size.

What are the outcomes of the present findings for turbo machinery? Importantly, the result of Bae[10] showing the presence of the Crow instability in the tip leakage vortex was not confirmed by our analysis. We provide solid indications that the vortex unsteadiness is strongly mitigated by the casing wall (compared to the wall free situation). On a theoretical basis, our work suggests that the instability is prevented by the wall due to the no-slip boundary condition. On an experimental basis, the rebound of the vortex and the lower circulation delays the time of appearance of the Crow instability (t_b is larger).

As for now, the contradiction between our results and those of Bae[10] remains a matter of controversy. Bae's dissertation is convincing but it lacks important details about the way the Crow instability was detected. This contradiction could however stem from the specificity of our respective experimental set-ups. Bae used a cascade of compressor blades in which multiple blade passages could favour the Crow instability by cooperation between tip vortices or with elements of the secondary flow, rather than between the tip vortex and its image about the casing wall.

In the absence of the Crow instability in the tip clearance vortex, there is obviously no need to control the tip leakage vortex by acting on this physical mechanism specifically. However we showed that this type of control was possible in the wall free situation. We have tested, in particular, a simple device inspired by the results of chapter 6 (see appendix A). Our results are very preliminary, but such a research work could interest several applications where cooperative instabilities remain an important mechanism that could be exploited for accelerating vortex dissipation, e.g. aircraft wake, open rotors.

9.3 Recommendation for future works

i- The contradiction between Bae's results and ours deserves further inveestigation. In particular, it would be interesting to study a cascade similar to that of Bae's in order to, firstly, vary the number of blades and discriminate the effect of the other tip vortices and, secondly, to modify the boundary layer thickness and investigate the effect of secondary vorticity.

ii- The theoretical analysis of the Crow instability must be pursued in order to understand the influence of the no-slip boundary condition at the wall and of the subsequent formation of secondary vorticity there. For that purpose, one would need to perform 3D simulations of the interactions of a vortex with a wall. Existing studies in this field only concern the interaction of a vortex pair approaching a wall, see for instance Luton[101], and show the occurrence of the Crow instability in the secondary vortex formed at the wall.

iii- The experimental apparatus in the wall free configuration generates a mature Crow instability within the length of the test section. This represents a good basis for further experimental analysis of this instability. In particular we showed, in chapter 8, that tracking of the vortex center with PIV data gives valuable information on the instability. It would be interesting to have a time resolved tracking of the vortex center in order to better understand the displacement of the vortex and, based on spectral analysis, to analyse the contribution of the Crow instability. This is now possible with time resolved PIV. Concerning control, the apparatus used in appendix A showed encouraging results that deserve further investigations. There is, in particular, a need for a control apparatus that better matches the theoretical properties of the optimal perturbation described in chapter 6. Finally, we did not investigate the Widnall instability in the course of this study although some hot-wire data suggested its presence. It would therefore be interesting to do this investigation and to compare the frequency and the growth rate of this instability with theory.

Part IV

Appendix

A Control of the Crow instability

This appendix deals with the control of the Crow instability in the experimental vortex pair obtained without splitter plate. The control is achieved with an apparatus consisting of a forced oscillating string. In chapter 6 we presented theoretical results concerning, for some part, the optimization of the Crow instability in vortex pairs. Let us first recap our findings. Optimal amplification of the Crow instability is obtained by a perturbation whose vorticity is located in the vicinity of the upstream stagnation point. The y component of the vorticity is first stretched at the upstream stagnation point and rolled-up on the dividing streamline of the vortex pair. There, this vorticity induces the oscillations of the vortices corresponding to the Crow instability. Overall these results show that there is a potential for increasing the growth rate of the Crow instability. This can be accomplished by disturbing the vortex pair at the symmetry plane with y oriented vorticity.

In addition in chapter 8 we showed that the Crow instability occurs in the experimental flow in C1. The instability is detected by hot-wire measurements performed outside the vortex core. Moreover PIV allowed a characterization of the associated properties of the flow field.

The theoretical potential for optimizing the Crow instability and the existence of the Crow instability in the experiment constitute the motivation for the following attempt to control the Crow instability. We focus on the configuration C1 (no splitter plate) at $\tau = 7.5\%$. Note that since the Crow instability was not observed in configuration C2, the following control apparatus is of no interest for the tip leakage vortex in compressors. However it is hope to bring useful information for the general understanding of the control of vortex pairs.

Due to time and technical constraints the control apparatus used in the following study does not comply with all the requirements of the theory. The idea here is to disturb the vortex pair at its symmetry plane, but no consideration is made on the form of the perturbation. A discussion on this latter aspect will be made in the end. The control apparatus is a string stretched in between the two vortices of the pair. When it is set into the flow, the string produces vortex shedding at a frequency given by StU_∞/d where d is the diameter of the string and St is the Strouhal number. The Strouhal number of vortex shedding is $St = 0.2$. The Reynolds number based on the string diameter $\phi = 1mm$ is $Re_\Gamma = 4000$. In this regime laminar separation occurs at the rear of the string and vortices are shed at $f_v \simeq 9U_\infty/c$. There is an order of magnitude of difference between this frequency and that of the Crow instability. Using this frequency for the control is therefore not possible. Ensuring the equality of the two frequencies would require a string at least ten times bigger, which is not conceivable given the dimensions of the model. Hence it was decided that the string would be oscillated at a frequency f_f by playing on the self-oscillations f_s of the string and using an actuator to maintain these oscillations.

The description of the natural oscillations of a string is a basic problem of mechanics. If y_s is the amplitude of the oscillations and x_s spans the string axis, the evolution of y_s versus x_s is obtained by solving the equation

$$\frac{\partial^2 y_s}{\partial x_s^2} = \frac{1}{\nu_s^2}\frac{\partial^2 y_s}{\partial t^2} \tag{A.1}$$

where $\nu_s = \sqrt{T_s/\mu_s}$, T_s being the tension of the string and μ_s the linear mass. The frequency of the oscillations at the wavelength λ is $f_s = \nu_s/\lambda$. The first mode of oscillation occurring in the experiment is the one corresponding to $\lambda = 2L$ where L is the spanwise dimension of the

test section. It results into oscillations whose nodes are at the two ends of the string. Overtones add up at multiples of the fundamental frequency.

The shedding frequency being much larger than that of the string, we expect that the oscillations of the string will induce the oscillation of the vortex shedding. No study could be found in the literature on the effect of an oscillating string in a free stream. Most studies investigate the problem of vortex induced oscillations of flexible cylinder in relation to the structural problems that occur in offshore and thermal power engineering applications (see Balckburn[21] and Chen[30]). In Blackburn[21] the authors investigate the peculiar regime when $f_v \simeq f_s$ by forcing the oscillation of a cylinder at f_s. The control of these oscillations is an important matter, see Chen[30].

Another flow in which the effect of a cylinder is of interest is the open cavity flow. An example is the design of non damaging weapons bays for military aircrafts. Open cavities exhibit acoustic resonances which provoke high acoustic and pressure variations as explained by Illy[71], Stanek[140] and Cattafesta[26]. These fluctuations result in high loads that can damage the mechanical parts contained in the cavity. A real-life experience of this acoustic resonance is the unpleasant beating air pressure provoked by the opening of a window in a car. Cavity modes are known as Rossiter modes. One solution to suppress these modes is to put a cylinder upstream of the cavity at a certain distance from the wall. This was done first by McGrath[109] and later detailed by Illy[71]. The rod acts as a stabilizer of the flow. Stanek[140] suggests that the vortex shedding downstream of the rod induces an acceleration of the turbulent energy cascade by excitation of the high frequencies in the dissipation range. This in return decreases the energy at the lower frequencies where the Rossiter modes operate. This explanation follows the one given by Wiltse and Glezer [156] corresponding to the response of a jet to high frequency forcing.

The organization of the chapter is the following. The first section deals with the presentation and the properties of the control apparatus. The results are then detailed, first in case when the string is set still and then when it is oscillated. The last part is dedicated to concluding remarks and to recommendations for future works.

A.1 Details of the apparatus

The control apparatus is made of an oscillating string such as those used in musical instruments. The string spans the test section of the wind tunnel, as shown in figure A.1. At rest the string is at $y = 0$ and aligned with the x direction. The left end of the string is attached to the inside of the test section while the right end is attached to a point outside the test section. The side window of the test section comprises a vertically elongated hole through which the string passes and is allowed to move. The oscillations of the string are maintained by a periodic excitation imposed by a rotating disc that has four rods attached to it at the same radius and uniformly distributed along the perimeter. Every rod acts as a plectrum. The string is thus hit four times at every rotation of the disc.

The motor is attached to an horizontal plane at the right side of the test section. The tension of the string (and consequently, its natural frequency) can be varied by a specific mechanism placed where the string is attached at the right end. The string and its actuator can be set at different longitudinal z positions. However only one position was investigated, at $z = 0.1$ downstream of the wing trailing edge. The diameter of the string was varied between 0.3mm to 2.3mm. However only diameters below $1mm$ could be oscillated, because the motor was not powerful enough to move string of larger diameter.

The adjustment of the system is based on the coincidence between the natural frequency of the string and the frequency of the passing rods. When these frequencies are equal, the whole system is in harmony. This regime is characterized by nice oscillations of the string in the plane (x, y) that is transverse to the free stream, as illustrated by the dashed lines in figure A.1. Moreover the belly of the oscillation is at the middle of the string. Without harmony, the

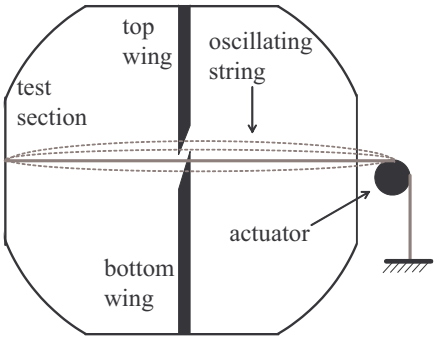

Figure A.1: Schematic of the control apparatus. The string is set perpendicular to the free stream at $z = 0.1$. Dashed lines indicate the oscillations of the string. The actuator at the right is used to maintain the oscillations. The right side of the test section has a hole through which the string passes.

oscillations of the string are disorganized, which is evidenced by the existence of multiple nods and bellies.

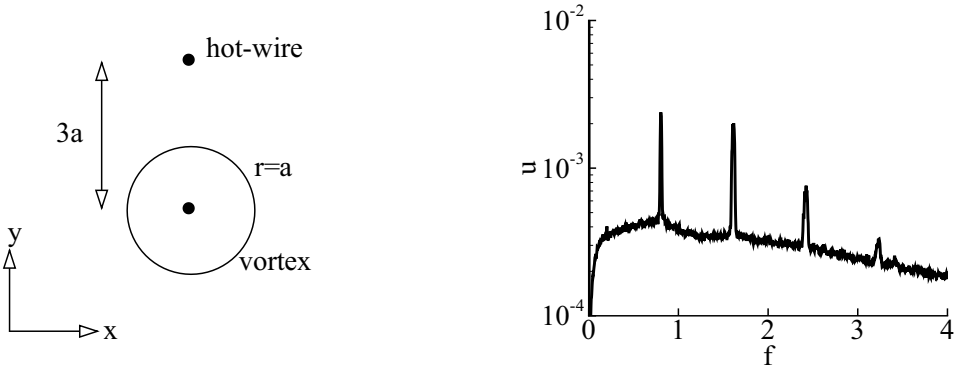

(a) (b)

Figure A.2: (a) Schematic of the vortex (represented by the circle) and location of the measurement with the hot-wire. Longitudinal position is $z = 2.5$, (a) power spectral density of u measured at this location.

The frequency of the oscillations is measured by a hot-wire located at $z = 2.5$ and at a distance $3a$ above the vortex center, as schematized in figure A.2(a). This is the location where the Crow instability was detected in chapter 8. The oscillations of the string are convected there by the flow and appear as a very narrow peak in the spectrum shown in figure A.2(b). Harmonics containing strong energy also appear in this data. In practice, the adjustment of the forcing frequency is done in the following way

i - The motor is switched on. In general the frequency of the passing rod is not equal to the string natural frequency,

ii - The tension of the string is adjusted so that its natural frequency matches that of the passing rod,

iii - The string oscillation frequency is measured in real time with a spectral analyzer,

v - The forcing frequency is then progressively adjusted by modifying repeatedly the motor rotation speed and the string tension until harmony is reached. At every step the forcing frequency is controlled with the spectral analyzer.

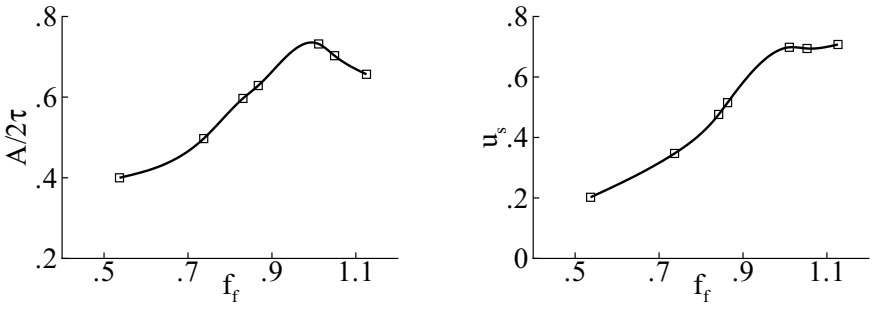

Figure A.3: (a) Amplitude A of the string oscillations as a function of the forcing frequency. A is normalized on 2τ the distance between the wing tips. (b) Oscillation velocity u_s of the string normalized on W_∞ versus the forcing frequency.

Several difficulties arise from the use of an oscillating string for flow control. First the amplitude A of the oscillations changes with frequency. Figure A.3(a) shows that the amplitude increases with frequency. Secondly the range of forcing frequencies allowed by the string is limited. The maximum frequency is $100Hz$. At $Re_\Gamma = 4.8.10^5$ the frequency of the Crow instability is $f_{Crow} = 140Hz$. Therefore no forcing can be achieved at this Reynolds number. This forced us to operate the wind tunnel at a lower free stream velocity corresponding to $Re_\Gamma = 2.10^5$. This reduced the Crow frequency down to $f_{Crow} \simeq 68Hz$, in adequation with the control range of frequencies. Thirdly the amplitude A of the string oscillations represents between 40% to 70% of the size of the gap as shown in figure A.3(a). Although this is less than the gap, it is somehow too large to fully comply with the requirements of the linear theory which imposes small perturbation of the mean flow. If we model the string oscillations as a sinusoidal displacement, then the maximum velocity u_s induced by the string is $u_s = 2\pi Af$. Values of u_s versus f_f are given in figure A.3(b). Perturbation velocities u_s imposed by the control represent a significant percentage of the free stream velocity. At the frequency of the Crow instability $f_{Crow} = 0.75$ (normalized on U_∞/c), the induced velocity is about 50% of the free stream and the amplitude of the oscillations represents 50% of the gap.

A.2 Results

A.2.1 Effect of the string diameter

Figure A.4(a) shows the influence of the diameter of the string upon the spectrum of the signal obtained with the hot wire at $z = 2.5$ and at a distance $3a$ from the top vortex of the pair (where the Crow instability was detected, see chapter 8). We observe that smaller than $1mm$ diameters have no effect on the signal. Modifications appear when the diameter is reads $\phi = 2.15$ and $2.3mm$. In these cases the energy of the signal is increased in the high frequencies.

To confirm the absence of influence of the string when $\phi \leq 1mm$, we repeated the measurement with the $1mm$ string oscillated at the Crow frequency. Results are plotted in figure A.4(b) and compared to the baseline case with no string. We see that the two curves almost superpose, meaning that below $1mm$ the string, either oscillating or not, has no effect on the instability at the location where the signal is measured. These results point out the need for $\phi > 1mm$. However, as noted earlier, the motor can not force the oscillation for such large string diameters. In order to address this problem we decided to thicken only the portion of the string which is

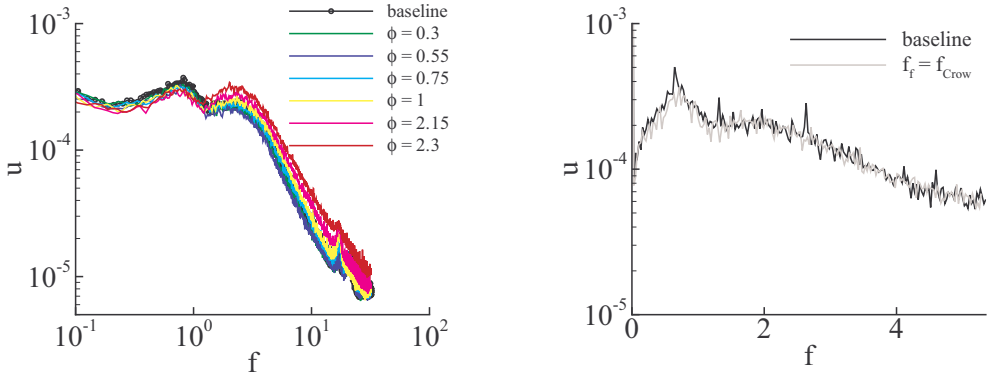

(a) String at rest

(b) Oscillating string $\phi = 1mm$

Figure A.4: Power density spectra of u. (a) Effect of the string diameter ϕ (in mm) on the spectrum. (b) Effect of the oscillation of the $\phi = 1mm$ string at $f_f = f_{Crow}$. f is normalized on U_∞/c.

in the region of the vortex pair. Therefore overall the rigidity of the string is not modified and the motor can still generate the oscillations. In practice we used a string with diameter $\phi = 0.55mm$ and slid a vinyl of diameter $\phi = 2.15mm$ over the prescribed portion.

Figure A.5 shows the comparison of the spectrum between the new string at rest and the baseline case. There is a subsequent change in the form of the spectrum with the addition of the string. Energy of fluctuations at frequencies greater than $f = 1$ (normalized on U_∞/c) are significantly increased whereas larger scale fluctuations are slightly reduced. The frequency of the vortex shedding produced by the string is indicated. No peak of energy associated to this shedding is seen in the spectrum. According to Wiltse[156], the direct excitation of the small scales in a free shear flow alters the dynamics of the energy cascade which results in an enhanced transfer of energy between the large and small scales. The situation here is similar to that described by Wiltse[156]. There is a high frequency generated by vortex shedding downstream of the string and a low frequency of the flow generated by the Crow instability. This analogy suggests that this forcing in the high frequency may be responsible for the increase of the energy cascade and thereby for the reduction of the energy of small scale fluctuations $f < 1$ (normalized on U_∞/c) and the increase of that of large scale fluctuations $f < 1$.

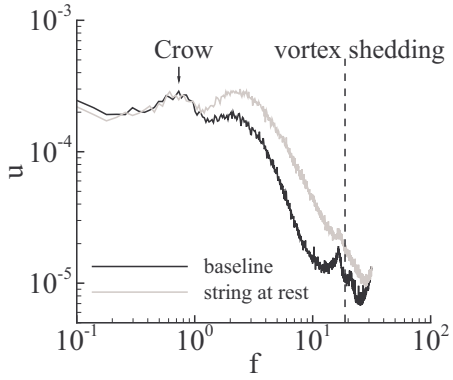

Figure A.5: Power spectral density of u. Comparison between the baseline and the case when the string $\phi = 2.15mm$ is a rest. f is normalized on U_∞/c.

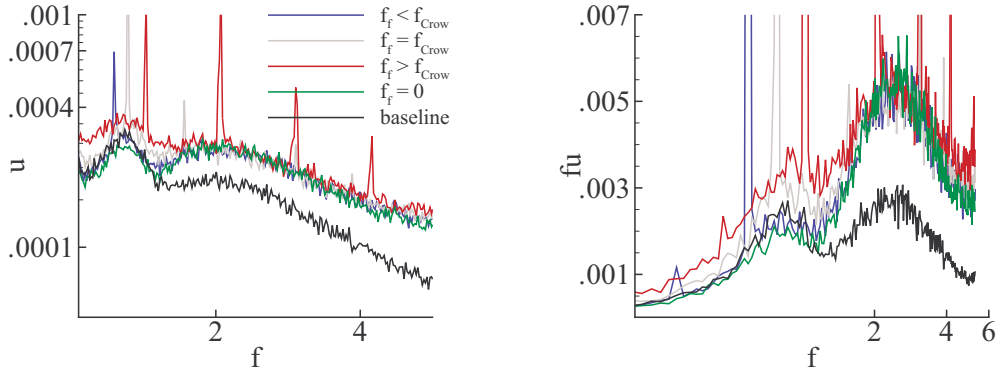

(a) (b)

Figure A.6: Power spectral density of u for various forcing frequencies f_f. (a) Log-lin plot, (b) Lin-log plot. f is normalized on U_∞/c.

A.2.2 Effect of the forcing frequency

Figure A.6 shows the modification of the spectrum when the string is oscillated for three different forcing frequencies: $f_f < f_{Crow}$, $f_f = f_{Crow}$ and $f_f > f_{Crow}$. An interesting observation is that the spectrum corresponding to $f > 1$ (normalized on U_∞/c) is the same with and without oscillations, as is evidenced by the exact superposition of the curve corresponding to the oscillating string and to the string at rest. Therefore high frequencies are not influenced by the oscillations of the string at the tested forcing frequencies. Inversely the part of the spectrum corresponding to $f < 1$ is modified by the oscillations. In the case $f_f < f_{Crow}$, no modification is observed. When $f_f = f_{Crow}$ a slight increase of the energy is observed. The increase is larger for $f_f > f_{Crow}$.

In order to evaluate the effect of the forcing frequency, we compare the energy E contained in the peak corresponding to the Crow instability with the baseline after removal of the energy contained in the ray of the forcing frequency. Results are reported in table A.1. We see that the introduction of the string without oscillations impacts unfavorably the energy of the peak. This is again the case when the string is oscillated at $f_f < f_{Crow}$ (blue line). However when it is oscillated at $f_f = f_{Crow}$ (light grey line) or $f_f > f_{Crow}$ (red line), there is a net gain of energy. Surprisingly, this gain is the greatest at the highest forcing frequency although it is not perfectly in resonance. This, as well as the loss when the frequency is lowered, may result from the increase of the amplitude of the oscillation with forcing frequency. Although it is difficult to distinguish the effect of the frequency and that of the amplitude, these results show that it is possible to increase the amplification of the Crow instability.

Forcing frequency	ΔE (%)
$f = 0$	-6
$f < f_{Crow}$	-2.3
$f = f_{Crow}$	$+8.5$
$f > f_{Crow}$	$+25$

Table A.1: Difference of energy content in the Crow instability between several forcing frequencies and the baseline case.

Conclusion

A preliminary control apparatus was designed in order to perturb the vortex pair in the symmetry plane as suggested by our results on the optimal amplification of the Crow instability. The properties of the apparatus were first described. Hot-wire measurements were then performed at the location where the Crow instability was detected in chapter 8. It is shown that the spectrum of the velocity is significantly modified when a string of diameter $\phi > 2mm$ is set at rest, on the symmetry line of the vortex pair. The energy content of the high frequencies increases while it slightly decreases at low frequencies, suggesting a mechanism of energy transfer from the large scales to the small scale as in Wiltse[156]. When the string is oscillated at the right frequency or higher, it is shown that the peak corresponding to the Crow instability is increased. Gains up to 10% are observed when $f_f \geq f_{Crow}$.

This method presents several drawbacks however. First, the string oscillations amplitude A increases with f_f and cannot be controlled. Secondly, the high velocity induced by the string oscillations does not agree with the assumption of small perturbation corresponding to the linear analysis. At last, the apparatus does not produce the right distribution of vorticity. The string sheds vorticity oriented along the x axis, as shown in figure A.7(a), but his does not corresponds to the vorticity field of the optimal perturbation described in the introduction of this chapter and in chapter 6. The optimal perturbation must be composed of y oriented vorticity periodically distorted along the z direction, as shown in figure A.7(b). The y vorticity must be moreover symmetric about the symmetry plane of the vortex pair and applied in the vicinity of the upstream stagnation point. The apparatus able to generate such a perturbation is yet to be defined.

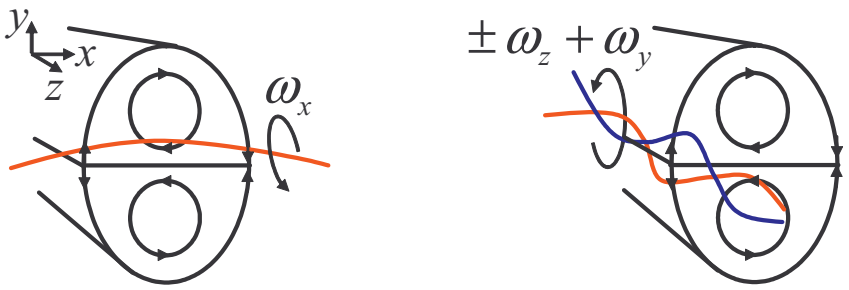

(a) (b)

Figure A.7: Vorticity induced by the control. (a) Present control. (b) Ideal control.

B Calibration of multi-hole pressure probes

Contrarily to other measurement techniques, in particular optical velocimetry (PIV, LDV), multi-hole pressure probes have the advantage that they provide a measure of the pressure for a wide range of flow angles. This information is particularly important for internal flows (turbomachines, nozzle, etc). The internal flow approach contrasts with that of most external flow investigations for which the sole measurement of the flow velocities and of the pressure at the walls allow the computation of the aerodynamic loads (lift, drag, and moments). The probe can also be advantageous in situations when the flow varies widely in magnitude and direction (see Babu[9]) as it accepts large flow angles (up to 80^o).

Most multi-hole pressure probes have nonetheless the inconvenient that they only give time-averaged quantities. Because of the small size of the probe (typically a few millimeters, so probe disturbances are small), it is difficult to include pressure sensors into the core of the probe. Sensors are in general located far from the probe and connected to it by vinyl tubes. The length and the inertia of the air contained in the tubes limit the bandwidth of the signal that gets to the sensors. If we suppose that the tubes are infinitely rigid then we can approximate that the pressure travels in the tube at the speed of sound a (in this part, a does not denote the vortex radius). If the tube length is L, the maximum frequency of the signal transported by the tube is $f_c = a/L$. For $L = 2m$ the cut-off frequency is $70Hz$. For a bandwidth of about $10kHz$, this law imposes $L \sim 30cm$. Note that the account of the flexibility of the tube causes additional reduction of the frequency cut-off.

The first probes were used with a sideslip nulling technique and they were calibrated in incidence, only. The sideslip was found by looking for the orientation of the probe that cancelled the differences between the opposed pressure external ports. As discussed by Pisasale[123], the inconvenient of this method is that it induces large flow blockages due to the sideslip adjusting mechanism in the wind tunnel test section.

Because of these short-comings non-nulling techniques that require no adjustment of the orientation of the probe in the test section were privileged. These techniques are based on a full calibration of the probe response against variations of the velocity vector and total pressure. The idea of the calibration is to subject the probe to flows of known flow direction and intensity and to use this data to build an interpolation map for the probe. In practice, two main techniques exist : the curve-fit method of Gallington[50] and the look-up table method of Zilliac[159]. Both were shown to give comparable results. A novel method based on Artificial Neural Network (ANN) also exists, see Kinser[84].

The number of data points needed for the calibration can be large. Gerner[51] uses 560 data points for a complete calibration in incompressible flow. Probe calibration is an important problem because it is expensive and time consuming. Every probe needs its own calibration which accounts for its own defects. Therefore methods that allow less calibration points are of primary interest.

Before proceeding further, we need to explain first how the pressure information delivered by the probe is related to the flow angle and magnitude. Consider for instance a seven hole pressure probe and label 7 the central port and from 1 to 6 the side ports dispatched every

60^o around the central port. A schematic of the probe head with the repartition of the holes is given in figure B.1. The flow incidence can be obtained by taking the difference between the ports 1 and 4.

$$C_{1-4} = \frac{P_1 - P_4}{\bar{P}} \tag{B.1}$$

Equivalently the side-slip relates to C_{2-5} and C_{3-6}. The pressure at the denominator is the mean pressure based on the side ports

$$\bar{P} = \sum_{i=1}^{6} \frac{P_i}{6} \tag{B.2}$$

At low flow angles $\bar{P}$ approximates the static pressure while the total pressure is measured at the central port P_7. Therefore the dynamic pressure can be evaluated by the difference between $\bar{P}$ and P_7. Of course all this is true at very low angles but in essence the principle is the same at higher flow angles.

The angular domain (angle of attack α, sideslip β) encompassed by the probe depends on the number of pressure ports. The angular domain increases with the number of ports. For example, a five hole probe (see Gerner[51]) can measure velocity vector up to 40^o. A seven holes probe will go up to 75^o. The reason for this runs in the fact that above certain angles, the flow detaches above downstream ports, which decouple the pressure information from the velocity vector. If less than two pressure ports give non detached flow information in one direction of angle then this angle can not be determined. Increasing the number of holes hence reduces this drawback and augments the limiting angle.

This detached flow phenomenon determines two regions for the probe: low angles and high angles. In the low angle regime the flow is attached over all pressure ports and the maximum pressure is measured at the central port. Typically, the angular domain of this regime corresponds to the cone angle of the probe that is generally between 30^o and 45^o. The high angle regime is defined for angles above these limits. In this regime the flow is detached over at least one port. In the case of the seven-hole pressure probe, seven sub regions can be defined depending on the side port that receives the highest pressure. Calibration techniques often use this subdivision in angular domains by applying different interpolation laws in each of them.

One fear about using probes is the interference it can provoke with the flow. It was shown by Devenport[39] that, in general, the probe does not modify the flow. An example for which the presence of a probe can be detrimental is that of vortex bursting. Using a probe in this condition is to be avoided. The vortices we investigate are however not concerned by this limitation.

The typical precision of a multi-hole pressure probe is illustrated in table B.1 from the work of Sumner[148]. It should be kept in mind that it is difficult to precisely assess the uncertainty on the measure delivered by a pressure probe. This is commonly done by testing several points outside the calibration data set. However this does not take into account parameters like the uncertainty of the calibration apparatus. Another difficulty arises when one uses the probe in a highly turbulent environment because the calibration is generally achieved in a low turbulent flow, see Tropea[153]. The effect of turbulence is therefore not accounted for in the calibration and is likely to bring large uncertainties on the measure.

Pitch angle	Yaw angle	Total pressure	Dynamic pressure	Velocity magnitude
3%	1.5%	5%	5%	3%

Table B.1: Typical precision of a seven-hole pressure probe.

This annex is devoted to a presentation of the calibration method of the seven hole pressure probe used in our wind tunnel tests only. This method is an in house method that was developed by Lesant[94]. More details can be found in this latter reference.

B.1 Data processing

B.1.1 Definition

A schematic of a seven holes pressure probe is given in figure B.1. The central hole is numbered 7 and the other at the side are numbered from 1 to 6 starting from the top. The

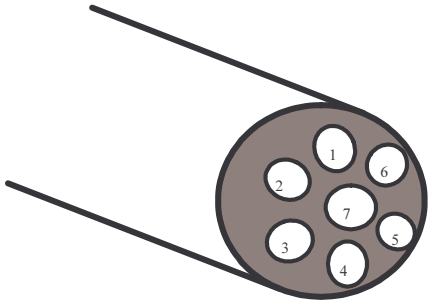

Figure B.1: Schematic of the seven holes probe and numbering of the holes.

direction of the probe being noted X, the transverse directions coplanar with the side holes are Y and Z. The velocity vector in these cartesian coordinates is $\boldsymbol{U} = (U_x, U_y, U_z)$. Two other systems of coordinates can be usefully defined, see figure B.2. The one that is used in the calibration apparatus detailed later is the polar system $(\|\boldsymbol{U}\|, \theta, \phi)$ where θ is the pitch angle and ϕ is the roll angle. Velocity components in cartesian coordinates are related to those in polar coordinates by the following relations

$$\begin{array}{rcl} U_x &=& \|\boldsymbol{U}\| cos(\theta) \\ U_y &=& \|\boldsymbol{U}\| sin(\theta) sin(\phi) \\ U_z &=& \|\boldsymbol{U}\| sin(\theta) cos(\phi) \end{array} \tag{B.3}$$

Similarly, as a function of the angle of attack α and sideslip β, we have

$$\begin{array}{rcl} U_x &=& \|\boldsymbol{U}\| cos(\alpha) cos(\beta) \\ U_y &=& -\|\boldsymbol{U}\| sin(\beta) \\ U_z &=& \|\boldsymbol{U}\| sin(\alpha) cos(\beta) \end{array} \tag{B.4}$$

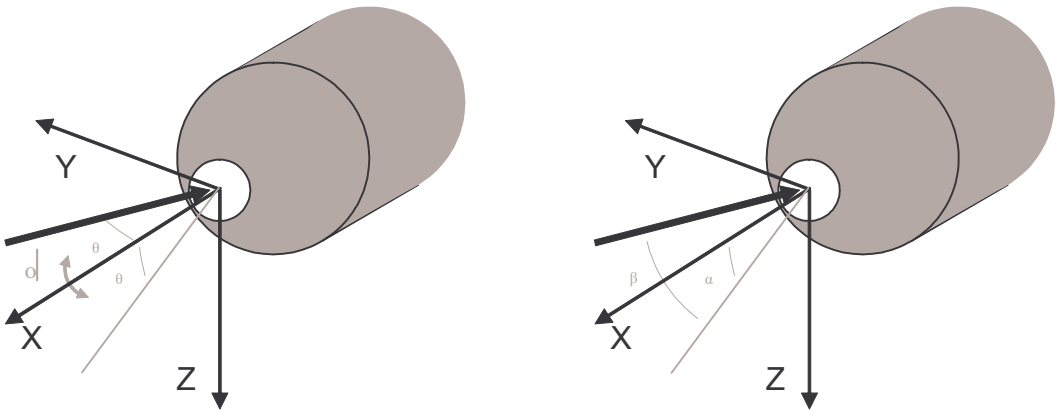

Figure B.2: Parameters for the angular orientation of the probe.

B.1.2 Calibration

In this part we detail the calibration method used for a seven holes probe. However the same method applies to a probe with a different number of holes. We first define the following 17 composite values:

i- C_1 to C_7 are the pressure at the ports. C_7 is the pressure at the central port.

ii- C_8 to C_{10} are the difference of pressure between opposed side ports. For example $C_8 = C_1 - C_4$

iii- C_{11} to C_{15} are the pressure difference between adjacent side ports. For example $C_{11} = C_2 - C_3$.

iv- C_{16} is the pressure at the central port minus the mean value taken over the external ports

v- C_{17} is the mean values over all ports.

Composites $C_{8\to10}$ correspond to the flow angle. The composite C_{16} corresponds to the velocity magnitude and C_{17} corresponds to the total pressure.

The probe is a sensor for which the input is the velocity vector (magnitude $\|\boldsymbol{U}\|$ and angles ϕ and θ, see figure B.2) and the outputs are the pressure at the ports. If we write the 17 relations between the inputs and outputs as f_k then we have

$$C_k = f_k\left(\|\boldsymbol{U}\|, \theta, \phi\right) \quad \text{for} \quad k = 1, ..., 17 \tag{B.5}$$

The objective of the data processing is to inverse this relation in order to determine the velocity vector from measurement of the pressure at the ports. Figure B.3 shows the typical evolution

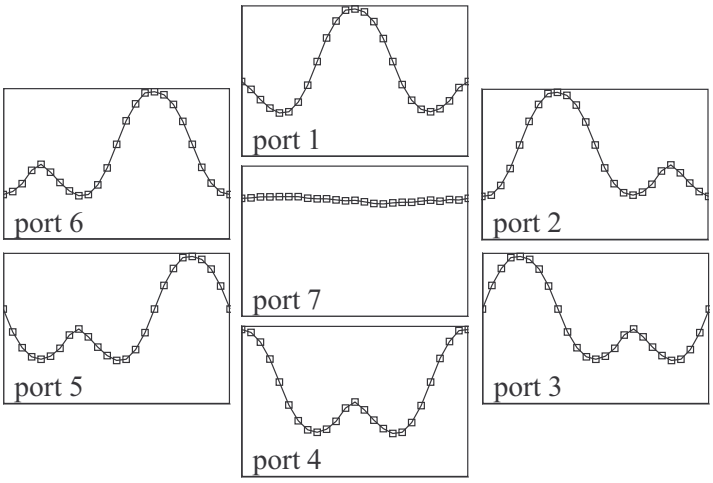

Figure B.3: Pressure at the ports as a function of ϕ. ϕ varies from 0^o to 360^o by 15^o increments.

of $C_{1\to7}$ with the roll angle ϕ for a given pitch angle θ for a regular probe. The signal C_7 at the central port does not vary as expected and the plots for the C_1 to C_6 are identical by a translation of $\pi/3$. One sees variation of the pressure over the angular range of the probe is complex. More specifically, relations f_k (B.5) are not single valued functions.

In the present method these curves are approximated locally by parabola. Every f_k is modelled by a second order polynomial function defined by parts that is valid only locally. The domain of validity is defined by $(\|\boldsymbol{U}\|, \theta, \phi)$ in $\|\boldsymbol{U}\| \pm \delta\|\boldsymbol{U}\|, \theta \pm \delta\theta, \phi \pm \delta\phi$.

$$\begin{aligned} C_k = f_k(\|\boldsymbol{U}\|, \phi, \theta) &= a_{k0} \\ &+ \|\boldsymbol{U}\|\left(a_{k1} + a_{k2}\phi + a_{k3}\theta + a_{k4}\phi^2 + a_{k5}\theta^2 + a_{k6}\phi\theta\right) \\ &+ \|\boldsymbol{U}\|^2\left(a_{k7} + a_{k8}\phi + a_{k9}\theta + a_{k10}\phi^2 + a_{k11}\theta^2 + a_{k12}\phi\theta\right) \end{aligned} \tag{B.6}$$

The entire domain S is divided into N sub-domains

$$S(i) = [\|\boldsymbol{U}\|, \theta, \phi \in (\phi(i) \pm \delta\phi, \theta(i) \pm \delta\theta, \|\boldsymbol{U}\|(i) \pm \delta\|\boldsymbol{U}\|)] \tag{B.7}$$

centered on N points $\phi(i)$, $\theta(i)$, $\|\boldsymbol{U}\|(i)$ with $i = 1, .., N$. We have that $S = \bigcup_i S(i)$. Every sub-domain $S(i)$ corresponds to an interpolation function $f_k(i)$ that models the relation between the pressure at the ports and the velocity vector and the total pressure. There is only one constraint on the local domain $S(i)$: the parabolic approximation needs to remain valid. Thus the domain $S(i)$ can not be "too large".

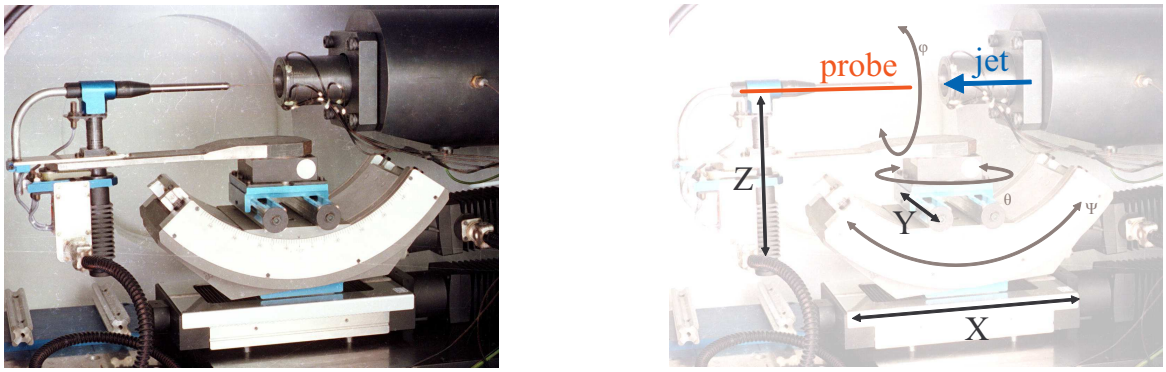

(a) (b)

Figure B.4: Open jet facility for probe calibration.

The determination of the 13 values $a_{kj}(i)$ is done by writing that $C_k(i) = f_k(i)$ for at least 13 points in $S(i)$ where C_k and $(\|\boldsymbol{U}\|, \theta, \phi)$ are simultaneously known. The relation f_k is completely determined by the coefficients $a_{kj}(i)$ for every i and k.

The inversion of the relation is performed by a Levenberg-Marquardt algorithm based on the minimization of the distance between the measured C_k and the curve $f_k(i)$ for $i = 1..N$

B.1.3 Calibration points and determination of the interpolation coefficients

The domain S is meshed with N calibration points, N being equal to $N_\theta \times N_\phi \times N_{\|\boldsymbol{U}\|}$. For a given velocity magnitude, N_θ values of θ are measured and for every value of θ, N_ϕ values of ϕ are measured. This is repeated $N_{\|\boldsymbol{U}\|}$ times, the number of velocity magnitudes that is tested. Every domain $S(i)$ is centered at the point $\phi(i), \theta(i), \|\boldsymbol{U}\|(i)$ and spans $\|\boldsymbol{U}\|(i-1)$ to $\|\boldsymbol{U}\|(i+1)$, $\theta(i-1)$ to $\theta(i+1)$ and $\phi(i-1)$ to $\phi(i+1)$. The interpolation is hence achieved in cubes that comprise three mesh points in each direction $\|\boldsymbol{U}\|$, θ and ϕ. A specific treatment is applied at the boundary of the domain (lower order interpolation).

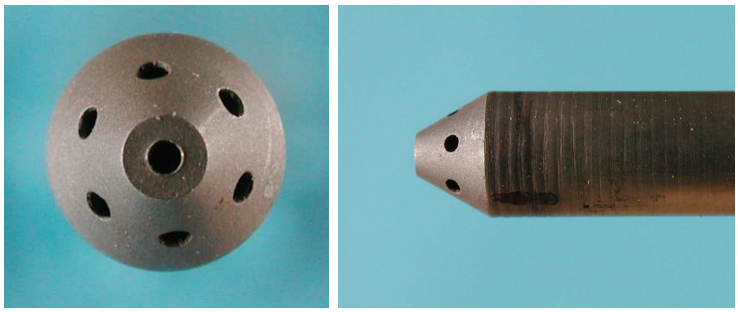

(a) Front view (b) Side view

Figure B.5: Front and side pictures of a seven-hole probe.

B.2 Illustration

B.2.1 Calibration facility

The open jet wind tunnel used for multi-hole probe calibration at ONERA-DAFE is shown in figure B.4. The probe is hardly visible because of its small diameter. The mechanical apparatus that holds the probe allows its adjustment (variations of θ, ϕ). The jet blows (from the right to the left) over a wide range of velocity and total pressure from incompressible to compressible flows.

B.2.2 Probes

Figure B.5 shows front and side views of a seven hole pressure probe. The probe diameter is $2mm$. We see that the surface of the probe have several irregularities that explain why it is unique and why every probe needs to be calibrated separately.

C Optimal perturbation of vortex pairs based on a reduced order model

In this appendix we present the numerical implementation and the application of a reduced order model (ROM) based on linear global modes for the calculation of the optimal perturbation of the vortex pair at the Crow wavelength. The results are compared to the optimal perturbation results obtained in chapter 6.

C.1 Model reduction

C.1.1 Method

We consider the linearized form of the Navier-Stokes equations for the perturbation flow $(\boldsymbol{u}, p) = (iu_x, iu_y, u_z, ip)\, e^{ikz}$:

$$\frac{\partial \boldsymbol{u}}{\partial t} + \nabla \boldsymbol{u} \cdot \boldsymbol{U} = -\nabla p + \nabla \boldsymbol{U} \cdot \boldsymbol{u} + \frac{1}{Re_\Gamma} \triangle \boldsymbol{u} \tag{C.1}$$

that we write in a matrix format $A\boldsymbol{u} = B\frac{\partial \boldsymbol{u}}{\partial t}$ with A the matrix of the linearized operator and B the projection of the perturbation field on the velocity field. This equation admits normal modes solutions in the form $\hat{\boldsymbol{u}}_j e^{\sigma_j t}$ that form a basis. Suppose we approximate a given perturbation by selecting N modes in this basis, the perturbation field is then given by

$$\boldsymbol{u} = \sum_{j=1}^{N} a_j \hat{\boldsymbol{u}}_j e^{\sigma_j t} \tag{C.2}$$

The N selected modes constitute the reduced order model for the perturbation. If N is large enough we expect that the dynamics described by the reduced order model agrees with the full simulation. With increasing N, the solution must converge towards the real perturbation. The linear combination of the modes with coefficients a_j can be usefully written in a matrix format

$$\boldsymbol{u} = \boldsymbol{V} e^{\sigma t} \boldsymbol{a} \quad \text{where} \quad \boldsymbol{V} = \begin{pmatrix} \hat{\boldsymbol{u}}_1 & \hat{\boldsymbol{u}}_2 & \hat{\boldsymbol{u}}_3 & \dots & \hat{\boldsymbol{u}}_N \end{pmatrix} \quad , \quad \boldsymbol{a} = \begin{pmatrix} a_1 \\ a_2 \\ a_3 \\ \vdots \\ a_N \end{pmatrix}$$
$$\text{and} \quad e^{\sigma t} = \begin{pmatrix} e^{\sigma_1 t} & & & & \\ & e^{\sigma_2 t} & & & \\ & & e^{\sigma_3 t} & & \\ & & & \ddots & \\ & & & & e^{\sigma_N t} \end{pmatrix} \tag{C.3}$$

where the matrix $\boldsymbol{V}$ contains the normal modes and $e^{\sigma t}$ is the matrix exponential describing the temporal evolution of these modes.

The objective of the optimization is to calculate the optimal perturbation. The optimal perturbation maximizes the kinetic energy of the initial perturbation $\boldsymbol{u}_0$ at t_{opt} among all other possible initial perturbations. The energy of the perturbation is

$$E(t) =< \boldsymbol{u}, B\boldsymbol{u} >= \int_S \boldsymbol{u}^* B\boldsymbol{u} dS \tag{C.4}$$

where S is the computational domain and * is the complex conjugate. The notation $< \cdot, \cdot >$ is the scalar product. The gain of energy is the ratio of the energy at time t to the initial energy. That's the quantity that we want to maximize. By using the matrix format and the reduced order model, we can write the energy gain like

$$G(t) = \frac{< \boldsymbol{V} e^{\lambda t}\mathbf{a}, BVe^{\lambda t}\mathbf{a} >}{< V\mathbf{a}, BV\mathbf{a} >} \tag{C.5}$$

and with further transformation

$$G(t) = \frac{< \boldsymbol{a}, e^{\sigma t *}\boldsymbol{V}^* B\boldsymbol{V} e^{\sigma t}\boldsymbol{a} >}{< \boldsymbol{a}, \boldsymbol{V}^* B\boldsymbol{V}\boldsymbol{a} >} \tag{C.6}$$

Let us write $Q_t = e^{\sigma t *}\boldsymbol{V}^* B\boldsymbol{V} e^{\sigma t}$. The optimization amounts to finding the maximum eigenvalue α_{max} and its corresponding eigenvector $\boldsymbol{a}_{max}$ of the following eigenvalue problem

$$Q_t\boldsymbol{a} = \alpha Q_{t=0}\boldsymbol{a} \tag{C.7}$$

To solve this problem, one need to do the following steps:

i- Calculate N normal modes $\boldsymbol{u}_j$ of the base flow $\boldsymbol{U}$ and their complex frequency σ_j

ii- Calculate the matrix Q_t of the scalar products between the N modes

iii- Compute the eigenvalues of problem (C.7)

In practice an important question when building a reduced order model concerns the choice of the modes. In the present case, it seems legitimate to take the N most amplified modes. However other solutions could be adopted. For instance, a filtering of the modes can first be applied to evacuate certain modes that would not be appropriate based on either numerical or physical arguments.

C.1.2 Numerical implementation

Once the N modes are calculated and selected, a list is created in which the modes are ordered by decreasing growth rate. The cross-products between modes are then calculated in order to build the matrix $Q_{t=0}$. This matrix being hermitian, only the upper right triangle is calculated. At this point we use the *zheev* routine of the LAPACK library (see Anderson[3]) to check that the eigenvalues of the matrix $Q_{t=0}$ are real (a hermitian matrix is characterized by real eigenvalues). The matrix Q_t is eventually calculated by multiplying $Q_{t=0}$ by the exponential matrix $e^{\sigma t}$ and its transpose conjugate.

The resolution of the matrix eigenproblem is achieved by the routine *zggev* in LAPACK that computes the eigenvalues and eigenvectors of a complex nonsymmetric matrix problem. This is preferred to the routine *zhegv* that deals with a Hermitian definite eigenproblem that should in principle be used since the matrix Q_t is hermitian positive. The *zggev* routine is more robust in case numerical difficulties arise (for instance numerical precision can deteriorate the differences between certain modes and render the matrix Q_t non hermitian). It gives complex eigenvalues which imaginary part is zero if the matrix Q_t is hermitian and deviate from zero otherwise. Therefore the imaginary part gives a useful estimate of the quality of the reduced order model and of the numerics.

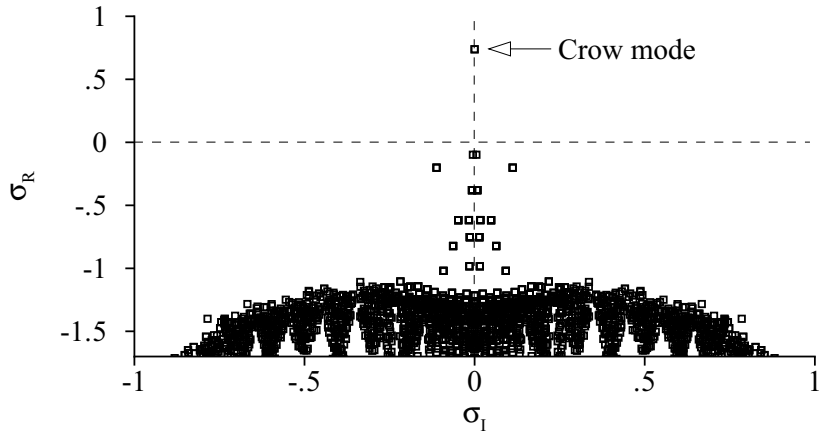

Figure C.1: Spectrum of the normal mode frequencies.

C.2 Results

C.2.1 Spectrum

The method was applied to the case of the Crow instability in the vortex pair at $a/b = 0.2$, $k = 0.18$ at infinite swirl number and $Re_\Gamma = 4000$ and $t_{opt} = 6$. In this case, we already have the optimal curve that was obtained by using the adjoint in chapter 6. This result is the baseline result against which the results delivered by the reduced order model is to be compared. In the absence of axial flow in the core of the vortices, every normal mode of frequency σ has a corresponding mode of frequency σ^*. Therefore only one half of the spectrum corresponding to $\sigma_I > 0$ was computed. The method used to compute the normal modes is described in chapter 3. Figure C.1 shows the spectrum of the normal mode frequencies. The Crow mode is the only one that has a positive growth rate. Note that the growth rate σ_R is normalized on t_b (see (2.27)) and the temporal frequency σ_I is normalized on t_a.

C.2.2 Optimal gain

The optimal gain was calculated for $N = 400$ and $N = 796$ modes. We observe that the two curves are very close to each other but there is no convergence towards the optimal result obtained with the adjoint mode.

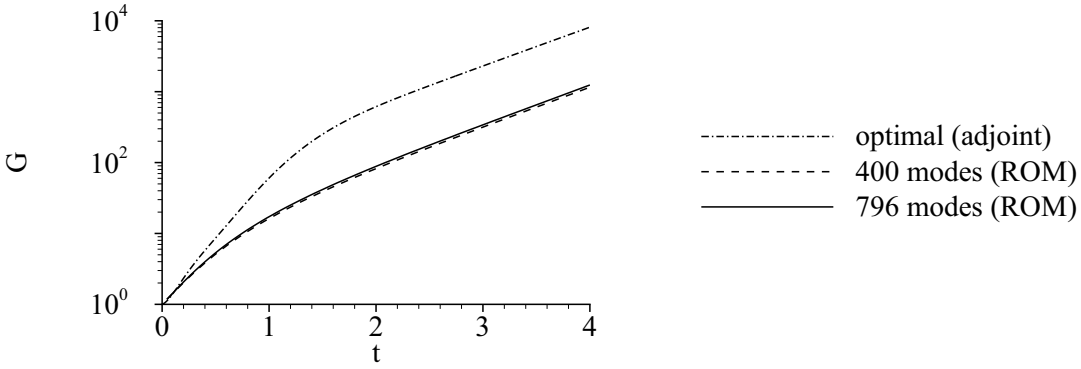

Figure C.2: Optimal amplification G as a function of time normalized on t_b for $t_{opt} = 6$. Comparison between the results obtained with the ROM and that obtained with the adjoint mode (result detailed in chapter 6).

C.3 Conclusion

This section described an optimization technique based on a reduced order model for the perturbations in the vortex pair at the wavelength of the Crow instability. We first presented the method and its numerical implementation. The results were then detailed. Although a relatively large number of modes were used, the convergence is not attained. However the shape of the optimal curve is retrieved.

The failure of the reduced order model to converge with a low number of modes may be a sign that the normal modes may not be an adequate basis. This idea is supported by the fact that normal modes are not modes based on an energetic criterion, but modes that describe the dynamics contained in the linear equations. This failure may be a hint that ROM should be built on different basis. Alternatives exist: POD, balanced POD for example.

D Impulse of a vortex in the vicinity of a wall

In this part we investigate the moment of the vorticity distribution in the semi-plane schematized in figure D.1, bounded by a wall at $y = 0$ and containing one vortex placed at (x_c, y_c). This plane is denoted by V and its frontier is ∂V.

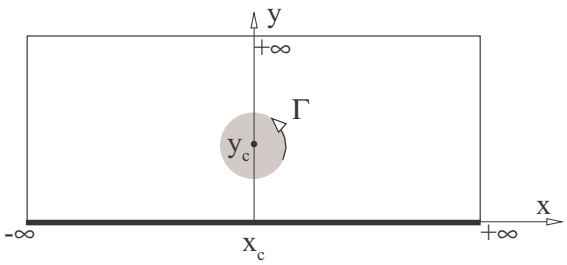

Figure D.1: Schematic of the vortex in the vicinity of a wall. The grey disk denotes the vortex, placed at (x_c, y_c). The wall is represented by the thick line at $y = 0$.

The goal here is to explain the effect of the wall on the dynamics of the vortex, in particular its drifting motion.

D.1 Definition

D.1.1 Circulation

The circulation Γ is given by

$$\Gamma = \int_{\partial V} \boldsymbol{u} \cdot \boldsymbol{n} dl = \int_{-\infty}^{\infty} \int_{0}^{\infty} \omega dx dy \tag{D.1}$$

where $\boldsymbol{n}$ is the local direction of the curve enclosing V.

D.1.2 Impulse

The impulse of the fluid contained in V is a vector denoted $\boldsymbol{I}$ and defined by

$$\boldsymbol{I} = \int_V \boldsymbol{x} \times \boldsymbol{\omega} dx dy = \begin{pmatrix} \int_V y\omega dx dy \\ \\ -\int_V x\omega dx dy \end{pmatrix} \tag{D.2}$$

We use the following notation for the x and y components of the impulsion:

$$\begin{aligned} I_x &= \int_V x\omega dxdy \\ I_y &= \int_V y\omega dxdy \end{aligned} \tag{D.3}$$

The barycenter (x_c, y_c) of the vorticity is deduced from the previous quantities

$$\begin{aligned} x_c &= \frac{I_x}{\Gamma} \\ y_c &= \frac{I_y}{\Gamma} \end{aligned} \tag{D.4}$$

D.2 Time variation

The circulation Γ, and the impulse components I_x and I_y are conserved for a domain enclosing isolated vorticity. This is not true anymore in the presence of a wall because the wall induces losses of vorticity by friction. We have from the equation of axial vorticity

$$\frac{\partial \omega}{\partial t} + (\boldsymbol{u} \cdot \nabla)\,\omega = \nu \Delta \omega \tag{D.5}$$

This equation states that vorticity is a planar transported scalar that diffuses by viscosity.

D.2.1 Circulation

The time derivative of the circulation is

$$\frac{d\Gamma}{dt} = \int_V \frac{\partial \omega}{\partial t} dxdy \tag{D.6}$$

Using (D.5), we have

$$\frac{d\Gamma}{dt} = \int_V \left(-u_x \frac{\partial \omega}{\partial x} - u_y \frac{\partial \omega}{\partial y} + \nu \Delta \omega \right) dxdy \tag{D.7}$$

Using the continuity $\dfrac{\partial u}{\partial x} + \dfrac{\partial v}{\partial y} = 0$ equation, the first term in the RHS of (D.7) can be transformed in the following way

$$\int_V \left(-u_x \frac{\partial \omega}{\partial x} - u_y \frac{\partial \omega}{\partial y} \right) dxdy = \int_V \left(-\frac{\partial u\omega}{\partial x} - \frac{\partial v\omega}{\partial y} \right) dxdy = -\int_{\partial V} \boldsymbol{n} \cdot \begin{pmatrix} u_x\omega \\ u_y\omega \end{pmatrix} ds \tag{D.8}$$

while the second term in the RHS of (D.7) gives

$$\int_V \Delta\omega dxdy = \int_{\partial V} (\boldsymbol{n} \cdot \nabla)\,\omega ds = \int_{-\infty}^{+\infty} \frac{\partial \omega}{\partial y}|_{y=0} dx \tag{D.9}$$

Finally we see that the circulation is decreased due to the viscous friction at the wall

$$\frac{d\Gamma}{dt} = -\nu \int_{-\infty}^{+\infty} \frac{\partial \omega}{\partial y}|_{y=0} dx \tag{D.10}$$

D.2.2 Variation of the impulse

Following the same method, we have that the variation of the y component of the impulse is

$$\frac{dI_x}{dt} = \int_V x \frac{\partial \omega}{\partial t} dxdy \tag{D.11}$$

Using (D.5), we have

$$\frac{d\Gamma}{dt} = \int_V \left(-xu_x \frac{\partial \omega}{\partial x} - xu_y \frac{\partial \omega}{\partial y} + \nu x \Delta \omega \right) dxdy \tag{D.12}$$

The following relation holds

$$\int_V \left(-xu_x \frac{\partial \omega}{\partial x} - xu_y \frac{\partial \omega}{\partial y} \right) dxdy = \int_{-\infty}^{+\infty} \frac{u_x^2}{2}|_{y=0} dx \tag{D.13}$$

This term vanishes if no slip boundary condition holds at $y = 0$. We finally get

$$\frac{dI_x}{dt} = -\int_{-\infty}^{+\infty} \frac{u_x^2}{2}|_{y=0} dx - \nu \int_{-\infty}^{+\infty} x \frac{\partial \omega}{\partial y}|_{y=0} dx \tag{D.14}$$

The variation of the x component of the impulse is given by

$$\frac{dI_y}{dt} = \int_V y \frac{\partial \omega}{\partial t} dxdy \tag{D.15}$$

Using the same artifact as previously, one obtains

$$\frac{dI_y}{dt} = -\nu \int_{-\infty}^{+\infty} \omega|_{y=0} dx \tag{D.16}$$

D.2.3 Inviscid limit

For an inviscid medium the previous results write

$$\boxed{\begin{aligned} \frac{d\Gamma}{dt} &= 0 \\ \frac{dI_x}{dt} &= 0 \\ \frac{dI_y}{dt} &= -\int_{-\infty}^{+\infty} \frac{u_x^2}{2}|_{y=0} dx \end{aligned}} \tag{D.17}$$

The velocity u induced by the dipole at $y = 0$ is

$$u_x = \frac{\Gamma y_c}{\pi \left(x^2 + y_c^2 \right)} \tag{D.18}$$

and the integral of the $u^2/2$ term being

$$\int_{-\infty}^{+\infty} \frac{u_x^2}{2}|_{y=0} dx = \frac{\Gamma^2}{2\pi^2 y_c} \int_{-\infty}^{+\infty} \frac{dx}{\left(x^2 + 1 \right)^2} = \frac{\Gamma^2}{2\pi b} \tag{D.19}$$

We have that

$$\frac{dx_c}{dt} = \frac{\Gamma}{4\pi y_c} \tag{D.20}$$

In an inviscid medium, the dipole hence drifts steadily at a velocity $U_{drift} = \dfrac{\Gamma}{2\pi b}$.

D.2.4 Effect of the viscosity

For a viscous fluid, from (D.10), (D.14) and (D.16), it comes

$$\boxed{\begin{aligned}\frac{d\Gamma}{dt} &= \nu\int_{-\infty}^{+\infty}\frac{\partial^2 u_x}{\partial y^2}|_{y=0}dx\\ \frac{dI_x}{dt} &= \nu\int_{-\infty}^{+\infty}x\frac{\partial^2 u_x}{\partial y^2}|_{y=0}dx\\ \frac{dI_y}{dt} &= \nu\int_{-\infty}^{+\infty}\frac{\partial u_x}{\partial y}|_{y=0}dx\end{aligned}} \tag{D.21}$$

where we have used the relation between the vorticity and the velocity. The barycenter of the vorticity (x_c, y_c) moves according to the following relations

$$\begin{aligned}\frac{dx_c}{dt} &= \frac{1}{\Gamma}\frac{dI_x}{dt} - \frac{x_c}{\Gamma}\frac{d\Gamma}{dt}\\ \frac{dx_c}{dt} &= \frac{1}{\Gamma}\frac{dI_x}{dt} - \frac{x_c}{\Gamma}\frac{d\Gamma}{dt}\end{aligned} \tag{D.22}$$

The motion parallel to the wall is described by the first equation, which gives

$$\frac{dx_c}{dt} = \frac{\nu}{\Gamma}\int_{-\infty}^{+\infty}(x-x_c)\frac{\partial^2 u_x}{\partial y^2}|_{y=0}dx \tag{D.23}$$

At the wall $y = 0$ the Navier-Stokes equation for the x direction reduces to the equilibrium between the pressure gradient and viscous diffusion, namely:

$$0 = -\frac{1}{\rho}\frac{\partial p}{\partial x} + \nu\frac{\partial^2 u_x}{\partial y^2} \tag{D.24}$$

so that (D.23) becomes:

$$\frac{dx_c}{dt} = \frac{1}{\rho\Gamma}\int_{-\infty}^{+\infty}(x-x_c)\frac{\partial p}{\partial x}dx \tag{D.25}$$

Figure D.2(a) schematizes how pressure varies in the vicinity of the vortex, the latter being a low pressure region. We see that $\partial p/\partial x$ is positive (negative) for x positive (negative), so that the sign of the integral in (D.25) is dictated solely by the sign of Γ. Therefore for a positive (negative) circulation, the vortex drifts to the right (left). This is in agreement with the observed motion.

The pressure induced by the vortex is hardly modified by the wall. A good model of the pressure variations is obtained by considering the velocity u induced by the vortex pair at its mid-plane, which was already given in (D.18). Using Bernoulli's formula, pressure at the wall is

$$p = p_\infty - \frac{1}{2}\rho u_x^2 \tag{D.26}$$

and

$$\frac{\partial p}{\partial x} = \frac{4\rho\Gamma y_c^2}{\pi^2}\frac{x-x_c}{\left(y_c^2+(x-x_c)^2\right)^3} \tag{D.27}$$

Finally, (D.25) leads to

$$\frac{dx_c}{dt} = \frac{2\Gamma}{\pi^2 y_c}\int_{-\infty}^{+\infty}\frac{x^2}{(1+x^2)^3}dx = \frac{\Gamma}{2\pi b} \tag{D.28}$$

The inviscid value of the drift velocity is retrieved, which shows that, concerning the drift velocity, the effect of the wall is exactly the same as that of an image vortex.

Note that vorticity of sign opposite to that of the vortex is induced at the wall by the no-slip boundary condition. This is schematized in figure D.2(b). Qualitatively, this vorticity also explains the drifting motion of the vortex. As is observed in chapter 7, this wall vorticity is entrained upward by the vortex and causes its rebound.

(a) (b)

Figure D.2: (a) Pressure gradients induced by the vortex. (b) Schematic of the vorticity layer induced at the wall by the no-slip boundary condition.

E Optimal perturbation of a vortex sheet for fast destabilization of the trailing vortices

The following study is based on the optimal perturbation analysis corresponding to chapter 6. The difference is that we now consider the roll-up of the vortex sheet issuing from a lifting wing as the base flow. This work was presented in the AIAA conference that took place in Seattle in 2008.

Abstract

In this paper we investigate by numerical simulations the evolution of three-dimensional perturbations on a rolling-up vortex sheet produced by a wing that flies at constant speed. The objective is to find mechanisms of energy growth that allow large amplification of energy at the wavelength of the Crow instability in the far field of the wake of aircrafts. A direct two-dimensional simulation of the vortex sheet shows that the flow spirals into two opposite trailing vortices. We first evaluate the end of the roll-up stage by comparing the distribution of vorticity in the vortices to that of a Lamb-Oseen vortex. Then a stability analysis of the steady trailing vortices indicates that the flow is unstable to the Crow instability. An optimal perturbation is used to investigate the mechanisms of energy growth in the rolling-up vortex sheet at the wavelength of previously characterized Crow instability. A mechanism at short time is found that corresponds to an Orr mechanism which is related to the mean shear in the vortex sheet and a large time mechanism is also observed that is related to the optimal amplification of the Crow instability by initial vorticity in the middle plane of the wake already investigated by Brion [23].

Nomenclature

x, y, z	Cartesian coordinates
Γ	Circulation
l	Semi-span of the vortex sheet
d	Thickness of the vortex sheet
S	Computational domain
U, V, P	Base flow velocity and pressure
u, v, w, p	Perturbation velocity and pressure
ν	Kinematic viscosity
Re	Reynolds number
$E(t)$	Energy of the perturbation

P_i Snapshot of the base flow at time t_i

E.1 Introduction

The security of air traffic depends on several parameters, one of great importance being the wake vortex hazard issue. The use of large aircrafts has increased the necessity to alleviate the danger associated by the trailing vortices. As no solution has been found so far, the safety of air traffic especially at landing relies on separation rules between following aircrafts, with great penalty for the largest. With this issue as a motivation, many scientific studies have looked into the dynamics of these trailing vortices in the past century. Although very stable coherent structures, trailing vortices were shown to be unstable to two types of three-dimensional instabilities : the Crow and Widnall instabilities, that are respectively characterized by large and short wavelengths. These discoveries marked the beginning of plans to use these instabilities to destroy the trailing vortices. In this view, Fabre[43] and Crouch[33] showed that four vortex systems can increase significantly the growth rate of the Crow instability. Recent experiments using real aircrafts equipped with flapping devices tend to prove the validity of such systems (private communication). The work of Brion[23] showed the more general result that the Crow instability can be amplified optimally by perturbing the trailing vortices in their middle plane by vertically distributed axial vorticity at the wavelength of Crow. Such initial vorticity is amplified at the lower hyperbolic stagnation point of the vortex pair and induces the Crow instability at least twice faster than in the case when no initial perturbation is applied.

Although of considerable interest, these approaches neglect one important phenomenon on the practical point of view. The near field of the aircraft wake sees the formation of the trailing vortices by the roll-up of the initial wake produced at the wing trailing edge. As the control of the wake can only be performed from the body of the aircraft (distant actuation like plasma remains science fiction for this kind of application), it implies that the effect of the roll-up needs to be evaluated in order to correctly design such systems. This observation is the main motivation of the present work. The idea is to model a wing flying at constant velocity by a vortex sheet and to study the evolution of three-dimensional perturbations imposed to the flow.

As explained by Saffman [130] the vortex sheet is not an equilibrium solution and spirals due to the infinite velocity at the tips into a pair of counter rotating vortices. The evolution of the vortex sheet is described by the Birkhoff-Rott equation. Among others, Moore [114], Kaden [80] and Schwartz [134] worked on the solution of this equation in the case of the semi-infinite one-dimensional vortex sheet and derived important laws to describe the roll-up. Although an important matter, the effect of three-dimensional perturbation on finite vortex sheets seems to have never been investigated before, see Saffman [130]. Abid[1] look at the stability of a vortex sheet roll-up at the Kelvin Helmholtz instability but the sheet they consider is infinitely periodic.

The objective of the study is to find linear mechanisms of amplification of the energy of the perturbations imposed to the rolling-up vortex sheet at the wavelength of the Crow instability that affects the final trailing vortices. Considering aircraft wakes, such mechanisms could help destabilizing the trailing vortices. The investigation is performed by numerical tools that include direct simulations by a finite element method and an optimal perturbation algorithm based an adjoint approach.

The study of linear mechanisms of energy amplification has been related to a modal approach of the linearized dynamics for a long time. Yet the insufficiency of this approach resulted in the study of transient growth of energy which has lead to important advances in the past decade (see Schmid [133]). The identification of the lift-up and Orr mechanisms in plane shear flows (see Butler and Farrel [25]) as well as the recent discovery of transient energy growth in single vortices by Antkowiak[5] and Pradeep[124] allow for a better comprehension of the transition of many types of flow. Transient analysis are based on optimal perturbation algorithms. The

specificity here is that the base flow varies in time, contrarily to most perturbation analysis. We will see that the unsteadiness of the base flow brings up specific problems for the calculation of the perturbations.

The paper is organized as follows. First the evolution of the vortex sheet is described along with the numerical method. We then explain the mathematical framework of the perturbation analysis and the optimal perturbation algorithm. In the third part we discuss the results obtained by the former analysis.

E.2 The vortex sheet

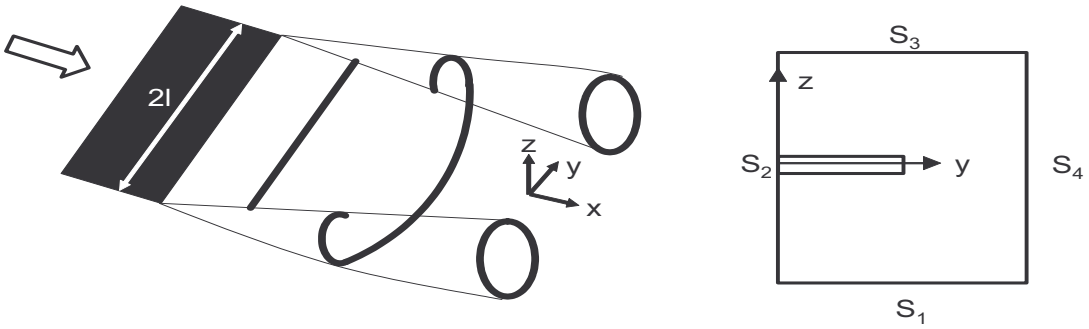

Figure E.1: Roll-up of the vortex sheet produced by a wing (left) and computational domain $S = \{(y, z)|y > 0\}$ (right).

A three-dimensional wing set in motion in an incompressible fluid with constant velocity is represented by a two dimensional vortex sheet of strength $\omega(y, z)$ normal to the direction of motion as schematized in figure E.1. Cartesian coordinates are used throughout the study with x the axial direction of motion, y the span wise direction and z the vertical direction. The length of the initial vortex sheet is $2l$ and its strength is Γ. For numerical reasons, we decided to model the wake of a cusped that has a vanishing chord at its tip which results in zero vorticity at the tips of the vortex sheet. Therefore we circumvent the problem of dealing with infinite tip vorticity like in the case of the elliptical loading. The case of the cusped wing was examined by Schwartz [134] who gives the following shape for the vorticity distribution along the span

$$\omega(y, z) = y/l \left(1 - y^2/l^2\right)^{3/2} e^{-\frac{z^2}{d^2}} \quad , \quad \Gamma = \int_S \omega(y, z) dy dz \tag{E.1}$$

where ω is the axial vorticity along x. Compared to the formula given in the article, we add the term $e^{-\frac{z^2}{d^2}}$ where d is the thickness of the vortex sheet. A ratio $d/l = 0.05$ is used. The integration domain S corresponds to positive values of y. Thinner vortex sheet would have been preferred for better realism but as the thinness increases the refinement of the mesh, it is the limited computing resources that drove our choice.

The span of the wing serves as the reference length scale. The time reference is the turn over time of the initial vortex sheet is equal to $t^* = \frac{4l^2}{\Gamma}$ which is the mean time a particle of fluid needs do one revolution in the initial vortex sheet. The Reynolds number is $Re = \frac{\Gamma}{\nu}$ where ν is the kinematic viscosity of the fluid. In the study, we set $Re = 4000$. The flow is described by the velocity and pressure field $(U, V, 0, P)$ and evolves according to the incompressible Navier-Stokes equations in cartesian coordinates and constant density :

$$\begin{gathered} \partial_t \boldsymbol{U} + \boldsymbol{U}\nabla\boldsymbol{U} = -\nabla P + \tfrac{1}{Re}\Delta\boldsymbol{U} \\ \nabla \cdot \boldsymbol{U} = 0 \\ \boldsymbol{U}(t = 0) = \boldsymbol{U}_0 \end{gathered} \tag{E.2}$$

The solution of these equations is obtained by numerical computations that are carried out throughout the study by a finite element method. We use P2-P1 Taylor-Hood elements for space discretization (P2 for the velocity and P1 for the pressure) and a second order time scheme. The numerical solver has been validated in previous studies [23]. The computational domain shown in figure E.1 is rectangular with dimensions of the following extent $\{y = 0, 5l; z = -3l, 3l\}$ to ensure independence to wall effects. Only half of the vortex sheet is computed, the other half influence being modelled by a symmetry boundary condition at the $y = 0$ boundary (S2). The vortex sheet moves downward under self induction. To keep the vortical region in the fine mesh in the center of the domain, we impose the inlet velocity $\Gamma/4\pi l$ at the bottom boundary S1 and a Neumann condition at the top boundary S3. The boundary condition at the side S4 is also a symmetry condition. The convergence of the numerical discretization was controlled

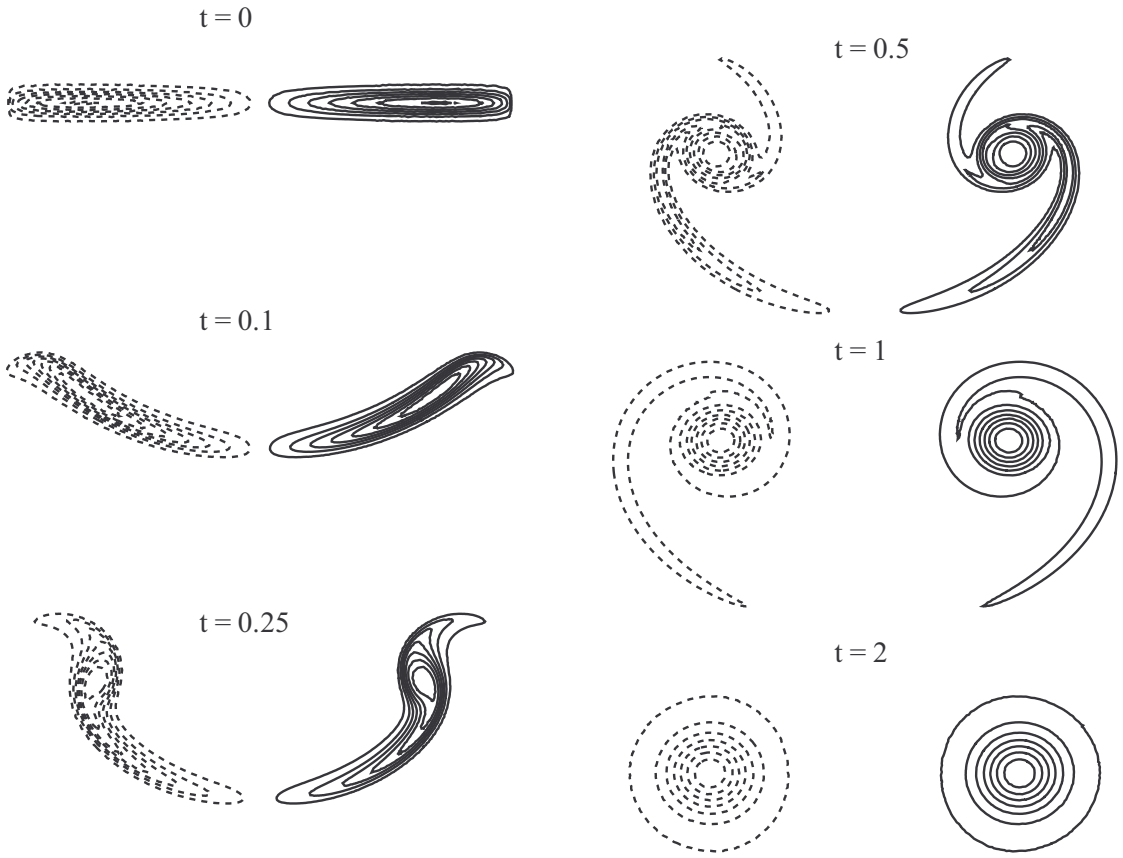

Figure E.2: Contours of the axial vorticity of the base flow between $t = 0$ and $t = 2$. The initial vortex sheet rolls-up into two opposite vortices. Dashed line indicate negative vorticity. The minimum contour value is always at least an order of magnitude smaller than the maximum.

by comparing the results with those obtained by doubling either the size of the computational domain or the refinement. The variation of the circulation Γ did not exceed 1% in all simulations and the value of $\int_S y\omega dS$ did not show variations greater than 4%.

The evolution of the vortex sheet computed numerically from time 0 to time 3.75 is shown in figure E.2. The sheet is flat at the beginning and spirals quickly until $t = 2$ when two opposite axisymmetric vortices are clearly formed. We characterize these vortices by their aspect ratio a/b where is a is their radius (taken at the maximum of tangential velocity) and b the distance between the centers of vorticity (taken at the maximum of vorticity). It is found that $a/b = 0.15$

at final time $t = 3.75$. As a Lamb-Oseen vortices, these vortices of small aspect ratio evolve mainly through viscous diffusion which increases their core size. The viscous time scale in this study is $t_\nu = 4l^2/\nu$ and is much smaller than t^* as $t^*/t_\nu = 1/Re$. Two periods of the evolution of the vortex sheet can hence be distinguished. The first period until $t = 2$ is the roll-up and the second period from $t = 2$ corresponds to the slow diffusion of the vortices.

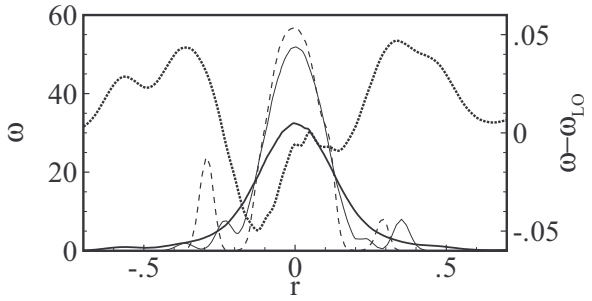

Figure E.3: Profile of the axial vorticity (left axis) at $t = 0.5$ (dashed line), $t = 1$ (thin line) and $t = 2$ (thick line) and comparison (dotted line) $\omega - \omega_{Lamb-Oseen}$ of the profile at $t = 2$ to that of a Lamb-Oseen given by $\omega_{Lamb-Oseen} = \Gamma/\pi a^2 e^{-r^2/a^2}$ where a and Γ are identical that to the flow at $t = 2$. Note that the profiles of vorticity have been extracted along direction where variations were the greatest.

To check the end of the roll-up period at $t = 2$, we plot in figure E.3 the radial profiles of vorticity about the maximum of vorticity at $t = 0.5, 1, 2$. The profiles at $t = 0.5$ and $t = 1$ exhibit bumps of vorticity outside the core region which correspond to the filaments of vorticity that spiral around the core at these snap shots. At $t = 2$ these bumps of vorticity become negligible in the profile and the difference with the Lamb-Oseen becomes very small (less than 4% as shown by the dotted line). All the vorticity of the wake is confined into the vortices after $t = 2$.

E.3 Perturbation analysis

The evolution of small perturbations $\boldsymbol{u}(y, z, t)e^{ikx}$ superimposed on the base flow $\boldsymbol{U}(y, z, t)$ with k the axial wavenumber, $\boldsymbol{u} = (u, v, w, p)$ the three-dimensional perturbations and $\boldsymbol{U}(t) = (0, V, W, P)$ the time dependent base flow is described by the incompressible linearized Navier-Stokes equations

$$\begin{gathered} \partial_t \boldsymbol{u} + \boldsymbol{U}(t)\nabla\boldsymbol{u} = -\nabla p - \boldsymbol{u}\nabla\boldsymbol{U}(t) + \tfrac{1}{Re}\Delta\boldsymbol{u} \\ \nabla \cdot \boldsymbol{u} = 0 \\ \boldsymbol{u}(t = 0) = \boldsymbol{u}_0 \end{gathered} \tag{E.3}$$

where $\boldsymbol{n}$ is the normal vector at the boundary of S and $\boldsymbol{u}_0$ is the initial perturbation. The solution of these equations are obtained by the finite element method described earlier. The base flow represents the evolution of the vortex sheet from $t = 0$ to $t = 7.5$. It description is given in figure E.4. Between $t = 0$ and $t = 2$, the vortex sheet spirals. At $t = 2$ the two trailing vortices are formed and evolves by diffusion until $t = 3.75$. Between $t = 3.75$ and $t = 7.5$ the base flow is frozen in order to save computational time in the computation of the linearized equations. This choice is legitimated by the fact that the time scale $t_{tv} = 2\pi a^2/\nu$ of

Initial sheet	$\xrightarrow{roll-up}$	Vortex pair	$\xrightarrow{freeze}$	Vortex pair
0		3.75		7.5

Figure E.4: Description of the base flow for the linear study.

the trailing vortices is very large compared to the time scale $t_{pert} = 2\pi b^2/\Gamma$ of the perturbations as $t_\nu/t_{pert} = Re(a/b)^2 \simeq 10^2$. It can be considered that the perturbations evolve on a steady base flow when the trailing vortices are formed. The stability of this final stage of the base

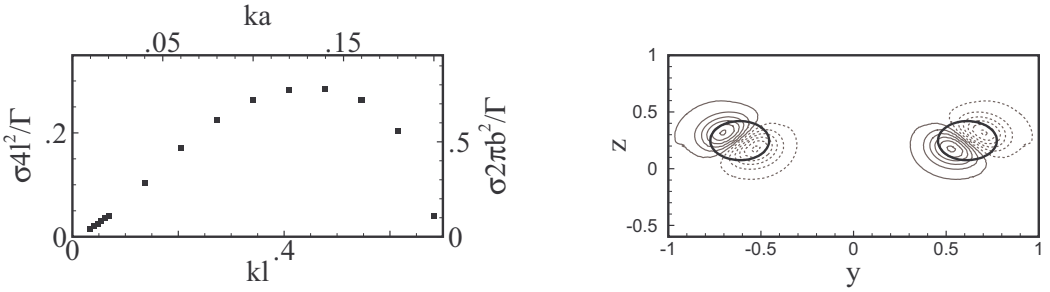

(a) (b)

Figure E.5: (a) Growth rate σ of the most unstable mode at time $t = 3.75$ as a function of the wavenumber. (b) Contours of the axial vorticity corresponding to the Crow instability.

flow evolution is investigated by the method presented in Brion [23] which solves a generalized eigenvalue problem $A\hat{\boldsymbol{u}} = \sigma B\hat{\boldsymbol{u}}$, where A represents the direct linearized equations with the steady trailing vortices. The wavenumber of the perturbations is varied in order to find the most amplified perturbation. Figure E.5 shows the growth rate of the leading eigenmode (these modes are steady). The structure of the most unstable mode at $k = 0.48$ displayed in the right represents the displacement of the vortices in a plane at about 45 degrees about the horizontal which characterizes the Crow instability. We use the usual (see Crow [34]) normalization in the right and top axis lines in order to check the validity of the computations. The adjoint mode of the Crow instability obtained by solving $A^+\hat{\boldsymbol{u}} = \sigma B\hat{\boldsymbol{u}}$ where A^+ is the adjoint matrix is also computed.

The base flow after roll-up is unstable at the wavelength of Crow. Therefore if the initial vortex sheet is perturbed at this wavelength, the Crow instability will naturally grow in the trailing vortices. However the time when the Crow instability will appear depends on the initial perturbation. We already know that large amplification of perturbation energy is possible in vortical flows (see Antkowiak [5] and Brion [23]). We expect it to be the case here. Therefore a well chosen perturbation should be able to boost the Crow instability in the base flow. To find such an initial perturbation we use an optimization algorithm that maximizes the energy of the perturbation at time t given a unitary initial energy

$$E(t) = \|\boldsymbol{u}\|^2 \text{ given } E(0) = 1 \tag{E.4}$$

and the algorithm solves

$$\max_{\boldsymbol{u}_0} E(t) \tag{E.5}$$

The energy is based on the following scalar product

$$< \boldsymbol{u}_1, \boldsymbol{u}_2 >= \int_\Omega (u_1^* u_2 + v_1^* v_2 + w_1^* w_2)\, dydz \tag{E.6}$$

where * denotes the complex conjugate. The algorithm used for $t \in [0, 7.5]$ gives the curve of the optimal energy gain as a function of the time of optimization and the corresponding optimal perturbation $\boldsymbol{u}_0$. The details of the algorithm are given in the appendix. It relies on a gradient method based on adjoint linearized simulations which equations write

$$\begin{gathered} \partial_t \boldsymbol{u}^+ - \boldsymbol{U}(T-t)\nabla\boldsymbol{u}^+ = -\nabla p^+ - \boldsymbol{u}^+\nabla\boldsymbol{U}^T(T-t) + \tfrac{1}{Re}\Delta\boldsymbol{u}^+ \\ \nabla\cdot\boldsymbol{u}^+ = 0 \\ \boldsymbol{u}^+(t=0) = \boldsymbol{u}_0^+ \end{gathered} \tag{E.7}$$

where ^{T} denotes the transpose matrix. These equations are solved backward in time which make the adjoint equations more difficult to solve than the direct equations as the base flow depends on time in the linearized equations. To solve the direct set one can solve the equations of the base flow along the direct equations and obtain the full dynamics. Yet to solve the adjoint equations, one would need to solve the set of base flow equations backward in time which is impossible. To solve this problem we chose to keep snapshots of the evolution of the base flow and then use an interpolation scheme to have the base flow at any time between the recorded snapshots. The number of snapshot that one can keep depends on the available memory in the computer. We call n the number of snapshots P_i of the base flow that are taken at times t_i for $i = 0..n$ with $t_0 = 0$ and $t_n = 7.5$. We note $\Delta t_i(i) = t_{i+1} - t_i$ for $i = 1..n-1$ which in a general case does not have to be constant. Here though we chose a constant $\Delta t_i = \Delta t_{num}$ the numerical time step which is the minimum value one can take when the base flow is obtained numerically. If the flow was known experimentally, the minimum time step could be imposed by technical properties of the photographic equipment for instance. Therefore it always has a minimum value.

Given the set of records $P_{i=0..n}$, the picture of the base flow $P(t)$ is computed by a spline interpolation

$$\begin{gathered} P(t) = a_i t^3 + b_i t^2 + c_i t + d_i \qquad \text{for} \qquad t_i \leq t \leq t_{i+1} \quad , \quad i \in 0..n-1 \\ \text{and} \qquad a_0 = a_{n-1} = 0 \end{gathered} \tag{E.8}$$

Note that the interpolation is second order at the first and last intervals. There are $4n-2$ unknowns a_i, b_i and c_i to determine in order to define the interpolation scheme, which requires an equal number of relations. For every interval $i = 0..n-1$, we have the following constraints

$$\begin{gathered} a_i t_i^3 + b_i t_i^2 + c_i t_i + d_i = P(t_i) \\ a_i t_{i+1}^3 + b_i t_{i+1}^2 + c_i t_{i+1} + d_i = P(t_{i+1}) \end{gathered} \tag{E.9}$$

Also the derivatives have to be continuous between intervals, which can be written for every interval $i = 2..n-2$

$$\begin{gathered} \frac{dP(t_i)}{dt} = 3a_i t_i^2 + 2b_i t_i + c_i = \frac{P_{i+1} - P_{i-1}}{2\delta t} \\ \frac{dP(t_{i+1})}{dt} = 3a_i t_{i+1}^2 + 2b_i t_{i+1} + c_i = \frac{P_{i+2} - P_i}{2\delta t} \end{gathered} \tag{E.10}$$

The derivatives at every record point is taken as the slope between the adjacent recorded snapshots. There are 4 relations for every interval except the last and the first for which we have 3 relations. In total, we hence have the required number of relations to compute the constant of the interpolation scheme. The simulation of the base flow required 7500 iterations. Given 2.5Mb per snapshot, the total memory requirement amounts to 20Gb. This imposes severe constraints on the size of the mesh used in the computations. It was found by preliminary investigations that interpolation schemes that don't respect the continuity of the derivative of the flow at the record points systematically caused divergence of the linearized simulations. The interpolation scheme was implemented in the numerical method. The influence of the time step $\Delta t_i / \Delta t_{num}$ was investigated by performing direct numerical simulations for values of this parameter ranging from 1 to 100 and by comparing the evolution of the perturbation energy in every cases. The reference case corresponds to the minimum value of this parameter which is 1. This means that we use all the snapshots taken during the simulation of the base flow. Values up to 30 showed the same results than the reference case but greater values showed diverging results. The divergence is caused by the loss of important information in the evolution of the base flow that changes rapidly in the beginning of the roll-up. Figure E.6 indeed shows by evaluating the variation of the vorticity field between every numerical time step that the variations are much larger before $t = 2$.

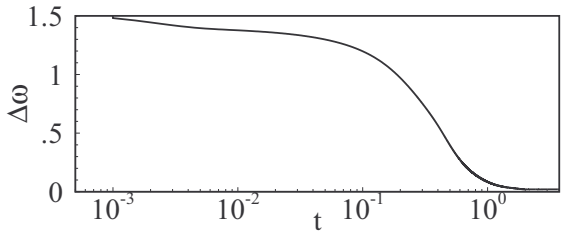

Figure E.6: Variation $\Delta\omega = \|\omega(t + \Delta t_{num}) - \omega(t)\|^{1/2}$ of the vorticity during the simulation of the vortex sheet.

E.4 Results

Figure E.7 displays the energy amplification of the perturbation as a function of time. The plain line is the envelope of the possible energy gain. It is obtained by fitting the results of the optimal algorithm at different optimization times (shown by the circle symbols) with a spline curve. The thin line corresponds to the energy gain obtained by the optimal perturbation at $t = 7.5$. The dashed line is the energy amplification of the adjoint mode put on the frozen trailing vortices at initial time. Two parts can be distinguished in the optimal curve. The

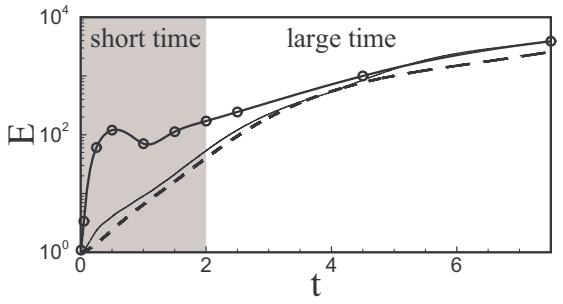

Figure E.7: Energy gain as a function of time for three initial conditions. (thick plain) envelope of the possible energy gain, (thin plain) optimal perturbation at $t = 7.5$, (dashed) adjoint of the final vortex pair.

energy grows significantly at the beginning and reaches a peak $E\,(t = 0.5) = 120$. It decreases afterwards until $t = 1$ and then increases again, until final time. The interval of time of the first peak corresponds to the time of the roll-up $t = 2$ already noticed in the study of the evolution of the vortex sheet while the continuous increase of energy after $t = 2$ corresponds to the time period of the trailing vortices. Therefore it seems that there is a first mechanism of amplification that is related to the roll-up of the vortex sheet and a second mechanism related to the trailing vortices.

The optimal perturbation leading to the first peak of energy gain is depicted in figure E.8. The large amplification is visualized by the intensification of the contour levels. The perturbation is initially inside the vortex sheet and remains there during the roll-up. We remark that the structure has a span wise pseudo periodicity of wavenumber $\alpha \simeq 30$ reminiscent of the Orr mechanism which is a two dimensional mechanism of energy growth in shear flows (see Butler and Farrel [25]). Suppose a base flow with velocity $\boldsymbol{V} = V(z)\boldsymbol{e}_y$ and two-dimensional perturbations $\boldsymbol{u} = (0, v, w, p)$ in the system of coordinates used here. The inviscid rate of energy growth is given by

$$\frac{dE}{dt} = -\int_{-\infty}^{\infty} \frac{\partial V}{\partial z} vw dz \tag{E.11}$$

The energy of the perturbations can grow by extraction of energy from the mean shear through the Reynolds stress vw. In the left side of figure E.8 we plot the profiles of $V(z)$ and vw in

a vertical section of the initial vortex sheet. The situation is characterized by $V'(z) < 0$ and positive vw therefore there seems indeed to be a local production of energy corresponding to the Orr mechanism in the vortex sheet at the beginning of its evolution.

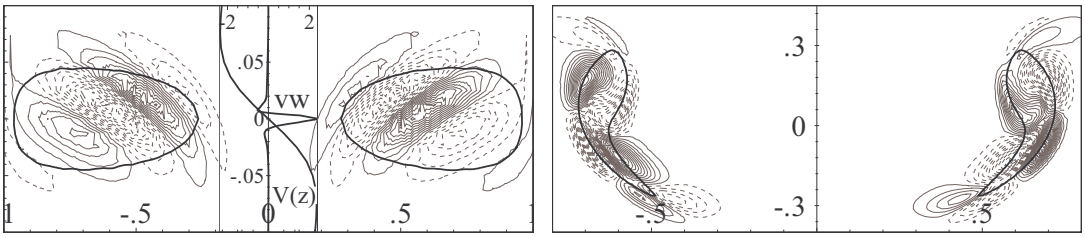

(a) (b)

Figure E.8: Contours perturbation vorticity of the optimal perturbation for the optimization time 0.5 at times (a) $t = 0$ and (b) $t = 0.5$. Negative vorticity is dashed. Axis range have been adapted for better clarity. The black line marks the structure of the base flow axial vorticity. The vertical profile through the vortex sheet at $y = 0.65$ of span wise basic velocity and perturbation Reynolds stress vw are shown (left) in the middle frame in which Top and bottom labels correspond respectively to $V(z)$ and vw.

To validate this scenario, we consider the entire flow instead of one profile. We notice that the peak of energy gain results from a steep slope dE/dt of the optimal curve at initial time. From the definition of the energy and by using the properties of the adjoint operator, the rate of increase of energy can be written

$$\frac{dE(t)}{dt} =< \boldsymbol{u}, \left(A + A^{+}\right) \boldsymbol{u} > \tag{E.12}$$

where A and A^{+} are the direct and adjoint matrix of the linear dynamics and depend on time. As the convection is reversed in the adjoint dynamics contained in A^{+} compared to the direct dynamics contained in A, it is found that $A + A^{+} = -2D + 2V + 2C$ where $D = 1/2\left(\nabla \boldsymbol{U} + \nabla \boldsymbol{U}^{T}\right)$ is the two dimensional (in the plane (y, z)) deformation tensor of the base flow, V is the viscous diffusion and C is the continuity equation. Note that the pressure terms disappear in the addition of the matrices as the flow is supposed incompressible. To investigate the effect of the deformations on the initial perturbations, we compute the eigenvectors $\boldsymbol{V}_1$ and $\boldsymbol{V}_2$ in the plane $(0, y, z)$ and the eigenvalues ϵ_1 and ϵ_2 of D. The first (second) eigenvalue ϵ_1 (ϵ_2) corresponds to the stretching (compression) term in the direction of $\boldsymbol{V}_1$ ($\boldsymbol{V}_2$). It is found that $\epsilon_{1,2} = \pm\epsilon$ have opposite values at all times like in linear flows. Given a perturbation $\boldsymbol{u}$ that is incompressible, the inviscid rate of energy growth equals to

$$\frac{dE}{dt} = -2 \int_S \epsilon \left(u_1^2 - u_2^2\right) dydz \tag{E.13}$$

where u_1 and u_2 are the components of perturbation velocity respectively along $\boldsymbol{V}_1$ and $\boldsymbol{V}_2$. The contours of $\epsilon \left(u_1^2 - u_2^2\right)$ are displayed in figure E.9 and are strictly negative which results in production of energy. The orientation of the eigenvectors schematized by arrows in the figure and that of the initial perturbation correspond to the Orr mechanism. The perturbation is initially oriented in the compression direction. The final perturbation shows that the region of positive vw have been rotated in the direction of the stretching by the mean shear flow therefore producing energy by the Orr mechanism. An approximation of the inviscid rate of energy gain produced by this mechanism can be obtained by the computing the integral of $-2\epsilon \left(u_1^2 - u_2^2\right)$ over the entire domain. Such operation gives $dE/dt \simeq 500$ which gives $E \simeq 250$ at $t = 0.5$. This is to be compared with the value $E = 120$ obtained by the optimization process. The difference lies in the effect of the viscosity that reduces the gain of energy. The span wise wavenumber non

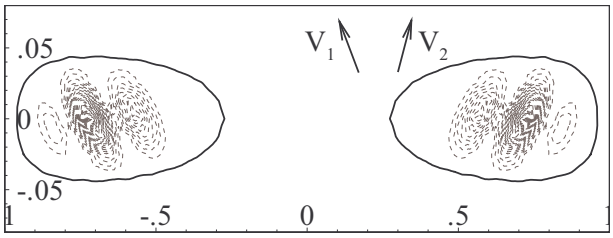

Figure E.9: Contours of density of inviscid rate of energy growth. Arrows show the directions of stretching and compression in the vortex sheet.

dimensionalized by the thickness of the vortex sheet gives $\alpha d = 1.5$ which compares well with the result found by Butler and Farrel [25] in a Poiseuille flow. It is thought that parameters like the extent of the vortex sheet and the vorticity distribution greatly influence the appearance of the Orr mechanism and its potential increase of energy. In particular, thinner vortex sheet are expected to give higher $V'(z)$ and higher energy gains by the Orr mechanism.

Figure E.10 shows the modification of the mean shear by the roll-up of the vortex sheet. The shear is very strong in the initial flow and quickly decreases during the roll-up. After $t = 1$, the maximum of shear is smaller by an order of magnitude. The decrease of energy after the first peak in figure E.7 corresponds to the loss of coherence of the shear region in which the Orr mechanism operates. Therefore the end of the roll-up stops the primary growth of energy.

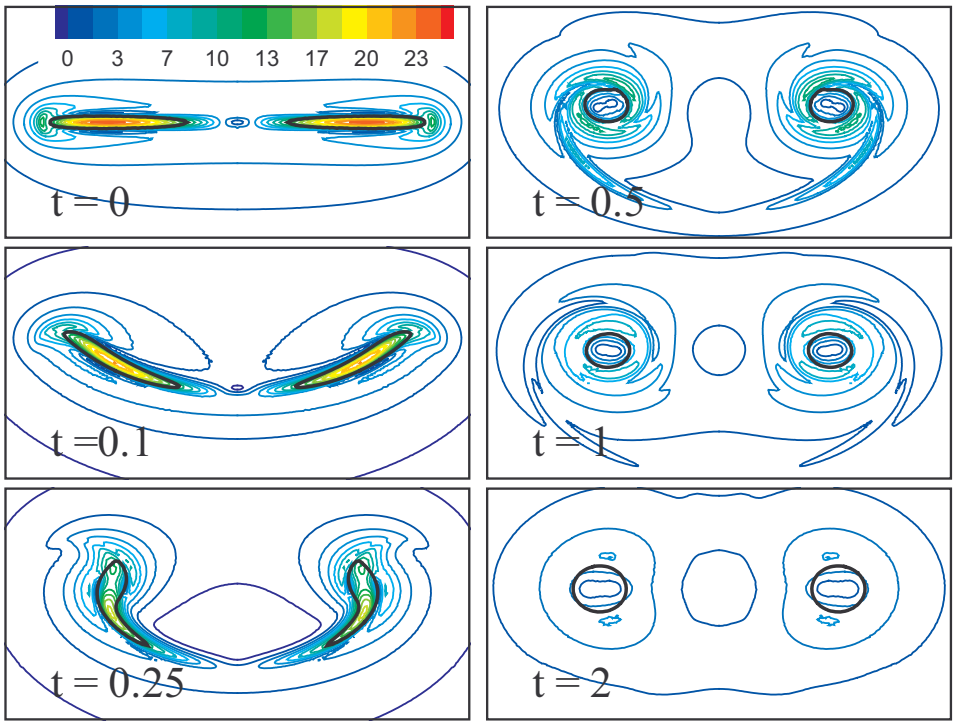

Figure E.10: ϵ at different snap shots of the vortex sheet evolution.

The optimal perturbation for final time $t = 7.5$ is displayed in figure E.11. The initial perturbation is located in the middle plane of the initial flow, which is the analog of the result found by Brion [23] for the optimal amplification of the Crow instability in a pair of opposite vortices. The final perturbation is the Crow instability presented earlier. The energy growth of the initial perturbation is shown in figure E.7 by the thin line. The dashed line represents the energy amplification of the adjoint of the Crow instability in the vortex pair. The two curves show great similarity which proves that the mechanism of the optimal amplification of the Crow instability also operates in the case of the roll-up. The perturbation is not influenced by the first

mechanism of energy growth. Therefore the two mechanisms do not cooperate. Nonetheless the effect of the roll-up is positive to fasten the Crow instability as a larger gain is obtained with roll-up than without.

The fact that the initial optimal perturbation is the same with and without roll-up show that the mechanism of optimal amplification of the Crow instability does not depend on the form of the distribution of basic vorticity. As the optimal perturbation is initially in the potential region, it is only weakly influenced by the roll-up.

E.5 Conclusion

In this paper, we focused our attention on the linear evolution of perturbations on a rolling-up vortex sheet. We first analyze the roll-up of the vortex sheet and showed that after $t = 2$ the flow is completely rolled-up into two trailing vortices. We then investigated the evolution of small perturbations on the base flow that includes the roll-up of the vortex sheet and the frozen trailing vortices. The results of the optimal perturbation showed that two mechanisms of energy amplification operate. Energy can be amplified during the roll-up by the Orr mechanism while after the roll-up stops it the mechanism of the amplification of the Crow instability that produces energy. It is found that the two mechanisms do not cooperate. The whole study shows that the roll-up process does not preclude the Crow instability and is even beneficial in terms of energy gains.

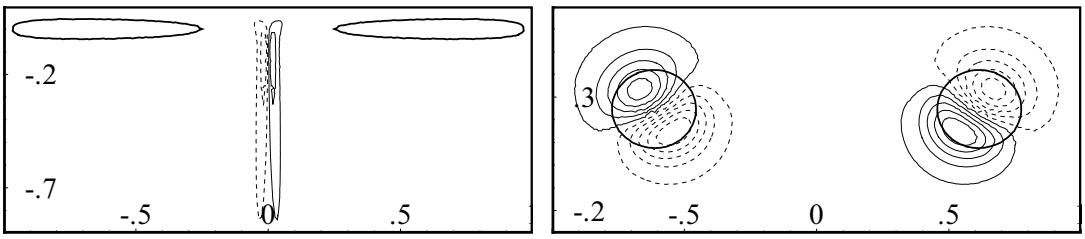

(a) Initial perturbation (b) Final perturbation

Figure E.11: Iso-contours of perturbation axial vorticity of the optimal perturbation at final time. (a) Initial perturbation. (b) final perturbation. Negative vorticity is dashed.

The method presented in the paper can be applied to more realistic aircraft wakes with for instance inclusion of the effect of flaps, exhaust jet and axial velocity. Also the study was limited to perturbations at the wavelength of the Crow instability. As it is a very long wavelength close to a two-dimensional flow, we observed the appearance of the Orr mechanism in the optimal perturbation analysis. Further efforts would be needed to investigate the mechanism of energy amplification at other wavelengths. We may in particular wonder about the possibility of having the lift-up mechanism in the vortex sheet for shorter wavelengths. The lift-up mechanism is well described by Butler [25] who shows among other details that the lift-up mechanism is about ten times slower than the Orr mechanism. Considering the rapidity of the roll-up of the vortex sheet, we are tempted to answer that the lift-up does not have time to operate. Another point of importance is whether the roll-up allows the appearance of the short wavelengths Widnall instabilities in the trailing vortices. Eventually it has to be stressed that no experimental data exists to compare with the numerical simulations. This also rises the question of the applicability of the control based on the mechanisms of energy amplification highlighted here.

Appendix

Optimization technique

The search for the initial perturbation that gives the highest gain of energy at time T is achieved by an adjoint based gradient method. The cost functional is the objective to be maximized.

$$J\left(\boldsymbol{u}_0, \boldsymbol{u}\right) = \frac{E(t)}{E(0)} \tag{E.14}$$

The perturbations should verify the set of equations and the boundary conditions (E.3). Therefore these conditions are applied by lagrange multipliers $\boldsymbol{u}^+$ in a lagrangian operator that writes

$$L\left(\boldsymbol{u}, \boldsymbol{u}_0, \boldsymbol{u}^+, \boldsymbol{u}_0^+\right) = J(\boldsymbol{u}, \boldsymbol{u}_0) - \langle \boldsymbol{u}^+, (A\boldsymbol{u} - B\partial_t \boldsymbol{u})\rangle - \langle \boldsymbol{u}_0^+, \boldsymbol{u} - \boldsymbol{u}_0\rangle \tag{E.15}$$

The optimal corresponds to the point $\boldsymbol{u}_0$ where $\nabla L = 0$ which gives the following relations

$$\nabla L \cdot \boldsymbol{u}^+ = 0 \rightarrow \left\{ \begin{array}{c} A\boldsymbol{u} = B\partial_t \boldsymbol{u} \\ \boldsymbol{u}(t=0) = \boldsymbol{u_0} \end{array} \right. \tag{E.16}$$

$$\nabla L \cdot \boldsymbol{u} = 0 \rightarrow \left\{ \begin{array}{c} A^+\boldsymbol{u}^+ = B\partial_t \boldsymbol{u}^+ \\ \boldsymbol{u}(t=T) = \frac{2B\boldsymbol{u}(T)}{E(0)} \end{array} \right. \tag{E.17}$$

$$\nabla L \cdot \boldsymbol{u}_0 = 0 \rightarrow \left\{ \nabla L \cdot \boldsymbol{u}_0 = -2\frac{E(T)}{E(0)^2} B\boldsymbol{u}_0 + B\boldsymbol{u}_0^+ \right. \tag{E.18}$$

where the derivative $\nabla L \cdot \boldsymbol{u}$ is defined by

$$\lim_{\epsilon \rightarrow 0} \frac{L(\boldsymbol{u} + \epsilon\delta\boldsymbol{u}, \boldsymbol{u}_0, \boldsymbol{u}^+, \boldsymbol{u}_0^+) - L\left(\boldsymbol{u}, \boldsymbol{u}_0, \boldsymbol{u}^+, \boldsymbol{u}_0^+\right)}{\epsilon\delta\boldsymbol{u}} \tag{E.19}$$

and A and A^+ are the direct and adjoint operators

$$A = \begin{pmatrix} -\mathcal{C} + \mathcal{V} & 0 & 0 & -k \\ 0 & -\partial_y V - \mathcal{C} + \mathcal{V} & -\partial_y W & -\partial_x \\ 0 & -\partial_z V & -\partial_z W - \mathcal{C} + \mathcal{V} & -\partial_z \\ -k & \partial_y & \partial_z & 0 \end{pmatrix} \tag{E.20}$$

(E.21)

$$A^+ = \begin{pmatrix} \mathcal{C} + \mathcal{V} & 0 & 0 & k \\ 0 & -\partial_y V + \mathcal{C} + \mathcal{V} & -\partial_z V & \partial_x \\ 0 & -\partial_y W & -\partial_z W + \mathcal{C} + \mathcal{V} & \partial_z \\ -k & \partial_y & \partial_z & 0 \end{pmatrix} \tag{E.22}$$

with C the convection by the base flow and V the viscous diffusion. Starting from an arbitrary initial condition $\boldsymbol{u}_0$, the following procedure is applied iteratively in order to calculate the optimal perturbation :

1- compute $\boldsymbol{u}(T)$ by solving the direct equations (E.3)

2- compute the adjoint $\boldsymbol{u}^+(T)$ with relation (E.17)

3- solve the adjoint equation backward in time to obtain $\boldsymbol{u}^+(0)$

3- compute the gradient $(\nabla L \cdot \boldsymbol{u}_0)_0$

4- solve equations (E.3) initialized by $(\nabla L \cdot \boldsymbol{u}_0)_0$ so as to obtain $(\nabla L \cdot \boldsymbol{u}_0)_T$ at time T

5- The new initial perturbation is $\boldsymbol{u}_{0_{NEW}} = \boldsymbol{u}_0 + \alpha(\nabla L \cdot \boldsymbol{u}_0)_0$ and the new final perturbation is $\boldsymbol{u}_{T_{NEW}} = \boldsymbol{u}(T) + \alpha(\nabla L \cdot \boldsymbol{u}_0)_T$. α is set so that J is maximum (this require to solve a second order quadratic equation).

4- From the value of α, compute the new $\boldsymbol{u}_{0_{NEW}}$ and $\boldsymbol{u}_{T_{NEW}}$

7- Iterate from 2 until convergence is reached $\|\boldsymbol{u}_{0_{NEW}} - \boldsymbol{u}_0\| \leq 10^{-3}$

F Optimal amplification of the Crow instability

The following work is a publication (Brion[23]) based on the optimal perturbation analysis of vortex pairs contained in chapter 6.

Abstract

A mechanism for promoting the Crow instability in a counter-rotating vortex pair is presented within the framework of linear dynamics. It consists in (1) the creation of a periodic array of vortex rings along the length of the vortices by stretching of vorticity at the leading hyperbolic point of the dipole and (2) the deformation of the vortices by the vortex rings leading to the Crow instability. A reduction of the characteristic time of the Crow instability by a factor of roughly 2 can be obtained by this mechanism.

Vortex hazard caused by aircraft trailing vortices has gained much attention these past decades with the advent of jumbo jets. In certain situations, vortex wakes collapse through a chain process including deformation of columnar vortices by the Crow instability, vortex linking, and turbulence [138]. One way to alleviate vortex hazard is to accelerate the process by exciting the intrinsic instabilities of the wake. This is the idea developed in this article in which we optimize the energy of the Crow perturbation by means of an appropriate initial

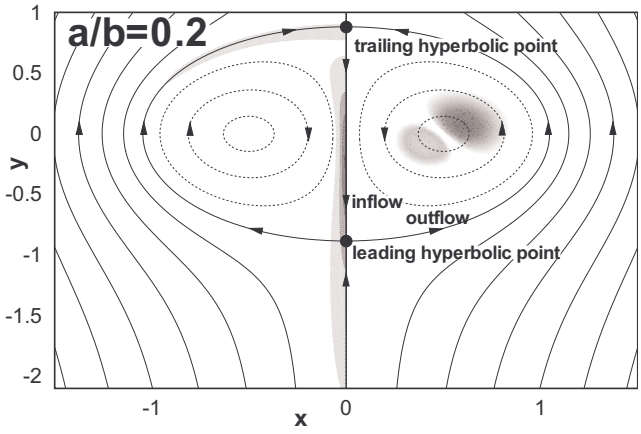

Figure F.1: Streamlines of the basic counter-rotating vortex pair (arrows indicate the direction of the flow). Right side : disturbance $\tilde{\omega}_z$ of the Crow mode at $k = 0.9$. Left side : disturbance $\tilde{\omega}_x$ of the adjoint of the Crow mode. ω_z is odd and $\tilde{\omega}_x$ is even about the symmetry plane of the dipole. Note that the figure has been enlarged in the x-direction for clarity.

perturbation. The growth rate of the Crow instability was first derived by Crow [34]. Vortices of the pair deform by mutual induction and oscillate in a plane inclined at approximately 45° about the horizontal. The oscillations grow exponentially in amplitude until the point when the two vortices touch each other, leading to final collapse. Several studies like the one of Crow and Bate[35] showed that exciting the vortex pair at the wavelength of the mutual induction instability could be efficient in accelerating the chain process. Other studies like the ones of Crouch [33] and Fabre, Jacquin and Loof [45] showed by a vortex filament method that systems of four vortices exhibit much larger amplification rates than the Crow instability. While these previous studies arbitrarily specify the structure of the perturbation as vortex filaments, in this letter we use a global stability method based on a finite element discretization with a high number of degrees of freedom which presupposes no particular shape for the initial perturbation. In the case of a single Lamb-Oseen vortex, Antkowiak and Brancher [5] and Pradeep and Hussain [124] have already reported that the optimal perturbation takes the form of spirals of vorticity outside the vortex core, which suggests that a similar mechanism of amplification can be expected in the case of the dipole as far as the two vortices are not too close to each other. Yet this suggestion is partially hindered by the presence of two hyperbolic stagnation points (hereafter simply referred as hyperbolic points, "hyperbolic" standing for the hyperbolicity of the streamlines in the vicinity of these points, see figure F.1) in the flow that are also known [87] to behave as energy amplifiers. The main objective of the study is to understand the roles that these two dynamics (the one of the vortex and the one of the hyperbolic point) play in the optimal amplification of the Crow instability.

Base flow The basic flow is a two-dimensional pair of counter-rotating vortices symmetric with respect to $x = 0$ which may [136] be characterized by the aspect ratio a/b of the dipole (see figure F.1). Cartesian coordinates (x, y, z) are used throughout the study. Let us define S the computational domain, ∂S the far field boundaries, and $S^+ = S_{|x\geq 0}$ the right domain. These definitions allow us to define a as the radius of the vortices by $\Gamma a^2 = \iint_{S^+} \Omega_z \|\boldsymbol{x} - \boldsymbol{x_C}\|^2 dS$ with $\boldsymbol{x_C} = (x_C, y_C) = 1/\Gamma \iint_{S^+} \Omega_z \boldsymbol{x} dS$ the center of the right vortex, $\Gamma = \iint_S^+ \Omega_z dS$ its circulation, $b = 2x_C$ the distance between the vortex centers and Ω_z the axial basic vorticity. We consider a dipole at $a/b = 0.2$ obtained by a two-dimensional DNS started with an initial dipole characterized by $a/b(t = 0) = 0.1$ and composed of two Lamb-Oseen vortices. This procedure produces a dipole which is a solution of the 2D incompressible steady Navier-Stokes equations (which is not the case initially) in the reference frame attached to the dipole (the pair drifts at a velocity of approximately $2\pi b/\Gamma$ under mutual velocity induction). The computational domain is S^+ and a symmetry boundary condition is used at the symmetry plane of the dipole to account for the left vortex. Streamlines of the flow are drawn in figure F.1. During the simulation the two vortices basically diffuse under the effect of viscosity with a viscous time scale $T_\nu = 2\pi a^2/\nu$ and adapt under the strain mutually induced by one vortex onto the other. The time scale $T_{3d} = 2\pi b^2/\Gamma$ of the three-dimensional perturbations is much smaller than T_ν, as $T_\nu/T_{3d} = Re\,(a/b)^2$ and $Re = \Gamma/\nu = 3600$. The base flow can consequently be considered as quasi-steady for the forthcoming stability analysis. We note $(\mathbf{U}, P)$ the basic state (where $\mathbf{U} = (U, V, 0)$) which is assumed homogeneous in the axial direction z. In the following T_{3d} and b are used as reference time and length scales. Time $t = 1$ is the time needed to have order 1 deformation of the vortices by the Crow instability.

Stability theory In order to study the linear behavior of the dipole, we superimpose a small disturbance $\mathbf{q} = (\mathbf{u}, p)$ where $\mathbf{u} = (u, v, w)$ onto the background flow $(\mathbf{U}, P)$. Considering a Fourier decomposition of the form $\mathbf{q}(x, y, t) = (\tilde{u}, \tilde{v}, i\tilde{w}, \tilde{p})\,(x, y, t)e^{ikz} + c.c.$ where k is the axial wavenumber, the evolution of $\tilde{\mathbf{q}} = (\tilde{u}, \tilde{v}, \tilde{w}, \tilde{p})$ is given by the initial value problem (F.1) derived from the incompressible Navier-Stokes equations linearized about the basic state $(\mathbf{U}, P)$.

$$B\partial_t \tilde{\mathbf{q}} = A\tilde{\mathbf{q}} \quad , \quad \tilde{\mathbf{q}}(t = 0) = \tilde{\mathbf{q}}_0 \quad , \quad \tilde{\mathbf{q}}_{|\partial S} = 0 \tag{F.1}$$

$$A=\begin{pmatrix} -\partial_x U - \mathcal{C} + \mathcal{V} & -\partial_y U & 0 & -\partial_x \\ -\partial_x V & -\partial_y V - \mathcal{C} + \mathcal{V} & 0 & -\partial_y \\ 0 & 0 & -\mathcal{C} + \mathcal{V} & -k \\ \partial_x & \partial_y & -k & 0 \end{pmatrix} \tag{F.2}$$

We noted $\mathcal{C} = U\partial_x + V\partial_y$ the convection of the perturbation by the base flow, $\mathcal{V} = 2\pi/Re\left(\partial_{xx} + \partial_{yy} - k^2\right)$ the viscous term and $B = diag(1,1,1,0)$. If we consider a normal mode decomposition of the form $\tilde{\mathbf{q}}(x,y,t) = \hat{\mathbf{q}}(x,y)e^{\sigma t}$ with $\sigma = \sigma_R + i\sigma_I$ a complex number, the equation yields the eigen problem

$$A\hat{\mathbf{q}} = \sigma B\hat{\mathbf{q}} \quad , \quad \hat{\mathbf{q}}_{|\partial S} = 0 \tag{F.3}$$

The eigenmodes $\hat{\mathbf{q}}$ of the eigen problem (F.3) are called direct modes. An adjoint problem can similarly be defined with a continuous adjoint operator A^+ given by the relation $(\tilde{\mathbf{q}}_1, A\tilde{\mathbf{q}}_2) = (A^+\tilde{\mathbf{q}}_1, \tilde{\mathbf{q}}_2)$ whatever $\tilde{\mathbf{q}}_{1,2}$ where the scalar product is given by $(\tilde{\mathbf{q}}_1, \tilde{\mathbf{q}}_2) = \iint_S \tilde{\mathbf{q}}_1^* \cdot \tilde{\mathbf{q}}_2 dS$ and where * denotes the conjugate. The eigenmodes $\hat{\mathbf{q}}^+$ of A^+, called the adjoint modes, are solution of a generalized eigen problem similar to (F.3) given by

$$A^+\hat{\mathbf{q}}^+ = \sigma^+ B\hat{\mathbf{q}}^+ \quad , \quad \hat{\mathbf{q}}^+_{|\partial S} = 0 \tag{F.4}$$

$$A^+=\begin{pmatrix} -\partial_x U + \mathcal{C} + \mathcal{V} & -\partial_x V & 0 & \partial_x \\ -\partial_y U & -\partial_y V + \mathcal{C} + \mathcal{V} & 0 & \partial_y \\ 0 & 0 & \mathcal{C} + \mathcal{V} & k \\ \partial_x & \partial_y & -k & 0 \end{pmatrix} \tag{F.5}$$

In comparison to the direct problem described by A, the convection in A^+ is reversed and the off-diagonal terms $-\partial_x V$ and $-\partial_y U$ are exchanged. Any direct mode has a corresponding adjoint mode and their eigenvalues are conjugate to each other.

A finite element method with P2 space discretization for the velocity and P1 for the pressure is used to discretize the sparse matrices A, A^+ and B (size 5.10^5). Problems (F.3) and (F.4) are then solved by an Arnoldi method based on a shift and invert strategy (ARPACK package). The matrix inverse is solved thanks to a direct sparse LU solver (UMFPACK package). Once calculated, the direct and adjoint eigenmodes are normalized so that $(\hat{\mathbf{q}}_i, B\hat{\mathbf{q}}_i) = 1$, $\left(\hat{\mathbf{q}}_i^+, B\hat{\mathbf{q}}_i\right) = 1$ and the bi-orthogonality condition $\left(\hat{\mathbf{q}}_i^+, B\hat{\mathbf{q}}_j\right) = 0$ if $i \neq j$ is verified.

Energy gain The dynamics of (F.1) will always be driven by the most unstable direct eigenmode at large time. It can be shown (see Schmid and Henningson [133]) that a specific initialization which consists in the adjoint mode $\hat{\mathbf{q}}^+_{max}$ of the most unstable direct mode $\hat{\mathbf{q}}_{max}$

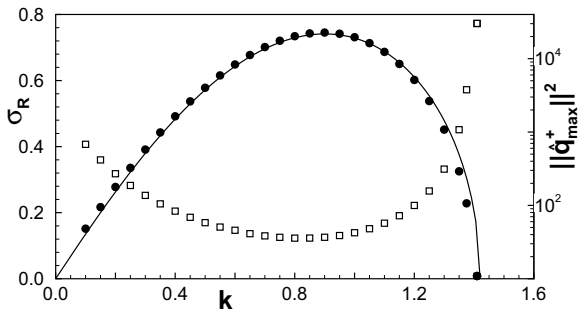

Figure F.2: Computed (filled points) growth rate σ_R of the Crow instability as a function of the axial wavenumber compared to the theory of Crow (line). Empty squares show the non normal gain $\|\hat{\mathbf{q}}^+_{max}\|^2$. Note that the Crow eigenmodes are non-oscillating ($\sigma_I = 0$). $Re = 3600$, $a/b = 0.2$.

will yield the perturbation with the maximum energy at large time. Defining the energy gain of a perturbation $\tilde{\mathbf{q}}(t)$ by

$$G(t) = \|\tilde{\mathbf{q}}(t)\|^2/\|\tilde{\mathbf{q}}(0)\|^2 \tag{F.6}$$

where the norm $\|\cdot\|$ is based on the scalar product $(\cdot, B\cdot)$, it may be shown that the maximum energy gain is $G_{max}(t) = \|\hat{\mathbf{q}}^+_{max}\|^2 e^{2\sigma_{max}t}$ obtained for $\tilde{\mathbf{q}}(0) = \hat{\mathbf{q}}^+_{max}$. The non-normal gain $\|\hat{\mathbf{q}}^+_{max}\|^2$ is the increase in amplification achieved by an initialization with the adjoint mode compared to an initialization with the direct mode.

Figure F.2 reports the variation of the growth rate and the non-normal gain of the Crow instability with the wavenumber k. The most unstable Crow mode occurs for $k = 0.9$. The related direct mode is depicted in the right side of figure (F.1) and the adjoint in the left side (the reason for showing $\hat{\omega}_x$ will be apparent later). The numerical code is validated against the theoretical inviscid growth rate given by Crow [34] and Saffman [130]. It is to our knowledge the first time the growth rate of Crow is calculated so successfully by a global method.

According to figure F.2, the non-normal gain is greater as the growth rate is smaller. The minimum which equals 36 is reached for the most unstable mode at $k = 0.9$. This means that disturbing the dipole with the adjoint of the most unstable Crow mode gives an amplification 36 times greater at large time than a modal disturbance by the direct mode. The potential acceleration of the Crow instability related to this gain amounts to an interesting $\log(36)/(2\sigma_{max}) \simeq 2.5$ time units. This non-normal gain can even be higher, i.e. 10^3 to 10^4 if the disturbance is chosen at a wavenumber k corresponding to lower growth rates. The influences of the Reynolds number and of the aspect ratio a/b of the dipole on the non-normal gain were also explored. Note that $\|\hat{q}^+_{max}\|^2$ increases slowly with Re ($\|\hat{q}^+_{max}\|^2 = 44$ for Re=9000) and decreases slowly with a/b ($\|\hat{q}^+_{max}\|^2 = 53$ for $a/b = 0.17$). These results clearly state the high potential of the adjoint approach.

Linearized simulations The sole value of the non-normal gain is not enough to conclude on the efficiency of the adjoint disturbance as the time needed to reach it is not known. Therefore linearized simulations solving the problem (F.1) in time were launched with the different initializations evoked earlier (legend refers to figure F.3) : the direct mode at $k = 0.9$ (long dash), the adjoint mode at $k = 0.9$ (thick solid), the adjoint at $k = 0.2$ (short dash) and the adjoint at $k = 1.4$ (dot) (note that the remaining curve is discussed at the end of the paper). The previously described finite element method is used with a time discretization carried out by a 2^{nd} order Lagrange-Galerkin method.

In figure F.3 we see that the curve of the adjoint mode at $k = 0.9$ reaches an asymptote parallel to the modal growth (a straight line in the logscale). This shows that after $t = 1.5$ the adjoint perturbation has reached the direct modal structure and is amplified accordingly. The associated increase of amplification amounts to 36 as predicted by the non-normal gain, while in terms of time difference the value 2.5 obtained earlier is approximately recovered. This

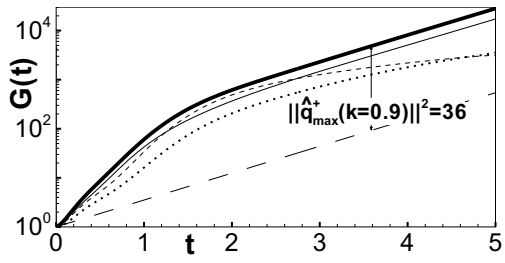

Figure F.3: Comparison between modal energy growth at $k = 0.9$ (long dash), adjoint energy growth at $k = 0.9$ (thick solid), energy growth induced by a perturbation (thin solid) containing $\tilde{\omega}_x$ on the symmetry axis, and most unstable perturbations at $k = 0.2$ (short dash) and $k = 1.4$ (dot). $Re = 3600$, $a/b = 0.2$.

implies that once the transient period of amplification $t = 1.5$ is over, the disturbance of the dipole by the adjoint perturbation provides an amplitude perturbation identical to that of the natural Crow instability on a time scale reduced by 2.5. Sparlart [138] and Crow and Bate [35] note a time period of 5 to 6 for the lifespan of trailing vortices. This means that a reduction of 2.5 shrinks by almost a half this characteristic lifespan, which could be of great interest for the aeronautical industry. Energy amplification corresponding to initial perturbation by the adjoint modes at $k = 0.2$ and $k = 1.4$ do not exhibit the expected strong energy gains quick enough, i.e. the transient period is greater than $t = 5$. This renders these cases useless and justifies that we only focus on the case $k = 0.9$ of the most unstable Crow mode.

Optimal mechanism Figure F.4 shows the steps leading to the optimal amplification of the Crow instability. The mechanism basically consists in amplification of $\tilde{\omega}_x$ at the leading hyperbolic point region (upper row, a-c) followed by the induction of the Crow instability in the vortex cores (lower row, c-d). As shown by Lagnado et al. [87] transient energy growth at hyperbolic points occurs for initial vorticity parallel to the stretching direction. Indeed, at the leading hyperbolic point (figure F.1) the equation for vorticity perturbation reduces to

$$\partial_t \tilde{\omega}_x = \gamma \tilde{\omega}_x + 2\pi/Re \triangle \tilde{\omega}_x \tag{F.7}$$

$$\partial_t \tilde{\omega}_y = -\gamma \tilde{\omega}_y + 2\pi/Re \triangle \tilde{\omega}_y \tag{F.8}$$

$$\partial_t \tilde{\omega}_z = 2\pi/Re \triangle \tilde{\omega}_z \tag{F.9}$$

where $\gamma = \partial_x U = -\partial_y V \sim +1.7$ is the strain rate in the vicinity of the hyperbolic point. As a result, the initial perturbation with $\tilde{\omega}_x$ experiences a strong amplification as it passes in the vicinity the leading hyperbolic point due to the stretching along the outflow streamline.

As the streamline bends up, $\tilde{\omega}_x$ is tilted (b) leading to formation of $\tilde{\omega}_y$. Together $\tilde{\omega}_x$ and $\tilde{\omega}_y$ form a partial vortex ring around the dipole (c). This vortex ring creates axial and radial velocities within the dipole by the Biot Savart law and eventually induces axial vorticity in the regions where Ω_z is strong thanks to the production terms in the linearized equation of $\tilde{\omega}_z$

$$\partial_t \tilde{\omega}_z + \underbrace{U_\theta/r \partial_\theta \tilde{\omega}_z}_{convection} = \underbrace{-\tilde{u}_r \partial_r \Omega_z + k\Omega_z \tilde{u}_z}_{production} + \underbrace{\nu \triangle \tilde{\omega}_z}_{diffusion} \tag{F.10}$$

As in the case of a single vortex [5] [124], the previous description of the optimal mechanism suggests that bending modes of the vortices are optimally induced by vortex rings which partially

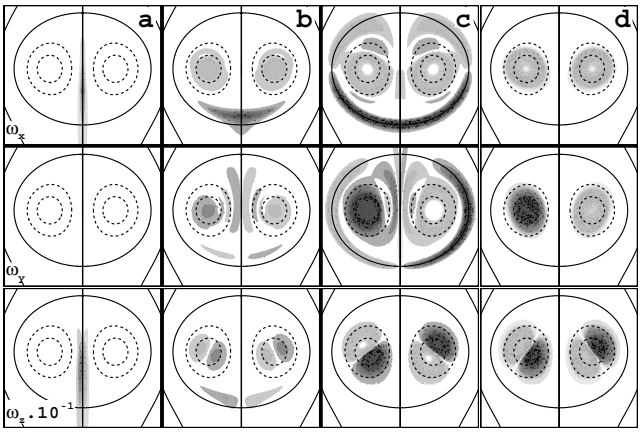

Figure F.4: Streamlines of the base flow and contours of perturbation vorticity through time evolution of the adjoint Crow mode (a-c: $t = 0.046; 0.41; 0.94$) at $k = 0.9$. Column d represents the final Crow mode (a-c contour and d contour levels are different). Contours (a-d) of $\tilde{\omega}_z$ are 10 times smaller than those of $\tilde{\omega}_x$ and $\tilde{\omega}_y$ to allow the use of the same contour levels. $Re = 3600$, $a/b = 0.2$.

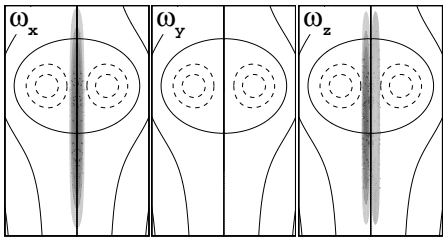

Figure F.5: Initial perturbation containing $\tilde{\omega}_x$ and $\tilde{\omega}_z$ and no $\tilde{\omega}_y$ at $k = 0.9$. Note that $\tilde{\omega}_x$ also represents $\tilde{f}_y$ as $\tilde{\omega}_x = -\tilde{f}_y/k$.

circles the rotational flow. Following this idea, the question of the optimal perturbation reduces to the question of how to optimally produce such partial vortex rings. While in the case of the single vortex, it is the unrolling [5] [124] of the spirals of vorticity around the vortex that forms them, in the case of the dipole, it is the leading hyperbolic point which plays that role. The results of these two configurations (dipole and single vortex) tend to suggest that the way to optimally disturb any compact distribution of vorticity is to create one or several partial vortex rings around it. Such a generalization could be investigated in a future study.

A question arises about the lack of a role for the trailing hyperbolic point. If it was to play a role, it would need an initial $\tilde{\omega}_y$ distribution located at its inflow streamline that would then be amplified along $x = 0$ between the two vortices. But due to the symmetry of the perturbation, it appears that only the leading hyperbolic point can be efficiently used for vorticity stretching. Indeed non zero $\tilde{\omega}_x$ can be located on the stretching line of the leading hyperbolic point whereas $\tilde{\omega}_y$ being anti-symmetric is zero on the stretching line of the trailing hyperbolic point. Moreover because of the resultant dipolar distribution of $\tilde{\omega}_y$, only a weak velocity induction in the vortex core could take place, which would less efficiently induce the Crow instability.

Optimal forcing While defining a practical method to trigger this amplification in real flows is out of the scope of this letter, it is still interesting to study theoretically the effect of control devices or background turbulence by modelling them by forces in the linearized equations. Solving an initial value problem initialized by $\tilde{\mathbf{q}}_0 = (\tilde{\mathbf{u}}_0, \tilde{p}_0)$ is equivalent to applying a force $\tilde{\mathbf{F}}\delta(t)$ (δ is the Dirac function) to a flow field at rest [130]. Integrating the equation for the perturbation vorticity $\tilde{\boldsymbol{\omega}}$ over an infinitesimal time interval leads to $\tilde{\boldsymbol{\omega}}_0 = \nabla \times \tilde{\mathbf{F}}$. The initial velocity field corresponding to the initial forcing is thus given by $\tilde{\mathbf{u}}_0 = \tilde{\mathbf{F}} + \nabla\tilde{h}$ where $\tilde{h}$ satisfies a Poisson equation $\nabla \cdot \tilde{\mathbf{F}} = -\triangle\tilde{h}$ (with homogeneous Dirichlet boundary conditions on ∂S and a Neumann boundary condition on the symmetry plane) as $\nabla \cdot \tilde{\mathbf{u}}_0 = 0$. An initial perturbation can hence be interpreted in terms of a force acting initially in the momentum equation. As a result, the optimal perturbation is also to be interpreted as the optimal force for destabilizing the dipole. The control needed to have $\tilde{\omega}_x$ at the central plane of the dipole can consist in applying a vertical force $\tilde{\mathbf{F}} = (0, \tilde{f}_y, 0)$ at the same location. This leads to $\tilde{\boldsymbol{\omega}}_0 = (-k\tilde{f}_y, 0, \partial_x\tilde{f}_y)$ as desired (no $\tilde{\omega}_y$). We chose an analytical expression for $\tilde{\mathbf{F}}$ with $\tilde{f}_y = (1+\cos(x/a_x))(1+\cos((y-y_0)/a_y)$ for $|x| \leq \pi a_x$ and $|y - y_0| \leq \pi a_y$ (y_0, a_x and a_y which control the location and the form of the distribution are $y_0 = -0.8$, $a_x = 0.05$, $a_y = 0.7$ for $k = 0.9$) and zero everywhere else as shown in figure F.5. The corresponding initial velocity field $\tilde{\mathbf{u}}_0$ is obtained by solving the preceding Poisson equation. Only 2% of the energy contained in $\tilde{\mathbf{F}}$ is lost in the projection process as $\|\tilde{\mathbf{u}}_0\|/\|\tilde{\mathbf{F}}\| = 0.98$ ($\|\tilde{\mathbf{F}}\| = \int_S(\tilde{f}_x^2 + \tilde{f}_y^2 + \tilde{f}_z^2)dS$). Figure F.3 shows the gain in energy obtained by this forcing (thin solid line) and it is clear that the amplification, although not optimal, is significant. A similar perturbation with initial $\tilde{\omega}_y$ and $\tilde{\omega}_z$ and no $\tilde{\omega}_x$ (generated by $\tilde{f}_x$ instead of $\tilde{f}_y$) leads to no non-normal gain (not shown here). This confirms the physical mechanism involving $\tilde{\omega}_x$ as a necessary ingredient for optimal destabilization of the dipole and the fact that it is possible to create this quasi optimal perturbation with a force having a simple distribution.

These results clearly open new perspectives and challenges for controlling vortex pairs in real flows.

References

[1] Abid, M., and Verga, A. Stability of a vortex sheet roll-up. *Physics of Fluids 14* (2002), 3829.

[2] Allaire, G. *Analyse numérique et optimisation*. Éd. de l&École Polytechnique, 2005.

[3] Anderson, E., Bai, Z., Bischof, C., Blackford, S., Demmel, J., Dongarra, J., Du Croz, J., Greenbaum, A., Hammarling, S., McKenney, A., et al. *LAPACK Users' guide*. Society for Industrial Mathematics, 1999.

[4] Antkowiak, A. *Dynamique aux temps courts d'un tourbillon isolé*. PhD thesis, Université Paul Sabatier, 2005.

[5] Antkowiak, A., and Brancher, P. Transient energy growth for the Lamb–Oseen vortex. *Physics of Fluids 16* (2004), L1.

[6] Antkowiak, A., and Brancher, P. On vortex rings around vortices: an optimal mechanism. *Journal of Fluid Mechanics 578* (2007), 295–304.

[7] Arendt, S., Fritts, D., and Andreassen, O. The initial value problem for kelvin vortex waves. *J. Fluid Mech. 344* (1997), 181–212.

[8] Ash, R., and Khorrami, M. *Vortex stability*. Fluid Vortices edited by S.I. Green, Kluwer 1995, 1995.

[9] Babu, C., Govardhan, M., and Sitaram, N. A method of calibration of a seven-hole pressure probe for measuring highly three-dimensional flows. *Measurement Science Technology 9* (1998), 468–476.

[10] Bae, J. *Active control of tip clearance flow in axial compressors*. PhD thesis, Massachusetts Institute of Technology, 2001.

[11] Bailey, S., and Tavoularis, S. Measurements of the velocity field of a wing-tip vortex, wandering in grid turbulence. *J. Fluid Mech. 601* (2008), 281–315.

[12] Bailey, S., Tavoularis, S., and Lee, B. Effects of freestream turbulence on wing-tip vortex formation and near field. *Journal of aircraft 43*, 5 (2006), 1282.

[13] Bandyopadhyay, P., Ash, R., and Stead, D. The organized nature of a turbulent trailing vortex. In *AIAA, Fluid Dynamics, Plasma Dynamics and Lasers Conference, 21 st, Seattle, WA* (1990), p. 1990.

[14] Batchelor, G. Axial flow in trailing line vortices. *Journal of Fluid Mechanics Digital Archive 20*, 04 (1964), 645–658.

[15] Bearman, P. Investigation of the flow behind a two-dimensional model with a blunt trailing edge and fitted with splitter plates. *J. Fluid Mech 21*, part 2 (1965), 241–256.

[16] Bearman, P., Heyes, A., Lear, C., and Smith, D. Natural and forced evolution of a counter rotating vortex pair. *Experiments in Fluids 40*, 1 (2006), 98–105.

[17] Bearman, P., Heyes, A., Lear, C., and Smith, D. Evolution of a forced counter rotating vortex pair for two selected forcing frequencies. *Experiments in Fluids 43*, 4 (2007), 501–507.

[18] Beninati, M., and Marshall, J. An experimental study of the effect of free-stream turbulence on a trailing vortex. *Experiments in Fluids 38* (2005), 244–257.

[19] Billant, P., Brancher, P., and Chomaz, J.-M. Three-dimensional stability of a vortex pair. *Physics of Fluids 11* (1999), 2069–2077.

[20] Bindon, J. The measurement and formation of tip clearance loss. *ASME Journal of Turbomachinery 111*, 2 (1989), 257–263.

[21] Blackburn, H., and Henderson, R. A study of two-dimensional flow past an oscillating cylinder. *J. Fluid Mech. 385* (1999), 255–286.

[22] Boulon, O., Callenaere, M., Franc, J., and Michel, J. An experimental insight into the effect of confinement on tip vortex cavitation of an elliptical hydrofoil. *Journal of Fluid Mechanics 390* (1999), 1–23.

[23] Brion, V., Sipp, D., and Jacquin, L. Optimal amplification of the Crow instability. *Physics of Fluids 19* (2007), 111703.

[24] Bristol, R., Ortega, J., Marcus, P., and Savas, O. On cooperative instabilities of parallel vortex pairs. *Journal of Fluid Mechanics 517* (2004), 331–358.

[25] Butler, K., and Farrell, B. Three-dimensional optimal perturbations in viscous shear flow. *Physics of Fluids A: Fluid Dynamics 4* (1992), 1637.

[26] Cattafesta, L., Williams, D., Rowley, C., and Alvi, F. Review of active control of flow-induced cavity resonance. *AIAA paper 3567* (2003), 2003.

[27] Chandrasekhar, S. The hydrodynamic stability of inviscid flow between coaxial cylinders. *Proc. N. A. S. 46* (1960), 137–141.

[28] Chaplygin, S. One case of vortex motion in fluid. *Trans. Phys. Sct. Imperial Moscow Soc. Friends of Natural Sciences 11, N 2* (1903), 11–14.

[29] Chen, G., Greitzer, E., Tan, C., and Marble, F. Similarity analysis of compressor tip clearance flow structure. *Journal of Turbomachinery 113* (1991), 260.

[30] Chen, Z., and Aubry, N. Closed-loop control of vortex-induced vibration. *Communications in Nonlinear Science and Numerical Simulation 10* (2005), 287–297.

[31] Comte-Bellot, G. Les méthodes de mesure physique de la turbulence. *J. Phys. Suppl 37* (1976), 67–78.

[32] Crook, A., Greitzer, E., Tan, C., and Adamczyk, J. Numerical simulation of compressor endwall and casing treatment flow phenomena. *Journal of Turbomachinery 115* (1993), 501.

[33] Crouch, J. Instability and transient growth for two trailing-vortex pairs. *Journal of Fluid Mechanics 350* (1997), 311–330.

[34] Crow, S. Stability theory for a pair of trailing vortices. *AIAA Journal 41*, 7 (1970), 293–300.

[35] Crow, S., and Bate, E. Lifespan of trailing vortices in a turbulent atmosphere. *Journal of Aircraft 13* (1976), 476–482.

[36] Danaila, I. *Étude des instabilité et des structures cohérentes dans la zone de proche sortie d'un jet axisymétrique.* PhD thesis, Université Aix-Marseille II, France, 1997.

[37] Davis, T. Users'guide for the unsymmetric-pattern multifrontal package (UMFPACK). *Tech. ReportTR-93-020, Computer and Information Sciences Dept., Univ. of Florida* (1993).

[38] Denton, J. Loss mechanisms in turbomachines. *Journal of Turbomachinery 115*, 4 (1993), 621–656.

[39] Devenport, W., Rife, M., Liapis, S., and Follin, G. The structure and development of a wing-tip vortex. *Journal of Fluid Mechanics Digital Archive 312* (1996), 67–106.

[40] Devenport, W., Wittmer, K., Muthanna, C., Bereketab, S., and Moore, J. Turbulence structure of a tip-leakage vortex wake. *AIAA paper* (1997), 97–0440.

[41] Devenport, W., Zsoldos, J., and Vogel, C. The structure and development of a counter-rotating wing-tip vortex pair. *Journal of Fluid Mechanics 332* (1997), 71–104.

[42] Dritschel, D. A general theory for two-dimensional vortex interactions. *J. Fluid Mech. 293* (1995), 269–303.

[43] Fabre, D. *Instabilités et instationnarités dans les tourbillons: application aux sillages d'avions.* PhD thesis, Université Paris VI, 2002.

[44] Fabre, D., and Jacquin, L. Viscous instabilities in trailing vortices at large swirl numbers. *Journal of Fluid Mechanics 500* (2004), 239–262.

[45] Fabre, D., Jacquin, L., and Loof, A. Optimal perturbations in a four-vortex aircraft wake in counter-rotating configuration. *Journal of Fluid Mechanics 451* (2002), 319–328.

[46] Fabre, D. Sipp, D., and Jacquin, L. Kelvin waves and the singular modes of the lamb-oseen vortex. *Journal of Fluid Mechanics 551* (2006), 235–274.

[47] Farrell, K., and Billet, M. A correlation of leakage vortex cavitation in axial-flow pumps. *ASME Journal of Fluids Engineering 120* (1994), 345–353.

[48] Flor, J., and van Heijst, G. An experimental study of dipolar vortex structures in a stratified fluid. *Journal of Fluid Mechanics 279* (1994), 101–133.

[49] Gallaire, F. *Instabilité dans les jets tournants et contrôle de l'éclatement tourbillonnaire.* PhD thesis, École Polytechnique, France, 2002.

[50] Gallington, R. Measurement of very large flow angles with non-nulling seven-hole probe. *Aeronautics Digest, USAFA-TR-80-17 17* (1980), 60–68.

[51] Gerner, A., Maurer, C., and Gallington, R. Non-nulling seven-hole probes for high angle flow measurement. *Experiments in Fluids 2* (1984), 95–103.

[52] Gerz, T., Holzapfel, F., and Darracq, D. Commercial aircraft wake vortices. *Progress in Aerospace Sciences 38* (2002), 181–208.

[53] Gopalan, S., Katz, J., and Liu, H. Effect of gap size on tip leakage cavitation inception, associated noise and flow structure. *Journal of Fluids Engineering 124*, 4 (2002), 994–1004.

[54] Gourdain, N. *Simulation numérique des phénomènes de dcollement tournant dans les compresseurs axiaux.* PhD thesis, Ecole Centrale de Lyon, 2005.

[55] Gourdain, N., and Leboeuf, F. Unsteady Simulation of an Axial Compressor Stage With Casing and Blade Passive Treatments. *Journal of Turbomachinery 131* (2009), 021013.

[56] Govindaraju, S., and Saffman, P. Flow in a turbulent trailing vortex. *The Physics of Fluids 14(10)* (1971), 2074–2080.

[57] Graff, M. *Effects of stator pressure field on upstream rotor performance.* PhD thesis, MIT, 1996.

[58] Graftieaux, L., Michard, M., and Grosjean, N. Combining PIV, POD and vortex identification algorithms for the study of unsteady turbulent swirling flows. *Measurement Science and Technology 12*, 9 (2001), 1422–1429.

[59] Greitzer, E., Tan, C., and Graf, M. *Internal Flow: Concepts and Applications.* Cambridge University Press, 2004.

[60] Haertig, M., Pfeifer, H., and von Stein, H. Comparaison entre les mésures par anémometre a fil chaud et par méthode Doppler différentielle en lumière laser. *ISL NOTICE N 25/71* (1971).

[61] Hah, C., Bergner, J., and Schiffer, H. Short Length-scale rotating stall inception in a transonic axial compressor - criteria and mechanisms, 2006.

[62] Han, J., Lin, Y.-L., Schowalter, D., and Arya, S. Large eddy simulation of aircraft wake vortices within homogeneous turbulence: Crow instability. *AIAA Journal 38(2)* (2000), 292–300.

[63] Hathaway, M. Passive Endwall Treatments for Enhancing Stability.

[64] Heaton, C. Optimal growth of the Batchelor vortex viscous modes. *Journal of Fluid Mechanics 592* (2007), 495–505.

[65] Heaton, C., and Peake, N. Transient growth in vortices with axial flow. *Journal of Fluid Mechanics 587* (2007), 271–301.

[66] Heyes, A., Jones, R., and Smith, D. Wandering of wing-tip vortices. In *12 th International Symposium on Applications of Laser Techniques to Fluid Mechanics, Lisbon, Portugal* (2004), pp. 12–15.

[67] Hinze, J. Author Turbulence; an introduction to its mechanism and theory. *New York, McGraw-Hill, 1959.* (1959).

[68] Holton, J. An introduction to dynamic meteorology. In *2nd ed.* Academic, New York, chap 8, 1979.

[69] Hopfinger, E., Browand, F., and Gagne, Y. Turbulence and waves in a rotating tank. *J. Fluid Mech. 125* (1982), 505–534.

[70] Huerre, P., and Rossi, M. Hydrodynamic instabilities in open flows. In *Cambridge university press.* Godrèche, C. and Manneville, P. (eds), 1906, pp. 164–169.

[71] Illy, H. *Contrôle de l'écoulement au-dessus d'une cavité en régime transsonique.* PhD thesis, École Centrale Lyon, 2005.

[72] Inoue, M., and Furukawa, M. Physics of tip clearance flow in turbomachinery. *ASME paper FEDSM2002-31184* (2002).

[73] Inoue, M., and Kuroumaru, M. Structure of tip clearance flow in an isolated axial compressor rotor. *Transactions of the ASME 111* (1989).

[74] Jacquin, L. Phenomenological description and simplified modelling of the vortex wake issuing from a jet in a crossflow. *Recherche Aérospatiale-French edition-* (1994), 117–117.

[75] Jacquin, L., Fabre, D., Geffroy, P., and Coustols, E. The properties of a transport aircraft wake in the extended near field- An experimental study. In *AIAA, Aerospace Sciences Meeting and Exhibit, 39 th, Reno, NV* (2001).

[76] Jacquin, L., and Pantano, C. On the persistence of trailing vortices. *J. Fluid Mech. 471* (2002), 159–168.

[77] Jensen, K. Flow measurements. *Journal of the Brazilian Society of Mechanical Sciences and Engineering 26* (2004), 400–419.

[78] Jeong, J., and Hussain, F. On the identification of a vortex. *Journal of Fluid Mechanics Digital Archive 285* (2006), 69–94.

[79] Jiang, H., Lu, Y., Yuan, W., and Li, Q. An experimental investigation on the unsteady excitation effect of casing treatment on a low speed compressor. *Proceedings of GT2007, ASME Turbo Expo 2007: Power for land, sea and air* (2007).

[80] Kaden, H. Aufwicklung einer unstabilen Unstetigkeitsfläche. *Archive of Applied Mechanics (Ingenieur Archiv) 2*, 2 (1931), 140–168.

[81] Kamm, J. *Shape and stability of twodimensional uniform vorticity regions*. PhD thesis, California Institue of Technology, Pasadena, 1987.

[82] Kang, E., Tan, C., and Breuer, K. Control of leakage flows using periodic excitation. In *Fluids 2000 Conference and Exhibit, Denver, CO* (2000).

[83] Khorrami, M. On the viscous modes of instability of a trailing line vortex. *J. Fluid Mech. 225* (1991), 197–212.

[84] Kinser, R., Furey, D., and Rediniotis, O. Calibration neural network for a novel omni-directional velocity probe-probenet. *ASME* (1996).

[85] Kress, W., and Lotstedt, P. Time step restrictions using semi-implicit methods for the incompressible Navier-Stokes equations. Tech. rep., Tech. Rep, 2004.

[86] Lacaze, L., Ryan, K., and Le Dizes, S. Elliptic instability in a strained batchelor vortex. *J. Fluid Mech. 577* (2007), 341–361.

[87] Lagnado, R., Phan-Thien, N., and Leal, L. The stability of two-dimensional linear flows. *Physics of Fluids 27* (1984), 1094.

[88] Lakshminarayana, B., and Horlock, J. Tip-clearance flow and losses for an isolated compressor blade. *Aeronautical Research Council Reports and Memoranda 3316* (1963).

[89] Lakshminarayana, B., Zaccaria, M., and Marathe, B. Structure of the tip clearance flow in axial flow compressors. *Tenth internation sympposium on air breathing engines, september 1-6 1991, Nottimgham, U.K.* (1992).

[90] Lamb, H. Hydrodynamics. In *Cambridge university press*. 1906.

[91] Laporte, F., and Corjon, A. Direct nupmerical simulation of the elliptic instability of a vortex pair. *Physcis of Fluids 12*, 5 (2000), 1016–1031.

[92] Le Dizes, S. Viscous critical-layer analysis of vortex normal modes. *Studies in applied mathematics 112* (2004), 315–332.

[93] Le Dizès, S., and Fabre, D. Large-Reynolds-number asymptotic analysis of viscous centre modes in vortices. *Journal of Fluid Mechanics 585* (2007), 153–180.

[94] Le Sant, Y. *Le Logiciel de traitement ODP*, 2008.

[95] Lehoucq, R., Sorensen, D., and Yang, C. ARPACK users' guide: solution of large-scale eigenvalue problems with implicitly restarted Arnoldi methods.

[96] Leibovitch, S., and Stewartson, K. A sufficient condition for the instability of columnar vortices. *J. Fluid Mech. 126* (1983), 335–356.

[97] Lessen, M., Singh, P., and Paillet, F. The stability of a trailing line vortex. part 1. inviscid theory. *Journal of Fluid Mechanics 63*, 4 (1974), 753–763.

[98] Leweke, T., and Williamson, C. Cooperative elliptic instability of a vortex pair. *Journal of Fluid Mechanics 360* (1998), 85–119.

[99] Liu, H.-T. Effects of ambient turbulence on the decay of a trailing vortex wake. *J. of Aircraft 29(2)* (1992), 255–263.

[100] Loiseleux, T., Chomaz, J., and Huerre, P. The effect of swirl on jets and wakes: linear instability of the rankine vortex with axial flow. *Physics of Fluids 10(5)* (1998), 1120–1134.

[101] Luton, J., and Ragab, S. The three-dimensional interaction of a vortex pair with a wall. *Physics of Fluids 9* (1997), 2967.

[102] Ma, R., and Devenport, W. Tip gap effects on the unsteady behavior of a tip leakage vortex. *AIAA journal 45*, 7 (2007), 1713–1724.

[103] Mailach, R., Sauer, H., and Vogeler, K. The periodical interaction of the tip clearance flow in the blade rows of axial compressors. *ASME Paper* (2001), 0299.

[104] Martin, J., and Meiburg, E. On the stability of the swirling jet shear layer. *Physics of Fluids 6(1)* (1993), 424–426.

[105] Martin, J., and Meiburg, E. Nonlinear axisymmetric and three-dimensional vorticity dynamics in a swirling jet model. *Physics of Fluids 8(7)* (1996), 1917–1928.

[106] Martin, J., and Meiburg, E. The growth and nonlinear evolution of helical perturbations in a swirling jet model. *Eur. J. Mech. B/Fluids 17(4)* (1998), 639–651.

[107] Maxworthy, T., Hopfinger, E., and Redekopp, L. Wave motions on vortex core. *J. Fluid Mech. 151* (1985), 141–165.

[108] Mayer, E., and Powell, K. Viscous and inviscid instabilities of a trailing vortex. *Journal of Fluid Mechanics 245* (1992), 91–114.

[109] McGrath, S., and Shaw, L. Active control of shallow cavity acoustic resonance. *AIAA paper 1949* (1996), 1996.

[110] Mehta, R., and Bradshaw, P. Design rules for small low speed wind tunnels. *Aeronautical Journal 83*, 827 (1979), 443–449.

[111] Melander, M., and Hussain, F. Core dynamics on a vortex column. *Fluid Dyn. Res. 13* (1994), 1–37.

[112] Meleshko, V., and van Heijst, G. On chaplygin's investigations of twodimensional vortex structures in an inviscid fluid. *J. Fluid Mech. 272* (1994), 157–182.

[113] Moffatt, H. *Dynamique des fluides*. Éd. de l&École Polytechnique, 1995.

[114] Moore, D. The rolling up of a semi-infinite vortex sheet. *Proceedings of the Royal Society of London. Series A, Mathematical and Physical Sciences* (1975), 417–430.

[115] Moore, D., and Saffman, P. Structure of a line vortex in an imposed strain. *Aircraft Wake Turbulence* (1971), 339–354.

[116] Nycander, J. Refutation of stability proofs for dipole vortices. *Physics of Fluids A 4 3* (1991), 467–476.

[117] Olendaru, C., and Sellier, A. Viscous effects in the absolute-convective instability of the batchelor vortex. *J. Fluid Mech. 459* (2002), 371–396.

[118] Pailhas, G., and Touvet, Y. Turbulence et instabilité de deux tourbillons contrarotatifs de bouts d'ailes avec le sol. *AAAF. Orleans, mars* (2000).

[119] Payne, F., Ng, T., and Nelson, R. Seven hole probe measurement of leading edege vortex flows. *Experiments in Fluids 7* (1989), 1–8.

[120] Phillips, W., and Graham, J. Reynolds-stress measurements in a turbulent trailing vortex. *J. Fluid Mech. 147* (1984), 353–371.

[121] Pierrehumbert, R. A family of steady, translating vortex pairs with distributed vorticity. *Journal of Fluid Mechanics 99*, 1 (1980), 129–144.

[122] Pironneau, O., Hecht, F., Hyaric, A., and Ohtsuka, K. FreeFEM. *URL: http://www.freefem.org* (2006).

[123] Pisasale, A., and Ahmed, N. A novel method for extending the calibration range of five-hole probe for highly three-dimensional flows. *Flow measurement and Instrumentation 13* (2002), 23–30.

[124] Pradeep, D., and Hussain, F. Transient growth of perturbations in a vortex column. *Journal of Fluid Mechanics 550* (2006), 251–288.

[125] Rains, D. *Tip clearance flows in axial flow compressors and pump*. PhD thesis, California Institute of Technology, 1954.

[126] Rayleigh, L. On the stability, or instability, of certain fluid motions. *Proc. London Math. Soc. s1-11* (1879), 57–72.

[127] Rayleigh, L. On the dynamics of revolving fluids. *Proc. R. Soc. Lond. 93* (1917), 148–154.

[128] Risso, F., Corjon, A., and Stoessel, A. Direct numerical simulations of wake vortices in intense homogeneous turbulence. *AIAA Journal 35(6)* (1997), 1030–1040.

[129] Robinson, A., and Saffman, P. Three-dimensional stability of an elliptical vortex in a straining field. *J. Fluid Mech. 142* (1984), 451–466.

[130] Saffman, P. *Vortex dynamics*. Cambridge monograph on mechanics and applied mathematics, 1992.

[131] Saffman, P., and Szeto, R. Equilibrium shapes of a pair of equal uniform vortices. *Physics of Fluids 23(12)* (1980), 2339–2342.

[132] Sarpkaya, T., and Daly, J. Effect of ambient turbulence on trailing vortices. *Journal of aircraft 24*, 6 (1987), 399–404.

[133] Schmid, P., and Henningson, D. *Stability and transition in shear flows*. Springer, 2001.

[134] Schwartz, L. A semi-analytic approach to the self-induced motion of vortex sheets. *Journal of Fluid Mechanics Digital Archive 111* (1981), 475–490.

[135] Sipp, D., and Jacquin, L. Widnall instabilities in vortex pairs. *Physics of Fluids 15*, 7 (2003), 1861–1874.

[136] Sipp, D., Jacquin, L., and Cosssu, C. Self-adaptation and viscous selection in concentrated two-dimensional vortex dipoles. *Physics of Fluids 12* (2000), 245.

[137] Sirakov, B., and Tan, C. Effect of unsteady stator wake rotor double leakage tip clearance flow interaction on time-average compressor performance. *Journal of Turbomachinery 125* (2003), 465.

[138] Spalart, P. Airplane trailing vortices. *Annual Review of Fluid Mechanics 30*, 1 (1998), 107–138.

[139] Spalart, P., and Wray, A. Initiation of the Crow instability by atmospheric turbulence. *NASA Ames Research Center, The Characterisation and Modification of Wakes from Lifting Vehicles in Fluids p(SEE N 97-17635 01-02)* (1996).

[140] Stanek, M., Raman, G., Kibens, V., Ross, J., Odedra, J., and Peto, J. Control of cavity resonance through very high frequency forcing. In *AIAA/CEAS, Aeroacoustics Conference and Exhibit, 6 th(21 st AIAA Aeroacoustics Conference), Lahaina, HI* (2000).

[141] Stewartson, K., and Brown, S. Near-neutral centre-modes as inviscid perturbations to a trailing line vortex. *J. Fluid Mech. 156* (1985), 387–399.

[142] Stewartson, K., and Capell, K. On the stability of ring modes in a trailing line vortex: the upper neutral points. *J. Fluid Mech. 156* (1985), 369–386.

[143] Stewartson, K., Ng, T., and Brown, S. Viscous centre modes in the stability of swirling poiseuille flow. *Phil. Trans. R. Soc. Lond. A 324* (1988), 473–512.

[144] Storer, J., and Cumpsty, N. Tip leakage flow in axial compressors. *Gas turbine and aeroengine congress and exposition* (1990).

[145] Storer, J., and Cumpsty, N. Tip leakage flow in axial compressors. *Journal of Turbomachinery 113* (1991), 252.

[146] Storer, J., and Cumpsty, N. An approximate analysis and prediction method for tip clearance loss in axial compressors. *Journal of Turbomachinery 116* (1994), 648.

[147] Storer, J., and Cumpsty, N. An approximate analysis and prediction method for tip clearance loss in axial compressors. *Journal of Turbomachinery 116* (1994), 648.

[148] Sumner, D. A comparison of data-reduction methods for a seven-hole probe. *Journal of Fluids Engineering 124* (2002), 523–527.

[149] Thomas, P., and Auerbach, D. The observation of the simultaneous development of a long-and a short-wave instability mode on a vortex pair. *Journal of Fluid Mechanics 265* (1994), 289–302.

[150] Thomson, W. L. K. On vortex atoms. *Proc. Roy. Soc. Edinburgh 6* (1867), 15–24.

[151] Tombach, I. Observations of atmospheric effects on vortex wake behaviour. *Journal of Aircraft* (1973), 641–647.

[152] Tritton, D. Physical Fluid Dynamics. In *Clarendon*. New York, 1988.

[153] Tropea, C., Yarin, A., and Foss, J. *Handbook of experimental fluid mechanics*. Springer-Verlag Berlin Heidelberg, 2007.

[154] Tsai, C.-Y., and Widnall, S. The stability of short waves on a straight vortex filament in a weak externally imposed strain field. *J. Fluid Mech. 73* (1976), 721–733.

[155] van Geffen, J., and van Heijst, G. Viscous evolution of 2d dipolar vortices. *Fluid Dynamics Research 22* (1998), 191–213.

[156] Wiltse, J., and Glezer, A. Direct excitation of small-scale motions in free shear flows. *Physics of Fluids 10* (1998), 2026–2036.

[157] Yamada, K., Furukawa, M., Inoue, M., and FUNAZAKI, K. Numerical analysis of tip leakage flow field in a transonic axial compressor rotor. *IGTC paper 95* (2003), 2003.

[158] You, D., Wang, M., Moin, P., and Mittal, R. Effects of tip-gap size on the tip-leakage flow in a turbomachinery cascade. *Physics of Fluids 18* (2006), 105102.

[159] Zilliac, G. Calibration of seven-hole pressure probes for use in fluid flows with large angularity. *NASA TM 102200* (1989).

[160] Zilliac, G., Chow, J., Dacles-Mariani, J., and Bradshaw, P. Turbulent structure of a wingtip vortex in the near field. *AIAA 24th Fluid dynamics conference, Orlando, Florida AIAA-93-3011* (1993).